ΕΘΝΙΚΟ ΜΕΤΣΟΒΙΟ ΠΟΛΥΤΕΧΝΕΙΟ
ΣΧΟΛΗ ΕΦΑΡΜΟΣΜΕΝΩΝ ΜΑΘΗΜΑΤΙΚΩΝ & ΦΥΣΙΚΩΝ ΕΠΙΣΤΗΜΩΝ
ΤΟΜΕΑΣ ΦΥΣΙΚΗΣ

ΕΘΝΙΚΟ ΚΕΝΤΡΟ ΕΡΕΥΝΩΝ ΦΥΣΙΚΩΝ ΕΠΙΣΤΗΜΩΝ "ΔΗΜΟΚΡΙΤΟΣ"
ΙΣΝΤΙΤΟΥΤΟ ΠΥΡΗΝΙΚΗΣ ΚΑΙ ΣΩΜΑΤΙΔΙΑΚΗΣ ΦΥΣΙΚΗΣ

Μελέτη της Ικανότητας Ανίχνευσης της Διάχυτης Ροής Αστροφυσικών Νετρίνο Υψηλής Ενέργειας με το Τηλεσκόπιο KM3NeT/ARCA

ΔΙΔΑΚΤΟΡΙΚΗ ΔΙΑΤΡΙΒΗ

του

Κωνσταντίνου Χ. Πικούνη

ΕΠΙΒΛΕΠΟΝΤΕΣ: Γεώργιος Τσιπολίτης
Καθηγητής Ε.Μ.Π.

Αικατερίνη Τζαμαριουδάκη
Διευθύντηρια Ερευνών Ε.Κ.Ε.Φ.Ε. "Δημόκριτος"

Χρήστος Μάρκου
Διευθυντής Ερευνών Ε.Κ.Ε.Φ.Ε. "Δημόκριτος"

NATIONAL TECHNICAL UNIVERSITY OF ATHENS
SCHOOL OF APPLIED MATHEMATICAL & PHYSICAL SCIENCES
DEPARTMENT OF PHYSICS

NATIONAL CENTER FOR SCIENTIFIC RESEARCH "DEMOKRITOS"
INSTITUTE OF NUCLEAR AND PARTICLE PHYSICS

Study of the Discovery Potential of the KM3NeT/ARCA Neutrino Telescope to the Diffuse Astrophysical High Energy Neutrino Flux

DOCTORAL OF PHILOSOPHY
PHYSICS

by

Konstantinos C. Pikounis

SUPERVISORS: Georgios Tsipollitis
Professor at the National Technical University of Athens

Ekaterini Tzamariudaki
Director of Research at NCSR "Demokritos"

Christos Markou
Director of Research at NCSR "Demokritos"

Abstract

Even though Cosmic Rays were discovered more than a century ago, the acceleration mechanisms of protons and heavier nuclei to ultra high energies still remain unknown. Being charged they are deflected by magnetic fields so they can not reveal the astrophysical objects responsible for their acceleration. Nevertheless, at the astrophysical objects where cosmic rays are accelerated, neutrinos are also produced. Neutrinos, being neutral, are not deflected by magnetic fields and they are not significantly absorbed by the interstellar medium, so, when detected, they can point back to their production sites. Neutrino telescopes are being deployed in the sea, in lakes and in the ice of Antarctica. They instrument large volumes of medium (water or ice) and they detect neutrinos indirectly by detecting Cherenkov light produced by neutrino-induced charged particles.

KM3NeT is a collaboration building the next generation neutrino telescopes in the Mediterranean Sea. Currently two detectors are being deployed by KM3NeT; the Oscillation Research with Cosmics in the Abyss - ORCA detector, which aims to study the fundamental properties of neutrinos as well as the Astroparticle Research with Cosmics in the Abyss - ARCA telescope. The main science objectives of the ARCA telescope are the detection of neutrinos from astrophysical sources and the measurement of the diffuse astrophysical high energy flux. In this thesis a study of the discovery potential of the KM3NeT/ARCA telescope to the diffuse astrophysical high energy neutrino flux using High Energy Starting Events (HESE) is presented. The use of HESE comprises a novel approach for the KM3NeT collaboration.

In Chapter 1 the production mechanisms of Cosmic Rays and astrophysical neutrinos are described. The detection principle of neutrino telescopes, the background for underwater neutrino telescopes as well as the major existing neutrino telescopes are presented in Chapter 2. The KM3NeT collaboration is described in Chapter 3 as well as the KM3NeT detectors. In Chapter 4 GRBNeT - a project that designed, built and successfully deployed an autonomous prototype neutrino detector is discussed. In the following chapter (Chapter 5) the tools used in KM3NeT to perform Monte Carlo simulations of the detector response to signal and background events as well as the reconstruction tools are detailed. CORSIKA program, which is the most widely used tool to simulate atmospheric showers, has been used in order to create a sample of background atmospheric events for the ARCA telescope. These efforts are detailed in Chapter 6. A novel tool, MAMBA rejection, created in order to select High Energy Starting Track events inside ARCA telescope and reject those track events that enter the detector, is described in Chapter 7. Moreover a sensitivity and a discovery potential analysis of ARCA to the diffuse astrophysical high energy neutrino flux using High Energy Starting Track events is described. Furthermore, a sample of background atmospheric events simulated with CORSIKA has been used to demonstrate the power of the self-veto effect (the rejection of atmospheric neutrinos, accompanied by muons created at the same atmospheric shower, interacting inside the detector by identifying the

muons entering the detector). In Chapter 8 a tool designed to differentiate shower-like from track-like events is detailed. Also, an analysis of the discovery potential of ARCA to the diffuse astrophysical high energy neutrino flux using only shower-like events selected by that tool is presented. The tools described in the previous chapters are combined in order to create a sample of High Energy Starting Events as described in Chapter 9. The discovery potential of ARCA to the diffuse astrophysical high energy neutrino flux using High Energy Starting Events is presented. ARCA is expected to make a 5σ discovery of the diffuse astrophysical high energy neutrino flux with a probability of 50% and 90% in less than 0.5 and approximately 0.8 years, respectively, using High Energy Starting Events.

Εισαγωγή

Οι κοσμικές ακτίνες παρατηρήθηκαν για πρώτη φορά πριν από έναν αιώνα, ακόμα όμως παραμένουν ασαφείς οι πηγές και ο μηχανισμός επιτάχυνσή τους, διότι σκεδάζονται από τα μαγνητικά πεδία των γαλαξιών και χάνονται οι πληροφορίες σχετικά με την προέλευσή τους. Παρόλα αυτά αναμένεται ότι στα αστροφυσικά αντικείμενα όπου οι κοσμικές ακτίνες επιταχύνονται σε υπέρυψηλές ενέργειες παράγονται και νετρίνο υψηλής ενέργειας. Τα νετρίνο δεν έχουν ηλεκτρικό φορτίο με αποτέλεσμα να μην σκεδάζονται από τα μαγνητικά πεδία και επειδή αλληλεπιδρούν ασθενώς με την ύλη πρακτικά δεν απορροφώνται. Η ανίχνευση, λοιπόν, νετρίνο αστροφυσικής προέλευσης, μπορεί να αποκαλύψει τα αστροφυσικά αντικείμενα όπου αυτά παράγονται και τα οποία είναι υπεύθυνα για την επιτάχυνση των κοσμικών ακτίνων. Συνεπώς τα νετρίνο αποτελούν μοναδικούς φορείς αστροφυσικής πληροφορίας. Τα τηλεσκόπια νετρίνο κατασκευάζονται στα βάθη θαλασσών, λιμνών ή στους πάγους της Ανταρκτικής, καταλαμβάνουν πολύ μεγάλους όγκους και ανιχνεύουν τα νετρίνο έμμεσα, καθώς ανιχνεύουν την ακτινοβολία Cherenkov που εκπέμπουν τα φορτισμένα σωματίδια τα οποία παράγονται κατά την αλληλεπίδραση των νετρίνο με την ύλη.

Το πείραμα KM3NeT κατασκευάζει ανιχνευτές νετρίνο νέας γενιάς. Υπό τη σκέπη του πειράματος αυτού ποντίζονται δύο ανιχνευτές νετρίνο στα βάθη της Μεσογείου θάλασσας, ο ανιχνευτής Oscillation Research with Cosmics in the Abyss - ORCA του οποίου ο κύριος επιστημονικός στόχος είναι η μελέτη των βασικών σωματιδιακών ιδιοτήτων των νετρίνο και το τηλεσκόπιο νετρίνο Astroparticle Research with Cosmics in the Abyss - ARCA. Οι κύριοι επιστημονικοί στόχοι του τηλεσκοπίου ARCA είναι η ανίχνευση νετρίνο από αστροφυσικές πηγές καθώς και η μελέτη της διάχυτης αστροφυσικής ροής νετρίνο υψηλής ενέργειας. Στην παρούσα διατριβή παρουσιάζεται η μελέτη της δυνατότητας ανακάλυψης της διάχυτης αστροφυσικής ροής νετρίνο υψηλής ενέργειας με το τηλεσκόπιο KM3NeT/ARCA, χρησιμοποιώντας γεγονότα υψηλής ενέργειας που αλληλεπιδρούν εντός του ανιχνευτή. Η χρήση τέτοιων γεγονότων αποτελεί μια καινοτόμο προσέγγιση για το πείραμα KM3NeT.

Η παρούσα διατριβή αποτελείται από εννέα κεφάλαια. Στο Κεφάλαιο 1 παρουσιάζονται οι μηχανισμοί επιτάχυνσης των κοσμικών ακτίνων και τα αστροφυσικά αντικείμενα που αναμένεται να παράγουν νετρίνο υψηλής ενέργειας. Στην συνέχεια στο Κεφάλαιο 2 περιγράφεται η αρχή ανίχνευσης νετρίνο υψηλής ενέργειας, το υπόβαθρο των υποθαλάσσιων τηλεσκοπίων νετρίνο καθώς και τα σημαντικότερα εν λειτουργία τηλεσκόπια νετρίνο. Το πείραμα KM3NeT και οι ανιχνευτές νετρίνο ORCA και ARCA παρουσιάζονται στο Κεφάλαιο 3. Στο Κεφάλαιο 4 περιγράφονται οι δραστηριότητες του ερευνητικού έργου GRBNeT στα πλαίσια του οποίου σχεδιάστηκε, κατασκευάστηκε και ποντίστηκε επιτυχώς αυτόνομος ανιχνευτής νετρίνο. Στο επόμενο κεφάλαιο (5) παρουσιάζονται τα εργαλεία λογισμικού που χρησιμοποιούνται στο πείραμα KM3NeT για την προσομοίωση της απόκρισης του τηλεσκοπίου νετρίνο ARCA σε γεγονότα σήματος και υποβάθρου. Για την προσομοίωση ατμοσφαιρικών καταιονισμών σωματιδίων το πιο διαδεδομένο πρόγραμμα είναι το πρόγραμμα CORSIKA το οποίο χρησιμοποι- ήθηκε για την προσομοίωση γεγονότων υποβάθρου για το τηλεσκόπιο ARCA. Στο Κεφάλαιο 6 αναλύονται

αυτές οι δραστηριότητες. Στο Κεφάλαιο 7 περιγράφεται ένα καινοτόμο εργαλείο, το MAMBA rejection, το οποίο δημιουργήθηκε για την αξιόπιστη επιλογή γεγονότων νετρίνο με την υπογραφή τροχιάς που αλληλεπιδρούν εντός του όγκου του τηλεσκοπίου ARCA και για την ταυτόχρονη απόρριψη γεγονότων τροχιάς που εισέρχονται σε αυτό. Επίσης ανα- πτύσσεται η μελέτη της ευαισθησίας του τηλεσκοπίου και της ικανότητας ανακάλυψης της διάχυτης ροής νετρίνο υψηλής ενέργειας αστροφυσικής προέλευσης, χρησιμοποιώντας γεγονότα τροχιάς που αλληλεπιδρούν μέσα στον όγκο του. Τέλος χρησιμοποιώντας προσομοιωμένα γεγονότα ατμοσφαιρικών καταιγισμών με το πρόγραμμα CORSIKA, καταδεικνύεται η αξία του self-veto effect, δηλαδή της απόρριψης ατμοσφαιρικών νετρίνο, τα οποία συνοδεύονται από ατμοσφαιρικά μιόνια που δημιουργήθηκαν στον ίδιο ατμοσφαιρικό καταιονισμό, και τα οποία αλληλεπιδρούν μέσα στον όγκο του ανιχνευτή λόγω της ανίχνευσης των εισερχομένων μιονίων. Στη συνέχεια, στο Κεφάλαιο 8, αναπτύσσεται άλλη μια καινοτόμος μέθοδος η οποία αναπτύχθηκε για την επιλογή των γεγονότων καταιγισμού και τον διαχωρισμό τους από τα γεγονότα τροχιάς. Επίσης αναλύεται και η μελέτη της ικανότητας ανακάλυψης της διάχυτης ροής νετρίνο υψηλής ενέργειας αστροφυσικής προέλευσης από το τηλεσκοπίο ARCA χρησιμοποιώντας μόνο γεγονότα καταιγισμού επιλεγέντα με την προαναφερθείσα μέθοδο. Τα εργαλεία που παρουσιάστηκαν στα δυο προηγούμενα κεφάλαια μπορούν να συνδυαστούν με αποτέλεσμα την επιλογή γεγονότων υψηλής ενέργειας που αλληλεπιδρούν μέσα στον όγκο του τηλεσκοπίου ARCA. Στο Κεφάλαιο 9 παρουσιάζεται η εν λόγω ανάλυση καθώς και η μελέτη της ικανότητας ανακάλυψης της διάχυτης ροής νετρίνο υψηλής ενέργειας αστροφυσικής προέλευσης από το τηλεσκοπίου ARCA χρησιμοποιώντας αυτά τα γεγονότα. Το τηλεσκόπιο ARCA αναμένεται να προβεί σε ανακάλυψη με επίπεδο σημαντικότητας 5σ με πιθανότητα 50% και 90% της διάχυτης ροής νετρίνο υψηλής ενέργειας αστροφυσικής προέλευσης σε λιγότερο από 0.5 χρόνια λειτουργίας και σε περίπου 0.8 λειτουργίας αντιστοίχως, γεγονότα υψηλής ενέργειας που αλληλεπιδρούν μέσα στον όγκο του. Τέλος το Κεφάλαιο 9 αποτελεί την κατακλείδα της παρούσας διδακτορικής διατριβής.

Acknowledgments

This PhD thesis is the conclusion of many years of hard work. In that period of time, I experienced both exciting and hard moments, moments I felt that I was fulfilling a life's purpose and really contributing to something bigger than myself and other moments I felt that I should reconsider the path I was following and choose a different one, a much simpler one... In these years, I learnt many things, saw many places and more importantly met many people, so many wonderful people that stood by me through these ups and downs that I would like to mention.

I would like to start by expressing my deepest gratitude to my supervisors Dr. Aikaterini (Katerina) Tzamarioudaki and Dr. Christos Markou, Directors of research in the Institute of Nuclear and Particle Physics (INPP) in NCSR "Demokritos". Both Katerina and Christos have been much more than supervisors to me and without their guidance and support I would probably not have completed this challenge. I want to thank Katerina for her continuous guidance, for her willingness to help me when I needed help and for always motivating me to improve. I would also like to thank Katerina for her help in reading and correcting this thesis. In addition, I want to express my gratitude to Christos for his support, for providing me with new and fresh ideas when problems occurred, and also for his efforts to offer me the best conditions to work (including finding funds for giving me the opportunity to attend conferences and schools). Also, I would like to thank my third supervisor Professor Yorgos Tsipolitis at the School of applied Mathematical and Physical Sciences of the National Technical University of Athens.

My thanks should also be addressed to all the people I have met in the KM3NeT collaboration, for everything I have learnt from them and for all the help they so generously offered me. I would like to thank specifically Dr. Rosa Coniglione, head of the High Energy Astrophysics working group, for inviting me in Catania and also Dr. Kay Graff for all his help with the IT services and with the problems concerning Lyon-CC cluster.

From the people of NCSR "Demokritos" I would like to thank Georgia Kareli for being such a positive and kind person and for generously providing help to overcome all the problem that occurred in the day to day activities of NCSR "Demokritos". I would also like to thank both Christos Filippidis and Georgios Smyris for their help to overcome any problems related to the computer-cluster of the INPP.

During the time I spent in NCSR "Demokritos" I met many people whom I want to acknowledge. Dr. Victoria Giakoumopoulou and Dr. Stilianos Kessisoglou for being always very helpful with all the questions I had with *ROOT*. Dr Iasonas Topsis-Giotis for his help with various different codes and for his assistance in "killing" any scarce free time over a chess board. Dr. Eleni Ntomari, for all her help with any problems I had and for always shedding a positive light on dark and difficult tasks. Many thanks should be addressed to Dr. Evangelia (Lilia) Drakopoulou for the valuable help she gave me throughout these years, for all the time we spent together in meetings, conferences, etc, and for being a very good

friend. George Androulakis, QA/QC manager of the KM3NeT collaboration, for providing us with his “High Quality” character and spirit and being there for me when I needed him. I would also like to thank all the above as well as Anna Sinopoulou, Dimitirs Tzanetatos, Dimitirs Stavropoulos, Dr. Ariadni Antonaki, Liza Paspalaki, Christos Bagatelas and Voula Tsagli for making my lunch breaks really enjoyable and for all the beautiful memories I have with them.

My utmost respect, love and gratitude belongs with my family. I will not detail my reasons here for they could easily fill many chapters of this manuscript. So, I just want dedicate my thesis to them and to thank each and every one of them: my wife Georgia, my parents Christos and Soula and my brother Nikos for being in my life.

Σας Ευχαριστώ!

Per aspera ad astra

Contents

Abbreviations

abbreviation	description
AGNs	Active Galactic Nuclei
ARCA	Astroparticle Research with Cosmics in the Abyss
BDT	Boosted Decision Tree
CC	Charge Current
CLU	Coincidence Logic Unit
CMB	cosmic microwave background
CR	Cosmic Rays
DAQ	Data Acquisition
DIS	Deep Inelastic Scatering
DOM	Digital Optical Module
DU	Detection Unit
GCN	Gamma-ray Coordinates Network
GRBs	Gamma Ray Bursts
HE	High Energy
HESE	High Energy Starting Events
HEST	High Energy Starting Tracks
HV	High Voltage
JTE	JTriggerEfficiency
MAMBA	Multiple Atmospheric Muon BAckground
MC	Monte Carlo
MDP	Model Discovery Potential
MRF	Model Rejection Factor
MRP	Model Rejection Potential
NC	Neutral Curent
OM	Optical Module
ORCA	Oscillation Research with Cosmics in the Abyss
OW	OneWeight
PDF	Probability Density Function
PMT	PhotoMultiplier Tube
ToT	Time over Threshold
UHECR	Ultra High Energy Cosmic Rays

Chapter 1

Κοσμικές Ακτίνες και Νετρίνο αστροφυσικής προέλευσης

1.1 Κοσμικές Ακτίνες

1.1.1 Γενικά

Η ατμόσφαιρα της Γης "βομβαρδίζεται" από ισοτροπική ροή φορτισμένων σωματιδίων που ονομάζονται κοσμικές ακτίνες (Cosmic Rays - CR) με ρυθμό περίπου 1 σωμάτιο /cm^2 /s. Η ανακάλυψή τους αποδίδεται στον Victor Hess ο οποίος, το 1912 χρησιμοποιώντας ένα αερόστατο, παρατήρησε ότι η ιονίζουσα ακτινοβολία σε ύψος περίπου 5 km είναι πολλαπλάσια αυτής που παρατηρείτο στην επιφάνεια της Γης. Αν και γνωρίζουμε την ύπαρξη των κοσμικών ακτίνων για περισσότερο από έναν αιώνα, παραμένουν ακόμα ασαφείς οι πηγές και ο μηχανισμός επιτάχυνσής τους καθώς αυτές σκεδάζονται από τα μαγνητικά πεδία των γαλαξιών με αποτέλεσμα να χάνεται η πληροφορία σχετικά με την προέλευσή τους. Είναι πλέον γνωστό ότι υπάρχουν πηγές στο σύμπαν ικανές να επιταχύνουν πρωτόνια και βαρύτερους πυρήνες σε ενέργειες της τάξης των 10^{11} GeV, δηλαδή σε ενέργειες 10^7 φορές μεγαλύτερες από αυτές που μπορούν να φτάσουν τα πρωτόνια στον επιταχυντή LHC του CERN. Οι σύγχρονες θεωρίες προβλέπουν την επιτάχυνση κοσμικών ακτίνων υπερ-υψηλών ενεργειών σε εξωτικά εξωγαλαξιακά αστροφυσικά αντικείμενα όπως είναι οι εκλάμψεις ακτίνων γ (Gamma Ray Bursts - GRBs) και οι ενεργοί γαλαξιακοί πυρήνες (Active Galactic Nuclei - AGNs), ενώ οι γαλαξιακές πηγές όπως οι υπερκαινοφανείς αστέρες (Supernovae) και τα υπολείμματά τους (Supernovae remnants) αναμένεται να μπορούν να επιταχύνουν κοσμικές ακτίνες σε ενέργειες της τάξης των 10^6 GeV [1].

1.1.2 Το φάσμα και η σύσταση της κοσμικής ακτινοβολίας

Το ενεργειακό φάσμα των κοσμικών ακτίνων (Εικόνα 1.1) εκτείνεται πάνω από 10 τάξεις μεγέθους (Εικόνα 1.1 αριστερά). Η ροή των κοσμικών ακτίνων μπορεί να προσεγγιστεί με ένα τριπλό νόμο δύναμης της μορφής: $\frac{dN}{dE} \propto E^{-\alpha}$ (αριθμός σωματιδίων ανά μονάδα επιφάνειας ανά μονάδα χρόνου και ανά μονάδα ενέργειας) όπου ο εκθέτης παίρνει τιμές [4, 5]:

- α ∼ 2.7 για 10 GeV < E < 3 PeV
- α ∼ 3.1 για 3 PeV < E < 3 EeV
- α ∼ 2.6 για 3 EeV < E (σε αυτή την ενεργειακή περιοχή η ροή παρουσιάζει κατώφλι αποκοπής - cutoff στα 100 EeV)

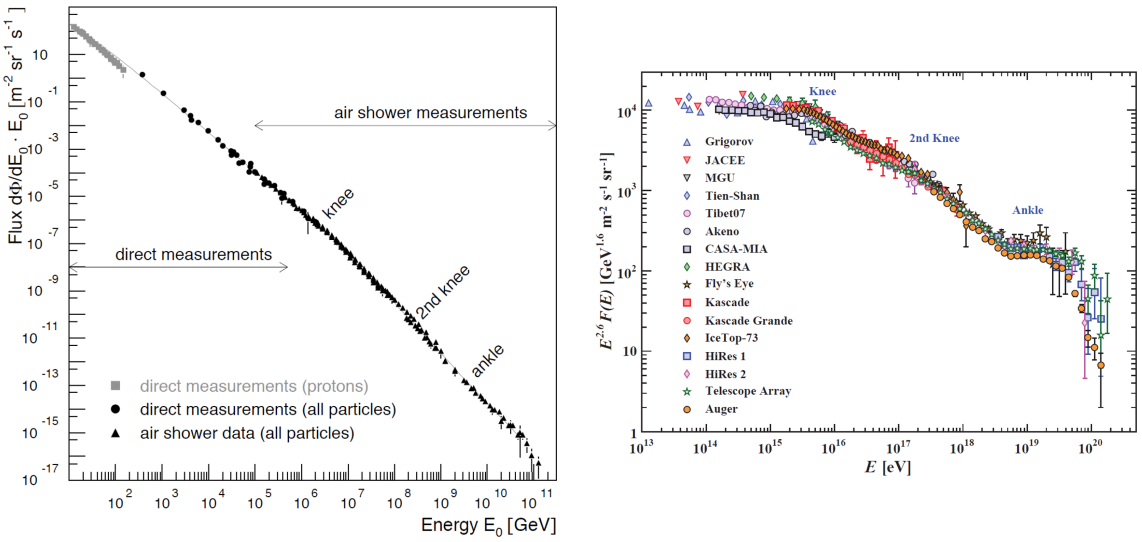

Figure 1.1: Η ροή της κοσμικής ακτινοβολίας συναρτήσει της ενέργειας των σωματιδίων. Σημειώνονται οι περιοχές knee και ankle. Αριστερά: Όλο το ενεργειακό εύρος. Εικόνα από [2]. Δεξιά: Οι μετρήσεις από διαφορετικά πειράματα στο ενεργειακό εύρος από 10 TeV. Εικόνα από [3].

Η περιοχή χαμηλής ενέργειας (E < 10 GeV) κυριαρχείται από τη συνεισφορά των φορτισμένων σωματιδίων του ηλιακού ανέμου συνεπώς η ροή σωματιδίων με τέτοιες ενέργειες αλλάζει ακολουθώντας τον ηλιακό κύκλο. Οι δυο περιοχές στις οποίες αλλάζει ο νόμος δύναμης χαρακτηρίζονται ως knee (∼ 3PeV) και ankle (∼ 3EeV). Στην Εικόνα 1.1 δεξιά όπου παρουσιάζεται το ενεργειακό φάσμα των κοσμικών ακτίνων για ενέργειες E > 10 TeV και η ροή έχει πολλαπλασιαστεί με $E^{2.6}$, διακρίνονται ευκρινέστερα τα knee και ankle.

Οι κοσμικές ακτίνες με ενέργειες έως το knee αλλά και μεγαλύτερες, θεωρούνται ότι προέρχονται από γαλαξιακές πηγές, όπως οι εκρήξεις υπερκαινοφανών και τα υπολείμματά τους. Λόγω του μαγνητικού πεδίου του Γαλαξία μας, οι κοσμικές ακτίνες παγιδεύονται σε αυτόν. Πιο συγκεκριμένα πρωτόνια με ενέργειες της τάξης των 10^{18}eV έχουν ακτίνα Larmor (γυροακτίνα) συγκρίσιμη με τις διαστάσεις της άλω του Γαλαξία μας, ενώ πρωτόνια με ενέργειες της τάξης των $5 \cdot 10^{18}$eV έχουν ακτίνα Larmor συγκρίσιμη με την ακτίνα του Γαλαξία μας. Επίσης, παρατηρήσεις δείχνουν ότι η σύσταση των κοσμικών ακτίνων γίνεται σταδιακά πιο πλούσια σε βαρύτερα στοιχεία καθώς η ενέργειά τους αυξάνει από το knee προς το ankle (βαρύτεροι πυρήνες έχουν μικρότερη ακτίνα larmor $L_R = \gamma \cdot mu_\perp/(|q| \cdot B)$). Συνεπώς, εκτιμάται ότι η συνεισφορά των κοσμικών ακτίνων που προέρχονται από εξωγαλαξιακές πηγές αυξάνει για ενέργειες που πλησιάζουν προς το ankle και ότι οι κοσμικές ακτίνες με ενέργεια μεγαλύτερη από αυτή του ankle προέρχονται αποκλειστικά από τέτοιες πηγές.

Στο φάσμα των κοσμικών ακτίνων στην περιοχή υπερ-υψηλής ενέργειας (Ultra High Energy Cosmic Rays - UHECRs) μετά το ankle, παρατηρείται κατώφλι αποκοπής ενέργειας περί τα 100 EeV. Σύμφωνα με θεωρητικά μοντέλα, οι κοσμικές ακτίνες με ενέργειες μεγαλύτερες από 10^{19}eV αλληλεπιδρούν με τα φωτόνια του μικροκυματικού υποβάθρου (cosmic microwave background - CMB) και παράγουν ένα σωματίδιο Δ^+ το οποίο διασπάται σε πιόνια και πρωτόνια ή νετρόνια με μικρότερες ενέργειες:

$$\begin{aligned} p + \gamma &\rightarrow \Delta^+ \rightarrow \pi^0 + p \\ p + \gamma &\rightarrow \Delta^+ \rightarrow \pi^+ + n \end{aligned} \tag{1.1}$$

Λόγω της πιο πάνω διαδικασίας, η απόσταση που μπορούν να διανύσουν τόσο υψηλοενεργειακές κοσμικές ακτίνες περιορίζεται καθώς το μήκος μέσης ελεύθερης διαδρομής (λαμβάνοντας υπόψιν την ενεργό διατομής της αλληλεπίδρασης και την ενεργειακή πυκνότητα των φωτονίων του μικροκυματικού υποβάθρου) είναι $\sim$ 50 Mpc για πρωτόνια με ενέργεια 10^{19}eV. Η διαδικασία αυτή είναι υπεύθυνη για το κατώφλι αποκοπής στην περιοχή υπερ-υψηλής ενέργειας του φάσματος των κοσμικών ακτίνων και ονομάζεται όριο Greisen–Zatsepin–Kuzmin (GZK limit).

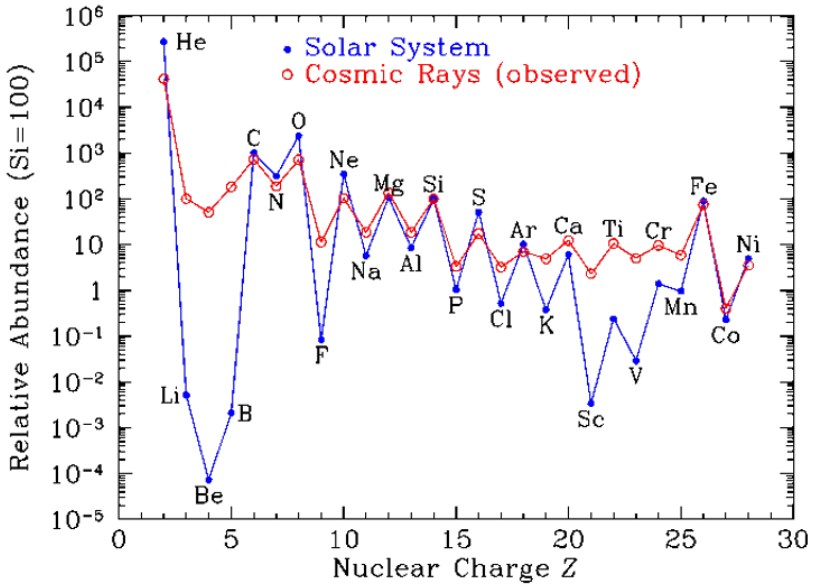

Figure 1.2: Η σύσταση των στοιχείων της κοσμικής ακτινοβολίας και του ηλιακού μας συστήματος. Εικόνα από [6].

Η σύσταση των στοιχείων που αποτελούν την κοσμική ακτινοβολία παρουσιάζει ομοιότητες με αυτή του ηλιακού μας συστήματος (Εικόνα 1.2) αλλά έχει 2 βασικές διαφορές [1, 4]. Η πρώτη διαφορά, που δεν είναι ακόμα πλήρως κατανοητή, είναι ότι η σχετική περιεκτικότητα σε Υδρογόνο στο ηλιακό μας σύστημα είναι πολύ μεγαλύτερη από αυτήν που παρατηρείται στις κοσμικές ακτίνες. Η δεύτερη είναι ότι οι περιεκτικότητες των ομάδων στοιχείων Li, Be, B και Sc, Ti, V, Cr, Mn είναι τάξεις μεγέθους μεγαλύτερες στις κοσμικές ακτίνες σε σχέση με αυτή που παρατηρείται στο ηλιακό μας σύστημα (Εικόνα 1.2). Τα στοιχεία αυτά δεν ευνοούνται κατά τις διαδικασίες της αστρικής πυρηνοσύνθεσης, αλλά παράγονται κυρίως από αντιδράσεις θραύσης βαρύτερων πυρήνων (κυρίως C, O και Fe) κατά την αλληλεπίδρασή τους με την μεσοαστρική ύλη. Απλοί υπολογισμοί (σχετικά με τη μέση ελεύθερη διαδρομή των μητρικών πυρήνων) δείχνουν ότι η απόσταση που πρέπει να διανύσουν οι μητρικοί πυρήνες πριν διασπαστούν στους παρατηρούμενους θυγατρικούς είναι πολύ μεγαλύτερη από τις διαστάσεις του Γαλαξία μας. Αυτό αποτελεί ισχυρή ένδειξη ότι οι κοσμικές ακτίνες παγιδεύονται από το μαγνητικό πεδίο του Γαλαξία μας και διαχέονται σε αυτόν.

Στην Εικόνα 1.3 παρουσιάζονται οι ροές των διαφόρων στοιχείων από τα οποία αποτελείται η κοσμική ακτινοβολία ως συνάρτηση της ενέργειας ανά πυρήνα. Στο ένθετο άνω δεξιά παρουσιάζεται η σχέση του λόγου της ροής πρωτονίων προς τη ροή πυρήνων ηλίου με τη μαγνητική ακαμψία (magnetic rigidity R = p·c/(Z·e)), από όπου φαίνεται ότι η συνεισφορά

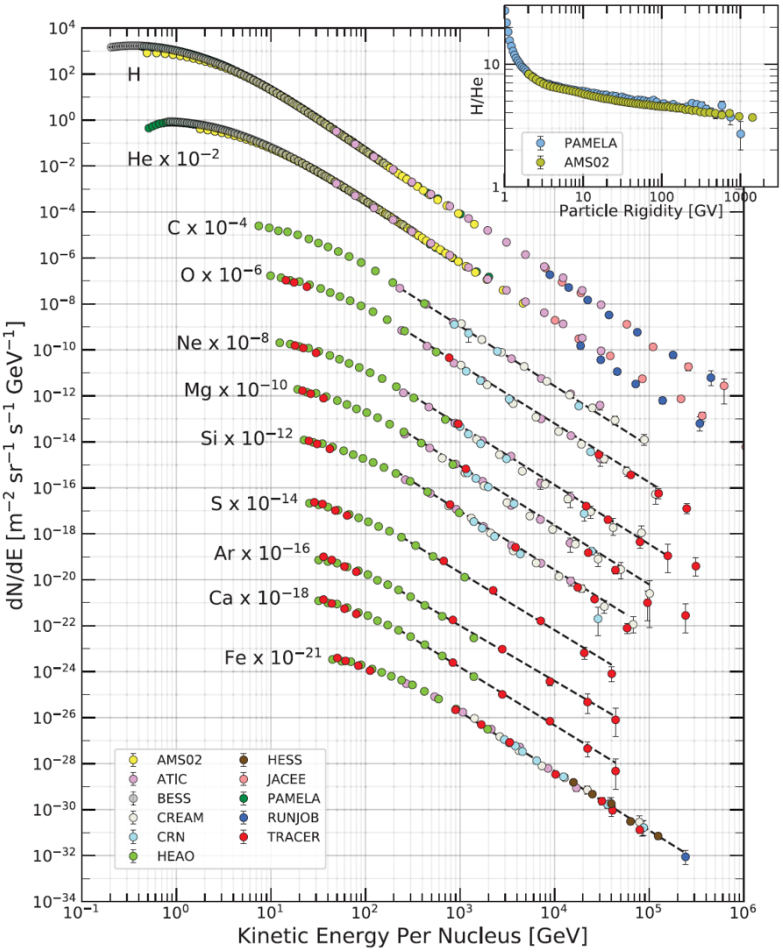

Figure 1.3: Ροή των στοιχείων των κοσμικών ακτίνων ως προς την ενέργεια ανά πυρήνα. Στο ένθετο παρουσιάζεται ο λόγος της ροής πρωτονίων προς τη ροή πυρήνων ηλίου ως προς τη μαγνητική ακαμψία. Εικόνα από [3].

των πρωτονίων ελαττώνεται καθώς αυξάνεται η ενέργεια των κοσμικών ακτίνων. Για την μοντελοποίηση της ροής των κοσμικών ακτίνων, είναι πολύ σημαντική η εύρεση μοντέλου το οποίο να συνδυάζει τα πειραματικά δεδομένα για την ροή κάθε στοιχείου (Εικόνα 1.3), να περιγράφει το ενεργειακό φάσμα όλων των σωματιδίων (Εικόνα 1.1) και ταυτόχρονα να βασίζεται και στην διαφορετική προέλευση (γαλαξιακή / εξωγαλαξιακή) των κοσμικών ακτίνων. Από τα πιο επιτυχημένα μοντέλα είναι αυτο του Hillas και η επέκταση των Gaisser, Stanev και Tilav [7, 8, 9]. Τα μοντέλα αυτά υποθέτουν τρεις (ή τέσσερις) πληθυσμούς σωματιδίων όπου οι δύο είναι γαλα- ξιακής προέλευσης και ο τρίτος (και τέταρτος) εξωγαλαξιακής. Δεχόμενοι ότι οι γαλαξιακές κοσμικές ακτίνες οι οποίες προέρχονται από επιτάχυνση σε υπολείμματα υπερκαινοφανών έχουν κατώφλι αποκοπής στην ενεργειακή περιοχή του knee και ότι οι κοσμικές ακτίνες εξωγαλαξιακής προέλευσης συνεισφέρουν κυρίως στην ενεργειακή περιοχή που ξεκινά από το ankle, απαιτείται τουλάχιστον ένας ακόμα πληθυσμός κοσμικών ακτίνων γαλαξιακής προέλευσης (Εικόνα 1.4) που προέρχονται από επιταχυντές με διαφορετικά χαρακτηριστικά.

Τελικά το φάσμα των κοσμικών ακτίνων δίνεται από τη σχέση:

$$\varphi(E) = \sum_{\iota} \sum_{j=1}^{3(4)} \alpha_{i,j} \cdot E^{-\gamma_{i,j}} \cdot exp(-\frac{E}{Z_i \cdot R_j}) \tag{1.2}$$

όπου ο δείκτης i αναφέρεται στα διάφορα στοιχεία των κοσμικών ακτίνων που υποθέτει το μοντέλο, ενώ ο δείκτης j στον πληθυσμό. Στην αναφορά [9] αναλύονται τα μοντέλα και οι διάφοροι συντελεστές της πιο πάνω σχέσης.

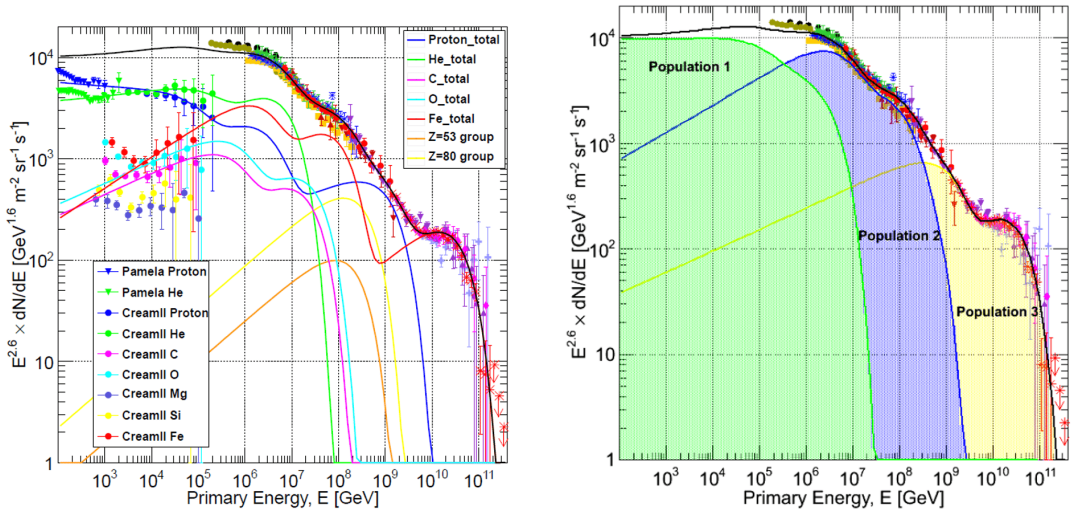

Figure 1.4: Το ενεργειακό φάσμα ροής των κοσμικών ακτίνων όπως περιγράφεται από τη σχέση 1.2 και παρατηρησιακά δεδομένα (σημεία). Αριστερά: Οι γραμμές παρουσιάζουν τη ροή κάθε στοιχείου του μοντέλου (άθροισμα όλων των πληθυσμών κάθε στοιχείου). Δεξιά: Οι περιοχές παρουσιάζουν τη ροή του κάθε πληθυσμού (άθροισμα όλων των στοιχείων του κάθε πληθυσμού). Εικόνα από [9].

1.1.3 Μηχανισμοί επιτάχυνσης σωματιδίων σε υψηλές ενέργειες

Ο κύριος μηχανισμός επιτάχυνσης σωματιδίων σε υψηλές ενέργειες είναι ο μηχανισμός Fermi πρώτης τάξης [1]. Ο μηχανισμός αυτός βρίσκει εφαρμογή κυρίως σε ροές πλάσματος που εμφανίζουν ασυνέχειες, όπως ωστικά κύματα (shocks). Τέτοιες ασυνέχειες δημιουργούνται σε υπερηχητικές ροές, όπως αυτές οι οποίες συνδέονται με εκρήξεις υπερκαινοφανών αστέρων ή σε περιοχές όπου τα υπολείμματα που έχουν δημιουργηθεί από τέτοιες εκρήξεις ή από τους εναπομείναντες pulsars αλληλεπιδρούν με την μεσοαστρική ύλη. Το ενεργειακό φάσμα των σωματιδίων που έχουν επιταχυνθεί από αυτό τον μηχανισμό είναι ένας νόμος δύναμης.

Η επιτάχυνση Fermi πρώτης τάξης οφείλεται στις συνεχείς μετωπικές κρούσεις σωματιδίων που διέρχονται από την περιοχή ισχυρής ασυνέχειας. Όπως φαίνεται στην Εικόνα 1.5, καθώς η διαταραχή διατρέχει το πλάσμα (Εικόνα 1.5 a) τα σωματίδια στην αδιατάρακτη περιοχή αφού διέλθουν από αυτή συγκρούονται μετωπικά με την ροή από την διαταραγμένη πλευρά (Εικόνα 1.5 c). Στην συνέχεια, και αφού βρεθούν στο σύστημα αναφοράς της διαταραγμένης πλευράς κινούνται τυχαία με πιθανότητα να διέλθουν στην αδιατάρακτη περιοχή όπου και συγκρούονται πάλι μετωπικά με την ροή του πλάσματος (Εικόνα 1.5 d). Το κέρδος ενέργειας των σωματιδίων σε κάθε διέλευση από την διαταραχή είναι της τάξης: $\Delta E/E \sim O(U/c)$. Δεδομένου ότι κάθε

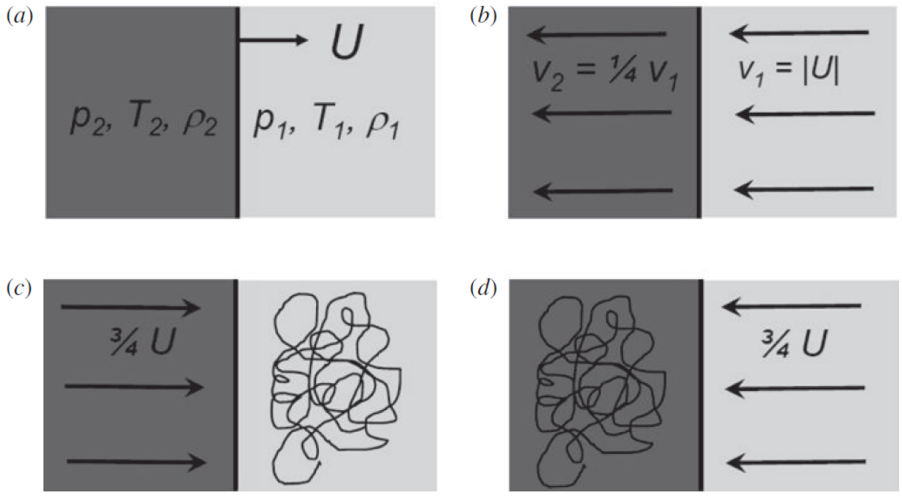

Figure 1.5: Διαταραχή διαδίδεται σε πλάσμα. (a) Η διαταραχή διαδίδεται με ταχύτητα U. Η περιοχή από όπου έχει διέλθει η διαταραχή έχει πυκνότητα ρ_2, πίεση p_2 και θερμοκρασία T_2, ενώ η αδιατάρακτη περιοχή έχει πυκνότητα ρ_1, πίεση p_1 και θερμοκρασία T_1. (b) Οι ταχύτητες του πλάσματος στις δυο περιοχές στο σύστημα αναφοράς της διαταραχής. (c) Η ταχύτητα του πλάσματος της διαταραγμένης περιοχής στο σύστημα αναφοράς της αδιατάρακτη περιοχής (όπου τα σωματίδια κινούντα χαοτικά). (d) Η ταχύτητα του πλάσματος της αδιατάρακτης περιοχής στο σύστημα αναφοράς της διαταραγμένης περιοχής (όπου τα σωματίδια κινούνται χαοτικά). Εικόνα από [10].

σωματίδιο μπορεί να διέλθει πολλές φορές από την διαταραχή (με γεωμετρικά ελαττούμενη πιθανότητα) και υποθέτοντας σχετικιστικές ταχύτητες το διαφορικό ενεργειακό φάσμα των σωματιδίων που διαφεύγουν είναι σε πρώτη προσέγγιση:

$$N(E)dE \sim E^{-2}dE \tag{1.3}$$

Επιπρόσθετη αύξηση της ενέργειας των φορτισμένων σωματιδίων στην περίπτωση της επιτάχυνσης Fermi πρώτης τάξης επιτυγχάνεται όταν οι 2 περιοχές του πλάσματος έχουν μαγνητικά πεδία διαφορετικής έντασης, με κάθετη συνιστώσα στην επιφάνεια της διαταραχής και το ηλεκτρικό πεδίο με παράλληλη συνιστώσα σε αυτή [1]. Σε αυτή την περίπτωση τα φορτισμένα σωματίδια καθώς διέρχονται από την διαταραχή, λόγω των διαφορετικών ακτίνων Larmor στις δυο περιοχές, ολισθαίνουν σε αυτή, συνεπώς κινούνται εντός μη κάθετου ηλεκτρικού πεδίου, κερδίζοντας ενέργεια.

1.2 Νετρίνο Αστροφυσική προέλευσης

1.2.1 Γενικά

Τα νετρίνο είναι λεπτόνια, ηλεκτρικά ουδέτερα και αλληλεπιδρούν μέσω της ασθενούς και της βαρυτικής αλληλεπίδρασης. Υπάρχουν τρία είδη (ή "γεύσεις") νετρίνο, όσες δηλαδή και οι οικογένειες των στοιχειωδών σωματιδίων του καθιερωμένου προτύπου: το νετρίνο του ηλεκτρονίου ν_e, το νετρίνο του μιονίου ν_μ και το το νετρίνο του ταυ ν_τ. Γνωρίζουμε ότι η μάζα τους είναι εξαιρετικά μικρή αλλά μη μηδενική και έχουν βρεθεί άνω όρια για αυτή. Για τον λόγο αυτό, συνήθως στην θεώρηση των αλληλεπιδράσεων των νετρίνο μελετάται μόνο η ασθενής αλληλεπίδραση και η βαρυτική αγνοείται.

Η ύπαρξη των νετρίνο προτάθηκε πρώτη φορά από τον Pauli το 1930 ώστε να ισχύει στη διάσπαση β η αρχή διατήρησης της ορμής, της ενέργειας και της στροφορμής , οι οποίες παραβιάζονταν υπό την θεώρηση της διάσπασης σε δύο προϊόντα. Η πρώτη πειραματική επιβεβαίωση της ύπαρξης των νετρίνο συνέβη το 1956 όταν δημοσιεύτηκαν τα αποτελέσματα του πειράματος "Cowan–Reines neutrino experiment", όπου αντινετρίνο (του ηλεκτρονίου) που παράγονταν σε πυρηνικό αντιδραστήρα ανιχνεύθηκαν ως αποτέλεσμα της αλληλεπίδρασής τους με πρωτόνια και της παραγωγής νετρονίων και ποζιτρονίων.

Λόγω τον ιδιοτήτων τους τα νετρίνο μπορούν να αποτελέσουν μοναδικούς "αγγελιοφόρους" κοσμικής πληροφορίας. Δεδομένου ότι είναι ουδέτερα δεν σκεδάζονται από τα μαγνητικά πεδία στο σύμπαν και κινούνται σε ευθείες τροχιές, σε αντίθεση με τα φορτισμένα σωμάτια της κοσμικής ακτινοβολίας. Συνεπώς όταν ανιχνευθούν μπορούν να δώσουν πληροφορίες για το σημείο παραγωγής τους. Επιπλέον λόγω του ότι αλληλεπιδρούν μόνο μέσω της ασθενούς αλληλεπίδρασης (αγνοώντας την βαρύτητα) μπορούν να διανύσουν εξαιρετικά μεγάλες αποστάσεις στο σύμπαν χωρίς να απορροφηθούν. Στην Εικόνα 1.6 παρουσιάζονται οι αποστάσεις από τις οποίες φωτόνια φτάνουν στη Γη συναρτήσει της ενέργειας των φωτονίων. Από την εικόνα αυτή φαίνεται ότι υπάρχουν περιοχές του σύμπαντος από τις οποίες φωτόνια υψηλής ενέργειας δεν μπορούν να φτάσουν στη Γη λόγω απορρόφησης, όμως από τις ίδιες περιοχές τα νετρίνο φτάνουν ανεμπόδιστα στην Γη.

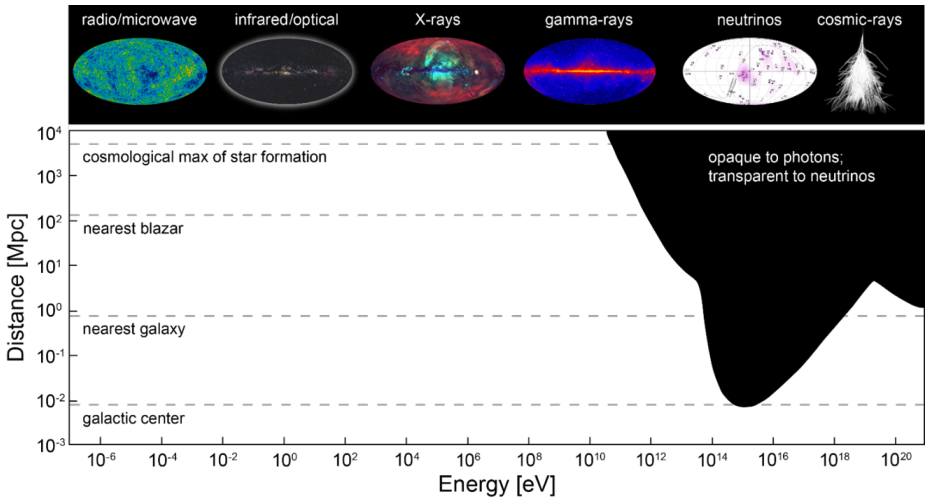

Figure 1.6: Οι αποστάσεις από τις οποίες φωτόνια φτάνουν στη Γη συναρτήσει της ενέργειας των φωτονίων. Εικόνα από [11].

1.2.2 Μηχανισμοί παραγωγής νετρίνο υψηλής ενέργειας από αστροφυσικής πηγές

Παραγωγή νετρίνο αναμένεται από τις πηγές στις οποίες αδρόνια επιταχύνονται σε υψηλές ενέργειες. Τα νετρίνο παράγονται κυρίως ως αποτέλεσμα διασπάσεων μεσονίων (κυρίως πιονίων) τα οποία παράγονται από αλληλεπιδράσεις πρωτονίων. Οι σημαντικότερες είναι οι αλληλεπιδράσεις πρωτονίου - πρωτονίου (ή πυρήνα):

$$p + p\,(nucleus) \rightarrow \pi^{\pm,0} + X \tag{1.4}$$

και πρωτονίου - φωτονίου (σχέση 1.1). Τα πιόνια με τη σειρά τους διασπώνται:

$$\begin{aligned} &\pi^+ \to \mu^+ + \nu_\mu \\ &\pi^- \to \mu^- + \overline{\nu_\mu} \\ &\pi^0 \to \gamma\gamma \text{ δεν παράγονται νετρίνο, μόνο φωτόνια} \end{aligned} \tag{1.5}$$

$$\begin{aligned} &\mu^+ \to e^+ + \overline{\nu_\mu} + \nu_e \\ &\mu^- \to e^- + \nu_\mu + \overline{\nu_e} \end{aligned}$$

Κατά την αλληλεπίδραση πρωτονίου - πρωτονίου (σχέση 1.4) είναι δυνατόν να δημιουργηθούν, με μικρότερη πιθανότητα, καόνια αντί για πιόνια. Τα καόνια διασπώνται κατά κύριο λόγο σε μιόνια και νετρίνο ή σε πιόνια.

$$\begin{aligned} &K^+ \to \mu^+ + \nu_\mu \qquad (63.6\%) \\ &K^+ \to \pi^+ + \pi^0 \qquad (20.7\%) \end{aligned} \tag{1.6}$$

Τέλος από την αλληλεπίδραση πρωτονίου - φωτονίου (σχέση 1.1) στην περίπτωση παραγωγής νετρονίου, αυτό διασπάται:

$$n \to p^+ + e^- + \overline{\nu_e} \tag{1.7}$$

Όπως αναφέρθηκε και πιο πάνω, η παραγωγή νετρίνο από πρωτόνια συμβαίνει κυρίως λόγω της διάσπασης πιονίων. Συνεπώς ο λόγος γεύσεων των παραχθέντων νετρίνο ν_e:ν_μ:ν_τ στην πηγή προσεγγίζει τον 1:2:0, όπως φαίνεται από τις σχέσεις 1.5. Παρόλα αυτά αναμένεται ότι τα νετρίνο αστροφυσικής προέλευσης φτάνουν στη Γη με λόγο γεύσεων 1:1:1 λόγω του φαινομένου της ταλάντωσης των νετρίνο.

1.2.3 Πιθανές αστροφυσικές πηγές παραγωγής νετρίνο

Παραγωγή νετρίνο αναμένεται από πηγές στις οποίες επιταχύνονται αδρόνια, συνεπώς οι αστροφυσικές πηγές από τις οποίες αναμένεται εκπομπή νετρίνο ταυτίζονται με τις πηγές της κοσμικής ακτινοβολίας. Οι πηγές αυτές κατατάσσονται σε δυο κατηγορίες τις γαλαξιακές και τις εξωγαλαξιακές.

1.2.3.1 Γαλαξιακές πηγές

Υπερκαινοφανείς αστέρες και κελυφωτά υπολείμματα:

Όταν ένας αστέρας μεγάλης μάζας εξαντλήσει τα ενεργειακά του αποθέματα, τελειώνει την "ζωή" του με μια θεαματική έκρηξη που ονομάζεται έκρηξη υπερκαινοφανούς (Supernova explosion). Κατά την έκρηξη αυτή ο αστέρας εκτινάσσει τα εξωτερικά στρώματα μάζας του. Η ενέργεια που εκλύεται σε αυτές τις εκρήξεις είναι της τάξης των 10^{51} erg. Το φαινόμενο ξεκινά με την κατάρρευση του πυρήνα που διαρκεί μερικά δευτερόλεπτα. Το ωστικό κύμα που δημιουργείται, χρειάζεται μερικές ώρες για να διαπεράσει όλη την έκταση του αστέρα. Μετά από εκατοντάδες χρόνια αρχίζει να δημιουργείται το υπόλειμμα ενώ η επιβράδυνση του ξεκινά μετά από χιλιάδες χρόνια [12]. Κατά την έκρηξη υπερκαινοφανούς, σωματίδια (κοσμικές ακτίνες) μπορούν να επιταχυνθούν σε ενέργειες μέχρι και περίπου 10^{15}eV. Αναμένεται ότι περίπου 3 εκρήξεις υπερκαινοφανών συμβαίνουν κάθε αιώνα στον Γαλαξία μας. Ο ρυθμός αυτός είναι αρκετός για να εξηγήσει την κοσμικές ακτίνες γαλαξιακής προέλευσης με ενέργεια μέχρι την περιοχή του knee [5].

Καθώς το ωστικό κύμα που δημιουργήθηκε από την έκρηξη υπερκαινοφανούς διατρέχει την μεσοαστρική ύλη μπορεί να δημιουργηθεί ένα κελυφωτό υπόλειμμα υπερκαινοφανούς. Τα υπο-

λείμματα αυτά ονομάστηκαν έτσι, διότι εκπομπή ακτινοβολίας παρατηρείται κυρίως από την περιφέρεια του υπολείμματος όπου το ωστικό κύμα αλληλεπιδρά με την μεσοαστρική ύλη. Στις περιοχές αυτές υπάρχουν οι κατάλληλες προϋποθέσεις για επιτάχυνση αδρονίων σε υψηλές ενέργειες άρα και για την παραγωγή νετρίνο. Συμπληρωματικά, συνήθως στα κελυφωτά υπολείμματα δεν παρατηρείται εκπομπή ακτινοβολίας από το κέντρο του κελύφους, αλλά υπάρχουν και εξαιρέσεις όπως το υπόλειμμα του Vela pulsar.

Διπλά συστήματα ακτίνων x:
Τα διπλά συστήματα ακτίνων-x αποτελούνται από ένα συμπαγές αστροφυσικό αντικείμενο και ένα άστρο-συνοδό. Ύλη από το άστρο προσπίπτει στο συμπαγές αντικείμενο και στις περιπτώσεις πού αυτή έχει στροφορμή σχηματίζεται δίσκος προσαύξησης καθώς και ισχυροί άνεμοι πλάσματος ή και πίδακες. Σε αυτό το περιβάλλον αδρόνια μπορούν να επιταχυνθούν σε υψηλές ενέργειες και συνεπώς αναμένεται και εκπομπή νετρίνο.

Το κέντρο του Γαλαξία μας και ο γαλαξιακός δίσκος:
Το κέντρο του Γαλαξία μας είναι ένα από τις εν δυνάμει πηγές νετρίνο. Σε αυτό συντελούν τόσο η πιθανή ύπαρξη υπερμεγέθους μελανής οπής στο SgrA*, όσο και η ύπαρξη πληθώρας αστροφυσικών αντικειμένων, όπως υπολείμματα υπερκαινοφανών και διπλά συστήματα ακτίνων x πλησίον αυτού [13]. Ο γαλαξιακός δίσκος αποτελεί επίσης πιθανή περιοχή από την οποία εκπέμπονται νετρίνο. Σε αυτόν υπάρχει μεγάλη συγκέντρωση σκόνης, η οποία αποτελεί στόχο για τα πρωτόνια των κοσμικών ακτίνων, συνεπώς η παραγωγή νετρίνο αναμένεται από τις αντιδράσεις πρωτονίου - πρωτονίου (πυρήνα) των κοσμικών ακτίνων με τη σκόνη.

1.2.3.2 Έξωγαλαξιακές πηγές

Εκλάμψεις ακτίνων γ:
Οι εκλάμψεις ακτίνων γ (Gamma Ray Bursts - GRBs) είναι τα πιο ενεργητικά φαινόμενα που έχουν παρατηρηθεί στο σύμπαν. Όπως υποδηλώνει και το όνομά τους, από GRBs παρατηρείται έντονη εκπομπή ακτίνων γ για ένα μικρό χρονικό διάστημα (από ms μέχρι και ώρες). Την έκλαμψη ακτίνων γ μπορεί να ακολουθήσει εκπομπή ακτινοβολίας σε μεγαλύτερα μήκη κύματος για μεγαλύτερα χρονικά διαστήματα (afterglow). Οι GRBs κατατάσσονται σε δύο κατηγορίες ανάλογα με την διάρκεια της έκλαμψης. Η πρώτη κατηγορία είναι οι εκλάμψεις μικρής διάρκειας (short GRBs) στις όποιες η έκλαμψη διαρκεί μέχρι δύο δευτερόλεπτα. Τα αστροφυσικά αντικείμενα που προκαλούν αυτού του είδους τις εκλάμψεις ακτίνων γ (προγεννήτορες), πιστεύεται ότι είναι η εκρηκτική συγχώνευση δύο αστέρων νετρονίων. Στη δεύτερη κατηγορία (long GRBs) κατατάσσονται οι εκλάμψεις με διάρκεια από 2 δευτερόλεπτα μέχρι και ώρες. Σε αυτή την κατηγορία ανήκουν η πλειοψηφία των GRBs και συνήθως παρατηρού- νται έντονα afterglows. Ο προγεννήτοράς τους πιστεύεται ότι είναι η κατάρρευση πολύ μαζικών αστέρων (συνήθως με μάζες μεγαλύτερες από $30M_{\odot}$) και περιγράφονται από το μοντέλο fireball [14]). Οι εκλάμψεις ακτίνων γ αποτελούν ιδανικό περιβάλλον στο οποίο αδρόνια επιταχύνονται σε υπερ-υψηλές ενέργειες.

Ενεργοί γαλαξιακοί πυρήνες
Οι ενεργοί γαλαξιακοί πυρήνες (Active Galactic Nuclei - AGNs) συνδέονται με κέντρα γαλαξιών στα οποία βρίσκονται υπερμεγέθεις μελανές οπές και η ακτινοβολούμενη ισχύς μπορεί να είναι ακόμα και κατά χιλιάδες φορές μεγαλύτερη από αυτή όλων των άστρων του γαλαξία [15]. Η εικόνα που παρουσιάζουν οι γαλαξίες στους οποίους βρίσκονται ενεργοί γαλαξιακοί πυρήνες (ή απλούστερα ενεργοί γαλαξίες) μπορεί να διαφέρει κατά πολύ, καθώς σε αυτούς εμπεριέχονται από γαλαξίες με τεράστιους ραδιολοβούς (με διαμέτρους της τάξης των kpc) σε μεγάλες απο-

στάσεις από τα κέντρα των γαλαξιών (της τάξης των kpc) μέχρι και γαλαξίες όπου από τον πυρήνα τους παρατηρείται εξαιρετικά έντονη μη θερμική εκπομπή ακτινοβολίας υπό τη μορφή νόμου δύναμης που εκτείνεται από τα ραδιοκύματα μέχρι και τις ακτίνες x. Παρά τις έντονες διαφορές στην μορφή τους, ένα μοντέλο μπορεί να περιγράψει όλα τα είδη των ενεργών γαλαξιών: Ύλη προσροφάται από την υπερμεγέθη μελανή οπή, σχηματίζεται δίσκος προσαύξησης και πίδακες. Από την περιοχή αυτή παράγεται έντονη, μη θερμική ακτινοβολία. Σε μεγαλύτερη απόσταση υπάρχει τόρος από σκόνη και νέφη που κινούνται με διαφορετικές ταχύτητες. Τελικά βλέπουμε διαφορετική "εικόνα" ανάλογα με την γωνία υπό την οποία παρατηρούμε τον γαλαξία όπως φαίνεται και την Εικόνα 1.7. Σε αυτό το περιβάλλον (δίσκος προσαύξησης, πίδακες, κλπ) εκτιμάται ότι αδρόνια επιταχύνονται σε υψηλές ενέργειες και συνεπώς οι AGNs θεωρούνται υποψήφιες πηγές κοσμικών ακτίνων και παραγωγής νετρίνο.

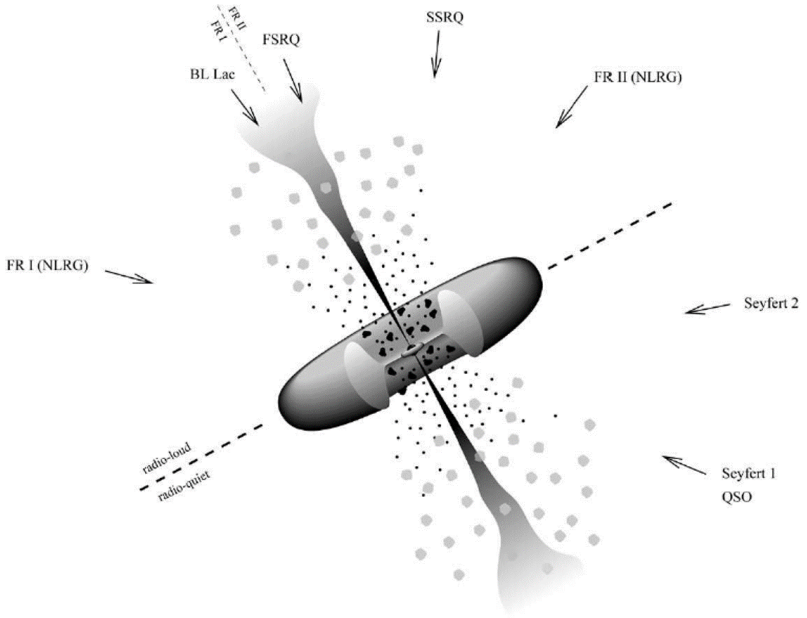

Figure 1.7: Το ενοποιημένο μοντέλο που περιγράφει τους ενεργούς γαλαξίες . Εικόνα από [16].

Νετρίνο από κοσμικές ακτίνες υπερ-υψηλής ενέργειας

Όπως αναφέρθηκε στο Κεφάλαιο 1.1.2 το φάσμα των κοσμικών ακτίνων παρουσιάζει κατώφλι αποκοπής με ενέργεια περί τα 100 EeV λόγω του ορίου GZK. Άμεση συνέπεια είναι η παραγωγή νετρίνο από τη διάσπαση πιονίων που παράγονται από τη διάσπαση του σωματιδίου Δ^+ σε φορτισμένο πιόνιο και νετρόνιο (σχέση 1.1). Από την διαδικασία αυτή αναμένεται ότι τα νετρίνο που παράγονται έχουν ενέργεια που μπορεί να υπερβεί τα 10^{12} GeV.

1.2.4 Αστρονομία multi-messenger

Στην αστρονομία, παραδοσιακά, μελετώντας κάποια πηγή σε διαφορετικό τμήμα του ηλεκτρομαγνητικού φάσματος μπορούσαν να εξαχθούν διαφορετικά συμπεράσματα για αυτή. Όμως για τα εξωτικά αστροφυσικά αντικείμενα η πληρέστερη κατανόησή τους μπορούσε να επιτευχθεί συνδυάζοντας την πληροφορία από τα διαφορετικά μήκη κύματος. Αντίστοιχα, σήμερα, η πληρέστερη κατανόηση εξωτικών αστροφυσικών αντικειμένων μπορεί να επιτευχθεί χρησιμοποιώντας την διαθέσιμη πληροφορία από παρατηρήσεις με διαφορετικούς διαδότες (φωτόνια, νετρίνο και βαρυτικά κύματα). Αυτή η προσέγγιση ονομάζεται multi-messenger astronomy.

Η πρώτη επιτυχία της multi-messenger astronomy συνέβη με την πρώτη παρατήρηση συγχώνευσης δύο αστέρων νετρονίων από την κοινοπραξία Ligo-Virgo και το τηλεσκόπιο Fermi, μέσω ανίχνευσης βαρυτικών κυμάτων και φωτονίων αντίστοιχα [17]. Η κοινοπραξία Ligo-Virgo ανίχνευσε την διέλευση βαρυτικών κυμάτων και μετά από 1.7s το τηλεσκόπιο Fermi με το όργανο GBM ανίχνευσε εκπομπή ακτινοβολίας γ που καταχωρήθηκε ως short GRB. Η ανίχνευση αυτή πυροδότησε μαζική καμπάνια παρατήρησης της περιοχής αυτής από διάφορα τηλεσκόπια σε διαφορετικές περιοχές του φάσματος. Με τον συσχετισμό των βαρυτικών κυμάτων με την έκλαμψη ακτίνων γ επιβεβαιώθηκε η μέχρι τότε υπόθεση (που βασιζόταν σε ισχυρές ενδείξεις) ότι οι προγεννήτορες των short GRBs είναι η συγχώνευση δύο αστέρων νετρονίων.

Η δεύτερη επιτυχία της multi-messenger astronomy συνέβη με τον συσχετισμό νετρίνο υψηλής ενέργειας που ανιχνεύθηκε από το τηλεσκόπιο νετρίνο IceCube (Κεφάλαιο 2.3.3) με γνωστό blazar ο οποίος βρισκόταν σε κατάσταση έκλαμψης [18]. Η ανίχνευση μιονίου από το τηλεσκόπιο νετρίνο IceCube, το οποίο είχε πολύ μεγάλη πιθανότητα να προήλθε από νετρίνο υψηλής ενέργειας, πυροδότησε έναν συναγερμό σε τηλεσκόπια μέσω του Gamma-ray Coordinates Network (GCN) [19]. Σε αυτό τον συναγερμό, μεταξύ άλλων, απάντησαν και τα τηλεσκόπια Fermi και MAGIC τα οποία εντόπισαν στην περιοχή του ουρανού που υπεδείκνυε το IceCube, τον γνωστό blazar TXS 0506+056 να βρίσκεται σε κατάσταση έκλαμψης. Μετά την παρατήρηση νετρίνο από τον ήλιο και τον υπερκαινοφανή 1987A είναι η πρώτη επιβεβαιωμένη (με $\sim 3\sigma$) ανίχνευση νετρίνο από αστροφυσική πηγή. Άμεση συνέπεια είναι η επιβεβαίωση ότι τα μοντέλα που προβλέπουν τους μηχανισμούς εκπομπής ακτινοβολίας από τον balzar TXS 0506+056 πρέπει να εμπεριέχουν και κάποια αδρονική συνιστώσα [20]. Επίσης, κάποια από τα μοντέλα που εμπεριέχουν αδρονικές συνιστώσες και περιγράφουν τη ροή νετρίνο και το ηλεκτρομαγνητικό φάσμα μπορεί να υποδεικνύουν ότι ο TXS 0506+056 είναι άλλου είδους ενεργός γαλαξίας από αυτό που θεωρούσε η αστροφυσική κοινότητα μέχρι τώρα [21].

1.3 Ατμοσφαιρικοί καταιονισμοί

Όταν τα σωματίδια της κοσμικής ακτινοβολία αλληλεπιδρούν με τα μόρια της ατμόσφαιρας δημιουργούν δευτερογενή σωματίδια τα όποια με τη σειρά τους είτε διασπώνται είτε αλληλεπιδρούν, με αποτέλεσμα την δημιουργία καταιονισμών από σωματίδια (atmospheric showers). Από αυτά, μόνο τα μιόνια και τα νετρίνο είναι αρκετά διεισδυτικά ώστε να μπορούν να διασχίσουν χιλιόμετρα νερού, πάγου ή του στερεού φλοιού της Γης ώστε να φτάσουν στις περιοχές όπου βρίσκονται τα τηλεσκόπια νετρίνο. Η μελέτη αυτών των σωματιδίων είναι πολύ σημαντική για πειράματα ανίχνευσης κοσμικών νετρίνο, καθώς αποτελούν την κύρια πηγή υποβάθρου.

Τα ατμοσφαιρικά μιόνια δημιουργούνται κυρίως από διασπάσεις πιονίων. Το φάσμα τους εκτείνεται σε ενέργειες που μπορούν να ξεπεράσουν και το 1 PeV. Μετρήσεις της ροής των ατμοσφαιρικών μιονίων έχουν διεξαχθεί από πολλά πειράματα και συνεπώς το φάσμα τους είναι γνωστό. Πιο συγκεκριμένα στην περιοχή υψηλής ενέργειας (10 TeV έως 1 PeV), τις πρόσφατες μετρήσεις του πειράματος IceCube τις προσεγγίσει πολύ καλά νόμος δύναμης με εκθέτη -3.76 ± 0.02 [22]. Επίσης η εξάρτηση της ροής τους από την πολική γωνία πλησιάζει πολύ το $\cos^2(\vartheta)$ [4].

Τα ατμοσφαιρικά νετρίνο υψηλής ενέργειας δημιουργούνται από διαφορετικούς μηχανισμούς. Αγνοώντας τα νετρίνο ηλεκτρονίου σχετικά χαμηλών ενεργειών (μέχρι λίγα GeV) στα όποια μεγάλη συνεισφορά έχει η διάσπαση μιονίων, οι κύριοι μηχανισμοί παραγωγής νετρίνο στην ατμοσφαίρα είναι από διασπάσεις πιονίων και καονίων καθώς και από διασπάσεις βαρύτερων σωματιδίων που περιέχουν charm ή bottom quarks. Τα νετρίνο που δημιουργούνται από τον πρώτο μηχανισμό χαρακτηρίζονται ως "conventional" ενώ αυτά που δημιουργούνται από

τον δεύτερο "prompt". Γενικά αναμένεται ότι το φάσμα των conventional νετρίνο μπορεί να προσομοιωθεί με νόμο δύναμης με εκθέτη -3.7 ενώ των prompt με νόμο δύναμης με εκθέτη -2.7 [5].

Τα conventional ατμοσφαιρικά νετρίνο μιονίου δημιουργούνται τόσο από διασπάσεις πιονίων όσο και από διασπάσεις καονίων. Στις χαμηλές ενέργειες πιο σημαντική είναι η συνεισφορά των νετρίνο που δημιουργήθηκαν από διασπάσεις πιονίων. Καθώς όμως η ενέργεια των σωματιδίων αυξάνει, αυξάνει και ο μέσος χρόνος ζωής τους (λόγω σχετικιστικής κίνησης) και η πιθανότητα των πιονίων να διασπαστούν ελαττώνεται, διότι αυξάνεται η πιθανότητά τους να αλληλεπιδράσουν με κάποιο σωματίδιο της ατμόσφαιρας. Συνεπώς η συνεισφορά των νετρίνο που έχουν δημιουργηθεί από τις διασπάσεις πιονίων ελαττώνεται, άρα αυξάνεται η συνεισφορά αυτών που δημιουργούνται από διασπάσεις καονίων. Τα conventional ατμοσφαιρικά νετρίνο ηλεκτρονίου δημιουργούνται κυρίως από διασπάσεις φορτισμένων και ουδέτερων καονίων. Η πιθανότητα διάσπασης φορτισμένων καονίων μέσω των καναλιών τα όποια παράγουν νετρίνο ηλεκτρονίου στην τελική κατάσταση είναι μικρότερη από 6%, συνεπώς αναμένεται ότι η conventional ροή ατμοσφαιρικών νετρίνο ηλεκτρονίου θα είναι τουλάχιστον μια τάξη μεγέθους μικρότερη από αυτή των νετρίνο μιονίου. Για τα prompt ατμοσφαιρικά νετρίνο, τα μοντέλα προβλέπουν παρόμοια παραγωγή νετρίνο ηλεκτρονίου και μιονίου.

Λόγω του ενδιαφέροντος που παρουσιάζουν τα ατμοσφαιρικά νετρίνο έχουν δημιουργηθεί διάφορα μοντέλα (τόσο θεωρητικά όσο και ημιαναλυτικά που βασίζονται σε προσομοιώσεις) που περιγράφουν τη ροή ατμοσφαιρικών νετρίνο. Τα πιο διαδεδομένα και επιτυχημένα μοντέλα που περιγραφούν την conventional ροή αξιοποιούν και δεδομένα από ατμοσφαιρικά μιόνια (τα οποία όπως αναφέρθηκε και πιο πάνω παράγονται με τους ίδιους μηχανισμούς) όπως το μοντέλο των Honda et al. [23]. Από τα μοντέλα που περιγράφουν την prompt συνιστώσα των ατμοσφαιρικών νετρίνο, από τα πιο διαδεδομένα είναι αυτό των Enberg et al. [24]. Στην Εικόνα 1.8 παρουσιάζονται οι conventional και prompt ροές ατμοσφαιρικών νετρίνο μιονίου και ηλεκτρονίου σύμφωνα με τα μοντέλα Honda et al. και Enberg et al. αντίστοιχα. Το τηλεσκόπιο νετρίνο IceCube δεν έχει μέχρι στιγμής ανιχνεύσει την prompt ροή ατμοσφαιρικών νετρίνο όπως περιγράφεται από το μοντέλο αυτό [25, 25]. Συνέπεια αυτού ήταν η αναθεώρηση του πιο πάνω μοντέλου [26, 27, 28].

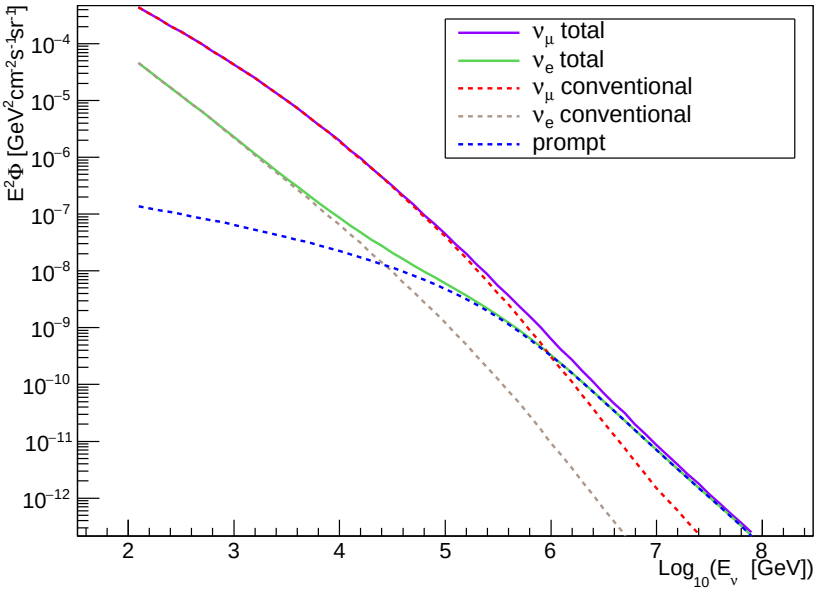

Figure 1.8: Conventional και prompt ροές ατμοσφαιρικών νετρίνο μιονίου και ηλεκτρονίου σύμφωνα με τα μοντέλα Honda et al και Enberg et al. αντίστοιχα, ως συνάρτηση της ενέργειας των νετρίνο.

Chapter 2

Τηλεσκόπια Νετρίνο

2.1 Αρχή ανίχνευσης

2.1.1 Αλληλεπιδράσεις νετρίνο υψηλής ενέργειας με την ύλη

Στο Κεφάλαιο 1.2 αναφέρθηκε ήδη ότι τα νετρίνο δεν έχουν φορτίο και αλληλεπιδρούν με την ύλη μέσω της ασθενούς αλληλεπίδρασης. Για τους λόγους αυτούς, τα νετρίνο ανιχνεύονται έμμεσα, καθώς δεν είναι δυνατή η ανίχνευση των ιδίων αλλά των προϊόντων της αλληλεπίδρασής τους με την ύλη. Η αναζήτηση νετρίνο αστροφυσικής προέλευσης επικεντρώνεται σε νετρίνο με ενέργειες μεγαλύτερες των εκατοντάδων GeV (υψηλές και υπέρ-υψηλές ενέργειες). Σε αυτή την ενεργειακή περιοχή τρία κανάλια αλληλεπίδρασης είναι τα σημαντικότερα (με ενεργό διατομή τάξεις μεγέθους μεγαλύτερη από τα υπόλοιπα):

- οι αλληλεπιδράσεις φορτισμένου ρεύματος (Charged Current - CC) με τα quark των νουκλεονίων της ύλης.
- οι αλληλεπιδράσεις ουδέτερου ρεύματος (Neutral Current - NC) με τα quark των νουκλεονίων της ύλης.
- η αλληλεπίδραση αντινετρίνο ηλεκτρονίου με ηλεκτρόνια παράγοντας ένα μποζόνιο W^-.

Γενικά οι αλληλεπιδράσεις φορτισμένου και ουδέτερου ρεύματος είναι αλληλεπιδράσεις σκέδασης των νετρίνο. Στην ενεργειακή περιοχή ενδιαφέροντος τα νετρίνο αλληλεπιδρούν με ένα από τα quark του αδρονίου και τμήμα της ενέργειας και της ορμής του νετρίνο μεταφέρεται στο quark. Συνεπώς, η σκέδαση των νετρίνο στην ενεργειακή περιοχή ενδιαφέροντος είναι βαθιά ανελαστική σκέδαση (Deep Inelastic Scattering - DIS). Η ενέργεια που μεταφέρεται στο quark, εκλύεται υπό την μορφή καταιγισμού αδρονικών σωματιδίων (hadronic cascade). Η ποσότητα της ενέργειας που μεταφέρεται από το νετρίνο στο quark και καταλήγει στην παραγωγή του καταιγισμού αδρονικών σωματιδίων περιγράφεται από την παράμετρο της ανελαστικότητας ή Bjorken y.

Κατά τις αλληλεπιδράσεις φορτισμένου ρεύματος, το νετρίνο αλληλεπιδρά με το quark μέσω ενός φορτισμένου μποζονίου $W^{\pm}$ και στην τελική κατάσταση παράγεται το λεπτόνιο που συνδέεται με το νετρίνο που αλληλεπίδρασε. Κατά τις αλληλεπιδράσεις ουδέτερου ρεύματος το νετρίνο και το quark αλληλεπιδρούν μέσω ενός ουδετέρου μποζονίου Z^0 και το νετρίνο σκεδάζεται. Στην Εικόνα 2.1 παρουσιάζονται διαγράμματα αυτών των αλληλεπιδράσεων. Ενώ στο κάτω όριο της περιοχής ενδιαφέροντος ($E_\nu < 10$ TeV) η ενεργός διατομή αυτών των αλληλεπιδράσεων είναι ευθέως ανάλογη της ενέργειας των νετρίνο, για την υπόλοιπη ενεργειακή

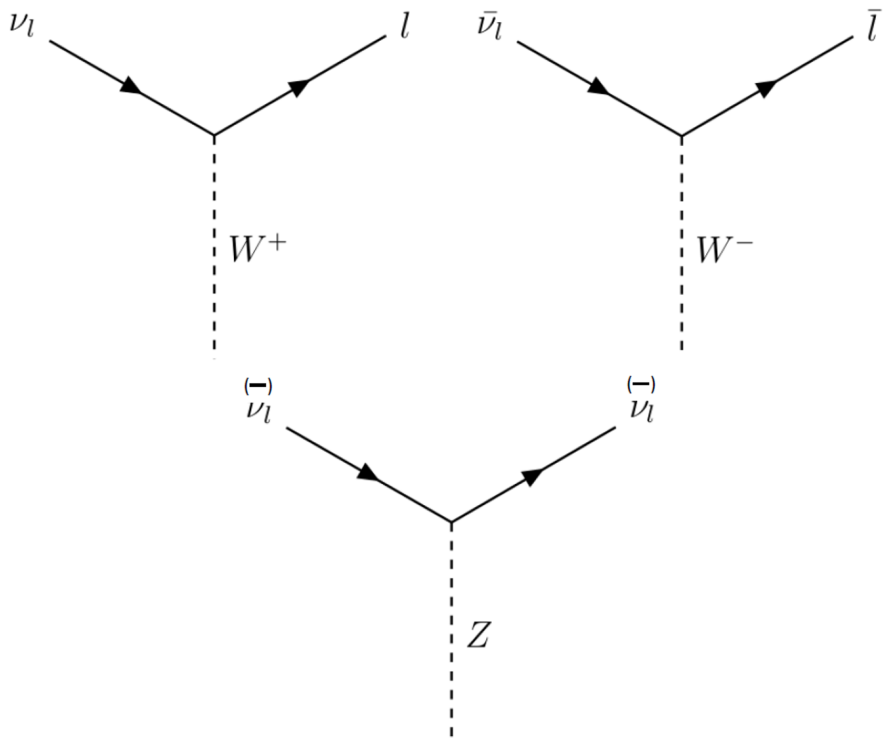

Figure 2.1: Αλληλεπιδράσεις φορτισμένου ρεύματος νετρίνο (επάνω αριστερά) και αντινετρίνο (επάνω δεξιά) και ουδετέρου ρεύματος (κάτω). Όπου $l = e$, μ ή τ. Εικόνα από [29].

περιοχή ($E_\nu \geq 10$ TeV) η ενεργός διατομή είναι ανάλογη της $E_\nu^{0.36}$ [5, 30, 31] όπως φαίνεται και από τις σχέσεις:

$$\begin{aligned} \sigma_\nu^{CC} &= 5.5 \cdot 10^{-36} \cdot E^{0.36} \text{cm}^2 \qquad E_\nu \geq 10\text{TeV} \\ \sigma_\nu^{NC} &= 2.3 \cdot 10^{-36} \cdot E^{0.36} \text{cm}^2 \qquad E_\nu \geq 10\text{TeV} \end{aligned} \tag{2.1}$$

Η ενεργός διατομή των αλληλεπιδράσεων φορτισμένου και ουδέτερου ρεύματος νετρίνο και αντινετρίνο ως συνάρτηση της ενέργειας του νετρίνο παρουσιάζονται στην Εικόνα 2.2 (αριστερά). Λόγω της αύξησης της ενεργού διατομής των αλληλεπιδράσεων των νετρίνο με την ύλη, η πιθανότητα νετρίνο υπερ-υψηλής ενέργειας να διασχίσουν τη Γη είναι πολύ μικρή, συνεπώς η αναζήτηση νετρίνο με τέτοιες ενέργειες επικεντρώνεται σε νετρίνο με οριζόντια διεύθυνση. Στην Εικόνα 2.2 (δεξιά) παρουσιάζεται η πιθανότητα που έχουν τα νετρίνο να διέλθουν από τη Γη ως προς την ενέργειά τους και το συνημίτονο της πολικής τους γωνίας. Ενδιαφέρον παρουσιάζει και το ποσοστό της ενέργειας που αποτίθεται στα quarks και δημιουργεί καταιγισμό αδρονικών σωματιδίων. Στην Εικόνα 2.3 παρουσιάζεται η μέση τιμή της παραμέτρου Bjorken y ως συνάρτηση της ενέργειας του νετρίνο. Στις αλληλεπιδράσεις νετρίνο μέχρι και ~ 100 TeV, μεταφέρεται μεγαλύτερο μέρος της ενέργειας του νετρίνο, κατά μέσο όρο, στον καταιγισμό αδρονικών σωματιδίων από ότι στις αλληλεπιδράσεις αντινετρίνο. Για μεγαλύτερες ενέργειες η μέση ανελαστικότητα ($< y >$) είναι ίδια για νετρίνο και αντινετρίνο και τείνει στην τιμή ~ 0.2.

Ενώ η σκέδαση νετρίνο από ηλεκτρόνια έχει μικρότερη ενεργό διατομή από τις αλληλεπιδράσεις νετρίνο με πυρήνες, εξαίρεση αποτελεί η αλληλεπίδραση αντινετρίνο του ηλεκτρονίου με ηλεκτρόνιο προς σχηματισμό μποζονίου W^-. Αυτό το κανάλι αλληλεπίδρασης ονομάζεται Glashow resonance καθώς προτάθηκε από τον Sheldon L. Glashow το 1959, ως μέθοδος

ανίχνευσης φορτισμένων ασταθών μποζονίων [32]. Η ενεργός διατομή αυτής της αλληλεπίδρασης εμφανίζει μέγιστο για αντινετρίνο ενέργειας 6.3 PeV [30]. Στην Εικόνα 2.2 (αριστερά) παρουσιάζεται και η ενεργός διατομή της πιο πάνω αλληλεπίδρασης σε σχέση με την ενέργεια του αντινετρίνο.

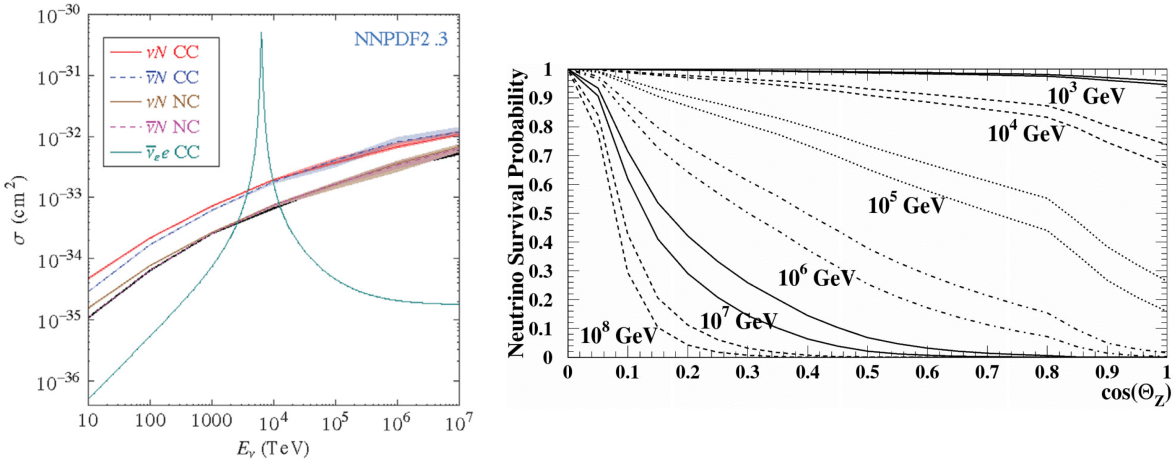

Figure 2.2: Αριστερά: Ενεργός διατομή των αλληλεπιδράσεων φορτισμένου και ουδέτερου ρεύματος για νετρίνο και αντινετρίνο και της αλληλεπίδρασης αντινετρίνο ηλεκτρονίου με ηλεκτρόνιο προς σχηματισμό μποζονίου W^-, σε σχέση με την ενέργεια του νετρίνο. Εικόνα από [29]. Δεξιά: Η πιθανότητα που έχουν τα νετρίνο να διέλθουν από τη Γη σε σχέση με την ενέργειά τους και το συνημίτονο της πολικής τους γωνίας. Στην άνω γραμμή που αντιστοιχεί σε κάθε ενέργεια έχουν ληφθεί υπόψιν μόνο αλληλεπιδράσεις φορτισμένου ρεύματος ενώ στην κάτω τόσο αλληλεπιδράσεις φορτισμένου όσο και ουδέτερου ρεύματος. Νετρίνο με οριζόντια διεύθυνση έχουν $cos(\Theta_z) = 0$ ενώ με διεύθυνση κατακόρυφη προς τα πάνω (διέρχονται από το κέντρο της Γης) έχουν $cos(\Theta_z) = 1$. Εικόνα από [33]

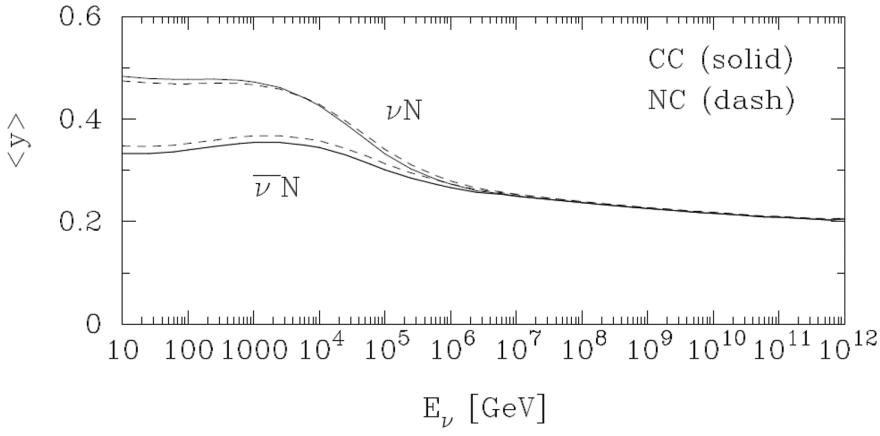

Figure 2.3: Η μέση ανελαστικότητα ($< y >$) για αλληλεπιδράσεις φορτισμένου (συνεχείς γραμμές) και ουδέτερου (διακεκομμένες γραμμές) ρεύματος για νετρίνο και αντινετρίνο, σε σχέση με την ενέργεια του νετρίνο. Εικόνα από [34].

2.1.2 Ακτινοβολία Cherenkov και ανίχνευσή της

Όταν φορτισμένα σωματίδια (όπως αυτά που δημιουργούνται από τις αλληλεπιδράσεις νετρίνο υψηλής ενέργειας με την ύλη) κινούνται μέσα σε κάποιο μέσο με ταχύτητα μεγαλύτερη από την ταχύτητα του φωτός στο μέσο αυτό, παράγεται ακτινοβολία Cherenkov. Η ακτινοβολία αυτή εκπέμπεται σε συγκεκριμένη γωνία (θ_c) σε σχέση με την τροχιά των σωματιδίων:

$$\cos(\theta_c) = \frac{1}{\beta \cdot \eta} \tag{2.2}$$

όπου $\beta = \frac{u}{c}$ και η ο δείκτης διάθλασης του μέσου στο οποίο κινείται το φορτισμένο σωματίδιο. Στην Εικόνα 2.4 παρουσιάζεται η χαρακτηριστική γωνία Cherenkov. Η φασματική κατανομή των φωτονίων που παράγονται δίνεται από τη σχέση:

$$\frac{dN}{dxd\lambda} = \frac{2\pi \cdot z^2 \cdot \alpha}{\lambda^2} \cdot \left(1 - \frac{1}{\beta^2 \cdot \eta^2}\right) \tag{2.3}$$

όπου λ το μήκος κύματος του εκπεμπόμενου φωτονίου και α η σταθερά της λεπτής υφής [5].

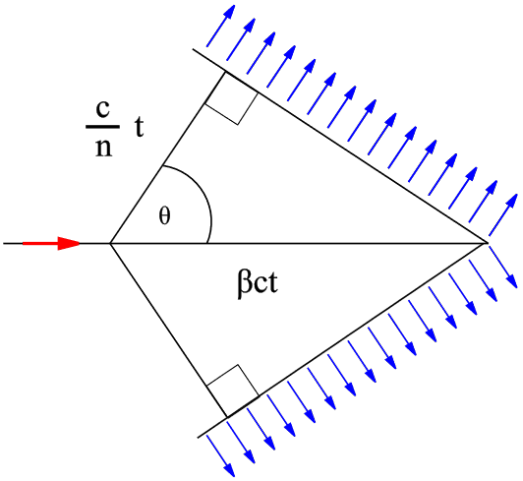

Figure 2.4: Σχηματική απεικόνιση της παραγωγής ακτινοβολίας Cherenkov υπό τη μορφή κώνου, γύρω από φορτισμένο σωματίδιο το οποίο κινείται σε μέσο με συντελεστή διάθλασης η και με ταχύτητα βc. Εικόνα από [35].

Η ανίχνευση νετρίνο υψηλής ενέργειας βασίζεται στην ανίχνευση της ακτινοβολίας Cherenkov η οποία δημιουργείται από τα σωματίδια που παράγονται κατά την αλληλεπίδραση των νετρίνο με την ύλη, συνεπώς οι ανιχνευτικές διατάξεις πρέπει να λειτουργούν σε περιβάλλον σκότους. Επίσης, δεδομένης της πολύ μικρής ενεργού διατομής της αλληλεπίδρασης των νετρίνο, οι ανιχνευτικές διατάξεις πρέπει να καταλαμβάνουν πολύ μεγάλο όγκο. Ένας επιπρόσθετος περιορισμός προέρχεται από τα ατμοσφαιρικά μιόνια (Κεφάλαιο 1.3), τα οποία καθώς διέρχονται μέσα από την ύλη παράγουν ακτινοβολία Cherenkov. Η ακτινοβολία αυτή υπερκαλύπτει το σήμα που παράγουν τα σωματίδια τα οποία προέρχονται από τις αλληλεπιδράσεις νετρίνο. Για τον λόγο αυτό οι ανιχνευτές νετρίνο υψηλής ενέργειας πρέπει να "θωρακίζονται" από τα ατμοσφαιρικά μιόνια.

Λαμβάνοντας υπόψιν τα παραπάνω, τα τηλεσκόπια νετρίνο υψηλής ενέργειας κατασκευάζονται στα βάθη της θάλασσας (ή βαθιών λιμνών) ή στα κατώτερα στρώματα των πάγων της Ανταρκτικής και αποτελούνται από (σχετικά) αραιά τοποθετημένους ανιχνευτές φωτός (φωτοπολλαπλασιαστές - PhotoMultiplier Tubes ή PMTs). Οι τοποθεσίες αυτές καλύπτουν όλους

τους περιορισμούς που προαναφέρθηκαν. Στη βαθιά θάλασσα (ή λίμνη ή πάγο) ικανοποιείται η απαίτηση του απόλυτου σκότους. Επίσης τα χιλιόμετρα νερού ή πάγου πάνω από τους ανιχνευτές αποτελούν θωράκιση από τα ατμοσφαιρικά μιόνια. Τέλος η επιλογή της διάταξης των φωτοπολλαπλασιαστών στον χώρο μπορεί να επιτρέψει την αξιοποίηση μεγάλου όγκου νερού ή πάγου ως ανιχνευτικό όγκο του τηλεσκοπίου νετρίνο.

2.1.3 Τοπολογίες γεγονότων

Η ακτινοβολία Cherenkov που παράγεται από διαφορετικά σωματίδια έχει διαφορετικά τοπολογικά χαρακτηριστικά. Τα μιόνια υψηλής ενέργειας μπορούν να διανύσουν πολλά χιλιόμετρα μέσα στο νερό, τον πάγο αλλά ακόμα και στον στερεό φλοιό της Γης πριν χάσουν την ενέργεια τους. Καθώς διέρχονται από την ύλη, εκπέμπουν φωτόνια Cherenkov υπό γωνία $\sim 42.5^o$. Συνεπώς το "ίχνος" που αφήνουν στον ανιχνευτή έχει γραμμική τοπολογία, η οποία συνήθως αναφέρεται ως (μιονική) τροχιά (muonic track ή απλώς track). Τα λεπτόνια ταυ έχουν παρόμοια συμπεριφορά με τα μιόνια, αλλά έχουν πολύ μικρότερο μέσο χρόνο ζωής ($2.9 \cdot 10^{-13}$ s) και πολύ μεγαλύτερη μάζα, συνεπώς ένα λεπτόνιο ταυ με ενέργεια ~ 100 TeV θα διανύσει μέση απόσταση ~ 5 m πριν διασπαστεί, ενώ ένα λεπτόνιο ταυ με ενέργεια ~ 1 PeV θα διανύσει μέση απόσταση ~ 50 m. Τα ηλεκτρόνια υψηλής ενέργειας διανύουν πολύ μικρές αποστάσεις καθώς χάνουν την ενέργειά τους δημιουργώντας ηλεκτρομαγνητικούς καταιγισμούς (φωτόνια υψηλής ενέργειας λόγω πέδησης, τα οποία δημιουργούν ζεύγη ηλεκτρονίου ποζιτρονίου και οι διαδικασίες αυτές επαναλαμβάνονται). Ο όγκος μέσα στον οποίο δημιουργούνται τα σωματίδια του ηλεκτρομαγνητικού καταιγισμού μπορεί να προσομοιωθεί με κύλινδρο (ομοαξονικό με την διεύθυνση του μητρικού σωματιδίου) διαμέτρου $10 - 20$ cm και μήκους $5 - 20$ m το οποίο αυξάνει, κατά προσέγγιση ανάλογα με τον λογάριθμο της ενέργειας που έχει αποτεθεί στον καταιγισμό [5]. Παρόμοια γεωμετρικά χαρακτηριστά παρουσιάζουν και οι καταιγισμοί αδρονικών σωματιδίων που παράγονται από τις αλληλεπιδράσεις νετρίνο με την ύλη. Τα φορτισμένα σωματίδια που παράγονται τόσο στους ηλεκτρομαγνητικούς όσο και στους αδρονικούς καταιγισμούς εκπέμπουν ακτινοβολία Cherenkov και πρακτικά όλη η ενέργεια που έχει αποτεθεί στον καταιγισμό (από το μητρικό σωματίδιο) μετατρέπεται σε ακτινοβολία. Συνεπώς με την ανίχνευση του φως που παράγεται από τους καταιγισμούς, είναι δυνατός ο υπολογισμός της ενέργειας του καταιγισμού. Λόγω της γεωμετρίας τους αλλά και της σχετικής απόστασης των φωτοπολλαπλασιαστών των τηλεσκοπίων νετρίνο, οι καταιγισμοί μπορούν να θεωρηθούν σχεδόν σημειακές πηγές εκπομπής φωτός. Στην Εικόνα 2.5 παρουσιάζονται οι τοπολογίες μιονικής τροχιάς και καταιγισμού σωματιδίων.

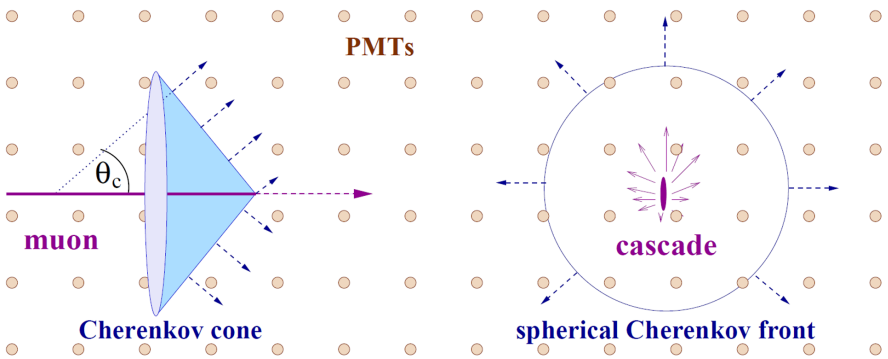

Figure 2.5: Η ακτινοβολία Cherenkov που παράγεται από μιόνιο (αριστερά) και από καταιγισμό σωματιδίων (δεξιά). Εικόνα από [5].

Τοπολογία τροχιάς παρουσιάζουν όλα τα μιόνια που εισέρχονται στον ανιχνευτή, είτε ατμοσφαιρικά είτε μιόνια που έχουν δημιουργηθεί από αλληλεπίδραση φορτισμένου ρεύματος νετρίνο μιονίου. Στην περίπτωση αλληλεπίδρασης φορτισμένου ρεύματος νετρίνο μιονίου η οποία συμβαίνει εντός του όγκου του ανιχνευτή, παρατηρούνται τόσο η τοπολογία καταιγισμού (στο σημείο αλληλεπίδρασης του νετρίνο) όσο και η τοπολογία τροχιάς (starting track).

Όλες οι αλληλεπιδράσεις ουδέτερου ρεύματος παρουσιάζουν τοπολογία καταιγισμού. Η ενέργεια του καταιγισμού δεν είναι ίση με την ενέργεια του μητρικού νετρίνο αλλά με την ενέργεια που μεταφέρθηκε από αυτό στο quark. Επίσης, τοπολογία καταιγισμού παράγουν και οι αλληλεπιδράσεις φορτισμένου ρεύματος νετρίνο του ηλεκτρονίου. Σε αυτή την περίπτωση η ενέργεια του μητρικού νετρίνο μεταφέρεται σε ένα quark που δημιουργεί τον αδρονικό καταιγισμό και σε ένα ηλεκτρόνιο που δημιουργεί ηλεκτρομαγνητικό καταιγισμό, συνεπώς όλη η ενέργεια του μητρικού νετρίνο καταλήγει στους καταιγισμούς. Εξαίρεση μπορεί να αποτελέσει η περίπτωση της αλληλεπίδρασης φορτισμένου ρεύματος αντινετρίνο του ηλεκτρονίου με ηλεκτρόνιο προς σχηματισμό μποζονίου W^- (Glashow resonance). Το μποζονίο W^- έχει πιθανότητα να διασπαστεί σε μιόνιο ($\sim 10\%$ [3]) ή να υπάρξει μιόνιο στην τελική κατάσταση (μετά τις διασπάσεις ασταθών ενδιάμεσων σωματιδίων), συνεπώς σε αυτές τις περιπτώσεις η τοπολογία που παρατηρείται είναι είτε μόνο τροχιά (αν η αλληλεπίδραση συμβεί εκτός του όγκου του ανιχνευτή και το μιόνιο φτάσει στον ανιχνευτή) ή τοπολογία καταιγισμού και τροχιάς (starting track).

Οι αλληλεπιδράσεις φορτισμένου ρεύματος νετρίνο του ταυ είναι δυνατόν να παράγουν πιο πολύπλοκες τοπολογίες αν το ταυ έχει μεγάλη ενέργεια. Αυτό συμβαίνει λόγω των διαφορετικών καναλιών διάσπασης του σωματιδίου. Το ταυ διασπάται σε μιόνιο, νετρίνο του ταυ και αντινετρίνο του μιονίου με πιθανότητα $\sim 17\%$, οπότε παρουσιάζει τοπολογία τροχιάς (είτε τοπολογία starting track αν το σημείο αλληλεπίδραση του νετρίνο βρίσκεται εντός του όγκου του ανιχνευτή). Στις υπόλοιπες περιπτώσεις (είτε διασπάται λεπτονικά σε ηλεκτρόνιο και δύο νετρίνο είτε διασπάται αδρονικά) το αποτέλεσμα είναι καταιγισμός σωματιδίων. Συνεπώς σε αυτές τις περιπτώσεις η τοπολογία της αλληλεπίδρασης φορτισμένου ρεύματος νετρίνο του ταυ είναι δυο καταιγισμοί που η απόστασή τους εξαρτάται από την ενέργεια του ταυ. Όπως ήδη αναφέρθηκε, ένα λεπτόνιο ταυ με ενέργεια ~ 100TeV μπορεί να διανύσει μερικά μέτρα πριν διασπαστεί, με αποτέλεσμα οι δυο καταιγισμοί να μην είναι διακριτοί αλλά να προσομοιάζουν με ένα καταιγισμό. Στην περιπτώση που το ταυ έχει μεγαλύτερη ενέργεια, η διακριτική ικανότητα του τηλεσκοπίου είναι ικανή ώστε να καταγραφούν ως δυο διαφορετικοί καταιγισμοί. Η τοπολογία τέτοιων γεγονότων λέγεται "double bang". Στον Πίνακα 2.1 παρατίθενται συνοπτικά οι τοπολογίες που παρουσιάζουν οι διαφορετικές αλληλεπιδράσεις νετρίνο.

αλληλεπίδραση νετρίνο	τοπολογία
NC όλα τα νετρίνο	καταιγισμός
CC ν_μ & $\overline{\nu_\mu}$	τροχιά ή starting track
CC ν_e	καταιγισμός
CC $\overline{\nu_e}$	καταιγισμός, τροχιά (μικρό ποσοστό του Glashow resonance)
CC ν_τ & $\overline{\nu_\tau}$	καταιγισμός (κυρίως), τροχιά ή starting track, double bang
ατμοσφαιρικά μιόνια	τροχιά

Table 2.1: Αλληλεπιδράσεις νετρίνο και η τοπολογία που παρουσιάζουν. Καταχρηστικά στον πίνακα παρουσιάζονται και τα ατμοσφαιρικά μιόνια.

2.2 Υπόβαθρο σήματος σε υποθαλάσσια τηλεσκόπια νετρίνο

Η σημαντικότερη πηγή υποβάθρου για τα τηλεσκόπια νετρίνο είναι τα ατμοσφαιρικά μιόνια και τα ατμοσφαιρικά νετρίνο. Όπως ήδη αναφέρθηκε στο κεφάλαιο 1.3 αυτά παράγονται όταν σωματίδια της κοσμικής ακτινοβολίας αλληλεπιδρούν με τα μόρια της ατμόσφαιρας. Στην Εικόνα 2.6 παρουσιάζεται η ροή ατμοσφαιρικών μιονίων (σε δύο διαφορετικά ισοδύναμα βάθη νερού) και νετρίνο (με διαφορετικό ενεργειακό εύρος) ως συνάρτηση του συνημιτόνου της πολικής γωνίας. Ενώ η ροή των ατμοσφαιρικών μιονίων είναι τάξεις μεγέθους μεγαλύτερη από αυτή των ατμοσφαιρικών νετρίνο, τα μιόνια δεν μπορούν να διαπεράσουν την Γη, με αποτέλεσμα να φτάνουν στον ανιχνευτή μόνο με καθοδικές διευθύνσεις ενώ τα νετρίνο φτάνουν στον ανιχνευτή από όλες τις διευθύνσεις. Η συνήθης μέθοδος απόρριψης του υποβάθρου των ατμοσφαιρών μιονίων είναι η επιλογή γεγονότων που είτε έχουν ανοδική τροχιά είτε αλληλεπιδρούν μέσα στον ανιχνευτή. Όσον αφορά στα ανιχνευθέντα νετρίνο, δεν υπάρχει τρόπος διαχωρισμού της προέλευσής τους (ατμοσφαιρική ή αστροφυσική) και για τον λόγο αυτό, στα πειράματα ανίχνευσης αστροφυσικών νετρίνο τα ατμοσφαιρικά χαρακτηρίζονται ως υπόβαθρο που δεν μπορεί να ελαττωθεί (irreducible background). Παρόλα αυτά, όπως φαίνεται στην Εικόνα 9.3 όπου παρουσιάζονται η ροή των ατμοσφαιρικών νετρίνο (conventional και prompt) και η διάχυτη ροή των αστροφυσικών νετρίνο όπως ανιχνεύθηκε από το πείραμα IceCube [36], στην περιοχή υψηλής ενέργειας η συνεισφορά των ατμοσφαιρικών νετρίνο είναι πολύ μικρή και συνεπώς σε αυτή την ενεργειακή περιοχή είναι κυρίαρχη η συνεισφορά από νετρίνο αστροφυσικής προέλευσης. Ενώ λοιπόν δεν είναι δυνατός ο διαχωρισμός του σήματος (αστροφυσικά νετρίνο) από το υπόβαθρο (ατμοσφαιρικά νετρίνο) για κάθε ανιχνευθέν γεγονός, είναι δυνατή η μελέτη της διάχυτης ροής νετρίνο εστιάζοντας στην περιοχή υψηλής ενέργειας.

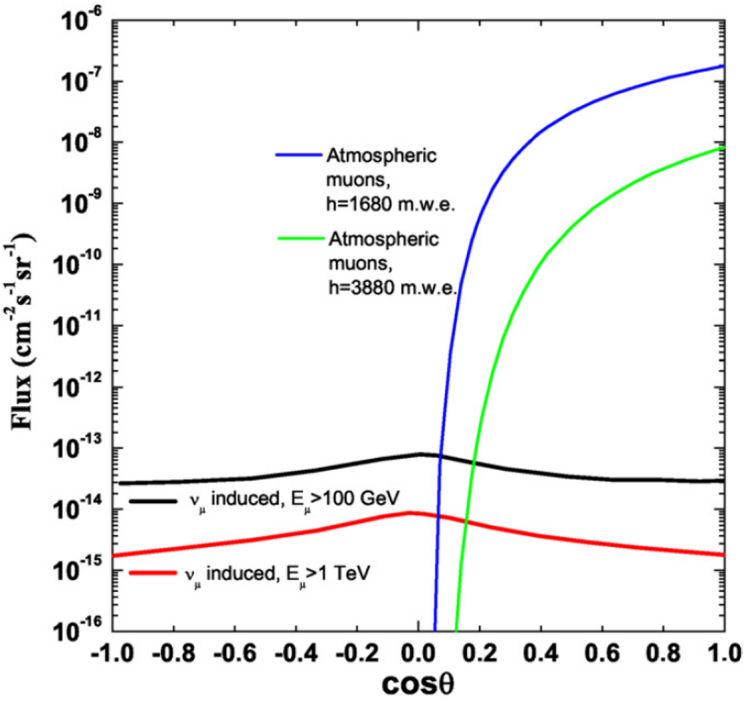

Figure 2.6: Ροή ατμοσφαιρικών μιονίων σε ισοδύναμα βάθη νερού $1680m$ *(με μπλε) και* $3880m$ *(με κόκκινο) και νετρίνο με ενέργειες* $E_\nu > 100$ *GeV (με μαύρο) και* $E_\nu > 1$ *TeV (με κόκκινο) ως συνάρτηση του συνημιτόνου της πολικής γωνίας. Εικόνα από [37].*

Για τα υποθαλάσσια τηλεσκόπια, πηγή οπτικού θορύβου αποτελούν οι ραδιενεργές διασπά-

σεις του ^{40}K. Το ^{40}K είναι ένα ραδιενεργό ισότοπο του καλίου, με χρόνο ημιζωής $\sim 1.3 \cdot 10^9$ χρόνια, που υπάρχει φυσικά στο θαλασσινό νερό σε μικρές ποσότητες. Το ^{40}K διασπάται είτε μέσω της διάσπασης β είτε λόγω πρόσληψης ηλεκτρονίου [35]:

$$\begin{aligned} {}^{40}K &\rightarrow {}^{40}Ca + e^- + \overline{\nu_e} \quad \text{B.R.} \sim 89.3\% \\ {}^{40}K + e^- &\rightarrow {}^{40}Ar + \nu_e + \gamma \quad \text{B.R.} \sim 10.7\% \end{aligned} \tag{2.4}$$

Κατά την διάσπαση β το ηλεκτρόνιο που παράγεται, συνήθως έχει ενέργεια ικανή ώστε να παράγει ακτινοβολία Cherenkov[38]. Επιπλέον το φωτόνιο (ακτίνα γ) που παράγεται κατά την πρόσληψη ηλεκτρονίου μπορεί να σκεδάσει ηλεκτρόνια σε υψηλές ενέργειες ικανά να παράγουν ακτινοβολία Cherenkov. Η ακτινοβολία αυτή εκπέμπεται τυχαία στο θαλασσινό νερό και συνεπώς αποτελεί οπτικό θόρυβο.

Μία ακόμα πηγή φωτός στα μεγάλα θαλάσσια βάθη που ποντίζονται τα τηλεσκόπια νετρίνο προέρχεται από ζωντανούς οργανισμούς. Το φαινόμενο αυτό ονομάζεται βιοφωταύγια. Οι παλμοί φωτός που παράγουν οι υποθαλάσσιοι οργανισμοί οι οποίοι βρίσκονται στα βάθη ενδιαφέροντος, ποικίλουν τόσο σε ένταση όσο και σε διάρκεια. Για παράδειγμα τα βακτήρια συνήθως παράγουν σταθερούς παλμούς διάρκειας ωρών, ενώ μεγαλύτεροι οργανισμοί παράγουν έντονη εκπομπή βραχέων παλμών διάρκειας δευτερολέπτων [35, 39]. Η ένταση του φαινομένου της βιοφωταύγιας διαφέρει από εποχή σε εποχή αλλά και από περιοχή σε περιοχή.

2.3 Τα σημαντικότερα εν λειτουργία τηλεσκόπια νετρίνο

2.3.1 Ιστορική αναδρομή

Η κατασκευή τηλεσκοπίων νετρίνο ξεκίνησε το 1976 με το "Deep Underwater Muon And Neutrino Detector" (DUMAND) project [40] το οποίο είχε ως στόχο την κατασκευή υποθαλάσσιου τηλεσκοπίου νετρίνο στον Ειρηνικό Ωκεανό στα ανοιχτά της νήσου Χαβάη. Ακολούθησε ο ανιχνευτής NT200 στην λίμνη Βαϊκάλη (Ρωσία), η οποία είναι η μεγαλύτερη και η βαθύτερη λίμνη στον κόσμο. Το πείραμα στη λίμνη Βαϊκάλη συνεχίζεται μέχρι και σήμερα, ο αρχικός ανιχνευτής έχει αναβαθμιστεί και η κατασκευή ενός σύγχρονου τηλεσκοπίου νετρίνο βρίσκεται σε εξέλιξη [41]. Συνέχεια στα τηλεσκόπια νετρίνο έδωσε το πείραμα "Antarctic Muon And Neutrino Detector Array" (AMANDA) [42] το όποιο τοποθετήθηκε στους πάγους της Ανταρκτικής. Την σκυτάλη στην κατασκευή τηλεσκοπίων νετρίνο πήρε η Ευρώπη που φιλοξένησε στη Μεσόγειο Θάλασσα τρία projects για την κατασκευή τηλεσκοπίων νετρίνο: το "Neutrino Extended Submarine Telescope with Oceanographic Research" (NESTOR) Project στην Ελλάδα [43], το NEMO στην Ιταλία [44] και το "Astronomy with a Neutrino Telescope and Abyss environmental RESearch" (ANTARES) στην Γαλλία [45].

2.3.2 ANTARES

Το τηλεσκόπιο νετρίνο ANTARES αποτελείται από 12 γραμμικές συστοιχίες ανιχνευτών ποντισμένες στη θαλάσσια περιοχή ~ 40 km νότια της Toulon, σε θαλάσσιο βάθος 2475 m. Σε κάθε συστοιχία φιλοξενούνται 75 οπτικά στοιχεία, οργανωμένα σε 25 "ορόφους" με 3 οπτικά στοιχεία στον καθένα, με προσανατολισμό 45^o προς τα κάτω. Κάθε οπτικό στοιχείο περιέχει ένα φωτοπολλαπλασιαστή διαμέτρου 10 ιντσών. Ο συνολικός όγκος του τηλεσκοπίου είναι ~ 0.01 km^3. Στην Εικόνα 2.7 παρουσιάζεται σχηματική απεικόνιση του τηλεσκοπίου. Το τηλεσκόπιο ANTARES τέθηκε σε λειτουργία τον Μάιο του 2008 και έκτοτε συλλέγει δεδομένα, ενώ η λειτουργία του αναμένεται να σταματήσει περί το 2020 [46, 47, 48]. Το τηλεσκόπιο νετρίνο ANTARES έχει ένα πλούσιο επιστημονικό πρόγραμμα που, εκτός των

άλλων, περιλαμβάνει αναζήτηση σημειακών πηγών εκπομπής νετρίνο, μελέτη της διάχυτης ροής νετρίνο αστροφυσική προέλευσης και πρόγραμμα multi-messenger αστρονομίας. Παρόλα αυτά, λόγω του μικρού του όγκου, δεν έχει την απαραίτητη ευαισθησία για την μελέτη νετρίνο κοσμικής προέλευσης, αλλά έχει θέσει άνω όρια στις αναμενόμενες ροές νετρίνο από σημειακές αστροφυσικές πηγές, από το κέντρο του Γαλαξία μας.

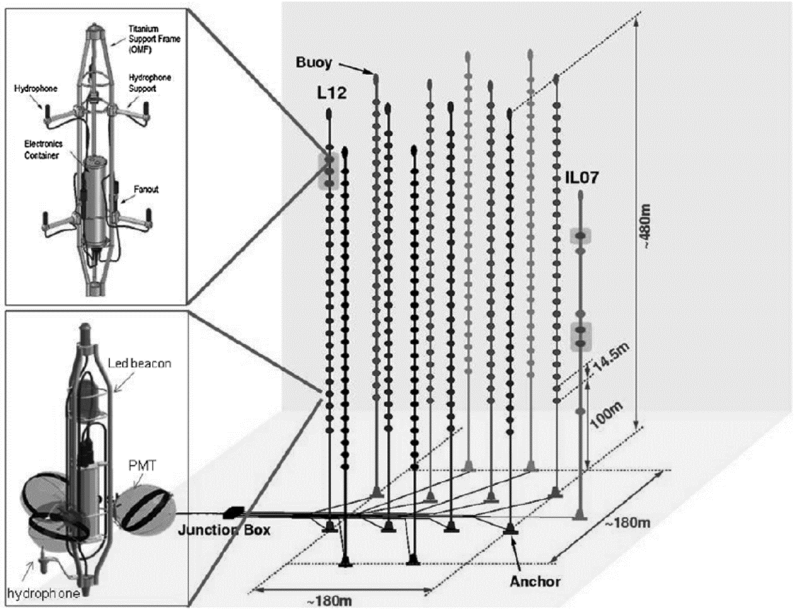

Figure 2.7: Σχηματική απεικόνιση του τηλεσκοπίου νετρίνο ANTARES. Εικόνα από [49].

2.3.3 IceCube

Το τηλεσκόπιο νετρίνο IceCube, που αποτελεί την αναβάθμιση του AMANDA, είναι το μεγαλύτερο εν λειτουργία τηλεσκόπιο νετρίνο. Βρίσκεται στην Ανταρκτική και η κατασκευή του ολοκληρώθηκε το 2010 [50, 51]. Το IceCube αποτελείται από 86 γραμμικές συστοιχίες ανιχνευτών και καταλαμβάνει όγκο 1 km^3. Κάθε γραμμική συστοιχία έχει ύψος $\sim$ 2.5 km και στο τελευταίο $\sim$ 1 km βρίσκονται 60 ψηφιακά οπτικά στοιχεία, που διαθέτουν έναν φωτοπολλαπλασιαστή διαμέτρου 10 ιντσών, σε απόσταση $\sim$ 17 m μεταξύ τους [52]. Οι 80 γραμμικές συστοιχίες απέχουν περίπου 125 m η κάθε μια από τις γειτονικότερες σε αυτή, ενώ 6 που βρίσκονται στο κέντρο του ανιχνευτή βρίσκονται πιο κοντά η μία στην άλλη και αποτελούν την διάταξη Deep Core. Στην επιφάνεια των πάγων πάνω από το τηλεσκόπιο βρίσκεται η διάταξη IceTop η οποία αποτελείται από 324 ψηφιακά οπτικά στοιχεία. Σκοπός του IceTop είναι η μελέτη των ατμοσφαιρικών καταιγισμών αλλά και η συσχέτισή τους με τα δεδομένα που συλλέγονται από το τηλεσκόπιο. Στην Εικόνα 2.8 παρουσιάζεται σχηματική απεικόνιση του τηλεσκοπίου νετρίνο IceCube.

Το IceCube είναι το πρώτο τηλεσκόπιο νετρίνο που ανίχνευσε νετρίνο αστροφυσικής προέλευσης. Από δεδομένα που αντιστοιχούν σε χρονική διάρκεια ανίχνευσης 7.5 χρόνων βρέθηκαν 103 γεγονότα νετρίνο υψηλής ενέργειας (όπου η ενέργεια που αποτέθηκε στον ανιχνευτή είναι μεγαλύτερη από 60 TeV) τα οποία αλληλεπίδρασαν μέσα στον ανιχνευτή. Τα γεγονότα αυτά παρουσιάζονται στην Εικόνα 2.9 και εκτιμάται ότι 75% από αυτά είναι αστροφυσικής προέλευσης [53]. Με βάση τη συγκεκριμένη επιλογή γεγονότων, αλλά και σε δείγματα γεγονότων επιλεγμένα με άλλες μεθόδους, το IceCube μελέτησε τη διάχυτη ροή

νετρίνο αστροφυσικής προέλευσης αλλά και την ροή ατμοσφαιρών νετρίνο (conventional και prompt) [53, 54, 55, 56, 25, 57]. Ένας άλλος επιστημονικός στόχος του IceCube σχετίζεται με την ανίχνευση νετρίνο του ταυ και την διάχυτη ροή αυτών των νετρίνο [54]. Τέλος, όπως αναφέρθηκε στο κεφάλαιο 1.2.4, ένα σημαντικό βήμα στην αστρονομία νετρίνο έγινε με τη συσχέτιση νετρίνο που ανιχνεύθηκε από το IceCube με τον blazar TXS 0506+056.

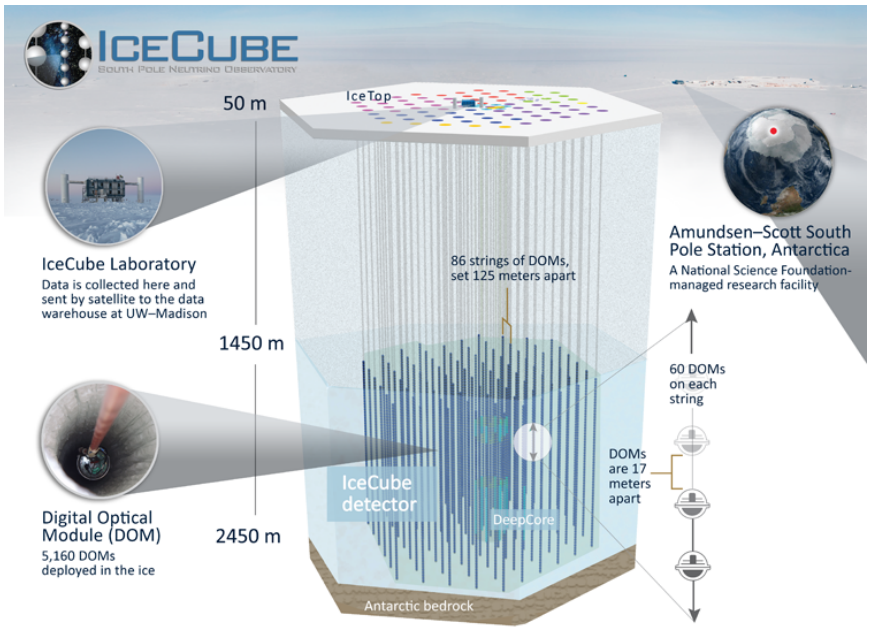

Figure 2.8: Σχηματική απεικόνιση του τηλεσκοπίου νετρίνο IceCube. Εικόνα από [52].

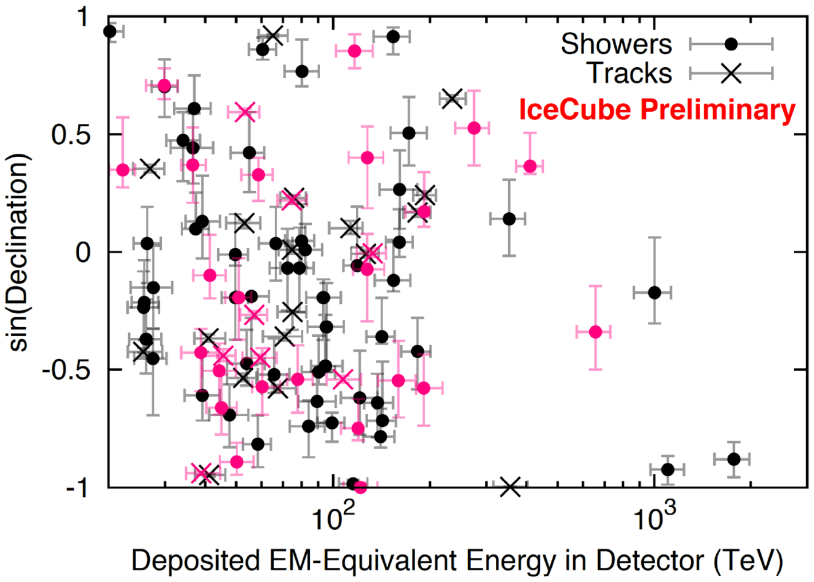

Figure 2.9: 103 *γεγονότα νετρίνο υψηλής ενέργειας που αλληλεπίδρασαν μέσα στο τηλεσκόπιο IceCube (7.5 χρόνια) σε σχέση με την απόκλιση (declination) και την ενέργεια που αποτέθηκε στον ανιχνευτή. Εικόνα από [53].*

Chapter 3

Το Πείραμα KM3NeT

3.1 Γενικά

Το πείραμα KM3NeT έχει ως στόχο την κατασκευή ανιχνευτών νετρίνο νέας γενιάς και την πόντισή τους στα βάθη της Μεσογείου. Τον Απρίλιο του 2019 στο πείραμα KM3NeT συμμετείχαν 53 ερευνητικά ιδρύματα και πανεπιστήμια από 17 χώρες σε 4 ηπείρους (Εικόνα 3.1) [58]. Τρεις τοποθεσίες στη Μεσόγειο Θάλασσα έχουν επιλεγεί από το πείραμα για την πόντιση των ανιχνευτικών διατάξεων (Εικόνα 3.1). Η πρώτη, KM3NeT-Fr, βρίσκεται περίπου 40 km νότια της Toulon (Γαλλία) και το θαλάσσιο βάθος είναι περίπου 2450 m. Ο παράκτιος σταθμός συλλογής δεδομένων και ελέγχου του ανιχνευτή βρίσκεται στο ινστιτούτο Michel Pacha στην πόλη La Seyne sur Mer. Η δεύτερη, KM3NeT-It, βρίσκεται περίπου 100 km νοτιοανατολικά του Portopalo di Capo Passero (Σικελία, Ιταλία) όπου βρίσκεται και ο παράκτιος σταθμός συλλογής δεδομένων και ελέγχου του ανιχνευτή και το θαλάσσιο βάθος είναι περίπου 3500 m. Τέλος, η τρίτη, KM3NeT-Gr, βρίσκεται στην θαλάσσια περιοχή ανοιχτά της Πύλου (Ελλάδα) σε απόσταση λίγων δεκάδων χιλιομέτρων από την ξηρά. Στην θαλάσσια περιοχή της Πύλου υπάρχουν βαθύπεδα με βάθη που κυμαίνονται από 3000 m μέχρι και πάνω από 4500 m. Επιπλέον υπάρχει παράκτιος σταθμός συλλογής δεδομένων και ελέγχου του ανιχνευτή ο οποίος όμως χρειάζεται αναβάθμιση τόσο των ηλεκτρικών όσο και των υπολογιστικών του συστημάτων[58]. Κοντά στην τοποθεσία KM3NeT-Fr λειτουργεί το τηλεσκόπιο νετρίνο ANTARES[59] ενώ στις τοποθεσίες KM3NeT-It και KM3NeT-Gr λειτουργούσαν τα πειράματα NEMO και NESTOR[60] αντίστοιχα. Οι φυσικές, γεωφυσικές και ωκεανογραφικές ιδιότητες και των τριών τοποθεσιών έχουν μελετηθεί λεπτομερώς[39]. Επίσης στις εν λόγω περιοχές το νερό έχει καλές οπτικές ιδιότητες, χαμηλά επίπεδα βιοφωταύγειας, τα θαλάσσια ρεύματα έχουν χαμηλές ταχύτητες και ο ρυθμός επικάθησης ιζήματος σε υποθαλλάσια αντικείμενα (sedimentation) είναι χαμηλός[61, 39].

Υπό την σκέπη του πειράματος KM3NeT κατασκευάζονται 2 ανιχνευτές νετρίνο. Ο ανιχνευτής νετρίνο ORCA - Oscillation Research with Cosmics in the Abyss και το τηλεσκόπιο νετρίνο υψηλής ενέργειας ARCA - Astroparticle Research with Cosmics in the Abyss. Ο ανιχνευτής ORCA ποντίζεται στη Γαλλία τοποθεσία ενώ το τηλεσκόπιο ARCA στην Ιτάλια. Ενώ και οι δυο ανιχνευτές χρησιμοποιούν την ίδια τεχνολογία, η διάταξή τους στον χώρο είναι διαφορετική διότι στοχεύουν στην ανίχνευση νετρίνο με διαφορετικό ενεργειακό εύρος.

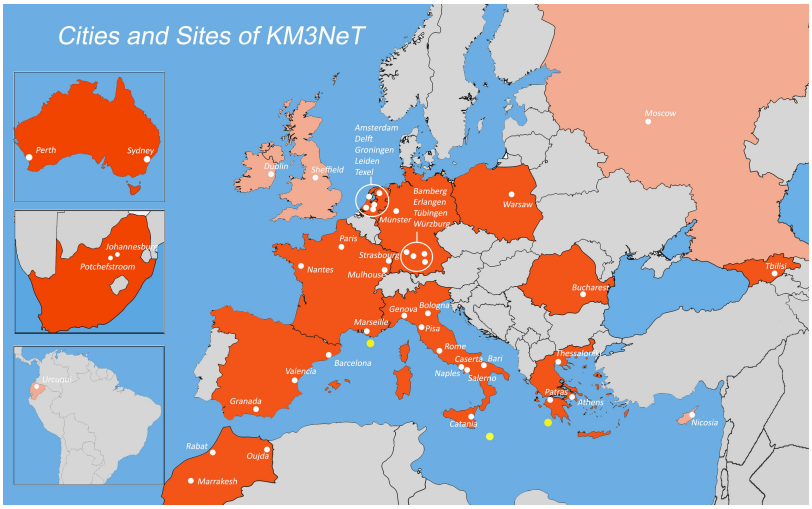

Figure 3.1: Οι πόλεις που φιλοξενούν Ερευνητικά Ιδρύματα ή Πανεπιστήμια που συμμετέχουν στο πείραμα KM3NeT τον Απρίλιο του 2019 *(άσπρο) και η θέση των τριών τοποθεσιών πόντισης των ανιχνευτών (κίτρινο)[58].*

3.2 Το ψηφιακό οπτικό στοιχείο (DOM) του πειράματος KM3NeT

3.2.1 Γενικά

Το καινοτόμο ψηφιακό οπτικό στοιχείο (Digital Optical Module - DOM) του πειράματος KM3NeT παρουσιάζεται στην Εικόνα 3.2 και περιέχει 31 φωτοπολλαπλασιαστές (PhotoMultiplier Tubes - PMTs) με διάμετρο φωτοκαθόδου 3 ίντσες [61, 62, 63]. Η συνολική επιφάνεια των φωτοκαθόδων των PMT σε κάθε DOM είναι περίπου 3 φορές μεγαλύτερη από αυτή των οπτικών στοιχείων με ένα PMT διαμέτρου 10 ιντσών προγενέστερων πειραμάτων ανίχνευσης νετρίνο όπως τα πειράματα ANATRES [64] και ICECUBE[65]. Οι 31 φωτοπολλαπλασιαστές είναι κατανεμημένοι έτσι ώστε να επιτυγχάνεται ισοτροπική γωνιακή κάλυψη. Επίσης επιτυγχάνεται ευκολότερη μέτρηση των φωτονίων που ανιχνεύονται από το DOM σε σχέση με οπτικά στοιχεία με ένα PMT μεγαλύτερης διαμέτρου, καθώς μια πρώτη ικανή προσέγγιση του αριθμού των ανιχνευθέντων φωτονίων είναι απλώς η μέτρηση των PMT που ανίχνευσαν φως. Τέλος χρησιμοποιώντας χρονικές συσχετίσεις μεταξύ των ανιχνευθέντων φωτονίων από τους PMT είναι δυνατή η απόρριψη του οπτικού θορύβου από τις ραδιενεργές διασπάσεις του ^{40}K.

3.2.2 Τα βασικότερα δομικά στοιχεία του DOM

Τα DOM του πειράματος KM3NeT έχουν σχεδιαστεί έτσι ώστε να αντέχουν στις συνθήκες πίεσης που επικρατούν στα μεγάλα θαλάσσια βάθη όπου ποντίζονται ο ανιχνευτής ORCA και το τηλεσκόπιο ARCA. Για αυτόν τον λόγο το DOM αποτελείται εξωτερικά από βοριοπυριτική γυάλινη σφαίρα διαμέτρου 17 ιντσών και πάχους 14mm (Vitrovex). Η σφαίρα σχηματίζεται με την ένωση δύο ημισφαιρίων και παρέχει ικανή αντοχή για πιέσεις τουλάχιστον 400bar. Επίσης η απορρόφηση φωτός στα μήκη κύματος ενδιαφέροντος ($\lambda \geq 350$ nm) είναι μικρότερη από 5%. Στην Εικόνα 3.3 παρουσιάζονται τα σημαντικότερα δομικά στοιχεία από τα οποία αποτελείται το DOM. Το άνω ημισφαίριο της γυάλινης σφαίρας επισημαίνεται ως B.

Από τους 31 PMT οι 12 βρίσκονται στο άνω ημισφαίριο ενώ οι υπόλοιποι 19 στο κάτω. Οι PMT τοποθετούνται στις εσοχές ενός ειδικά κατασκευασμένου πλαισίου στήριξης. Το πλαίσιο

Figure 3.2: Το ψηφιακό οπτικό στοιχείο του πειράματος KM3NeT.

αυτό αποτελείται από 2 τμήματα ένα για το άνω και ένα για το κάτω ημισφαίριο, είναι νάιλον και κατασκευάζεται από εκτυπωτές 3D (Εικόνα 3.3 J). Οι PMT συγκρατούνται με τσιμούχες (o-rings) στο πλαίσιο στήριξης και ο χώρος μεταξύ της γυάλινης σφαίρας και του πλαισίου στήριξης γεμίζει με ειδική γέλη (opticla gel) δυο συστατικών η οποία έχει περίπου τον ίδιο δείκτη διάθλαση (~ 1.40) με το γυαλί της σφαίρας (1.47) και των PMT ($1.51 - 1.54$). Η γέλη εκτός οπτικής ζεύξης γυάλινης σφαίρας - PMT προσφέρει και επιπλέον μηχανική στήριξη στους PMT και προστασία από κραδασμούς κατά την μεταφορά και πόντιση των DOM. Στο πλαίσιο στήριξης τοποθετούνται και ανακλαστικές ταινίες σε σχήμα δακτυλιδιού (Εικόνα 3.3 G) γύρω από κάθε PMT υπό γωνία 45^o με σκοπό την συλλογή περισσοτέρων φωτονίων (αύξηση 20% - 40%). Οι PMT τοποθετούνται ανά 6 σε 5 δακτυλίους με πολική γωνία 56^o, 72^o, 107^o, 123^o και 148^o και ένας PMT τοποθετείται στο νότιο πόλο του DOM (βρίσκεται δηλαδή σε πολική γωνία 180^o). Σε κάθε δακτύλιο οι PMT είναι τοποθετημένοι έτσι ώστε κάθε δυο γειτονικοί να σχηματίζουν αζιμουθιακή γωνία 30^o. Επίσης οι PMT του κάθε δακτυλίου είναι στραμμένοι ως προς τους PMT των γειτονικών δακτυλίων κατά γωνία $\sim 30^o$. Στην Εικόνα 3.2 φαίνεται η θέση των PMT στο DOM.

Στον χώρο του άνω ημισφαιρίου όπου δεν περιέχονται PMT τοποθετούνται τα ηλεκτρονικά του DOM (Εικόνα 3.3 D και E). Επίσης ένα σύστημα παθητικής ψύξης των ηλεκτρονικών τοποθετείται στον ίδιο χώρο με στόχο την απαγωγή της θερμότητας και την ευκολότερη μετάδοση της στο νερό. Το σύστημα αυτό αποτελείται από μια μεταλλική ράβδο που διατρέχει καθ'ύψος το DOM και καταλήγει σε μια διάταξη που έχει σχήμα μανιταριού και εφάπτεται στο άνω τμήμα του άνω ημισφαιρίου (Εικόνα 3.3 C). Το παθητικό σύστημα ψύξης εγγυάται ότι στο εσωτερικό του DOM οι θερμοκρασίες δεν θα ξεπερνούν τους 30^oC όταν λειτουργεί υπό κανονικές συνθήκες και βρίσκεται βυθισμένο σε νερό.

Στο άνω ημισφαίριο του DOM περιέχεται ένα LED flasher που μπορεί να εκπέμπει φως προς τα πάνω και χρησιμοποιείται για τη βαθμονόμηση της χρονικής απόκρισης των DOM όταν είναι ποντισμένα (Εικόνα 3.3 I). Επίσης περιέχεται ένα μανόμετρο για τον έλεγχο της πίεσης στο εσωτερικό DOM (Εικόνα 3.3 L). Το άνω ημισφαίριο της γυάλινης σφαίρας έχει δυο οπές. Στην μια είναι τοποθετημένη μια βαλβίδα κενού για την απορρόφηση αέρα ώστε να κλείσει το

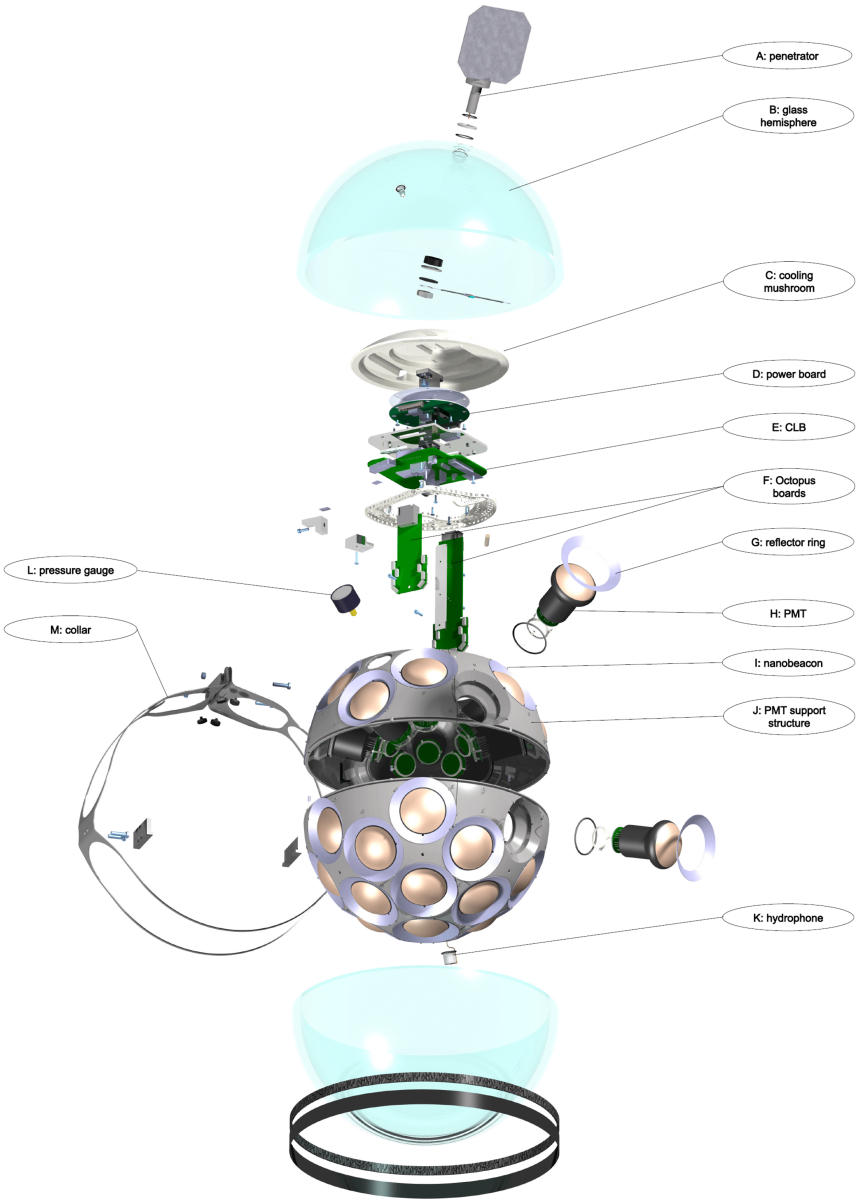

Figure 3.3: Τα σημαντικότερα δομικά στοιχεία από τα οποία αποτελείται το DOM του πειράματος KM3NeT. Εικόνα από [62].

DOM λόγω της υποπίεσης στο εσωτερικό του. Στη δεύτερη οπή τοποθετείται ένα εξάρτημα που ονομάζεται διακορευτής (Εικόνα 3.3 A). Από τον διακορευτή (penetrator) διέρχονται τα καλώδια που τροφοδοτούν με ηλεκτρική ισχύ το DOM και οι οπτικές ίνες που μεταφέρουν τα δεδομένα στον παράκτιο σταθμό συλλογής δεδομένων. Ο διακορευτής είναι κατασκευασμένος από τιτάνιο με τέτοιο τρόπο ώστε να αντέχει στις συνθήκες υψηλής πίεσης που επικρατούν στα μεγάλα θαλάσσια βάθη στα οποία ποντίζονται οι ανιχνευτές. Στο κάτω ημισφαίριο είναι τοποθετημένος ένας ακουστικός αισθητήρας (Εικόνα 3.3 K) ο οποίος εφάπτεται στην γυάλινη σφαίρα. Ο ακουστικός αισθητήρας αποτελεί τμήμα του συστήματος εύρεσης της σχετικής θέσης των DOM, με χρήση ηχητικών παλμών και ακρίβεια εκατοστών. Γύρω από το DOM τοποθετείται ένα κολάρο από τιτάνιο (Εικόνα 3.3 M) το οποίο σφίγγει τη γυάλινη σφαίρα.

Με το κολάρο, το DOM συγκρατείται σε 2 σκοινιά και 18 διαδοχικά DOM σχηματίζουν μια ανιχνευτική μονάδα (Detection Unit - DU).

3.2.3 Οι φωτοπολλαπλασιαστές

Για την επιλογή των φωτοπολλαπλασιαστών βασική προϋπόθεση, εκτός της άριστης απόδοσης, καθώς και της μεγιστοποίηση της συνολικής φωτοευαίσθητης επιφάνειας σε κάθε DOM, αποτέλεσαν και οι περιορισμοί που προήλθαν από στις διαστάσεις του DOM. Για τους πιο πάνω λόγους επιλέχθηκε (τουλάχιστον για την πρώτη φάση κατασκευής του πειράματος) ο φωτοπολλαπλασιαστής R12199 – 02 από την Hamammatsu [66]. Η μέση κβαντική απόδοση (quantum efficiency) αυτών των PMT είναι $> 23\%$ στα 404 nm και $> 20\%$ στα 470 nm και το transit time spread είναι < 5ns. Το dark count rate κυμαίνεται μέχρι 1500Hz[62] ενώ ο ρυθμός ανίχνευσης φωτονίων λόγω των ραδιενεργών διασπάσεων του ^{40}K είναι από 5kHz μέχρι 10kHz, καθιστώντας το dark count rate επιτρεπτό. Ένα επιπρόσθετο πλεονέκτημα των PMT είναι ότι λόγω του μικρού τους μεγέθους η επίδραση του μαγνητικού πεδίου της γης στην τροχιά των ηλεκτρονίων μπορεί να θεωρηθεί αμελητέα και συνεπώς δεν απαιτείται η μαγνητική τους θωράκιση.

3.2.4 Ελάττωση της συνεισφοράς του οπτικού θορύβου.

Χάρη στην δυνατότητα καταμέτρησης φωτονίων, κάθε μεμονωμένο DOM μπορεί να "αναγνωρίσει" αν τα φωτόνια που ανιχνεύει προέρχονται από μιόνια (είτε ατμοσφαιρικά είναι από αλληλεπίδραση φορτισμένου ρεύματος νετρίνο μιονίου) ή από αλληλεπιδράσεις νετρίνο από τον οπτικό θόρυβο. Τα φωτόνια που παράγονται λόγω των ραδιενεργών διασπάσεων του ^{40}K (οπτικός θόρυβος) δημιουργούνται τυχαία και δεν σχετίζονται μεταξύ τους. Αντίθετα, τα φωτόνια που παράγονται από μιόνια ή από αλληλεπιδράσεις νετρίνο (χωρίς να υποστούν σκεδάσεις) φτάνουν στους PMT του DOM με πολύ μικρές χρονικές διαφορές.

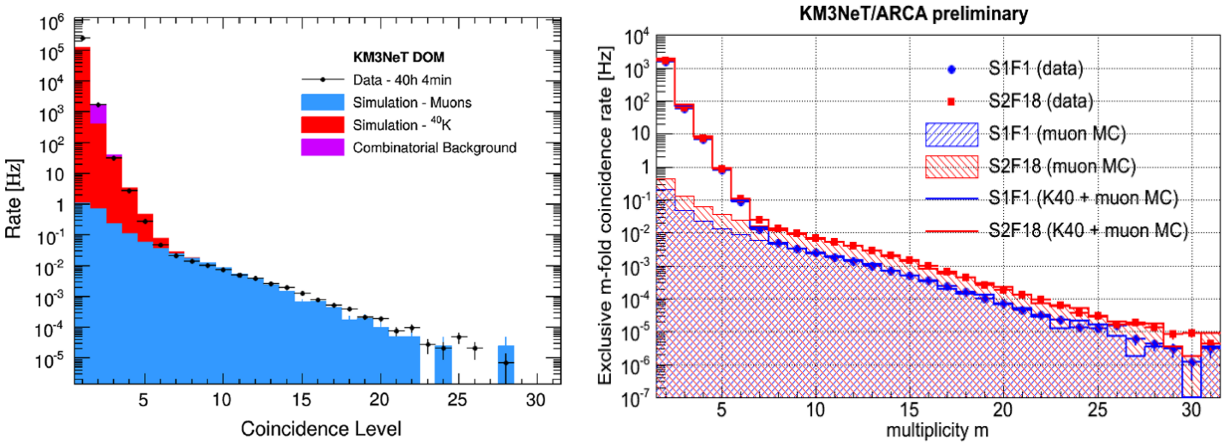

Figure 3.4: Συχνότητα με την οποία m PMT στο ίδιο DOM πραγματοποιούν ανίχνευση σε χρονικό παράθυρο 25 ns (multiplicity ή Coincidence level). Αριστερά: Δεδομένα και προσομοιώσεις (ατμοσφαιρικά μιόνια και οπτικός θόρυβος) για το test prototype DOM[67]. Δεξιά: Δεδομένα και προσομοιώσεις (ατμοσφαιρικά μιόνια και οπτικός θόρυβος) για 2 DOM από τις δυο πρώτες ποντισμένες ανιχνευτικές μονάδες του τηλεσκοπίου νετρίνο ARCA[68].

Ήδη από το test prototype DOM[67] αυτή η δυνατότητα του DOM είχε επιβεβαιωθεί. Επιπλέον επιβεβαίωση προσφέρουν τα δεδομένα από τις δυο πρώτες ποντισμένες ανιχνευτικές

μονάδες του τηλεσκοπίου νετρίνο ARCA. Στην Εικόνα 3.4 παρουσιάζονται τα δεδομένα από το test prototype DOM (αριστερά) και από τις δυο πρώτες ποντισμένες ανιχνευτικές μονάδες του τηλεσκοπίου νετρίνο ARCA (δεξιά). Από τις συγκρίσεις δεδομένων και προσομοιώσεων γίνεται φανερό ότι όταν 8 ή περισσότεροι PMT ανιχνεύσουν φωτόνια σε κάποιο μικρό χρονικό παράθυρο (εδώ 25ns) η συνεισφορά του θορύβου ελαχιστοποιείται ενώ επικρατεί η συνεισφορά φωτονίων που παράγονται από ατμοσφαιρικά μιόνια (η συνεισφορά φωτός από αλληλεπιδράσεις νετρίνο που αναμένεται να ανιχνευθεί από κάθε DOM μεμονωμένα είναι αμελητέα). Επιπλέον στην Εικόνα 3.4 δεξιά απεικονίζεται ο ρυθμός ανίχνευσής από 2 DOM που απέχουν περίπου 610m κατακόρυφη απόσταση. Μπορεί να παρατηρηθεί ότι ο ρυθμός ανίχνευσης συμπτώσεων < 7 είναι ίδιος και για τα 2 DOM, διότι οι ραδιενεργές διασπάσεις του ^{40}K δεν εξαρτώνται από το θαλάσσιο βάθος, ενώ ρυθμός ανίχνευσης συμπτώσεων ≥ 8 είναι σταθερά μικρότερος για το DOM που είναι ποντισμένο σε μεγαλύτερο βάθος καθώς λιγότερα ατμοσφαιρικά μιόνια φτάνουν σε μεγαλύτερο βάθος. Τα δεδομένα είναι σε συμφωνία με τις προσομοιώσεις ατμοσφαιρικών μιονίων.

3.3 Ο ανιχνευτής νετρίνο KM3NeT/ORCA

Ο ανιχνευτής νετρίνο ORCA είναι ένας από τους δύο ανιχνευτές που κατασκευάζονται από το πείραμα KM3NeT. Ο κύριος επιστημονικός στόχος του ανιχνευτή ORCA είναι η μελέτη της ιεραρχίας μάζας των νετρίνο μέσω της μελέτης της ταλάντωσης των ατμοσφαιρικών νετρίνο [69]. Ο ανιχνευτής ORCA στοχεύει στην ανίχνευση ατμοσφαιρικών νετρίνο με ενέργεια από λίγα GeV μέχρι και μερικές δεκάδες GeV. Σε αυτό το ενεργειακό εύρος εντοπίζεται η μέγιστη διαφορά στον αναμενόμενο ρυθμό ανίχνευσης νετρίνο ηλεκτρονίου και μιονίου τα οποία διέρχονται μέσα από την Γη, υποθέτοντας είτε την κανονική είτε την ανεστραμμένη ιεραρχία μάζας, λόγω της αλληλεπίδρασης των νετρίνο με την ύλη από την οποία διέρχονται. Για την επίτευξη του στόχου αυτού εκτός από τον ακριβή προσδιορισμό της ενέργειας των ανιχνευθέντων νετρίνο εξίσου σημαντική είναι και η ακριβής ανακατασκευή της διεύθυνσης του νετρίνο ώστε να μπορεί να προσδιοριστεί η πυκνότητα στήλης της μάζας της Γης από την οποία διήλθε κάθε νετρίνο.

Για την εύρεση της βέλτιστης διάταξης των οπτικών στοιχείων στον ανιχνευτή, κύριο κριτήριο είναι το ενεργειακό εύρος των νετρίνο ενδιαφέροντος. Τα DOM στις ανιχνευτικές του μονάδες του KM3NeT/ORCA απέχουν κατακόρυφη απόσταση 9m ενώ οι DU απέχουν οριζόντια απόσταση περίπου 20m. Ο ανιχνευτής, η κάτοψη του οποίου φαίνεται στην Εικόνα 3.5, θα αποτελείται από 115 DU και θα καταλαμβάνει όγκο περίπου 8Mton. Προσομοιώσεις έχουν δείξει ότι η πολική γωνιακή διακριτική ικανότητα του ανιχνευτή αναμένεται να έχει διάμεσο περίπου 5^o, ενώ η ενεργειακή του διακριτική ικανότητα αναμένεται να είναι περίπου 20% για γεγονότα καταιγισμού (αλληλεπίδρασης φορτισμένου ρεύματος νετρίνο ηλεκτρονίου) με ενέργεια νετρίνο ~ 10 GeV.

Εκτός του κύριου επιστημονικού στόχου, άλλοι βασικοί στόχοι του ανιχνευτή ORCA είναι:

- Η μελέτη της ανίχνευση νετρίνο ταυ λόγω ταλάντωσης ατμοσφαιρικών νετρίνο μιονίου.
- Η ανίχνευση νετρίνο από υπερκαινοφανείς αστέρες.
- Η διεξαγωγή τομογραφικής μελέτης της Γης αξιοποιώντας τις ταλαντώσεις των ατμοσφαιρικών νετρίνο.
- Η συμμετοχή στα Multi-messenger προγράμματα του πειράματος KM3NeT.
- Η μελέτη των κοσμικών ακτίνων μέσω της μελέτης ατμοσφαιρικών νετρίνο και μιονίων.

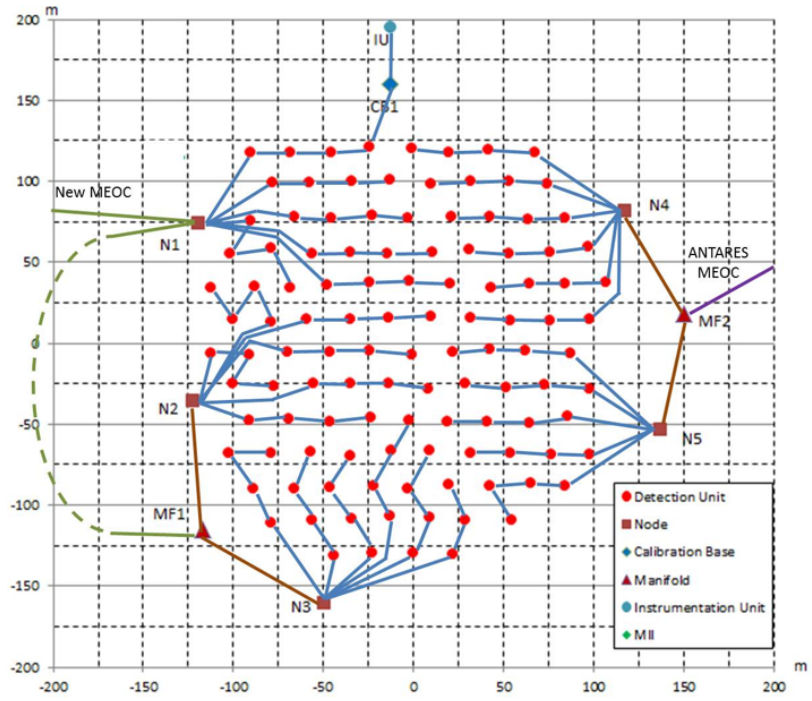

Figure 3.5: Κάτοψη του ανιχνευτή ORCA.

- Η μελέτη νετρίνο από αλληλεπιδράσεις σωματιδίων σκοτεινής ύλης που παγιδεύονται βαρυτικά σε μαζικά σώματα (όπως η Γη, ο Ήλιος ή το κέντρο του Γαλαξία μας).

Τον Ιούλιο του 2019 υπήρχαν 4 ποντισμένες ανιχνευτικές μονάδες του ανιχνευτή ORCA που συνέλεγαν δεδομένα.

3.4 Το τηλεσκόπιο νετρίνο KM3NeT/ARCA

Ο δεύτερος ανιχνευτής που κατασκευάζει το πείραμα KM3NeT είναι το τηλεσκόπιο νετρίνο ARCA. Οι κύριοι επιστημονικοί στόχοι του τηλεσκοπίου ARCA είναι η ανίχνευση νετρίνο υψηλής ενέργειας από σημειακές αστροφυσικές πηγές και η μελέτη της διάχυτης ροής νετρίνο υψηλών ενεργειών αστροφυσικής προέλευσης. Το ενεργειακό εύρος ενδιαφέροντος του τηλεσκοπίου ARCA είναι από TeV μέχρι και εκατοντάδες PeV. Λόγω της θέσης πόντισης του τηλεσκοπίου (Μεσόγειος Θάλασσα) περισσότερο από 85% του ουρανού είναι ορατό χρησιμοποιώντας νετρίνο μιονίου που έχουν ανοδική φορά (διέρχονται μέσα από τη Γη). Επιπλέον στο οπτικό πεδίο του τηλεσκοπίου (Εικόνα 3.6) βρίσκεται το κέντρο του Γαλαξία αλλά και το μεγαλύτερο τμήμα του Γαλαξιακού επιπέδου όπου βρίσκονται πληθώρα γαλαξιακών πηγών οι οποίες εν δυνάμει εκπέμπουν νετρίνο. Τα εξωγαλαξιακά αστροφυσικά αντικείμενα που αναμένεται να εκπέμπουν νετρίνο είναι ισοκατανεμημένα στον ουρανό.

Το τηλεσκόπιο ARCA, η κάτοψη του οποίου φαίνεται στην Εικόνα 7.6 (αριστερά), θα αποτελείται από δύο δομικές μονάδες. Κάθε δομική μονάδα θα αποτελείται από 115 DU. Τα DOM της κάθε DU απέχουν κατακόρυφη απόσταση 36m ενώ η οριζόντια απόσταση των γειτονικών DU είναι $\sim$ 90m. Η κάθε δομική μονάδα προσομοιάζει σε έναν κύλινδρο ακτίνας περίπου 500m και ύψους περίπου 610m, άρα και όγκου περίπου $0,5$ km^3 (Εικόνα 7.6 δεξιά). Συνεπώς το τηλέσκοπιο θα καταλαμβάνει όγκο 1 km^3. Η διάταξη των DOM έχει βελτιστοποιηθεί ώστε η ευαισθησία του τηλεσκοπίου να είναι μεγίστη σε νετρίνο με ενέργεια στο ενεργειακό

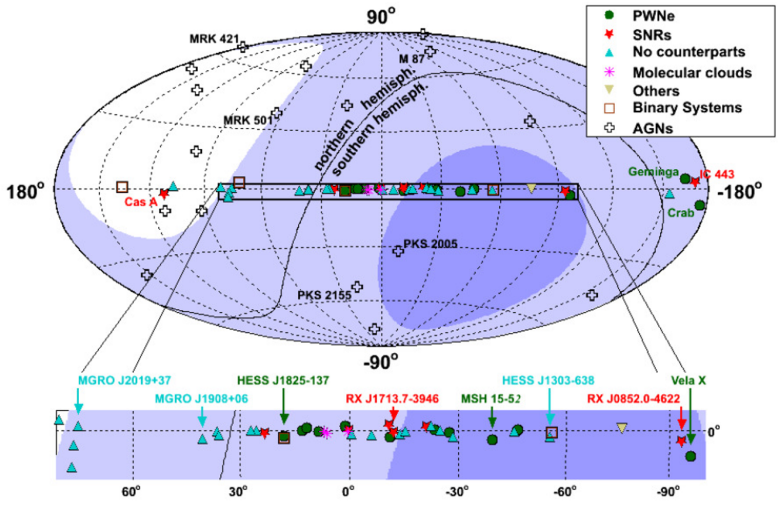

Figure 3.6: Το οπτικό πεδίο του τηλεσκοπίου ARCA. Οι περιοχές του ουρανού με σκούρο μπλε χρώμα είναι ορατές πάνω από 75% ανά ημέρα, ενώ αυτές με ανοιχτό μπλε πάνω από 25% χρησιμοποιώντας νετρίνο μιονίου με ανοδική φορά. Επίσης παρουσιάζονται αστροφυσικά αντικείμενα με έντονη εκπομπή σε ακτίνες-γ. Εικόνα από [35]

εύρος ενδιαφέροντος.

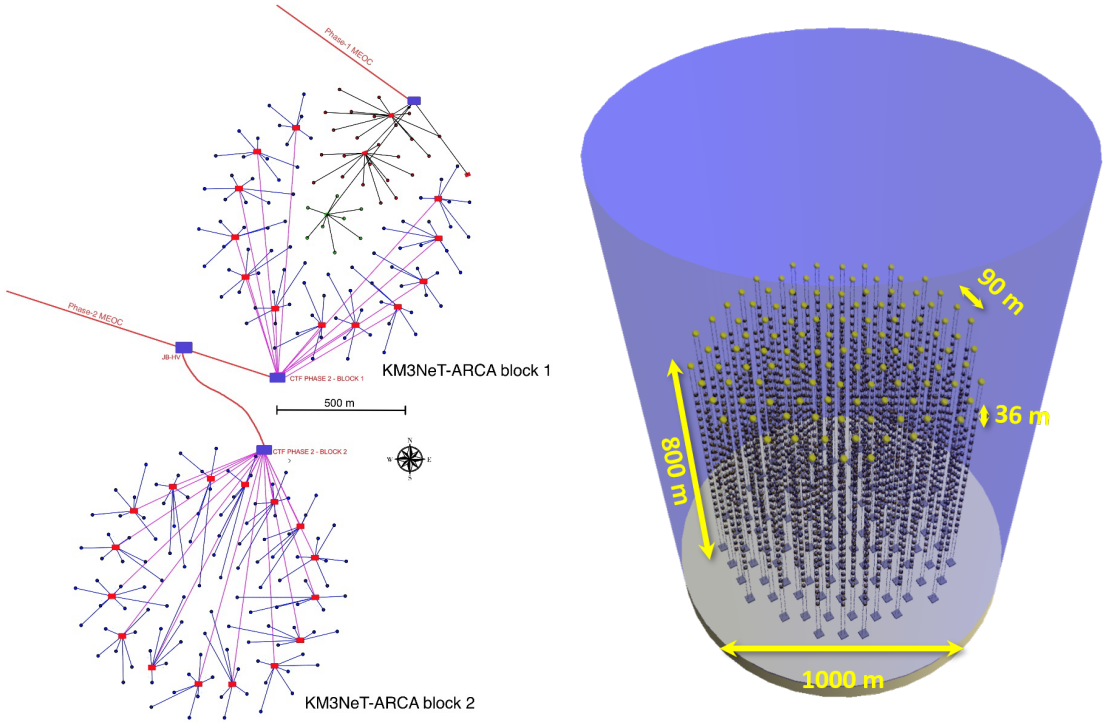

Figure 3.7: Αριστερά: Κάτοψη του ανιχνευτή ARCA. Δεξιά: Σχηματική απεικόνιση ενός δομικού στοιχείου του τηλεσκοπίου.

Οι οπτικές ιδιότητες του νερού είναι τέτοιες ώστε το μήκος απορρόφησης των φωτονίων (στο μήκος κύματος ενδιαφέροντος) να είναι μικρότερο από το μήκος σκέδασης, συνεπώς η σκέδαση των φωτονίων είναι δευτερεύουσας σημασίας (σε αντίθεση με τον πάγο όπου ισχύει το

αντίθετο). Οι οπτικές ιδιότητες του νερού σε συνδυασμό με την ικανότητα εύρεσης της διεύθυνσης των ανιχνευθέντων φωτονίων, επιτρέπουν ανακατασκευή της διεύθυνσης των νετρίνο με πρωτοφανή ακρίβεια για τηλεσκόπιο νετρίνο. Πιο συγκεκριμένα, εκτενείς προσομοιώσεις έδειξαν ότι η διάμεσος της γωνιακής διακριτικής ικανότητας για γεγονότα τροχιάς αναμένεται να είναι $< 0,2^o$ για γεγονότα με $E_{\mu\text{ονίου}} > 10$ TeV και $< 0,1^o$ για γεγονότα με $E_{\mu\text{ονίου}} > 100$ TeV, ενώ η ενεργειακή διακριτική ικανότητα αναμένεται να είναι περίπου 20% του λογαρίθμου της ενέργειας. Επιπλέον σε γεγονότα (αλληλεπίδρασης φορτισμένου ρεύματος νετρίνο ηλεκτρονίου) καταιγισμού με $E_{\nu\text{ετρίνο}} > 60$ TeV η διάμεσος της γωνιακής διακριτικής ικανότητας είναι $< 2^o$ και η ενεργειακή διακριτική ικανότητα είναι περίπου 5%. Η διακριτική ικανότητα του τηλεσκοπίου τόσο σε γεγονότα τροχιάς όσο και σε γεγονότα καταιγισμού αλλά και οι μέθοδοι ανακατασκευής, παρουσιάζονται αναλυτικότερα στο κεφάλαιο 5.5.

Εκτός των κύριων επιστημονικών στόχων, άλλοι βασικοί στόχοι του τηλεσκοπίου ARCA είναι:

- Η ανίχνευση νετρίνο ταυ στη διάχυτη ροή νετρίνο αστροφυσικής προέλευσης καθώς και ο προσδιορισμός της σύστασης των γεύσεων νετρίνο στη διάχυτη ροή αστροφυσικής προέλευσης.
- Η ανίχνευση νετρίνο από εκλάμψεις ακτίνων-γ.
- Η ανίχνευση νετρίνο από υπερκαινοφανείς αστέρες.
- Η συμμετοχή στα Multi-messenger προγράμματα του πειράματος KM3NeT.
- Η μελέτη των κοσμικών ακτίνων μέσω της μελέτης ατμοσφαιρικών νετρίνο και μιονίων.
- Η μελέτη νετρίνο από αλληλεπιδράσεις σωματιδίων σκοτεινής ύλης που παγιδεύονται βαρυτικά σε μαζικά σώματα (όπως η Γη, ο Ήλιος ή το κέντρο του γαλαξία μας).

Τον Ιούλιο του 2019 υπήρχαν 2 ποντισμένες ανιχνευτικές μονάδες του τηλεσκοπίου ARCA που συνέλεγαν δεδομένα.

Chapter 4

The GRBNeT Project: An Autonomous Neutrino Detector

4.1 General

Neutrinos from GRBs are expected to have very high energies and they are also expected to be more abundant than those created from other, less energetic, astrophysical objects. In order to detect such ultra high energy neutrinos the optimal detector layout is one where a very large volume is sparsely instrumented. High energy muons, created by ultra high energy neutrinos interacting via Charged Current (CC) interaction with the surrounding medium, can be detected and tracked traveling through such a sparse detector. However, building, providing power to, maintaining and handling the data of such a huge and sparse detector is quite cost ineffective and complicated. A detector consisting of autonomous detection units is a very interesting alternative.

Large scale facilities, like the KM3NeT/ARCA telescope, focus on the detection of galactic and extragalactic neutrino point sources as well as on the defuse neutrino flux. Increased sensitivity for the detection of ultra high energy neutrinos, like those expected from GRBs, can be achieved by sparsely instrumenting larger volumes. Since one of the of the most cost demanding parts of large underwater telescopes is the sea-bed network, needed for providing power to the detection units and transferring all data to shore, sparsely instrumenting larger volumes becomes cost ineffective. To this end, it is possible that a more cost effective way is to deploy autonomous detectors around existing large scale facilities like KM3NeT/ARCA. The sensitivity of the combined detector to ultra high energy neutrinos will be greatly enhanced compared to that of the initial large scale detector, due to the increase of the instrumented volume to several cubic kilometers.

To explore this possibility the Gamma Ray Burst Neutrino Telescope (GRBNeT) project [70, 71, 72] had been aiming to design, build and deploy an autonomous prototype neutrino detector. It was successfully completed with the deployment of a prototype detector on the 28th of October 2015. The GRBNeT project was funded by the Greek National Strategic Reference Frame Work (THALES Initiative 2011 – 2015) and it was a collaboration between the Institute of Nuclear and Particle Physics of N.C.S.R. Demokritos, the University of Athens and the Hellenic Center for Marine Research with more than 15 scientists and engineers participating. Special attention was paid to the autonomy of the GRBNeT prototype detector, as it was considered to be the most crucial part of the whole project. Thus the GRBNeT detector was designed to be autonomous both power-wise and in data-taking.

4.2 Mechanical design

The original GRBNeT design comprised four cross shaped titanium latticed frames (floors), having an arm length of approximately 7 m, arranged into two cluster. The distance between the cluster had been set to 300m while the floor to floor distance within the cluster to 40m. That detector layout would have allowed the possibility to perform local coincidence at trigger level at each cluster. Due to a budget reduction imposed to all "THALES" projects, the above design had been aborted and GRBNeT prototype was realized with two floors having a distance of 30m, as illustrated in the schematic representation of the GRBNeT detector in Figure 4.1. This layout suppressed the possibility of using local coincidences on the trigger level.

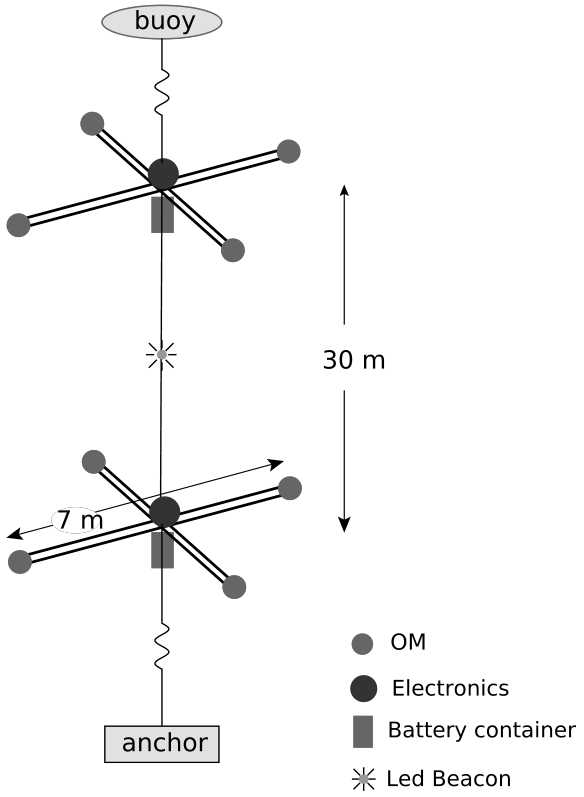

Figure 4.1: A schematic representation of the GRBNeT prototype detector.

Each floor had been equipped with 4 Optical Modules (OMs) similar to those used by NESTOR experiment [73, 74], the electronics' unit containing the necessary electronics for the operation of the OMs and the power unit containing the necessary batteries for each floor's operation. Each OM comprised a single 13" Hamamatsu R8055 PhotoMultiplier Tube (PMT) surrounded by a mu-metal mesh glued with silicon gel inside a 17" diameter, 1.5 mm thick glass sphere (VITROVEX). Detailed studies about the optimal OMs' orientations had conducted so that the GRBNeT detector layout was optimized for ultra-high energy neutrinos ($E_\nu \geq 1$ PeV). It was found that the optimal results were achieved when the OMs were facing horizontally. Moreover, when taking into consideration the geographical location of the deployment site (Mediterranean Sea), it was found that a detection unit with single PMT OMs facing horizontally has a full sky coverage during a day.

On each floor the electronics unit had been located in the center of the cross at the

upper side. All the necessary electronics for providing the 4 OMs with power and for the data acquisition were housed in a VITROVEX glass sphere. At the lower side the power unit, a 60 L plastic container filled with paraffin oil housing the necessary batteries for the operation of each floor, had been attached. The electronics unit had been connected with the 4 OMs and the power unit with deep sea cables. Ten VITROVEX glass spheres, contained in their plastic protective shells (hard hats), had been attached to the arms of each cross in order to provide the necessary buoyancy so that each floor would have negative weight in the seawater and would float to the sea surface once the anchor was released. They were positioned in such a way that the total torque was zero. Photographs of floors of GRBNeT prototype taken during the deployment (Section 4.5) are presented in Figure 4.2.

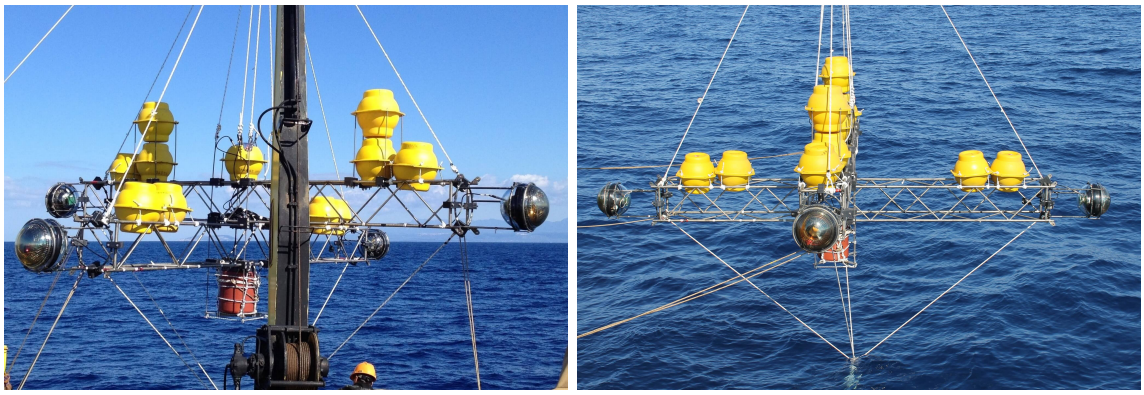

Figure 4.2: Left: A GRBNeT floor lifted from the deck of R/V AEGEO. Right: A GRBNeT floor just before submersion.

The two cross shaped floors had been separated by a 30 m rope and each one operated totally independent from the other. Two LED beacons, for redundancy, had been placed in the exact middle of the distance between the two floors. They had been designed to produce a pulse of light in a 12-hour time interval reaching all OMs in both floors simultaneously. Each beacon consisted of an RC circuit with 4 LEDs, powered by a 9 V battery. The beacons had been housed in a transparent plexiglas container filled with paraffin oil. The two beacons had a time offset of 6 hours, so artificial events were produced every 6 hours for testing purposes, triggered by an autonomous timer.

The main bouy unit had been separated by a 150 m rope from the upper floor. It consisted of 4 Vitrovex glass spheres in their plastic protective shells (hard hats) held together with a mechanical (cage like) structure made of iron, painted and equipped with anode protection. On the mechanical structure a VHF location unit had been attached along with flash lights to facilitate the detection of the prototype in case the recovery would have been conduced at night time. Even though each floor was buoyant the primary purpose of Main Buoy Unit had been to keep the whole structure in a vertical position.

The lowest part of the GRBNeT prototype was the anchor unit. The upper part of the anchor unit was a set of acoustic releases tied to the main rope and connected in parallel with an iron chain. The iron chain had also been connected to the mechanical structure of the anchor which was made from ordinary iron painted and equipped with anode protection. The weight of the anchor (600 kg) was enough to keep the whole prototype in place.

The backbone of the GRBNeT prototype was the main rope. It was a special double braid rope of 16 mm diameter, high mechanical strength (up to 6719 kg) and resistance to

corrosion. The length of the rope was 200 m and it had been equipped with the appropriate terminators and shackles for the different components to be attached to it. Additional double braid ropes of 14 mm diameter, 4 m length, high mechanical strength (up to 4994 kg) and resistance to corrosion had been used to securely attach each floor to the main rope.

4.3 Autonomy

As mentioned in Section 4.1 the autonomy of the GRBNeT prototype had been considered as the most crucial part of the whole project. For this reason very low power electronics had been designed and implemented and each floor had been equipped with a dedicated power unit, providing enough power for a 6-month operation period. Also all data produced by the prototype had been recorded in SD memory cards, rendering the GRBNeT prototype a fully autonomous neutrino detector prototype.

4.3.1 Low power electronics

The Data Acquisition (DAQ) and Slow Control had been implemented with custom made electronics in order to fulfill the requirements of low power consumption and autonomy. The original resistive divider design HV-controller of each PMT, had been replaced by a custom made Cockroft Walton (CW) voltage multiplier. This had been controlled by a HV control unit that utilized ultra-low power microcontrollers in order to retain the desired HV value for each different PMT. The delicate task of removing the resistive base enclosed in synthetic resin without causing any mechanical stress to the PMT, had been accomplished by the use of a chemical dissolvant. Some hours after applying the dissolvant, the texture of the resin became soft (almost jelly-like) and easy to remove without applying any force. During that time the PMT had been enclosed in a black bag to be protected from any light exposure. After this procedure had been completed, the CW voltage multiplier base was attached to each PMT. A PMT with the original resistive base enclosed in the resin and a PMT during the resin-removing procedure are shown in Figure 4.3 left and in Figure 4.4, a PMT with the CW-base attached is presented.

The Control Board was the analog system that distributed power from the power unit to each one of the OMs and all the electronic components. The analog pulses produced when photons hit a PMT had been compared to 4 different threshold levels by the use of discriminators. The four thresholds used were: 80, 800, 1200 and 2000 mV, which corresponded to pulses produced by 2, 20, 30 and 50 photo-electrons respectively. When a threshold was reached the discriminator produced a digital pulse with duration same to the time the analog signal remained above that specific threshold. These digital pulses acted as input to the digital circuit implemented on a Field Programmable Gate Array (FPGA) board. The Slow Control Unit, the second analog system directly connected to all 4 OMs of the floor, periodically recorded the HV values to an SD card. It also communicated via an I2C communication protocol with a compass and a tilt meter, located in the electronics unit of each floor, and recorded the readings to the same SD card. All records had been accompanied by a time stamp produced by an internal clock. The internal clocks of the Control Boards on each floor, had been synchronized with a GPS clock prior to the deployment.

The DAQ consisted of a Spartan-6 LX16 Evaluation FPGA board [75] designed to detect and record any possible signal from High Energy neutrinos. In order to identify this signal

Figure 4.3: Left: A PMT with the original resistive base enclosed in the resin. Right: A PMT during the resin-removing procedure.

and reject the noise (i.e. from ^{40}K) a trigger logic based on coincidences between the arrival time of pulses from the different OMs had been implemented at the Coincidence Logic Unit (CLU). This trigger had been refined by detailed simulations presented in Section 4.4. For accurate timing a Microsemi SA.45 s Chip Scale Atomic Clock had been used to provide a stable, low-jitter reference clock of 10 MHz and a Pulse-Per-Second (PPS) signal at the upper floor, while at the lower floor the FPGA clock had been used. By implementing both setups (with and without an atomic clock) at the prototype it would allow an accurate assessment of the performance of the FPGA clock at the offline analysis, having as reference the artificial events produced by the LED beacons.

As mentioned above, the digitized pulses were used as an input to the FPGA. The CLU searched for time coincidence of all pulses passing the second threshold ($\geq$ 20 photo-electrons). Each pulse initiated a 200 ns time window to open and as 3-fold coincidence the detection of two other pulses in that time window was considered. When a 3-fold coincidence occurred, the event was triggered and the time window expanded for an additional 100 ns. When the 300 ns time window expired, all the data produced by the detector during that time window were stored temporarily in a RAM block, to be permanently stored to a devoted high speed 64 Gb SD memory card via the SPI protocol. The SD card operated as SPI slave, while an SPI master had been developed in the FPGA to handle the read/write procedures. The average number of pulses per event and the number of events per minute found by the simulations of atmospheric muons (Section 4.4), indicated that 64 Gb of memory would be more than enough to store all the data produced per floor in a time period of operation of more than 6 months. For triggered events (300 ns time window) the following information had been recorded for all pulses produced at either one of the 4 PMTs of the floor passing the second threshold:

- the id of the PMT that produced each pulse
- the arrival time of each pulse compared to the arrival time of the first pulse that

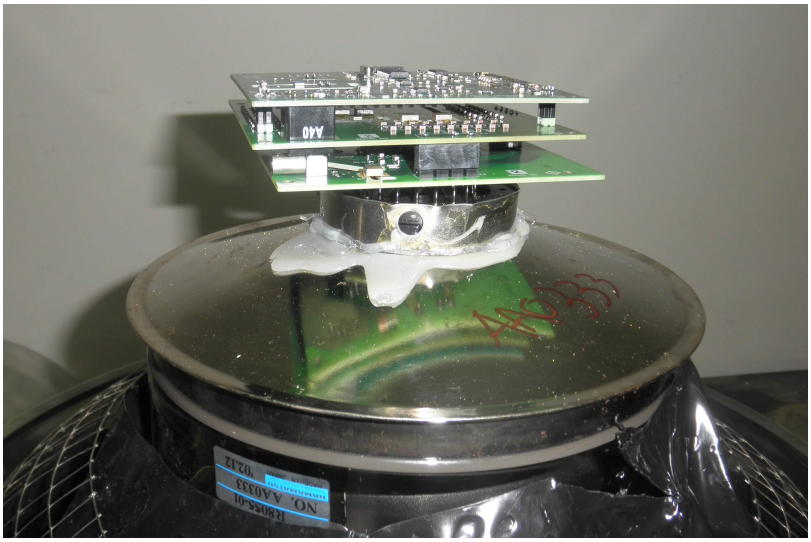

Figure 4.4: A PMT with a CW base.

initiated the time window

- the Time over Threshold (ToT) of the pulse.

And once per coincidence:

- the absolute arrival time of the first pulse that triggered the time window (necessary for the offline physics analysis).

The absolute time stamping has been considered as necessary since after the retrieval and during the off-line data analysis phase, the events recorded at each floor would need to be correlated to those detected at the other floor. Also the potential association of the recorded events to satellite or terrestrial telescope observations of GRBs (GRB alerts) occurred during the data-taking phase would be possible only if the absolute time would be available. For GRB alerts, such time correlations can provide a very powerful reduction on both the atmospheric muon and the atmospheric neutrino backgrounds. Furthermore, for any future applications, like the instrumentation of larger volumes around existing large scale facilities with GRBNeT-style strings, the correlation of the detected events by the GRBNeT-style strings to those detected by the underwater neutrino detector is of utmost importance.

The FPGA had also been programmed to record the number of pulses (rate) passing the first threshold. A counter was set per PMT and every 0.5s, at the end of this time period it was written to RAM along with the PMT id and it was reset to 0. These data had also been written to a devoted 64 Gb SD memory card communicating with the FPGA in the same way as that recording the coincidences. The first threshold had been used only to record the rate. The main contribution to the rate comes from the decay of ^{40}K in sea water. In order to perform an accurate measurement of the rate due to ^{40}K, the first threshold was chosen at 2 photo-electrons to avoid the contribution of the PMT dark rate (pulses created without any photon triggering the PMT).

Both the analog and digital electronics had been integrated and securely attached on a custom made mechanical structure, designed to fit inside a Vitrovex glass sphere which comprised the electronics unit of each floor of the GRBNeT prototype and to stay horizontal

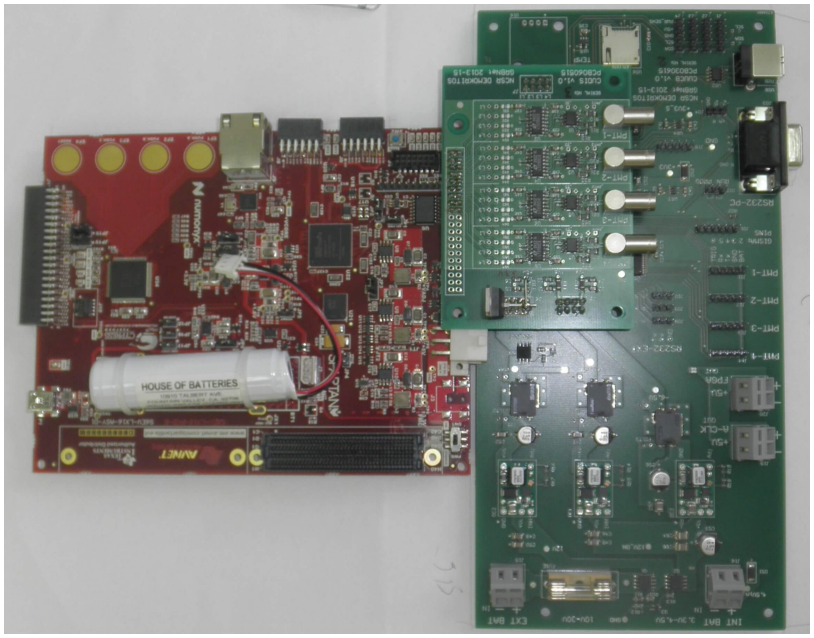

Figure 4.5: The boards of the electronics unit located at the lower floor of the GRBNeT prototype. On the left side of this picture the FPGA board is shown (red board) and on the right side the analog electronics of the Control Board and the Slow Control Unit (green boards).

even if the glass sphere was not perfectly horizontal. The only exception were the Cockroft Walton (CW) voltage multiplier and the HV control unit which had been attached to the PMTs. The electronics of the lower floor are shown in Figure 4.5. They were identical to those of the upper floor with the exception of the atomic clock used only in the upper floor. Five holes were very carefully drilled on the Vitrovex glass sphere housing the electronics and in each one a GIZMA series 35 7-pin connectors was fixed. Deep sea cables had been used to connect the 4 OMs and the power unit to the electronics unit at each floor. The integrated electronics unit is shown in Figure 4.6 left. The electronics unit had been placed inside a hard hat in order to be safely attached to the mechanical structure of GRBNeT prototype, as shown in Figure 4.6 right.

4.3.2 Power unit

The low power electronics discussed in the previous subsection had been powered by D type Varta alkaline batteries, arranged in clusters of 13 batteries in series. The batteries had been housed in the power units of each floor, allowing for the completely autonomous operation of each floor. The power unit comprised is shown in Figure 4.7 and it comprised a 60 L plastic container exposed to full depth pressure of 3000m, inside which 43 clusters of batteries had been placed. The compression of the diameter of the plastic container had been measured under pressure of 400 bar in a hyperbaric chamber filled with water and it was found to be approximately 3.2mm. A hole had been drilled on the top of the plastic container and a GISMA receptacle series 35 was placed. Each cluster of batteries had been enveloped in a plastic tube and the bottom of the plastic container had been covered with rectangular coconut fiber mats to minimize the probability of batteries short circuiting. Each cluster had been connected through protection diode in parallel with the

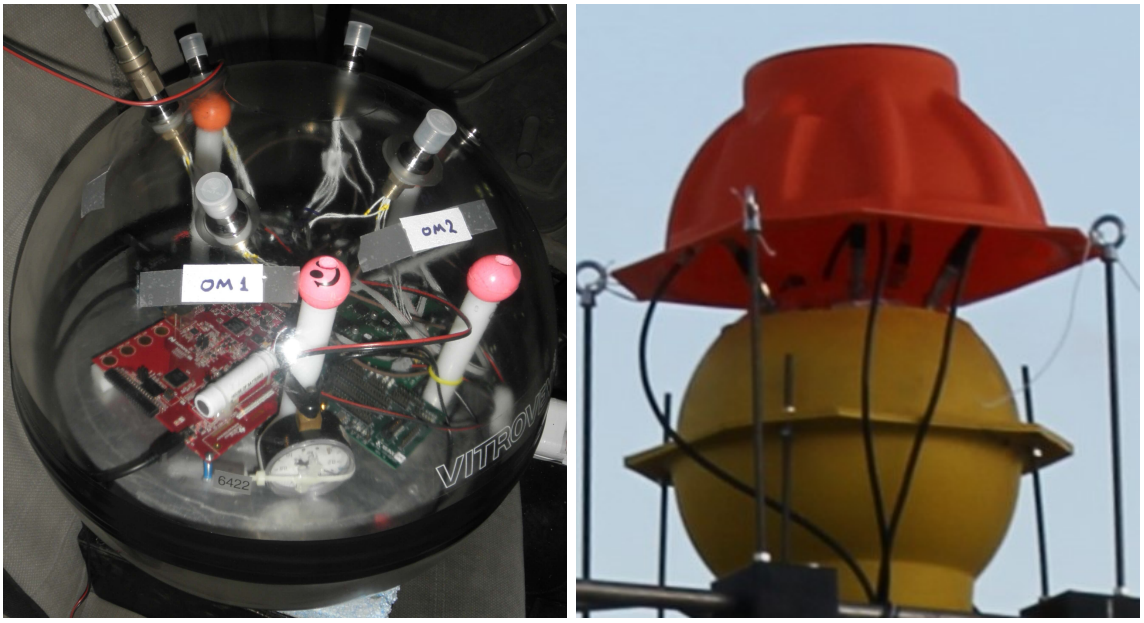

Figure 4.6: Left: The electronics unit of the GRBNeT. Right: The electronics unit attached to the GRBNeT prototype with all the deep sea cables (to the 4 OMs and the power unit) connected. The additional (orange) hard hat had been used for the safe transport to the deployment site and was removed just prior to the deployment.

other clusters and all clusters were connected to the conductors of the GISMA receptacle, so the nominal voltage (which was the same as that of 1 cluster) was 19.5 V and the initial voltage was 20.8 V. Finally the container had been filled with paraffin oil which acts as an insulator and is practically incompressible for the ambient pressure at 3000m depth.

Since the batteries were meant to be exposed to the full ambient pressure at a depth of 3000 m, a number of tests had been conducted beforehand to study the behavior of the batteries under pressure. First the durability of various brands of batteries had been tested in a hyperbaric chamber filled with water under the pressure of 400 bar. The outcome was that the shape of the batteries was distorted. For some brands the whole body had been distorted while in others the distortion was limited to the areas around the positive and / or negative terminals which were filled with air (by design). To prevent this effect small holes had been drilled in the positive and negative terminals (metal cups) and the tests were repeated. The distortion observed in the batteries with holes on their terminal was smaller and in some hardly noticeable. D type Varta alkaline batteries showed no distortion even at the initial tests, so there was no need to drill holes to their terminals. Consequently these batteries were chosen as power elements for the GRBNeT prototype.

Several tests had also been performed to study the discharge behavior of the batteries under pressure and no significant deviation was observed. The time needed for discharging for 7 batteries on a 10Ω resistance at 1 bar (3 batteries) and 400 bar (4 batteries) is presented in Figure 4.8 left, where the voltage drop of the batteries is shown versus the discharge time of each cell. The battery cluster capacity was also measured for 1 cluster of batteries under pressure of 400 bar. For this test one cluster had been placed in the plastic container (along with gravel) and it was connected to the conductors of the GISMA receptacle. The container had been filled with paraffin oil, sealed and then placed inside the hyperbaric chamber. A deep sea cable, reaching out of the chamber, had been connected to the power

Figure 4.7: A power unit of the GRBNeT Prototype

unit which remained to the pressure of 400 bar for 10 days. During the compression the battery cluster had been discharging through a 158 Ohm resistor in order to emulate the intensity of the electrical current (134mA) required by the electronics unit of the detector. The voltage of the battery cluster was logged at real time and the discharge curve is shown in Figure 4.8 right. From this curve the capacity of the battery cluster was calculated and found to be 17 Ah. Since 43 clusters were placed in each power unit, the total battery capacity of each power unit was approximately 730 Ah.

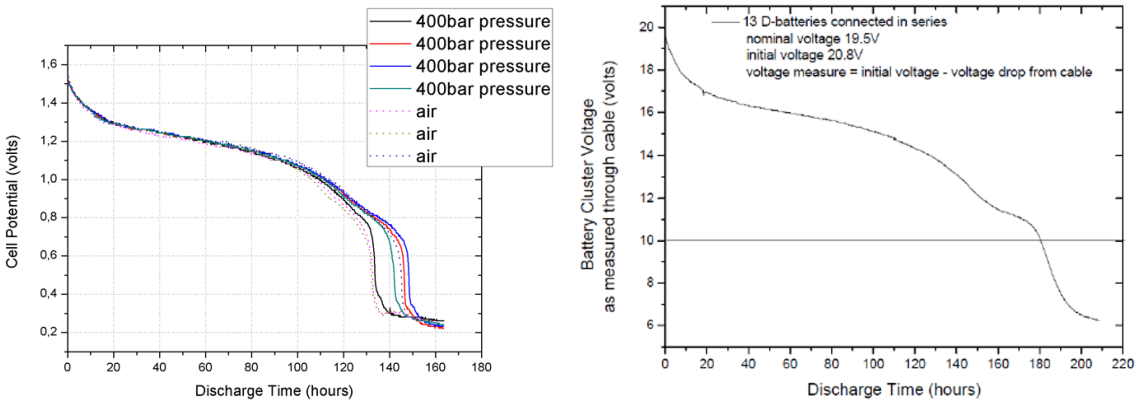

Figure 4.8: Left: The voltage (V) of seven batteries versus the discharge time of each cell. Dotted/solid lines correspond to batteries discharging in air/under pressure of 400 bar respectively. Right: Voltage with respect to time for a cluster of batteries discharging through a 158 Ohm resistor during compression to 400 bars.

4.4 Simulations and trigger studies

4.4.1 General

The aim of the GRBNeT prototype detector was to investigate the possibility of implementing autonomous detection units for increasing the detection ability for high energy neutrinos from GRBs. Even though this was only a prototype, detailed simulations had been conducted in order to optimize the trigger used at each floor to enhance the potential signal from High Energy (HE) neutrinos from GRBs and at the same time minimize the contribution from all background sources. These studies were necessary for the design of the electronic of the prototype to have a reliable estimation of the event rate. Also based on this event rate the thresholds of the discriminators (level above which the analog pulses produced by the PMTs were digitized and fed to the FPGA board) were set. Moreover, the work load of the FPGA board as well as of the necessary volume of the SD memory card on which the events (coincidences) were recorded for the given livetime of 6 months had been evaluated.

For these simulations the most up to date tools, at the time, developed and supported by the KM3NeT experiment had been used:

- Atmospheric muons had been generated using the *MUPAGE* program [76] (see chapter 5.2.2).
- High Energy neutrino events had been generated using the *ANIS* program [77].
- Muons had been propagated using the *MMC* program [78].
- The simulation of the response of the detector to the signal produced by muons, neutrinos and the optical noise due to ^{40}K decays in the seawater as well as all the physic analyses had been conducted using the SeaTray [79, 80] framework. SeaTray was developed for use in the KM3NeT Collaboration and it consisted of modules organized in IceTray framework developed and provided by the IceCube Collaboration.

When high energy muon neutrinos (i.e. from GRBs) interact with the matter (rock or sea water) via Charge Current (CC) interaction, high energy muons are produced. These muons can travel up to several kilometers in seawater before they lose their energy, so they can be detected at large distances from the interaction point. Moreover, in the energy range of interest, muons with higher energies lose more energy per unit length, so more light is produced per unit length, allowing an increased acceptance threshold of the detected pulses. By increasing the acceptance threshold the background from ^{40}K decays can be significantly suppressed while the expected signal from high energy muons (created by high energy neutrinos) suffers practically no loss. Furthermore, a high acceptance threshold for the detected pulses results to a decrease of the contribution of muons with lower energies, like atmospheric muons, or muons produced by CC interactions of atmospheric neutrinos.

Simulations and trigger studies were performed in two steps. Initially the multi-PMT OMs used in KM3NeT were implemented in the simulations and at the physics analysis level a modification was used to approximate the behavior of the large singe-PMT OMs used in the GRBNeT detector. The results of these analyses provided the initial input for the mechanical design and to the electronics working groups. They were followed by a detailed study simulating the actual detector geometry of the GRBNeT detector with the single 13 inch PMT OMs.

4.4.2 Initial simulations and trigger studies

4.4.2.1 Assumptions

For the first level trigger studies the simulated detector geometry was a rectangle with a 5.5 m side with an OM placed at each vertex. The signal produced at the OM used at GRBNeT was approximated by the signal produced by a multi-PMT KM3NeT DOM using only the 19 PMTs of the lower hemisphere of the DOM. In this subsection the term N photons, or N photon threshold refers to N photons detected by N different PMTs of the multi-PMT DOM. The orientation of the multi-PMT DOM was chosen in such a way so that the lower hemisphere was facing the horizon, to better approximate the GRBNeT detector geometry. At the time of these simulations and analysis the potential deployment site was at a depth of 3500m, so this depth was used in *MUPAGE* program for the generation of the atmospheric muon bundle events.

4.4.2.2 Evaluation of the contribution from ^{40}K decays - optical noise

For an autonomous underwater detector like GRBNeT it is very important to suppress the noise-only triggered events created by the photons produced by the decays of ^{40}K in seawater, in order to save storage space and lessen the load on the FPGA. For this purpose a sample of noise only events with a livetime of approximately 1 hour had been simulated. Although, during this time period approximately 4500 times an OM produced a pulse passing the 3 photon threshold, no event satisfied the trigger of 3 OMs producing pulses above the 3 photons threshold in time coincidence. As expected, a high acceptance threshold on each OM combined with a trigger based on local coincidences can successfully eliminate any false event triggered entirely from the contribution of ^{40}K decays.

4.4.2.3 Atmospheric muons contribution

In order to assess the contribution of atmospheric muon background to triggered events detailed simulations had been performed. The *MUPAGE* program had been used for the generation of atmospheric muon bundles on an area around the detector (called can) at a depth of 3500 m. Then the propagation of the muons, the light production and the detector response were simulated and random noise photons created by the decay of ^{40}K were added.

Although low energy muons had not been expected to contribute to the total trigger rate, atmospheric muon events in the energy range 10 GeV $\leq$ E$_{bundle}$ $\leq$ 100 GeV with a livetime of approximately 1 h, had been generated and simulated. In this period of time only 35 of the events produced at least 1 pulse passing the single photon threshold and none passing the 3 photons level.

Based on the above results a sample of atmospheric muons with bundle energies E$_{bundle}$ $\geq$ 100 GeV had been generated and simulated corresponding to a much larger livetime. In Figure 4.9 the bundle energy spectrum (left) and the zenith angle distribution (right) of these events are presented, for all event with at least 1 OM with a pulse passing the single photon threshold in black while the 3 and 5 photons level in blue and red respectively. As it can be observed by the trigger efficiency (lower) plots of Figure 4.9, these requirements tend to favor events with higher energies and events with larger zenith angles - closer to the horizon. Even without employing any local coincidence trigger, the rejection of low energy events is evident. The requirement of a pulse exceeding the 3 photons threshold has already provided a significant reduction of the atmospheric muon background and when the

condition of the 5 photons threshold is met approximately 95% of the atmospheric muon background is rejected.

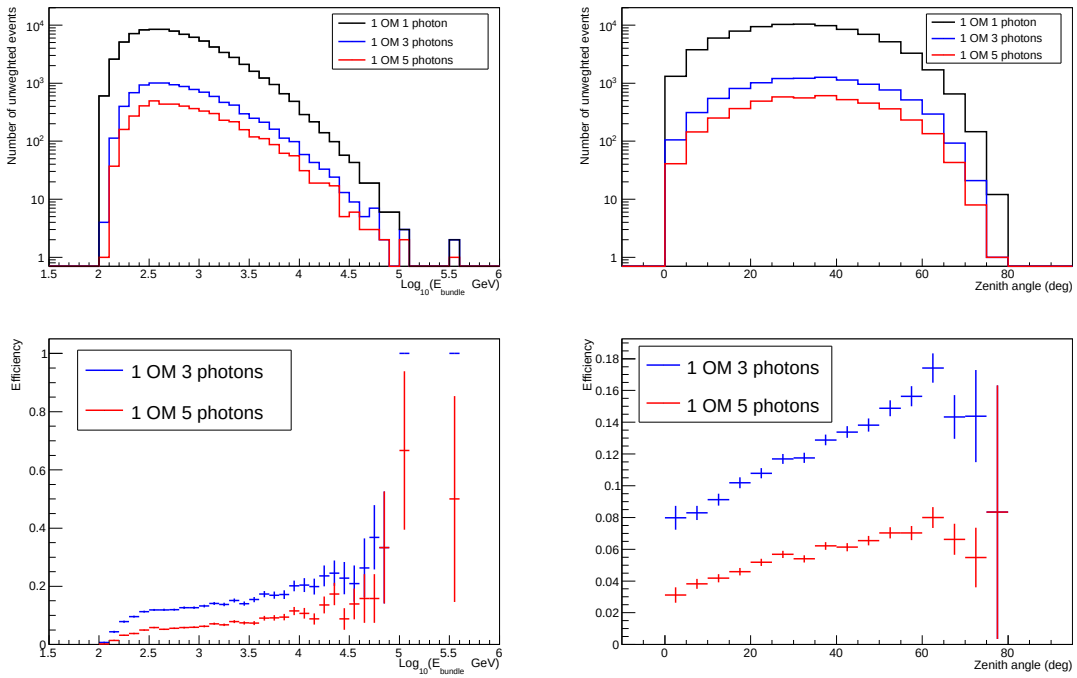

Figure 4.9: Top: Muons bundle energy spectrum (left) and zenith angle distribution (right) of simulated atmospheric muon events. Events with at least 1 OM with a pulse passing the single photon level in black, the 3 photons level in blue and the 5 photons level in red. Bottom: Ratios of number of events (trigger efficiency) passing the 3 photons level in blue and the 5 photons level in red with respect to the events with at least 1 OM with a pulse passing the single photon level. These ratios are shown for the bundle energy spectrum (left) and the zenith angle distribution (right)

A triggered based on local coincidences is expected to further reduce the contribution of the atmospheric muon background. Several different trigger setups had been studied. Those requiring signal from all 4 OMs had been excluded since in the unfortunate event of an OM malfunctioning these trigger conditions could have never been fulfilled. The optimal triggers are those requiring the coincidence of pulses from 3 OMs in a short time window (50 ns). In Figure 4.10 a comparison of different trigger setups is presented. The bundle energy spectrum (up) and the zenith angle disruption (down) are shown for all events with at least 1 OM with a pulse above the single photon threshold in black and for those events satisfying the trigger condition of 3 OMs producing pulses, in time coincidence, above the 3 and the 5 photons threshold in blue and red respectively. For completeness the events satisfying the condition of least 1 OM with a pulse above the 3 photons threshold is shown as a dashed line. By demanding 3 OMs with pulses above the 3 and 5 photons threshold to be in time coincidence, the atmospheric muon background is reduced by 95% and 98% respectively. The expected trigger rate for each case is approximately 0.32 Hz and 0.20 Hz respectively. Since the atmospheric muon background constitutes the major part of the trigger rate for the GRBNeT prototype, based on this analysis a first approximation of the trigger rate, resulting to the necessary storage space needed for the event recording for the

GRBNeT prototype was performed.

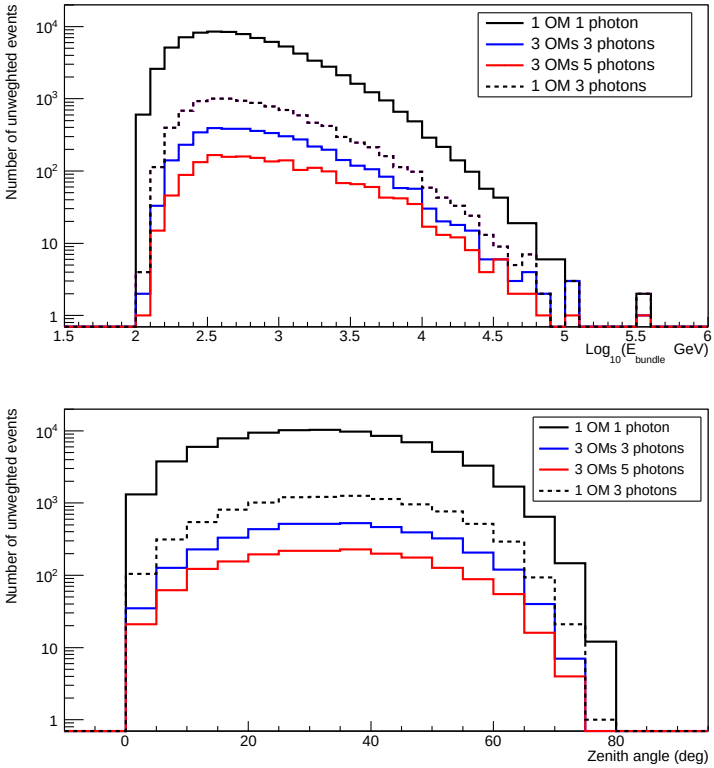

Figure 4.10: Muon bundle energy spectrum (up) and zenith angle distribution (down) of simulated atmospheric muon events. Events with at least 1 *OM with a pulse above the single and* 3 *photons thresholds are shown with black solid and dashed lines respectively. Events fulfilling the trigger conditions of* 3 *OMs producing pulses, in time coincidence, above the* 3 *and* 5 *photons thresholds are shown with blue and red lines respectively.*

4.4.2.4 Astrophysical and atmospheric neutrino contribution

To assess the impact of these trigger conditions to muons produced by atmospheric neutrinos, neutrinos from GRBs, and from the diffuse astrophysical flux, neutrino events had been generated with the *ANIS* program, following an unbroken power law E^{-1}, and the detector response was simulated. Since the statistics of the generated energy spectrum of atmospheric muons is poor in the high energy region (Subsection 4.4.2.3), the generated energy spectrum with a power law E^{-1} should provide useful information for the behavior of the trigger in the high energy region. In Figure 4.11 the muon energy spectrum (upper left) and the zenith angle distribution (upper right) are presented for these events, with at least 1 OM with a pulse above the single, 3 and 5 photons threshold in black, blue and red respectively. As it can be observed by the corresponding ratio (lower) plots, the trigger efficiency is really low for low muon energies but for events with $E_\mu > 10-50$ TeV it rapidly increases reaching up to 50% in the very high energy region.

The trigger conditions based on local coincidences had also been applied the sample of neutrino events. In Figure 4.12 the muon energy spectra (upper) and zenith distributions (lower) for events satisfying the trigger conditions of 3 OMs having pulses above the 3

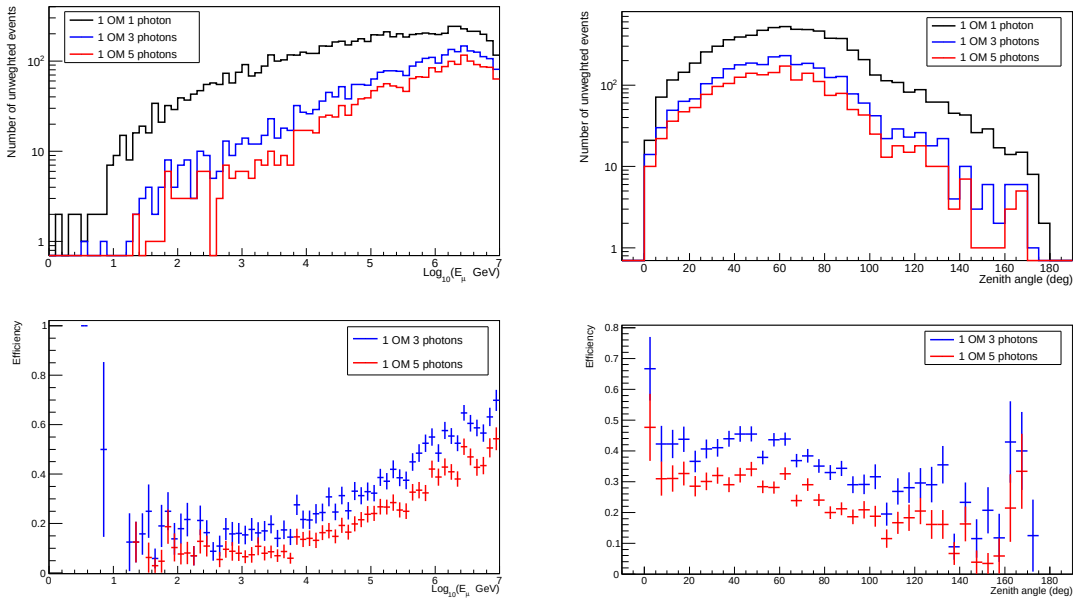

Figure 4.11: Top: Energy spectrum (left) and zenith angle distribution (right) of muons originating from neutrinos generated with a E^{-1} unbroken power law. Events with at least 1 *OM with a pulse above the single,* 3 *and* 5 *photons threshold in black, blue and red respectively. Bottom: Ratios of the number of events (trigger efficiency) passing the* 3 *and* 5 *photons threshold in blue and red, with respect to the events with at least* 1 *OM with a pulse above the single photon threshold. Ratios are presented as a function of the muon energy spectrum (left) and of the zenith angle (right)*

and 5 photons threshold which are in time coincidence, are shown with blue and red lines respectively. A comparison of Figures 4.10 and 4.12 shows that the efficiency of the two trigger conditions based on local coincidences is low for low energy muons (either atmospheric muons or low energy muons created by neutrino interactions) and increase as the muon energy increases to reach high efficiency values. As an example, the trigger efficiency for muons with $E_\mu \sim 1$ PeV is approximately 55% and 40% for the conditions of 3 OMs having pulses above the 3 and 5 photons threshold respectively. Taking into account the fact that no false noise-only events survived the trigger condition of 3 OMs having pulses in time coincidence above the 3 photons threshold, this trigger has been chosen for the inital trigger studies.

To estimate the expected rates and spectra for atmospheric, diffuse astrophysical neutrinos and neutrinos from GRBs, these simulated events were reweighed with the corresponding neutrino fluxes. For the neutrino flux from GRBs the Waxman - Bahcall model [81] was used, for the atmospheric neutrinos the Honda model with the knee correction [23] was used for the conventional flux combined to the Enberg model [24] to account for the prompt flux contribution and as astrophysical diffuse neutrino flux, the flux of equation 4.1 was used.

$$F_{diffuse} = 2.6 \cdot 10^{-8} \cdot E_\nu^{-2} \quad \text{GeV}^{-1}\text{cm}^{-2}\text{s}^{-1}\text{sr}^{-1} \tag{4.1}$$

Events were reweighed to the the desirable neutrino flux model (here either Waxman -

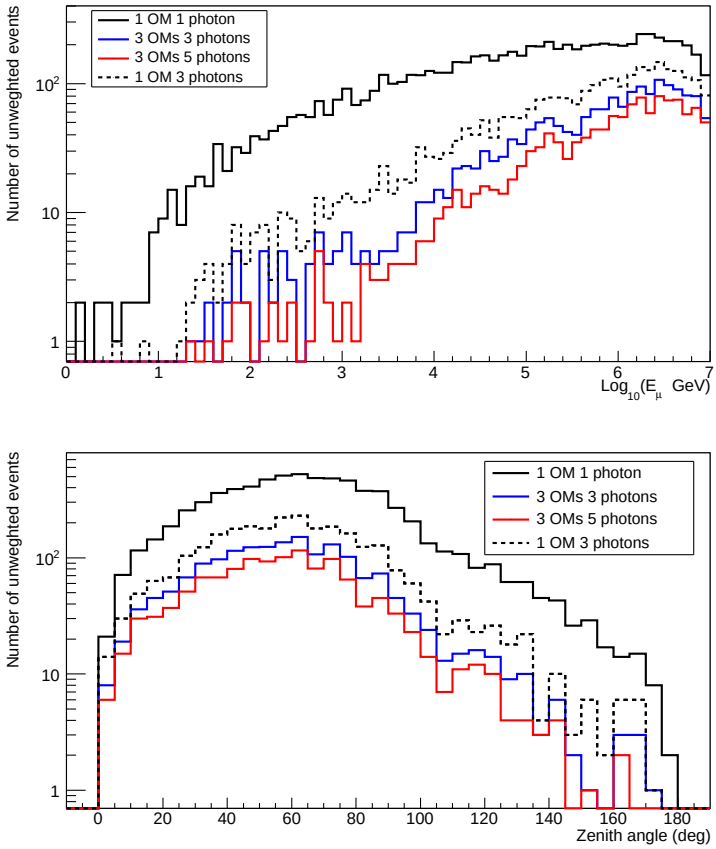

Figure 4.12: Energy spectrum (up) and zenith angle distribution (down) of muons originating from neutrinos generated with a E^{-1} unbroken power law. Events with at least 1 OM with a pulse above the single and 3 photons thresholds are shown with black solid and dashed lines respectively. Events fulfilling the trigger conditions of 3 OMs producing pulses, in time coincidence, above the 3 and 5 photons thresholds are shown with blue and red lines respectively.

Bahcall model or that of equation 4.1) using an event based weight w_i:

$$w_i = \frac{OW}{N_{evts}} \cdot F_{model}(E_\nu, zen) \cdot \frac{T}{1s} \tag{4.2}$$

where:

- OW is an event based quantity called "OneWeight" which incorporates all the necessary information for each event like the interaction probability, the generation spectrum and angular distribution as well as the generation energy range [82],
- N_{evts} is the total number of generated events used in the analysis,
- $F_{model}(E_\nu, zen)$ the neutrino flux model used which can be a function of the neutrino energy (E_ν), the zenith angle (zen) or both and
- T is the time of observation (livetime) in seconds.

The expected energy spectrum of muons produced by the interaction of neutrinos from GRBs, which fulfill the trigger condition of 3 OMs with pulses above the 3 photons threshold which are in time coincidence in one year time of observation for the GRBNeT prototype are shown in Figure 4.13. It is expected that approximately 9 neutrinos from GRBs will produce a muon that will give at least 1 photon in 1 OM in one year observation time of the GRBNeT prototype, 4 of which having muon energies above 100 TeV, where trigger efficiency is high. So it is expected that 1 such event will fulfill the trigger and will be recorded by the prototype per year. The expected energy spectra of muons produced by atmospheric neutrinos and of neutrinos from the diffuse astrophysical flux fulfilling the first level trigger conditions in one year livetime are shown in Figure 4.14 left, in black and red respectively. It can be observed that at the high energy region the main contribution comes from astrophysical neutrinos (either from the diffuse flux or from GRBs). Also, the expected energy spectra of atmospheric muons with $E_{bundle} \geq 100$GeV fulfilling the first level trigger conditions in one year livetime are presented in Figure 4.14 right for comparison.

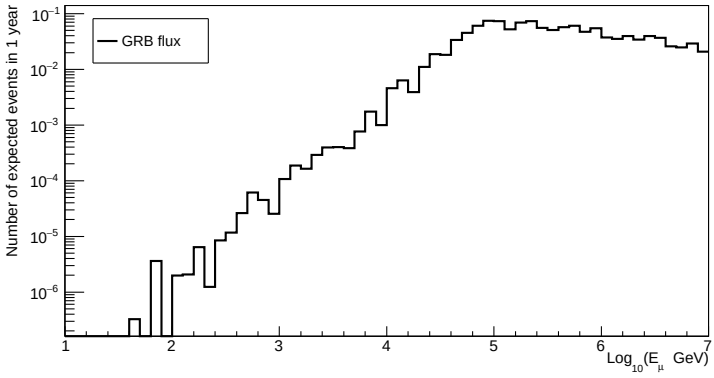

Figure 4.13: Expected energy spectrum of muons created by neutrinos from GRBs fulfilling the first level trigger requirements, in 1 *year of observation time for the GRBNeT prototype detector.*

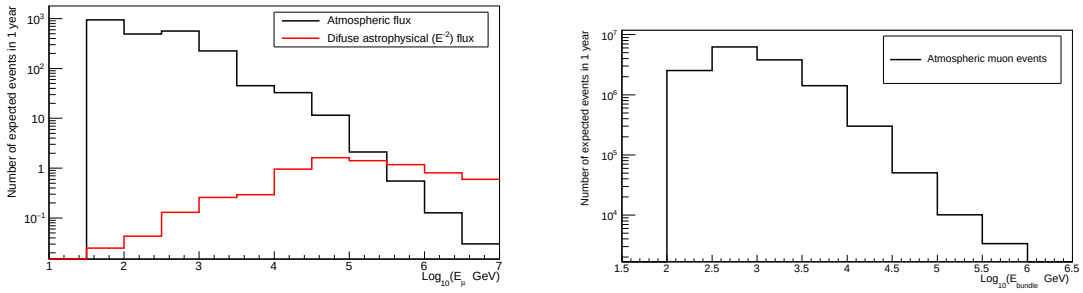

Figure 4.14: Left: Expected energy spectrum of muons created by atmospheric (black) and diffuse astrophysical (red) neutrinos, fulfilling the first level trigger conditions, in 1 *year of observation time. Right: Expected energy spectrum of atmospheric muons with* $E_{bundle} \geq 100\,GeV$ *fulfilling the first level trigger, in* 1 *year of observation time.*

4.4.2.5 Coincidences between floors

As mentioned in the previous subsection at high muon energies the contribution of astrophysical events is dominant. During these initial studies a coincidence between OMs in different floors was investigated as an option for a trigger. Even in the case of having each of the two floors functioning independently, realized after the budget cut, these studies can be proven very useful for the offline analysis of the data acquired, after the recovery of the GRBNeT prototype. From the various studies conducted the most effective was found to be the requirement of having at least 5 OMs with pulses above the 5 photons threshold in coincidence in both floors. For establishing a time coincidence between pulses from OMs in different floors a maximum time difference of 300 ns was required. The bundle energy spectrum of atmospheric muon events fulfilling this requirement and their zenith angle distribution are shown in Figure 4.15 . The equivalent plots for the muons produced by neutrinos generated with an E^{-1} spectrum are shown in Figure 4.16. As it is demonstrated in these plots, the requirement of having 5 OMs with pulses above the 5 photons threshold in time coincidence reduces the contribution of low energy muons (either atmospheric or crated by neutrinos). At the same time the number of accepted events by this requirement compared to those that satisfy the first level trigger is high for high energy events, reaching above 50% for muon energies above 1 PeV.

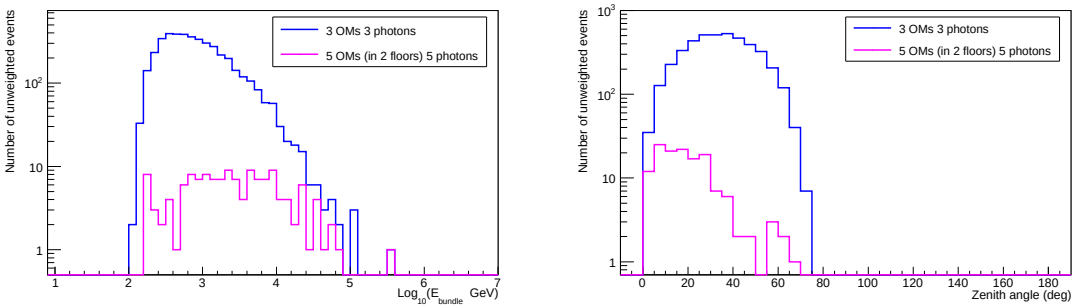

Figure 4.15: Bundle energy spectrum (left) and zenith angle distribution (right) of atmospheric muons. Blue: 3 OMs producing pulses, in time coincidence, above the 3 photons threshold (first level trigger). Magenta: 5 OMs producing pulses in time coincidence, above the 5 photons level.

4.4.3 Final simulations and trigger studies

In order to fully take into account the response of the single 13" Hamamatsu R8055 PMTs used in the GRBNeT OMs, new simulations were conducted. Also it had been decided that the GRBNeT prototype would be deployed at a depth of approximately 3000 m. So for these simulated events the geometry as well as the OMs used in the prototype that was deployed and the actual deployment depth had been taken into account and the simulated events were subsequently analyzed [83]. In this subsection the term N photons, or N photon photom threshold refers to a single pulse produced by N photo-electrons. In the SeaTray framework the variable "charge", closely related to the ToT of the pulse, was used in the simulation of the detector's response to store this information.

A sample of low energy atmospheric muons had been generated, simulated and it was used to confirm that the contribution of events with bundle energies $E_{bundle} < 100$ GeV is negligible. Then, three samples of atmospheric muons bundles had been generated with

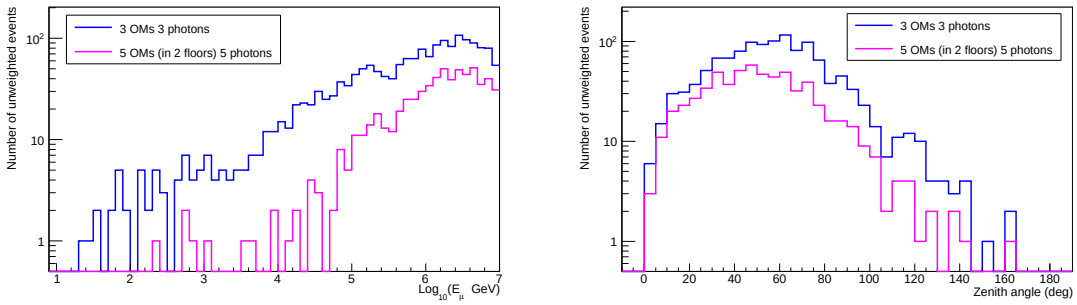

Figure 4.16: Energy spectrum (left) and zenith angle distribution (right) of muons originating from neutrinos generated with a E^{-1} unbroken power law. Blue: 3 OMs producing pulses, in time coincidence, above the 3 photons threshold (first level trigger). Magenta: 5 OMs producing pulses in time coincidence, above the 3 photons threshold.

MUPAGE, with $E_{bundle} \geq 100$ GeV, 1 TeV and 10 TeV and livetimes of approximately 17 h, 4.6 days and 41 days respectively (and the response of the detector was consequently simulated). Various combinations of local coincidences were studied with the aim of minimizing the contribution of atmospheric muon events to the trigger rate and at the same time having a high efficiency on high energy muons produced by neutrinos. The trigger requirement of 3 OMs producing pulses above the high acceptance threshold of 20 photons in time coincidence was chosen. Here, to establish time coincidence, a maximum time difference up to 200 ns was required.

The conditions of 3 OMs producing pulses above certain thresholds in time coincidence were applied to the first (low energy sample) using thresholds of 5, 10, 20 , 30 and 50 photons. By adopting the high threshold of 20 photons approximately 75 events per day were expected to be triggered per floor. This event rate could have been very easily handled by the electronics. Also less than 15% of these muon events had $E_{bundle} \leq 1$ TeV, already indicating that the trigger has been adapted to favor high energy muon events.

After applying the trigger condition to the atmospheric muon sample with $E_{bundle} \geq 1$ TeV, the expected trigger rate was found to be approximately 77 events per day per floor, 65 out of which belonging in the energy range of 1 TeV $\leq E_{bundle} <$ 10 TeV. The rate of triggered events can be considered comparable to that found by low energy sample considering the statistical errors of these samples. The contribution of atmospheric muon bundle events with higher bundle energies is really low due to the fact that the energy spectrum of atmospheric muons is very steep. Finally the same trigger condition was applied to the third sample with $E_{bundle} \geq 10$ TeV yielding consistent results.

To assess the impact of the trigger on muons produced by neutrinos, a sample of neutrino events in the energy range 10 GeV to 100 PeV with a spectral index -1.4 had been generated and the response of the detector was subsequently simulated. After reweighting these events to the astrophysical diffuse flux of equation 4.1, a trigger efficiency of approximately 15% was found for muon events with energies $E_\mu \geq 100$TeV for the GRBNeT prototype. Also more than 90% of the triggered events had $E_\mu \geq 100$TeV. Even though the trigger efficiency has not been very high, which is expected considering that it refers to one detection unit of the GRBNeT prototype, the final sample is a high purity sample of high energy muon events.

The potential gain on the detection of high energy neutrinos, by sparsely instrumenting the volume around an existing large-scale neutrino detector with autonomous units was

also explored in [83]. For these studies the KM3NeT/ARCA detector geometry had been used as and around it, 16 GRBNeT-type units had been positioned, equally spaced, in 2 concentric circles. A layout of the combined detector is shown in Figure 4.17. For these simulations all OMs (from the KM3NeT/ARCA strings and the GRBNeT-type units) had been approximated by the multi-PMT KM3NeT DOM. Two different configurations for the GRBNeT-type units were considered:

- **Config1**: 18 floors spaced by 36m distance (KM3NeT/ARCA type string)
- **Config2**: 6 floors spaced by 108m distance (simulated by masking the 2 floors following each unmasked floor).

In first configuration the increase of the number of OMs used compared to the KM3NeT/ARCA detector was approximately 56% while in the second it was approximately 19%. Neutrino events had been generated and the response of the detectors was simulated and the effective areas of the different configurations were compared. Since for this study the main objective was to use a trigger that favors high energy neutrinos, the requirement of having at least 12 OMs producing at least 2 pulses (from different PMTs) in time coincidence was used.

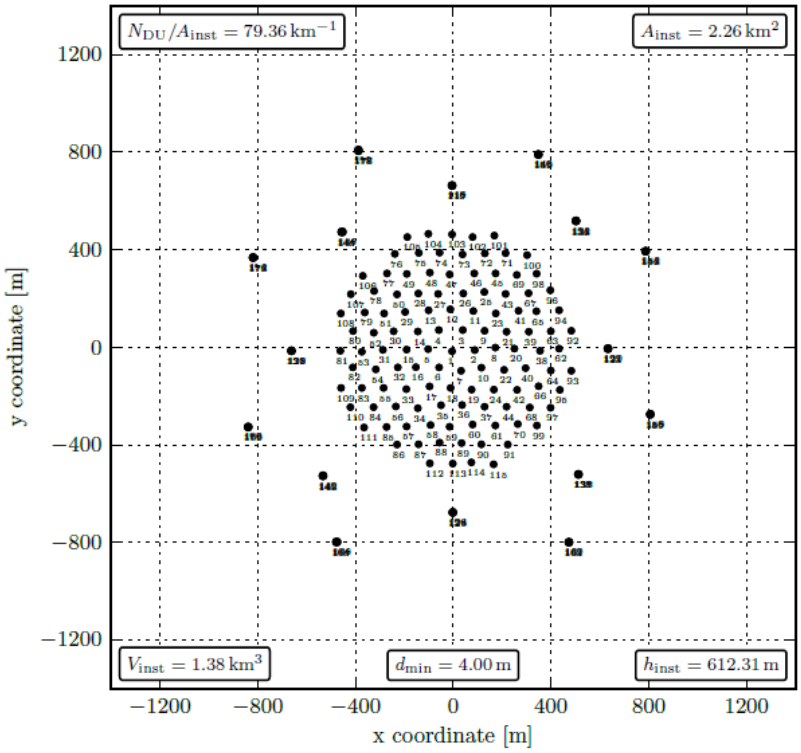

Figure 4.17: Layout of the KM3NeT/ARCA detector combined with the 16 GRBNeT-type units.

In Figure 4.18 left the effective areas of the KM3NeT/ARCA detector and the extended geometries using GRBNeT-type units with the two configurations are presented. As expected the effective areas of the extended geometries are larger than that of the KM3NeT/ARCA detector. In Figure 4.18 right, the ratio of the effective area of the extended L1 and L2 geometries over the effective area of the KM3NeT/ARCA detector are also shown. The effective area of the second extended geometry is close to that of the

KM3NeT/ARCA-like detector for low energy events. As the neutrino energy increases though, this effective area also increases and approaches the values of the effective area of the first extended geometry. The increase of the effective area of the second extended geometry compared to the standard KM3NeT/ARCA- effective area ranges from 10% for neutrino energies $E_\nu \geq 100$ TeV up to more than 50% for $E_\nu > 10$ PeV. Equivalently for the first extended geometry the increase ranges from more than 50% for $E_\nu \geq 100$ TeV up to 90% for $E_\nu > 10$ PeV.

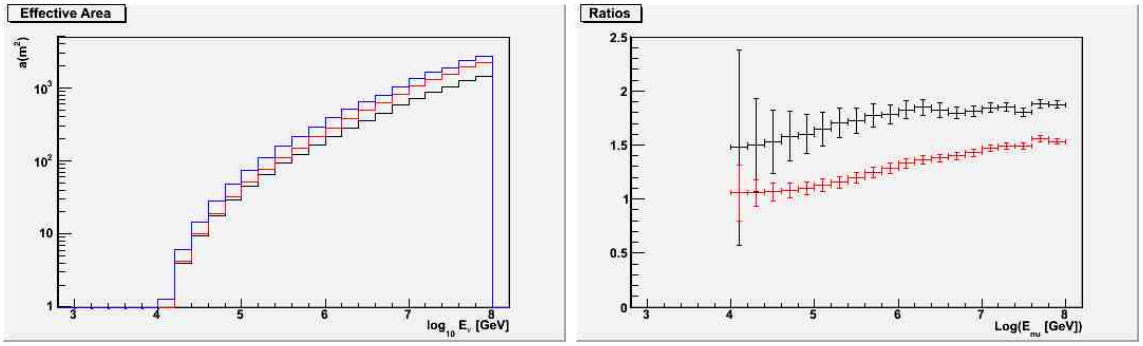

Figure 4.18: Left: The effective areas of the KM3NeT/ARCA detector (black) and the extended geometries using GRBNeT-type detection units in blue and red respectively. Right: Ratio of the effective area of the two extended geometries over the effective area of the KM3NeT/ARCA detector in back and red respectively. Plots taken from [83].

4.5 Deployment

A test deployment took place on the 15th of October 2014. During this operation the naked cross-shaped titanium latticed frame of a floor (without any other equipment attached to it) was loaded to the oceanographic ship "R/V AEGAEO" of the Hellenic Center for Marine Research[84]. Then it was taken to the open sea and it was submerged to a few tens of meters below the sea-surface. This procedure ensured the smooth deployment of the GRBNeT prototype since it allowed to the personnel of "R/V AEGAEO" to get accustomed to managing the unique shaped GRBNeT floors.

The GRBNeT prototype was deployed on the 28th of October 2015. It was assembled at the pier of the port of Pylos the previous day. All the parts of the prototype had been stored at the facilities of the NESTOR Institute [60], a few hundred meters from the assembly location. Firstly the hard hats containing the empty Vitrovex glass spheres used to provide each floor with buoyancy were attached to the cross-shaped titanium frame (the main "body" of each floor). Also, at each floor, 4 deep sea cables were attached and fixed to the titanium frame spanning from the position of the OMs to the positions of the electronics unit and one from the position of the power unit up to the positions of the electronics unit. Next, the power units were filled up to the brim with heavy paraffin oil, sealed very carefully so that no air was trapped inside the container and were integrated in the titanium frame. The oceanographic ship "R/V AEGAEO" arrived at the port of Pylos. The anchor unit, the main buoy unit, the ropes, the acoustic releases and the rest of the necessary equipment were loaded on the deck of AEGAEO and the ship left the harbor. In the evening, after the sun had set, the OMs arrived at the integration site. They were placed at the end of the titanium arms facing horizontally and the deep sea cables were

connected. Protective hard hats were placed on them until the actual deployment. The electronics units arrived last. They were placed at the upper part of each floor and the deep sea cables were connected (allowing the communication of the electronics with all 4 OMs). At the same time the proper deep sea cable was connected to the power units, providing the electronics with power. Prior to the electronics unit integration the clock of each electronic unit had been synchronized with the same GPS clock. The HV control units of all OMs had been programmed not to give power to the PMTs before a trigger by the FPGA was received. So a timer was set to each FPGA counting for a period of 2 weeks at the end of which this trigger was sent to the microcontrollers of the HV control units. The 2 weeks period had been considered as a reasonable time period for the PMTs to be de-excited by the light exposure during the integration procedure. After the integration procedure, the 2 fully integrated floors were left at the pier of the port of Pylos under the supervision of coastal guard.

On the 28th of October 2015 at 08:00 AEGAEO arrived at the port of Pylos . Both floors, were loaded on the deck of AEGAEO and they were safely placed in such a way to eliminate the possibility of damaging any OMs or equipment by disturbances caused by the sea or the weather. At about 09:00 members of the GRBNeT team embarked AEGAEO and the ship left the harbor. The deployment site was reached in approximately an hour and the distance from Pylos was around 20 km (or 12mi). The deployment site coordinates were 36^o 50.012'N 20^o 30.003'E and the depth was approximately $2,960$m. The deployment site position is shown in Figure 4.19 which can be reviewed using the link [85] of Google Maps.

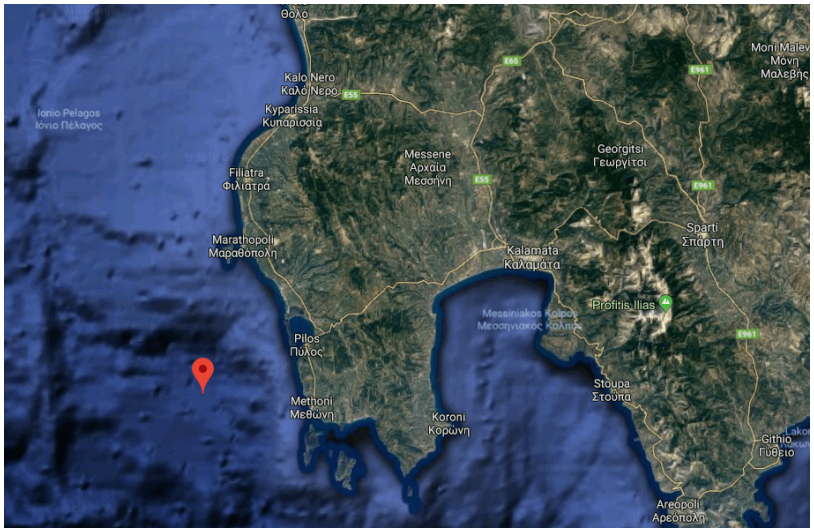

Figure 4.19: Map of western Peloponnese with the exact position of the deployment site marked.

When the site was reached the main engines of AEGAEO shut down so that the propeller would not cause any complications during the deployment, the ship was able to stay on site by using the dynamic positioning GPS system and its bow thrusters. Even though AEGAEO was equipped with a stern hydraulic A-frame, the unique design of the GRBNeT floors made the use of the A-frame very inconvenient, so the main crane was used for the deployment. All parts of the prototype were deployed successively starting from the anchor unit. The anchor unit was submerged by 100 m and it was safely attached to the side of the ship. Two releases, connected in parallel, were attached to the main rope and to the

anchor unit. The whole configuration was lowered so that the releases were deeper than the lower part of the keel of AEGAEO and the main rope was once again securely attached to the side of the ship. Next, the two floors were deployed. Each floor was attached to the main rope by its own rope system, it was lowered to the sea surface, then submerged deeper than the depth of the keel of AEGAEO and the main rope was securely attached to the side of the ship. Extra care was taken during the deployment of the floors so that their distance from the ship was adequate and while they were submerged to a depth larger than the keel of the ship no contact between the floor and the ship occurred. The two LED beacons were placed in the middle of the distance of the two floors. Then the main bouy unit was deployed following the same procedure.

Above the bouy unit, the upper end of the main rope was connected to an acoustic release which was connected to a wire rope with length more than 3000m controlled by a winch of AEGAEO. The submerged prototype was then lowered slowly with the winch until the anchor was approximately 100 m above the seabed. Then an acoustic signal was transmitted to the release attached to the wire cable and the prototype was left in free fall for the last 100 m. Here it should be mentioned that the anchor unit (including a metal chain and a rope) was specifically designed to allow, after the anchor had reached the seabed, enough space and time to the buoyant floors to decelerate, so to prevent them from reaching the seabed. Then the floors ascended up to the point where the whole prototype remained vertical due to the buoyancy and the weight of the anchor. The whole procedure was completed in approximately 3 hours. Finally the cable wire was pulled to the surface with the acoustic release still attached and the ship returned to the port of Pylos. In Figure 4.20 two photographs taken during the deployment of the GRBNeT prototype are shown.

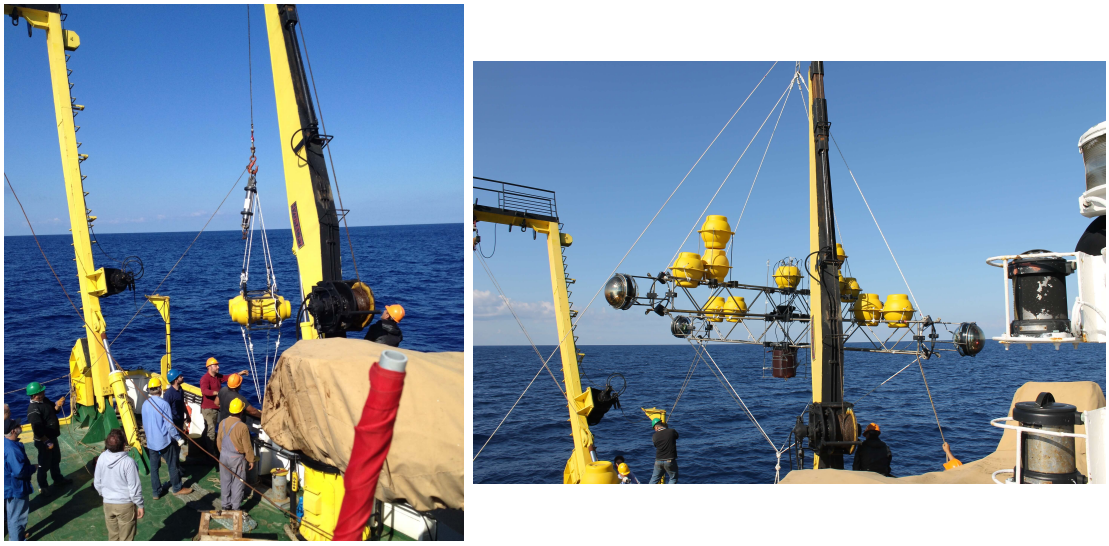

Figure 4.20: Left: Deployment of the main buoy unit. Right: Deployment of the lower floor.

4.6 Recovery

The GRBNeT prototype was scheduled to function for a time period of approximately 6 months. Nevertheless, it was decided to leave the prototype submerged for more than 1 year to assess any potential effects, such as water leakage and the effect of the pressure

on the power unit, for a longer time period. Approximately one and a half years after the deployment, on the 11 April 2017, a sea expedition was organized for the recovery of the prototype. Once again "R/V AEGAEO" was employed. Once AEGAEO had reached the deployment site an acoustic signal was emitted and the releases of the prototype, located just above the anchor unit, released the the prototype from the anchor unit. The prototype surfaced in less than 1 hour. The procedure was smooth and the ropes were not entangled. The overall condition of the prototype was excellent apart from some mild sedimentation observed on the top of the OMs (Figure 4.21). In Figure 4.22 two photographs taken during the recovery of the GRBNeT prototype are shown.

Figure 4.21: A photograph taken right after the recovery of the prototype on-board AEGAEO. The sedimentation can be observed along the scotch tape mainly on the top side of the OM, as expected.

Figure 4.22: Top: GRBNeT prototype floating on the sea surface. From left to right: the main buoy unit, the upper and the lower floor. The releases still attached on the main rope hold the lower floor a little more submerged than the upper one. Bottom: The upper floor is being lifted on board AEGAEO with it's main crane while the lower one "is waiting patiently" for it's turn .

Chapter 5

Simulation and Reconstruction Tools

5.1 General

The detector response to light produced by particles in the vicinity of the detector is simulated using Monte Carlo (MC) based tools. The steps followed in the simulation - reconstruction chain are listed below:

1. Generation of atmospheric muon bundles and neutrino interactions on the borders of and inside a cylindrical volume referred to as the "can".

2. Simulation of the light produced by the particles at the generation level.

3. Simulation of the response of the detector to the light produced by the particles and triggering.

4. Reconstruction of the particle trajectory and energy using information on the time and the position of the detected light.

The can is a cylindrical surface enclosing the instrumented volume and acts as a separation surface between the interior and the exterior volumes. All particles located out of the can are considered as being sufficiently far from the detector so that any light produced by them will not be detected. On the other hand, photons produced by particles located inside the can are assigned a probability of being detected, so light production is simulated. Geometrically the can is a cylinder concentric to the detector (also considered as a cylinder) with user defined dimensions, usually having a radius approximately 200m (more than 3 times the absorption length in water) larger than that of the detector, the upper lid of the can is located 200m above the upper lid of the detector and the lower lid is located on the seabed since any light produced in the rock is absorbed. As mentioned in Chapter 3.4 each ARCA block can be approximated by a cylinder with radius ~ 503m and height ~ 612m.

In this chapter the most important tools used to simulate and reconstruct the Monte Carlo events used for the physics analyses described in Chapters 7, 8 and 9 are described.

5.2 Generation tools

5.2.1 *GENHEN*

GENHEN [86] [87] is a Monte Carlo generator of neutrino and anti-neutrino interactions with matter, using the *CTEQ*6 [88] PDFs with NLO corrections to simulate the deep inelastic scattering mechanism and the *RSQ* [89] to simulate the quasi-elastic and resonant reactions. It was originally developed for the ANTARES experiment and is also used by the KM3NeT collaboration. *GENHEN* generates both Charged Current (CC) and Neutral Current (NC) neutrino interactions for all 3 neutrino flavors. The generation energy spectrum follows a user defined power law and the energy range can span from 10 GeV up to 1 EeV.

During the simulation procedure neutrinos are propagated through the Earth using the Preliminary reference Earth Model [90] density profile. For neutrinos interacting outside the can, the maximum possible distance of the particles produced (muons and τ leptons) is compared to the distance from the interaction vertex to the can. In case these particles are able to reach the can detailed simulations are conduced and they are transported to the can, otherwise they are disregarded. The propagation of muons is performed with *MUSIC* [91]. For neutrinos interacting inside the can all secondary particles are simulated and recorded. During the simulation, for each event, weights are calculated and recorded to the final output to account for the probability of transmission through the Earth, the probability interacting in the generation volume, as well as the generation spectrum. These weights are used when analyzing MC events, to reweight them to any user defined neutrino flux.

Staring from version *v7r5* [92], a new feature has been added to *GENHEN*. Since *GENHEN* already propagated muons created by ν_μ and $\overline{\nu_\mu}$ CC interactions from the interaction vertex to the can, the option to propagate, from the sea surface to the can, particles (muons and neutrinos) generated using other simulation programs like *CORSIKA* was added. For muons the energy losses are taken into account as they are propagated from the sea surface to the can, while neutrinos are geometrically propagated. For events with multiple neutrinos, the user chooses beforehand if all of them or just one will interact. If only one neutrino is chosen to interact per event, then in case there are multiple neutrinos in the events the one forced to interact can be chosen either randomly or by a formula assigning higher probability to neutrinos with higher energies. In all cases, proper weights are calculated taking into account the probability of transmission through the Earth, the probability of interacting in the generation volume and the weight created by the simulation code producing the particles at the sea level. These weights are written in the output.

5.2.2 *MUPAGE*

MUPAGE [76] is a fast Monte Carlo generator of atmospheric muons for underwater/ice detectors, originally developed for the ANTARES experiment and also by KM3NeT collaboration. Single or multiple muon (muon bundle) events are generated on an underwater can at a depth that is defined by the user.*MUPAGE* uses parametric formulas obtained by full *HEMAS* simulations assuming a specific CR model constrained by MACRO measurements of the atmospheric muon flux [93]. The multiplicity and the energy of the muons in a bundle are modeled as a function of distance from the axis of the shower. The parametric formulas are valid for muon bundles with zenith angles ranging from 0^o up to 85^o and for water (or water equivalent) vertical depth of the lower lid of the can ranging from 1.5 to

5.0km. With *MUPAGE* the time needed for the generation of muon bundles at the can is significantly short, thus making it possible, without requiring excessive computational resources, to generate atmospheric muon events with considerable livetimes.

5.2.3 *CORSIKA*

The *CORSIKA* (COsmic Ray SImulation for KAscade) program [94] is currently the most widely used simulation tool for atmospheric shower events initiated by cosmic ray particles, photons or neutrinos. All muons and neutrinos produced by the cosmic ray particle interactions in the atmosphere are recorded at the sea level. In KM3NeT the propagation of these particles to the can is conducted with *GENHEN* (chapter 5.2.1), or the *propa* code [95]. Chapter 6 is devoted to simulations with *CORSIKA* in KM3NeT.

5.3 Light simulation tools

5.3.1 *KM3*

After the generation step, the light produced by the particles in and on the can is simulated with the *KM3* program [87][96]. *KM3* generates and propagates light produced by muons and electromagnetic showers created either by electrons originating from ν_e and $\overline{\nu_e}$ CC interactions or bremsstrahlung photons from muons, in the sea water. Since simulating all possible interactions of each photon is an extremely CPU demanding process, *KM3* uses tables containing information about the Cherenkov photon wavelength dependence production, absorption and scattering created by full *GEANT* simulations. Muons are propagated with *MUSIC*; the muon tracks are divided in small segments (compared to the size of the detector) and for each segment Cherenkov photons are produced. For electromagnetic showers and highly energetic radiative losses from muons (also handled by *MUSIC*), light is produced according to the shower energy making use of electromagnetic-shower photon tables. All photons are tracked until they leave the can or get absorbed. Finally, the probability of a PMT to have been hit by photons, for all PMTs, is calculated using photon tables, taking also scattering into account. At this case the time of the incidence and the direction of the photon are recorded.

5.4 Simulation of the detector and triggering

5.4.1 *JTriggerEfficiency*

The next step is the simulation of all photons reaching the PMTs, originating either from particles created by neutrino interactions or atmospheric muons. Neutrino detectors deployed in the sea, suffer from the background of photons created by the byproducts of the radioactive decays of ^{40}K which is abundant in the sea water. The effect of this background is modeled as random hits with a rate r1 at each PMT and hits in 2, 3, 4 and 5-fold coincidences between different PMTs of the same OM with rates r2, r3, r4 and r5 respectively and it is taken into account at this step of the simulation chain. So, the final steps of the simulation process, apart from the simulation of optical noise due to ^{40}K decays, include the simulation of the response of the detector to all photons and the triggering. These are handled in the *Jpp* framework [97], the official simulation and analysis framework developed in the KM3NeT Collaboration.

JTriggerEfficiency [98, 99] is the *Jpp* module that performs the simulation of the PMT response to photons (either form particles created by neutrino interactions and atmospheric muons or by the byproducts of the radioactive decays of ^{40}K). First the geometry of the detector is loaded as well as a calibration file containing the efficiency of the PMTs. Then the background from ^{40}K decays is added. The values used for the rates have beed: r1 = 5000, r2 = 500, r3 = 50, r4 = 5 and r5 = 0.5 Hz. The response of the PMTs is simulated next converting the simulated light to the output pulses produced by each PMT. The characteristics of the PMTs used in KM3NeT are taken into account as well as the effect of the readout electronics. The time of arrival and the Time over Threshold (ToT) of each pulse (having a maximum value of 255 ns due to the PMT saturation effects at around 40 simultaneous photoelectrons [69]) are calculated and recorded.

The lsat step of the chain is the simulation of the trigger response. When a set of predefined conditions (trigger) is satisfied all detector activity is recorded (physics event). The triggers are optimized for the detection of muons or neutrino induced showers. In order to filter out the major contribution of the noise due to ^{40}K the trigger algorithm takes into account only hits from multiple PMTs in each DOM. A coincidence, in a short time window (Δt = 10 ns), of 2 or more hits from different PMTs is required for the hits to be considered for the triggering. Also the angle between the axes of the PMTs under consideration is required to be at maximum 90^o. Using this information, clusters of causally connected hits in a spherical (shower-like) or cyclical (track-like) geometry are formed and an event is triggered when such a causally connected cluster comprises at least 5 OMs.

5.5 Reconstruction tools

5.5.1 Cascade reconstruction *AAshowerFit*

The most commonly used cascade reconstruction in KM3NeT is *AAshowerFit* [69] which takes full advantage of the KM3NeT mulpti-PMT DOMs. *AAshowerFit* is used to reconstruct the position of the shower maximum, which in the energy range of interest of ARCA can be up to a few meters away from the neutrino interaction vertex, as well as the shower direction and energy. First selection and merging of hits in the DOM is performed and the vertex position is fitted by a minimization of the time residuals assuming a spherical expanding shell of light. Using MC simulated events the accuracy of the vertex estimation was found to reach values well below 0.5m in the high energy regime. A maximum likelihood method is used for reconstructing the shower direction and energy. All PMT hits within a certain time window around the time a direct photon from the vertex is expected, are used and the probability of having recorded one or more hits is fitted. This probability is estimated from simulations as a function of PMT distance and pointing direction to the shower, angle from the shower axis to the PMT position, and electromagnetic-equivalent cascade energy. For high energy ν_e CC events having the neutrino interaction vertex inside the volume of the KM3NeT/ARCA detector, the 1σ energy resolution is approximately 5% while the 1σ median directional resolution is of the order of 1.5^o, as shown in figure 5.1.

5.5.2 Track reconstruction

The track reconstruction algorithm providing the best results includes a series of *Jpp* modules. The chain used for the directional reconstruction (hereafter *JGandalf* chain) comprises 3 different modules [100] [69] [101]. The first module, *JPrefit*, performs a full solid angle scan using causally related PMT hits for a linear fit. The second module, *JSimplex*,

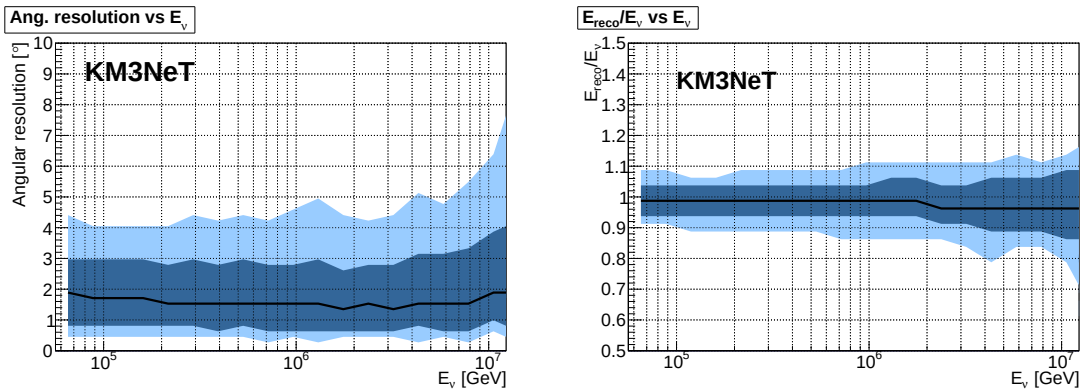

Figure 5.1: Directional (left) and energy resolution (right) for contained ν_e CC events. Black line: median value, blue band: 68% quantile and cyan band: 90% quantile. Figures from [69]

is based on the results of the previous step and on an M-estimator fit. The last module, *JGandalf*, utilizes the results from *JSimplex* and performs a likelihood fit using the Levenberg-Marquardt method. The Probability Density Functions (PDFs) are built using information about the Cherenkov light from the muon, the light from muon energy losses (ionization and bremsstrahlung) as well as the random optical background. In Figure 5.2 left the expected angular resolution for ν_μ CC events is presented. For neutrinos with $E_\nu > 100$ TeV a median angular resolution of less than 0.1^o can be reached.

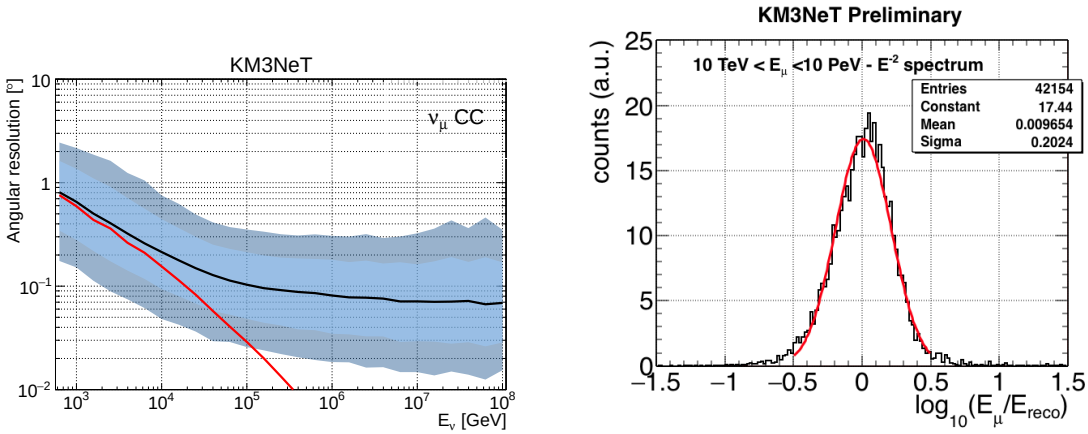

Figure 5.2: Resolutions for ν_μ CC events using the JGandalf chain after posing requirements on the reconstruction quality parameters in order to remove misreconstructed events. Left: Angular resolution. Black line: median value, blue band: 68% quantile and cyan band: 90% quantile, red line: median of the distribution of the angle between the neutrino and the muon at the interaction vertex. Figure from [69]. Right: Energy resolution for muons from ν_μ CC interactions following an E_ν^{-2} power law energy spectrum. A Gaussian fit is overlayed

For the muon energy reconstruction the module *JEnergy* [102] uses the output of *JGandalf* to identify the PMTs in the road width of the passing muon. Then a likelihood fit is performed on the muon energy. In figure 5.2 right the energy resolution for muons from

CC interactions of ν_μ with an E_ν^{-2} power law energy spectrum is presented. The resolution of the logarithm of the muon energy for the energy range indicted is approximately 20%. The last step of the track reconstruction chain is the the neutrino interaction vertex finding which is performed by the *JStart* module. Using the reconstructed track direction a one parameter scan is performed to locate the optimum point for the neutrino interaction along the reconstructed track.

Chapter 6

Atmospheric Air Shower Simulations

6.1 *CORSIKA*

Atmospheric muons constitute the most prominent background for neutrino telescopes. They are created by Cosmic Rays (CR) interacting with the particles of the atmosphere. Even though muons can travel several kilometers in sea water, ice or rock before loosing their energy reaching underwater and underground neutrino detectors, or detectors deployed in the polar ice, they can not cross the Earth, so up-going atmospheric muons can not reach the neutrino detectors. When CRs interact with atmospheric particles, neutrinos (ν_μ, $\overline{\nu_\mu}$, ν_e and $\overline{\nu_e}$) are also produced. These atmospheric neutrinos can reach the detectors from all directions and they can not be distinguished from astrophysical neutrinos on an event by event basis. Detailed study of atmospheric muons and atmospheric neutrinos is important in order to understand and suppress the contribution of these backgrounds to the astrophysical neutrino signal events. To this end simulations need to be conducted. The most common simulation strategies are described in the following paragraphs.

The first strategy is to use neutrino generators and then reweigh the generated neutrino events using an atmospheric neutrino flux. For the atmospheric muon background, tools such as the *MUPAGE* program (see chapter 5.2.2) have been created for fast simulation of atmospheric muon events at a certain depth of water (or water equivalent). Using this approach large samples of both atmospheric neutrino and atmospheric muon events can be generated fast, without requiring a large amount of computational resources. The drawback of this approach is that two different samples are generated while in reality atmospheric neutrinos and muons are created in the same showers, so an atmospheric neutrino can interact in the detector while a bundle of muons created at the same shower crosses the detector at the same time. By simulating two different samples of atmospheric events (one sample of neutrinos and another unrelated sample of muons) there is no possibility to conduct studies requiring the combined. Self veto refer to the identification of atmospheric neutrinos by detecting incoming muons to the detector created at the same atmospheric shower. By exploiting this effect it is possible to reject downgoing atmospheric neutrino events thus enhancing the contribution of astrophysical neutrinos. These events can be used as purely atmospheric events for analyses focusing on the energy correlations of muons and neutrinos created at the same atmospheric showers, or for analyses focusing on the detection of the prompt atmospheric flux.

This possibility is provided by the second strategy which is: fully simulating atmospheric

showers created when CRs interact with particles of the atmosphere. To this end the COsmic Ray SImulation for KAscade - *CORSIKA* program [94] is the most widely used simulation tool. *CORSIKA* fully simulates atmospheric shower events initiated by CR particles, photons or neutrinos. Different models can be chosen for the high and low energy interactions of particles. The particles created by each interaction are tracked until they interact with other particles, decay or reach the user defined level of observation. *CORSIKA* is a sophisticated and complex program in which interaction models and other parameters are defined by the user and a lot of computational power is needed to simulate a small sample of shower events. Even though *CORSIKA* simulations are computational intensive the output obtained is much more realistic compared to that obtained by using the previously mentioned (first) strategy. Since computational constrains do not allow, yet, for as large samples simulated by *CORSIKA* as with the first approach, both the above strategies are used in neutrino detection experiments.

In KM3NeT a large production of *CORSIKA* simulated events is foreseen. In order to investigate the impact of different high energy interaction models and other parameters, four different high energy interaction models were used to create smaller productions. The chosen high energy interaction models are *QGSJET* 01*c*, *QGSJETII*-04 and *EPOS LHC* from *CORSIKA* version *74005* and *SIBYLL* 2.3 from *CORSIKA* version 75000. For all productions the low energy interaction model used was *GHEISHA* 2002*d*. In the following section (6.2) the most important non default parameters used for these simulations will be elaborated [103] [104].

6.2 Parameters used in the simulations

6.2.1 General

While compiling *CORSIKA* the user is asked to choose from a number of parameters, or program options, that will be used for the simulations. As an example the user can chose the manner that particles containing a charm quark will be treated; they can either be treated implicitly by the high energy hadronic model or they can be treated explicitly taking fully into account their cross-sections and their lifetimes. After the successful compilation of *CORSIKA* these options cannot be modified or changed; to change them a recompilation is required. The steering parameters for the simulation are specified in a datacard. Unlike the program options, these parameters are used only to steer the specific simulation and can be changed between different *CORSIKA* executions. Such parameters are the CR spectrum index and the energy range used for each simulation.

6.2.2 Program parameters

Detector Geometry

The default contribution of the CR primary intensity is optimized for a flat detector. Since the KM3NeT/ARCA detector is not flat, the default option was not used. Instead, two different options were tested. The first option was **VOLUMECORR** for which the CR primary intensity distribution with respect to the zenith angle θ is:

$$I \propto (d/2)^2 \cdot \pi \cdot sin\theta \cdot (cos\theta + 4/\pi \cdot l/d \cdot sin\theta) \tag{6.1}$$

where l is the length and d is the diameter of the detector. For ARCA $l/d \approx 0.65$.
Nevertheless, as indicated in the *CORSIKA* user guide, while the **VOLUMECORR** option is optimized for detectors with a long vertical shape (like a string) the shape of ARCA

is more similar to a sphere rather than to a long vertical string. Consequently the **VOLUMEDET** option was also tested for which the primary intensity distribution with respect to the zenith angle (θ) is:

$$I \propto sin\theta \tag{6.2}$$

This primary intensity distribution respects only the solid angle element of the sky. The different intensity distributions for both options are shown in Figure 6.1.

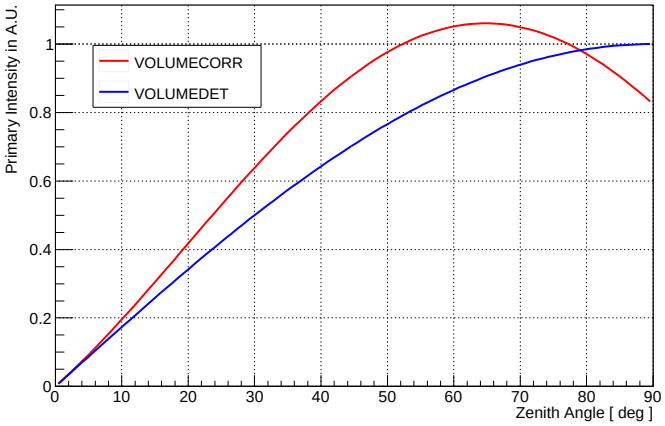

*Figure 6.1: The primary intensity distribution using options **VOUMECORR**, in red, and **VOLUMEDET**, in blue.*

Neutrinos

In order to take into account the exact kinematics of the two or three body decay of charged pions, kaons (leptonic modes) and muons to neutrinos (ν_μ, $\overline{\nu_\mu}$, ν_e and $\overline{\nu_e}$) option the **NEUTRINO** was used. Neutrinos are also tracked through the atmosphere down to the observation level disregarding any (highly improbable) interactions with atmospheric nuclei.

Charmed particles and tau leptons

Particles containing a charmed quark, can either be treated explicitly taking fully into account their cross-sections and lifetimes with the selection option **CHARMed**, or they can be treated implicitly by the high energy hadronic model. In case the option **CHARMed** is selected tau leptons are also considered and their interactions and decays are simulated. Option **CHARMed** is only compatible with interaction models allowing for charmed particles to be treated in this manner. The high energy interaction models compatible with the option **CHARMed** are *QGSJET* 01 from *CORSIKA* version *74005* and *SIBYLL* 2.3 from *CORSIKA* version 75000. For productions using another high energy interaction model (not compatible with the option **CHARMed**), the option **TAULEP** was selected. This option allows for a similar treatment of τ leptons as with the option **CHARMed**, so the treatment of τ leptons was enabled in all productions.

Atmosphere

In the standard *CORSIKA* atmospheric models, the atmosphere is approximated by a flat disk with density varying as the altitude changes. This approximation is not valid for CRs with zenith angles larger than 70^o, since for these zenith angle the curvature of the Earth's

atmosphere becomes important. Since the goal is to produce a sample of CR showers with (almost) full sky coverage, the simulation of events with larger zenith angles is necessary. For our purpose the option **CURVED** was selected. Using this option, for large zenith angles, the shape of the atmosphere is not considered as a flat disk but the curvature of the atmosphere is taken into consideration. In addition, ionization and radiative energy losses as well as the deflection of the CR primaries by the magnetic field of the Earth are taken into account, from the point the CR primary enters the atmosphere up to the point the first interaction takes place (which are deactivated in the standard compilation).
The option **UPWARD** which enables the treatment of up going particles, was also selected. This is necessary for simulating shower with zenith angles larger than 90^o. Even without the use of the option **CURVED**, *CORSIKA* allows for simulation of showers with zenith angles $110^o < \theta < 180^o$ as long as the option **UPWARD** is also selected. In our case the option **UPWARD** was used to make sure that all particles are considered in the simulation for the case of showers created near the horizon.
Finally the option **ATMEXT** which allows for the use of externally tabulated atmospheric models was also selected for the compilation of *CORSIKA*. With the appropriate steering parameters, this option allows for either choosing of one of the tabulated atmospheric models included in the *bernlohr* package or defining a user-provided model.

Precursors of muons and neutrinos
All particles that reach the observation level are written in the output file along with their position, momentum and time (with respect to the first interaction of the CR particle) at the observation level. In order to be able to identify the parent particle of each neutrino or muon written at the observation level additional information is required. Option **EHistory** allows for that additional information to be written in the output file, as long as this is specified in the datacard that steers the simulation. By selecting **EHistory** the momentum, position and interaction time of both the "mother" and the "grandmother" particles of neutrinos, muons and electrons can be written in the output file. This information is critical for studies involving the prompt atmospheric fluxes since the only way to distinguish between particles of the conventional or the prompt atmospheric flux component is by determining if their mother or grandmother particles had a charm quark. The information of the parent particles can be also useful to studies focusing on mother pions or kaons (and their ratios) responsible for creating atmospheric muons or neutrinos.

6.2.3 Steering parameters

Primaries
The primary CR particles simulated were p, He, C, N, O, Mg and Fe. This makes it possible to use various models to derive the neutrino and muon fluxes, like the H3A, H4A[8] and GST [9] models. The parameter used to specify the primary to be used for the simulation is **PRMPAR**.

Generation spectra and limits
The generation spectral index is defined with the parameter **ESLOPE**, and the parameter **ERANGE** is used to define the lower and upper energy limits. An E^{-1} power low spectrum for the energy range from 1 TeV up to 1 EeV was simulated in order to enhance the contribution of the high energy part of the spectrum. Although the dependence of the intensity of the CR primaries on the zenith angle was predetermined by the detector

geometry (Section 6.2.2), the range of the zenith and the azimuth angles used in the simulation of the showers was defined by parameters **THETAP** and **PHIP** respectively. In the simulations conducted azimuth (ϕ) angle ranged from -180^o up to 180^o (so the whole sky), while the zenith (θ) angle ranged from 0^o up to 87^o.

Minimum Particle Energy

In order to save computational resources the user is able to specify the minimum kinetic energy below which the particles will not be tracked by *CORSIKA* using the parameter **ECUTS**. Four different energy cuts are required: for hadrons (in case of nuclei this energy cut is applied on the energy per nucleon) and neutrinos, for muons, for electrons and finally for photons and π^0s.

As we are primarily interested in muons reaching the detector and in neutrinos with energies $E_\nu > 1$ TeV, the energy cuts were set to 1 TeV or to 0.5 TeV, depending on the primaries. In order to find the energy cut for muons the deployment depth of ARCA, 3500 m, was considered along with the fact that the upper DOM is located approximately 700 m above the sea bed. Since ARCA is optimized for the detection of high energy events, the minimum muon energy at sea level was determined by the requirement that muons, assuming a purely downgoing trajectory, after traveling through 2600 m of water should have energy at least of tens of GeVs. The Bethe-Bloch formula (6.3) was used to estimate the energy losses that a muon traveling in water suffers.

$$-\frac{dE}{dx} = a(E) + b(E) \cdot E \tag{6.3}$$

The first term accounts for the continuous losses due to ionization and the second one for the stochastic losses due to bremsstrahlung, pair production and photonuclear interactions. Here the values used were $a = 0.274$ GeV/m and $b = 3.485 \cdot 10^{-4}$ m^{-1} as reported in [105] assuming an average sea water density of 1.025 kg/m^3. Also considering the information provided by the muon propagation program *MUSIC* [91], purely downgoing muons with energy 1 TeV have a probability of $\sim 20\%$ to survive a distance of 2600 m of water equivalent as shown in Figure 6.2. Here it should be mentioned that these productions were created in order to find the best parameter values to be used for the full scale production so these energy cut will be refined and modified for the full scale production.

Atmospheric and magnetic field models

The Earth magnetic field of 44.7 nT with declination 3.2^o and inclination 51.55^o used for the simulations was extracted from [106] in [95] for the location of the ARCA detector. This is defined by the parameter **MAGNET**.

During these simulations the main atmospheric density model used was a user defined one not included in the *bernlohr* package, by assigning value 0 to the parameter **ATMOD**. This user defined model [95] was a five layer approximation of the yearly averaged atmospheric density above the ARCA deployment site extracted from [107]. The density of the lower four of the five layers was defined (parameters **ATMA**, **ATMB**, **ATMC** and **ATMLAY**) and for the fifth layer a linear decrease of the density was assumed. Simulations were also conducted using two different atmospheric models, one using an atmospheric density profile corresponding to the atmosphere above the ARCA deployment site at summer time and the other at winter time.

Precursors of muons and neutrinos

By activating option **EHistory** the possibility of saving the additional information men-

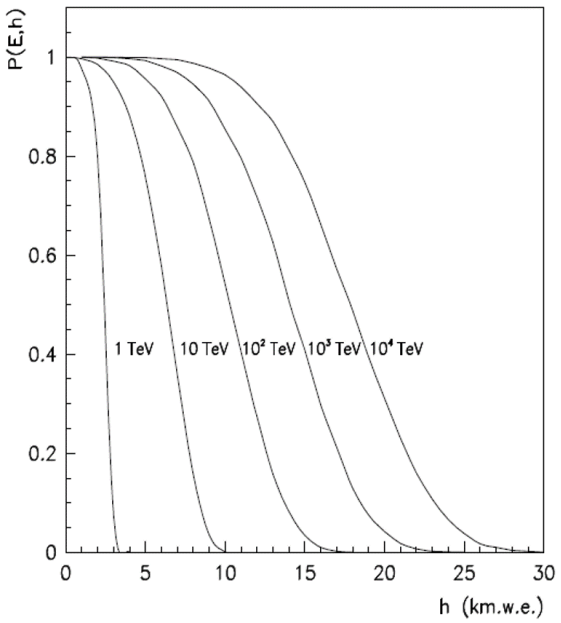

Figure 6.2: Survival probabilities for muons with different energies, as a function of the water equivalent depth by MUSIC. Plot from [91].

tioned in Section 6.2.2 in the output files for muons and neutrinos is activated. To have this information written in the output files parameters **MUADDI** and **NUADDI** (for muons and neutrinos respectively) need to be set to true (T) in the datacard steering the simulation.

6.3 *CORSIKA* productions for KM3NeT

Ysing the program and steering parameters mentioned in sections 6.2.2 and 6.2.3 respectively, five major and four minor productions were simulated with *CORSIKA*. In table 6.1 the high energy hadronic models used in the major productions, the options **CHARMed** and **TAULEP** and the number of simulated showers using protons and each of He, C, N, O, Mg and Fe as primaries, are indicated. In all five major productions:

- the low energy interaction model used was *GHEISHA* 2002*d*
- the atmospheric density model corresponding to the yearly averaged atmospheric density above the ARCA deployment site was used
- for the simulated primaries the energy range used was from 1TeV up to 1EeV, the energy spectrum followed an E^{-1} power law and the zenith range from 0^o up to 87^o.

Even though the high energy interaction model *QGSJET* 01*c* was one of the older models in *CORSIKA*, it was chosen for two productions, one with the option **CHARMed** and the other without it, in order to check the impact that option **CHARMed** has on the neutrinos and muons at sea level. In *CORSIKA* version *74005* the high energy interaction model *SIBYLL* 2.1 was also compatible with the option **CHARMed**, but even at the time of the release of the *CORSIKA* version it was already known that an update on the *SIBYLL*

	HE interaction model	**CHRAMed**	**TAULEP**	num of showers primary p	num of showers per primary for heavier primaries
1	*QGSJET* 01*c*	No	Yes	10^6	$2 \cdot 10^5$
2	*QGSJET* 01*c*	Yes	No	10^6	$2 \cdot 10^5$
3	*QGSJETII*-04	No	Yes	10^6	$2 \cdot 10^5$
4	*EPOS LHC*	No	Yes	10^6	$2 \cdot 10^5$
5	*SIBYLL* 2.3	Yes	No	10^6	$2 \cdot 10^5$

*Table 6.1: High energy models, **CHARMed** and **TAULEP** options used for the five major productions. Also the number of simulated showers using p and each of He, C, N, O, Mg and Fe as primaries are shown.*

model was expected at the next release. Thus *QGSJET* 01*c* was chosen to investigate the impact of the option **CHARMed**.

The first four productions indicated in table 6.1 were simulated in two steps. First, all the showers using protons as primaries were simulated and then all the showers using as primaries heavier nuclei. For those showers using protons as primaries all four energy cuts were set to 1 TeV while for those using heavier nuclei as primaries all four energy cuts were set to 0.5 TeV. In the last production of table 6.1, where *SIBYLL* 2.3 was used as high energy interaction model all four energy cuts were set to 1 TeV for all simulated showers irrespective of the primary used.

Apart from the productions mentioned in table 6.1, four smaller productions were also simulated. In the three productions described below, the high energy interaction model *SIBYLL* 2.3 and the low energy interaction *GHEISHA* 2002*d* model were used with **CHARMed** option.

- This minor production is identical to production five of Table 6.1, with the only difference that the atmospheric model of the U.S. standard atmosphere as parameterized by Linsley included in the *bernlohr* package of *CORSIKA* [104] was used. Even though this has the same number of showers simulated as all the major productions, it is not included in the list since the differences from production five of Table 6.1 are minimal. Here as well, all four energy cuts were set to 1 for all simulated showers irrespective of the primary CR used.

- For the second minor production the atmospheric model used was approximating the atmospheric density profile corresponding to the atmosphere above the ARCA deployment site at summer time. For this production only proton primaries were simulated and only 10^5 showers. All four energy cuts were set to 1 TeV.

- For the third minor production the atmospheric model used was approximating the atmospheric density profile corresponding to the atmosphere above the ARCA deployment site at winter time. For this production only proton primaries were simulated and only 10^5 showers. All four energy cuts were set to 1 TeV.

Finally one more production was simulated. The parameters used for this production were the same as production five of Table 6.1, with the difference that the minimum CR primary energy was set to 200 GeV and more importantly the energy cut used for hadrons

was set to 1 GeV, for muons also to 1 GeV, for electrons to 200 GeV and for photons and π^0s to 1 TeV. It should be mentioned that the default values used for the energy cuts are 0.3, 0.3, 0.003, 0.003 GeV respectively. In this production 1000 showers were simulated in 10 runs (making 100 shower per run). The average cpu time needed per run was approximately 15000 s, so the average cpu time per shower was 150 s. In major production five, where the **ECUTS** values were optimized so not to loose any muon events reaching the ARCA detector (paragraph "Minimum Particle Energy" of Section 6.2.3), the average cpu time needed per shower was $\sim$ 6.5 s, that is more than 20 times faster. This tiny statistics production was simulated just to illustrate that in order to be able to simulate a production with reasonable statistics, parameter **ECUTS** needs to be tuned in such a way that the average simulation time of each shower will be reasonable while, at the same time, no useful events to the physics analyses are lost due to high energy cut values.

6.4 Weighting *CORSIKA* events with a CR spectrum

In all productions simulated, an $E_{prim}{}^{-1}$ power law energy spectrum of CR primaries was used to enhance the statistics in the high energy part of the distribution. Since this is not a realistic CR spectrum, the events obtained need to be reweighted to the actual primaries CR energy spectrum. By weighting the events a value (weight) is assigned to each event, so the generation flux can be transformed to the chosen CR flux. The first step is to extract the flux used in the *CORSIKA* simulation, hereafter f_{CO}. The weight of each shower event is the ratio of the chosen CR flux, hereafter f_{CR}, over the flux used in the *CORSIKA* simulation.

In CR flux models, like [8] [9], an isotropic CR flux is assumed in the solid angle element $d\Omega$, so any dependence on the zenith angle used in *CORSIKA* simulations[1] should be eliminated. In those productions at which the option **VOLUMEDET** was used, the primary intensity distribution was already isotropic in $d\Omega$. Since the $E_{prim}{}^{-1}$ power law was used in the simulations:

$$f_{CO} = a \cdot E_{prim}^{-1} \tag{6.4}$$

The constant a in equation (6.4) can be determined by considering that the integral of $f_{CO}(E_{prim})$ in dE_{prim} and $d\Omega$ is equal to the number of simulated showers[2], hereafter N_{sim}, so in this case:

$$\int_{E_{prim\,min}}^{E_{prim\,max}} \int_0^{2\pi} \int_{0^o}^{87^o} f_{CO}(E_{prim})\, d\Omega\, dE_{prim} = N_{sim} \tag{6.5}$$

resulting to:

$$a = N_{sim} / \int_{E_{prim\,min}}^{E_{prim\,max}} \int_0^{2\pi} \int_{0^o}^{87^o} E_{prim}^{-1}\, d\Omega\, dE_{prim} \tag{6.6}$$

In productions not using the option **VOLUMEDET**, the flux was not isotropic in $d\Omega$. This should be taken into account for the correct calculation of the weight. In our case, where the **VOLUMECORR** option was used, the dependence of the intensity on the zenith angle (θ) is shown in equation (6.2), so the flux used in the simulation is:

$$f_{CO} = a \cdot E_{prim}^{-1} \cdot (cos\theta + 4/\pi \cdot l/d \cdot sin\theta) \tag{6.7}$$

[1] In *CORSIKA* simulations a flat spectrum in azimuth is assumed.

[2] Here the number of simulated showers refers to the initial number of simulated showers and not to the number of shower with particles reaching the observation level.

Again the constant a of equation (6.7) is determined by requiring the integral of $f_{CO}(E_{prim}, \theta)$ in dE_{prim} and $d\Omega$ to be equal to the number of simulated showers (N_{sim}), so:

$$\int_{E_{prim\,min}}^{E_{prim\,max}} \int_{0}^{2\pi} \int_{0^o}^{87^o} f_{CO}(E_{prim}, \theta)\, d\Omega\, dE_{prim} = N_{sim} \tag{6.8}$$

resulting to:

$$a = N_{sim} / \int_{E_{prim\,min}}^{E_{prim\,max}} \int_{0}^{2\pi} \int_{0^o}^{87^o} E_{prim}^{-1} \cdot (cos\theta + 4/\pi \cdot l/d \cdot sin\theta) \cdot sin\theta\, d\theta\, d\phi\, dE_{prim} \tag{6.9}$$

In both the above cases, either if there is a dependence on the zenith angle during the simulation or not, the weight of each shower event is:

$$Weight = \frac{f_{CR}}{f_{CO}} \tag{6.10}$$

where f_{CO} is found by the equations (6.7) or (6.4) respectively. At this point extra care should be given to the units in which each of the fluxes is measured. In *CORSIKA* length, time, energy and solid angle are measured in cm, s, GeV and sr respectively, so f_{CO} is measured in GeV^{-1} s^{-1} cm^{-2} sr^{-1}, while most fluxes, like in [8] [9], are given in GeV^{-1} s^{-1} m^{-2} sr^{-1}. Before finding the weight for each event both fluxes should be measured in the same units.

The weight as defined in equation (6.10) is, in general, dependent on the energy E_{prim} and the zenith angle θ_{prim} of the CR primary. When this weight is applied, the CR primaries are forced to follow the flux f_{CR} instead of the non physical f_{CO} used in the simulation. In the CR flux models more than one primaries are used, so to correctly weight the simulated events the above weighting technique should be followed for each simulated primary and the final flux is the sum of the fluxes produced by each primary. Since each shower is assigned in equation (6.10) all muons and neutrinos from the same shower have the same weight. After weighting neutrinos or muons with this weight the result is the expected rate (number of particles) per unit area and unit time (where area and time have the same units as those used in the fluxes) at the observation level, assuming the cosmic ray primaries used follow the flux f_{CR}. For a binned histogram of the expected flux of particles at the observation level, the binning of the histogram needs to be taken into account, so each particle with a certain energy and within a certain solid angle needs to be weighted by the weight in (6.10) divided by the corresponding bin width in energy and in solid angle.

6.5 Evaluating the impact of CHARMed option

The first teo major productions were generated using the same options with the exception of **TAULEP** and **CHARMed** which have been activated in each production respectively. These productions make it possible to compare particles at observation in order to reveal the impact of the parameter **CHARMed**.

In Figures 6.3,6.4 and 6.5 various physical parameters of the particles created in these productions are compared. In these plots unweighted events were used, so they illustrate the differences between the two productions assuming the nonphysical E^{-1} (generation) spectrum and do not contain information that can be directly related to a particle flux. Nevertheless, since the CR spectrum can be roughly approximated by an $E^{-2.7}$ power law [3] and the simulated CR showers have energies that range in six orders of magnitude, these

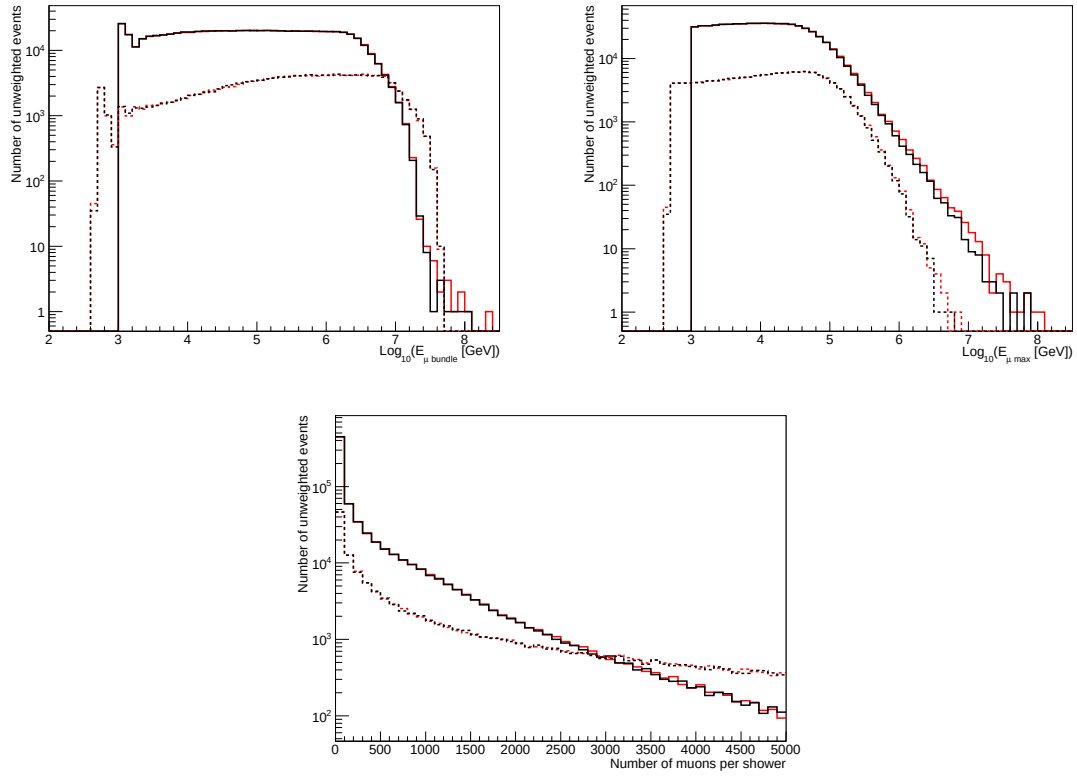

*Figure 6.3: Upper left: Logarithm of the bundle energy of all muons created at each shower. Upper right: Logarithm of the energy of the most energetic muon created at each shower. Lower: Number of muons reaching observation level for each shower. In all figures solid lines are used for particles created at showers where the primary CR particle is a proton and dashed lines when the primary CR particle is a $^{56}_{26}Fe$ nucleus. For both CR primaries: black lines are used for the production without the **CHARMed** option and red lines for the production with the **CHARMed** option activated.*

plots can be used to enhance and detect subtle differences between the different productions which might not be prominent after the convolution with the CR spectrum.

In Figure 6.3 a comparison of the bundle muon energy, the energy of the most energetic muon and the number of muons produced in each shower are shown. Even though seven different primaries were used for the simulations, here the results of only protons and $^{56}_{26}$Fe nuclei, the lighter and the heavier primaries, are compared. In both energy plots the difference in the low energy part between the two primaries is due to the different energy cuts, as already mentioned in 6.3. From the upper right plot where, the energy of the most energetic muon is presented, it seems that by using the option **CHARMed** the most energetic muons produced in the proton induced showers have slightly higher energies. A similar effect is true for muons produced by iron induced showers but this time it is much less prominent. By comparing the upper left and the lower plots where the bundle energy of muons and the number of muons in a shower are shown respectively, activating the option **CHARMed** does not seem to influence the distributions.

In Figure 6.4 a comparison of the total energy of all neutrinos and of the energy of the most energetic neutrino are shown. From the upper plots, where the neutrino bundle

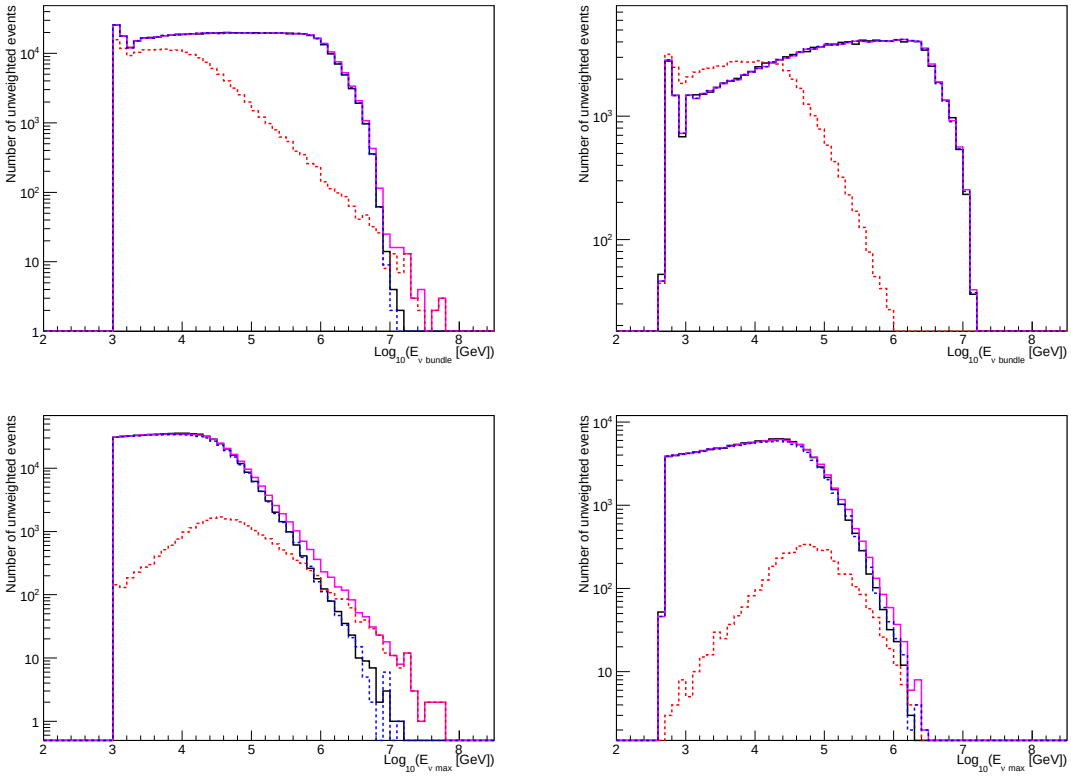

*Figure 6.4: Upper: Logarithm of the bundle energy of all neutrinos created at each shower using as CR primaries left: protons and right: $^{56}_{26}Fe$ nuclei. Lower: Logarithm of the energy of the most energetic neutrino created at each shower using as CR primaries left: protons and right: $^{56}_{26}Fe$ nuclei. Black solid lines: neutrinos from the production without the **CHARMed** option, magenta solid lines: neutrinos from the production with the **CHARMed** option activated, red dashed lines: from the second production neutrinos having a charmed precursor and blue dashed lines: neutrinos from the second production neutrinos not having a charmed precursor.*

energy is shown, it can be deduced that when the CR particle is a proton the use of option **CHARMed** results to slightly more energy been given to neutrinos than without this option activated. Moreover, the distribution of the total energy granted to neutrinos not having a charmed precursor in production two (option **CHARMed** activated) matches that of production one (without the option **CHARMed**). When the primary CR particle is an iron nucleus the neutrino bundle energy seems to be the same for both productions. The impact of the option **CHARMed** is more prominent in the lower plots of Figure 6.4 showing the energy of the most energetic neutrino of each shower. When option **CHARMed** is used the energy of the most energetic neutrinos is higher than without this option activated. Once more the distribution of the energy of the most energetic neutrino of each shower that does not have a charmed precursor for the second production, matches perfectly the distribution from the first production. This behavior is more prominent for showers produced by proton CR primaries but is also present in the case of iron nuclei CR primaries. Moreover, for showers produced by proton CR primaries the majority of most energetic neutrinos with energies above 1 PeV have a charmed precursor. Finally in Figure 6.5 where the number

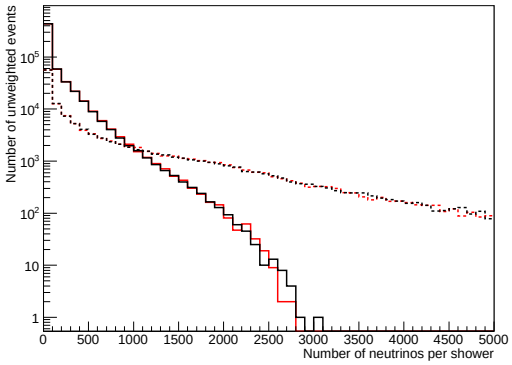

*Figure 6.5: Number of neutrinos reaching observation level for each shower. Solid lines are used for particles created at showers where the primary CR particle is a proton while dashed lines when the primary CR particle is a $^{56}_{26}Fe$ nucleus. Black lines are used for the production whithout the **CHARMed** option and red lines for the production with the **CHARMed** option activated.*

of produced neutrinos in each shower is shown, no difference is observed between these two productions.

Based on the comparisons of unweighted events it seems that the use of option **CHARMed** has a bigger effect on neutrinos than on muons. Also this effect seems to decrease as the primary CR becomes heavier. In order to further investigate the effect of option **CHARMed** to neutrinos, all relevant primaries simulated were taken into account and the neutrinos at sea level were weighted using the technique described in section 6.4. In Figure 6.6 the neutrino fluxes derived from the simulated showers at sea level are presented using the CR flux model H3a [8] containing both the CR flux knee and ankle. For both muon and electron neutrinos from the energy at which the prompt ([24] hereafter Enberg) flux becomes comparable to the conventional ([23] hereafter Honda) flux, the flux derived from the second production (with the option **CHARMed** activated) is higher than that derived from the first production (option **CHARMed** not activated). This effect is more prominent for electron neutrinos for which the conventional flux is much lower than that of muon neutrinos. Even though the use of option **CHARMed** results in a higher neutrino flux at the energy region where the prompt component becomes important, the production with the *QGSJET01* high energy model and with option **CHARMed** does not provide a satisfactory description of the neutrino flux at high energies. This can be attributed to the poor statistics in this energy region, as shown in Figures 6.4 and 6.6, and possibly to the high energy interaction model.

6.6 Evaluating the impact of different high energy interaction models

The high energy interaction models used in the five major productions were *SIBYLL* 2.3, *EPOS LHC*, *QGSJET*01*c* and *QGSJETII*. *SIBYLL* 2.3 [108] is one of the most recent high energy interaction models since the assumptions and approximations of the previous *SIBYLL* 2.1 model were revisited and improved using recent LHC data. Also a phenomenological model was used for the the production of charm particles. *EPOS LHC* [109] is a

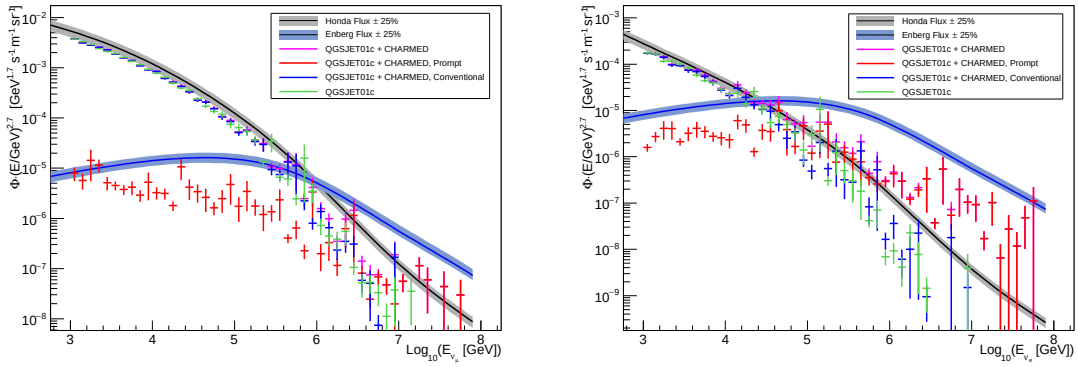

*Figure 6.6: Neutrino fluxes at sea level. The theoretical fluxes by Honda [23] and Enberg [24] are presented with black and blue inside a ±25% gray and light blue band respectively. The flux derived without the option **CHARMed** is presented in green. The production with the option **CHARMed** activated is shown in magenta, the contribution of those neutrinos with a charmed precursor in red while those without a charmed precursor in blue. In the low energy region where the contribution of the prompt component is negligible the magenta points coincide with the blue. Left: Flux of ν_μ and $\overline{\nu_\mu}$. Right: Flux of ν_e and $\overline{\nu_e}$.*

phenomenological high energy interaction model incorporating data from LHC. *QGSJET II* [110] is also a generator for high energy hadronic and nuclear collisions which was also revisited and adjusted using LHC data. Though *QGSJET*01*c* is the oldest of the four models used, it allowed for the use of option **CHARMed** unlike the most recent models *EPOS LHC* and *QGSJETII*.

In order to evaluate the impact the different high energy interaction models have on the final output, the neutrino fluxes derived from all five major productions were compared to each other and to the conventional (Honda) and prompt (Enberg) fluxes. In Figure 6.7 the muon (left) and electron (right) neutrino fluxes, derived using H3a model for the CR flux, are shown. For the low energy part, where the prompt component is not important, *EPOS* model seems to better match the Honda flux, closely followed by *SIBYLL* 2.3 model. The fluxes derived by *QGSJET* models deviate more from the Honda flux but they are still within the 25% band. For the high energy part where the prompt flux is the dominant component, *SIBYLL* 2.3 model agrees with the Enberg flux while the rest of the models produce much lower fluxes. At this point it should be stressed that the statistics at this region is low and this is reflected on the statistical errors. Nevertheless *SIBYLL* 2.3 model outperforms the rest of the models used at this energy range. Also at this energy region *QGSJET*01*c* with option **CHARMed** and *EPOS* model seem to produce comparable results from muon neutrino fluxes even though *EPOS* is not compatible with the explicit treatment of charmed particles by the option **CHARMed**. Finally in the intermediate energy range the deviation of fluxes derived by the *QGSJET* models from the theoretical fluxes is not as prominent as in the high energy region but it is still observed, while models *EPOS* and *SIBYLL* 2.3 seem to produce similarly good results. Since model *SIBYLL* 2.3 seems to be more compatible with both the Honda and Enberg neutrino fluxes a ratio plot of the fluxes derived by the rest of the high energy interaction models to *SIBYLL* 2.3 is also shown in Figure 6.7. Even in the low energy region where the contribution of the prompt neutrino flux is negligible and the statistics is better compared to higher energies, on average, the flux derived by *EPOS* is lower by approximately 20% to 25% while the

fluxes derived by the *QGSJET* models is lower by 30% to 40% compared to *SIBYLL* 2.3. These differences illustrate the fact that the use of different high energy hadronic interaction models can have a great impact on the final fluxes derived.

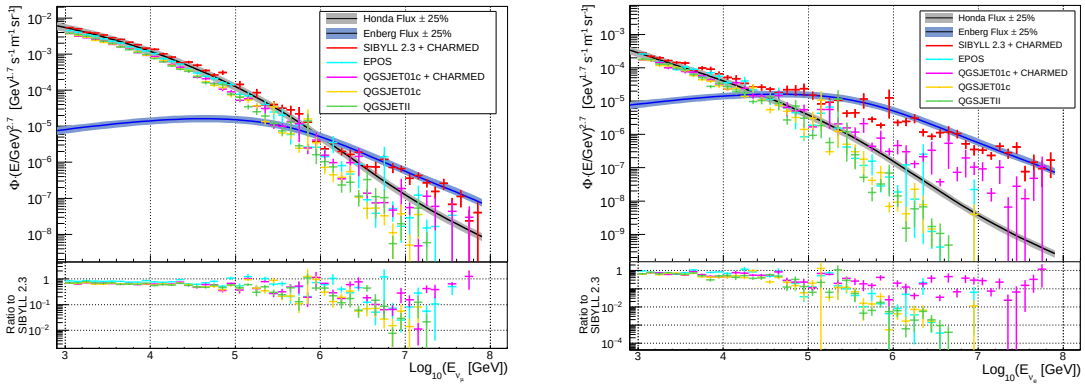

Figure 6.7: Neutrino fluxes at sea level. Honda and Enberg neutrino fluxes are presented with black and blue inside a ±25% gray and light blue band respectively. Below each plot a ratio of the flux derived by each model with respect to the flux derived by the production using SIBYLL 2.3 is shown (color code is the same). Left: Flux of ν_μ and $\overline{\nu_\mu}$. Right: Flux of ν_e and $\overline{\nu_e}$.

6.7 Evaluating the impact of different atmospheric models

In all five major productions a user defined atmospheric density model describing the yearly averaged atmosphere above the deployment site of the ARCA telescope was used as mentioned in section 6.2.2. Even though this is the best possible approximation used in the simulations, three more productions were made using the parameters of the fifth major production in Table 6.1 while changing the atmospheric model. First, the atmospheric model of the U.S. standard atmosphere as parameterized by Linsley [104], included in the *bernlohr* package of *CORSIKA*, was used by setting steering parameter **MODATM** to 1. A production with the same statistics as the fifth major production was simulated. The neutrino fluxes at sea level from both these productions are shown in Figure 6.8 for muon (left) and electron (right) neutrinos. It can be observed that the impact of using different atmospheric models is really low. In the low energy part where there is enough statistics, on average, the difference of the two fluxes is at the per-mil level.

For the other two productions user defined atmospheric models used were implemented, describing the atmospheric density above the deployment site of ARCA at summer and winter time. Since it is already established that using a totally different atmospheric model has a negligible difference on the neutrino fluxes and the atmospheric models used for these productions are much closer to the one used in the fifth major production, only 10% of the number of showers were simulated and only using protons as CR primaries. In Figure 6.9 the energy of the most energetic muon (left) and neutrino (right), for the same number of simulated showers, is shown for all four productions using different atmospheric models. In these plots unweighted events were used to enhance any energy dependent differences. Once more it can be observed that the impact of different atmospheric models on simulated neutrinos and muons at sea level is negligible, of the order of per-mil for the low energy

part, and is not distinguishable from the statistical fluctuations.

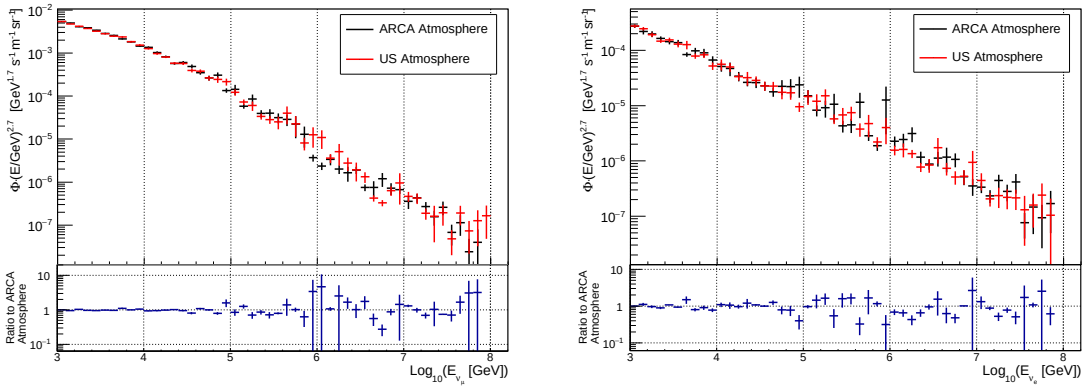

Figure 6.8: Neutrino fluxes at sea level derived using an atmospheric density model describing the yearly averaged density of the atmosphere above the deployment site of ARCA, in black, and the atmospheric model of the U.S. standard atmosphere as parameterized by Linsley, in red. Below each plot the ratio of the fluxes derived by using these atmospheric models is shown. Left: Flux of ν_μ and $\overline{\nu_\mu}$. Right: Flux of ν_e and $\overline{\nu_e}$.

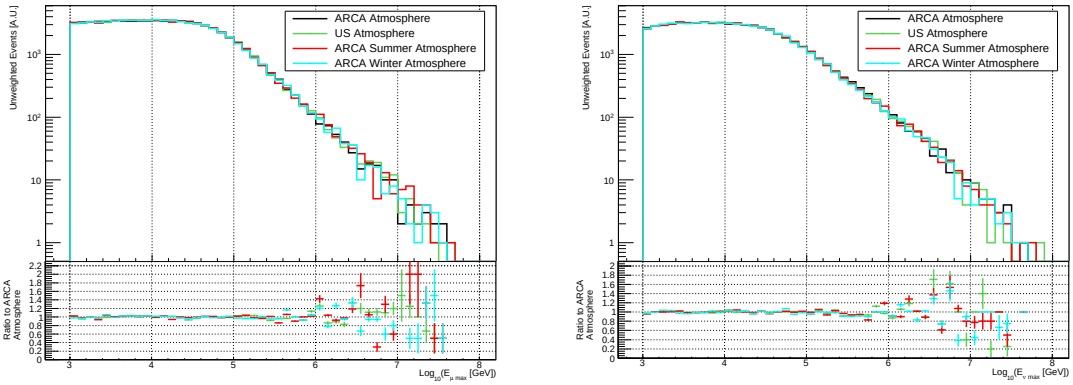

Figure 6.9: Logarithm of the energy of the most energetic muon, left, and neutrino, right, created at each shower using protons as CR primaries protons. Atmospheric models used: atmospheric density above the ARCA deployment site black for yearly averaged, red for summer, cyan for winter; green for the U.S. standard atmosphere as parameterized by Linsley. Below each plot, the ratios of the energy distributions derived by each model with respect to that derived by using the atmospheric density model above the ARCA deployment site are shown (color code is the same).

6.8 Evaluating the impact of different CR models

Even though the CR flux used for weighting the output of *CORSIKA* simulations in order to retrieve the neutrino and muon fluxes is not part of the simulation process, it is very important for the final results. In order to evaluate the effect of using different CR flux models when weighting *CORSIKA* events, fluxes derived from the fifth production (Table

6.1) weighted with H3a and H4a from [8] and with GST3 and GST4 from [9] CR models are shown in Figure 6.10.

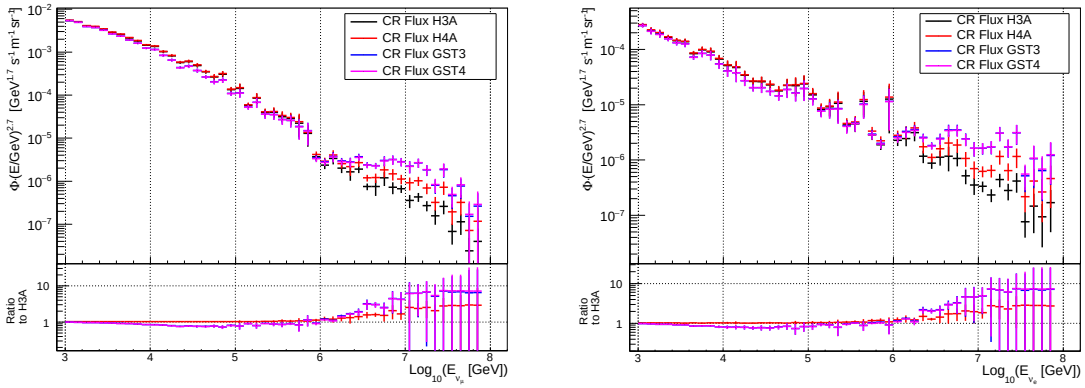

Figure 6.10: Neutrino fluxes at sea level derived using CR flux models: black for H3A, red for H4A, blue for GST3 and magenta for GST4 model. Below each plot a ratio of the flux derived by each CR model with respect to the flux derived by using the H3A model is shown (color code is the same). Left: Flux of ν_μ and $\overline{\nu_\mu}$. Right: Flux of ν_e and $\overline{\nu_e}$.

The CR primaries used for models H3a and H4a are different from those used for GST3 and GST4 models. In the former, primaries CNO are grouped together and Mg-Si primaries are used while in latter primaries C and O have different contributions to the total flux and also no Mg-Si primaries are used. Moreover, the differences between H3a and H4a originate from different parametrization of the extra-galactic component of the CR flux, which is also true for the GST3 and GST4 models which additionally have slightly different parametrization for the high energy galactic CR component. This is reflected in the differences between the neutrino fluxes derived by each model at the high energy part. From the ratio plots of Figure 6.10 it can be observed that for the low energy region there is no observable difference between the fluxes derived using models H3a and H4a and the same holds for the models GST3 and GST4. The neutrino fluxes derived using GST models are lower by as much as 20% compared to those derived by H3a in the low energy part.

6.9 Conclusion

Detailed air shower simulations can provide a very powerful tool to determine the muon and neutrino background for neutrino telescopes, so in KM3NeT effort was made to use *CORSIKA* to simulate the atmospheric background. In this section various Monte Carlo simulated air shower productions with *CORSIKA* are detailed with the purpose to identify the best parameters to be used for a production intended for physics analyses with the ARCA telescope. Several different simulations parameters have been tested. The high energy interaction model used in the simulation has the strongest effect on the final output. Also important is the choice of CR flux used to weight the simulated neutrinos and muons. Moreover, attention should be paid to the values used for the energy cuts in order to ensure a reliable production with the least possible computational resources. The tests performed, which are described in this section indicate that the fifth major production as described in Table 6.1, in which *SIBYLL* 2.3 is used as the high energy interaction model with the

option *CHARMed* activated, provides a satisfactory description of the theoretical models for the atmospheric neutrino fluxes. Therefore this is considered as the best candidate to be propagated to the can (Section 5.2.1) and to be used for a physics analyses.

Chapter 7

MAMBA Rejection: A Tool To Reject Incoming Track Events To The KM3NeT/ARCA Detector.

7.1 Introduction

The standard approach in KM3NeT to achieve a strong suppression of the atmospheric muon background which is necessary for the track channel has been the requirement that events are reconstructed as upgoing. Alternatively, a significant reduction of the atmospheric muon background can also be achieved by requiring the neutrino interaction vertex to be located inside the volume of the detector (starting track events). Another advantage of selecting starting track events is the reduction of the atmospheric neutrino background which can be achieved by applying a self-veto. Usually, for neutrino telescopes, atmospheric neutrinos are an "irreducible" background since they cannot be differentiated by any means from astrophysical neutrinos. They are produced in the same atmospheric showers in which atmospheric muons are also created. Thus, when these neutrinos reach the detector and interact, there is a high probability that at the same time, muons from the same shower cross the detector. Such atmospheric neutrinos accompanied by muons (energetic enough to leave a detectable trace while crossing the detector) can be reliably classified as atmospheric by identifying the through going accompanying muons. This way by selecting starting track events a reduction of the so called "irreducible" neutrino background can be achieved. In addition, by selecting starting events we expect to obtain a more accurate measurement of the neutrino energy, in contrast to through-going muon tracks events for which the measurement of the muon energy can only provide a lower limit of the neutrino energy. This, in turn, is expected to lead to a better estimation of the astrophysical diffuse flux spectrum. Finally, since no restrictions are pose on the reconstructed zenith angle of the selected events, a full sky coverage is achieved.

Even though an analysis based on starting track events has a lot of advantages, it also has a few disadvantages and strict requirements that need to be met. Firstly, even though a sample of starting track events has a higher purity on astrophysical neutrinos than a sample of upgoing muon tracks, it also comprises less events, since only a fraction of ν_μ and $\overline{\nu_\mu}$ charged current interactions happen inside the instrumented volume. As already mentioned in Chapter 2.2 the expected rate of atmospheric muons reaching the ARCA detector is many orders of magnitude larger than the rate expected from neutrinos. So a tool that rejects incoming events to ARCA should practically reject all the atmospheric

muon events while, at the same time, it should have a high efficiency for real starting track events. The rejection of atmospheric muon events is very important as the fraction of remaining miss-classified atmospheric muons could easily overwhelm the neutirno signal.

For an astrophysical diffuse flux analysis the only possible way to differentiate between astrophysical and atmospheric neutrinos, apart from the self-veto effect, is on a statistical basis by their energy, as already mentioned in Chapter 2.2. The astrophysical signal is more prominent than the atmospheric background in the High Energy (HE) region. A tool, Multiple Atmospheric Muon BAckground (or MAMBA) rejection, has been designed to identify High Energy Starting Track (HEST) events and to efficiently reject through going events to the ARCA detector.

For the development and testing of the MAMBA rejection tool and for the subsequent analyses conducted in this chapter the following samples of MC events were used:

1. Samples of all flavors of neutrino events simulated with *GENEHN*.

2. Two different samples of atmospheric muon events simulated with *MUPAGE*. The first one comprising events with $E_{bundle} \geq 10$ TeV having a livetime of approximately 3 months for 1 ARCA block and the second comprising events with $E_{bundle} \geq 50$ TeV having a livetime of approximately 3 years for 1 ARCA block. Even though the energy range of the sample with $E_{bundle} \geq 10$ TeV extends to bundle energies well above 50 TeV, both samples were used in their full energy range in order to achieve better statistics in the high energy region.

3. A sample of atmospheric neutrino events simulated with *CORSIKA*. The particles (muons and neutrinos) were propagated to the ARCA can with *GENHEN*. This sample was created by the output of the fifth *CORSIKA* production detailed in Chapter 6.3. It comprised eight subproductions of ν_μ, $\overline{\nu_\mu}$, ν_e and $\overline{\nu_e}$ events interacting inside the can via CC or NC interactions, so each *CORSIKA* event was processed at maximum eight times. Events were not included only in the case that no neutrino from the predefined flavor had been produced in that simulated shower. Otherwise all particles were propagated from the sea surface to the can and one neutrino was chosen to interact inside the can. This sample was only used for the self-veto studies.

7.2 MAMBA rejection

7.2.1 General

Multiple Atmospheric Muon BAckground (MAMBA) rejection has been designed to reject incoming muons to the ARCA detector and select HEST neutrino events. Since the focus is on HE events, only neutrino events with $E_\nu > 30$ TeV are considered as signal events. The MAMBA rejection consists of the following steps:

- Selecting events passing the quality cuts of the reconstruction.
- Selecting events with the reconstructed vertex inside a fiducial volume, which is slightly smaller that the instrumented volume of ARCA.
- Using a Boosted Decision Tree (BDT) classifier with ten event based variables to make the final differentiation.

These steps are detailed in the following subsections.

7.2.2 Selecting track events with a good angular resolution

The first step is to select track events which pass the quality cuts of the reconstruction and is therefore expected that the reconstruction of the muon direction is reliable (hereafter "well reconstructed" track events). In order to select these events, the quality requirements introduced in[111] have been used. These requirements are the following:

- the negative logarithm of the reconstructed track fit likelihood to be less than -60 and
- logarithm of the directional error parameter β_0 to be less than -2.8.

As illustrated in figure 7.1 for both atmospheric muon events (right) as well as ν_μ and $\overline{\nu_\mu}$ CC events (left) the efficiency of these requirements is quite high ($> 65\%$) for events with an angular resolution better than 1^o and drops rapidly as the angular resolution increases.

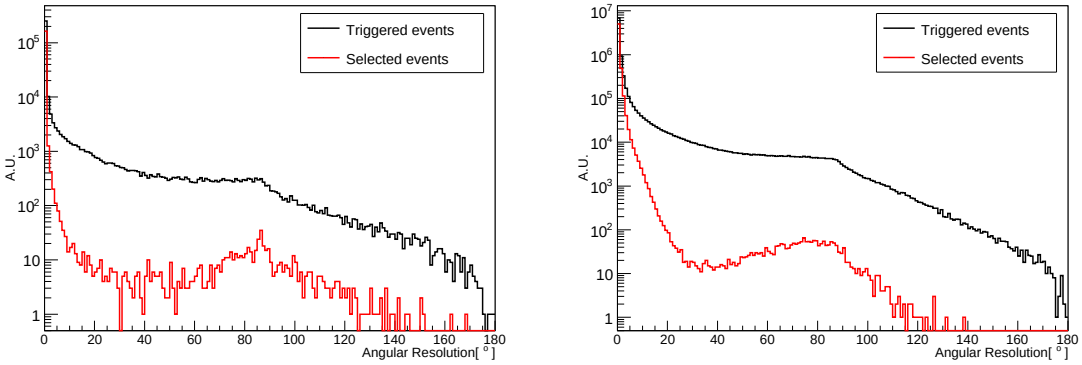

Figure 7.1: The angular resolution for ν_μ and $\overline{\nu_\mu}$ CC events (left) and for atmospheric muon events (right). Triggered events are shown in black while the events surviving the quality requirements in red.

7.2.3 Interaction vertex finding method and containment of the reconstructed vertex

The containment of the reconstructed vertex is a very powerful tool to reject the large majority of incoming events to the detector, so all events with reconstructed vertices outside a fiducial volume (slightly smaller than the volume of the detector) have been rejected. This fiducial volume has been chosen to be a cylinder coaxial to the detector with a radius of 455m, which is smaller than the radius of ARCA by approximately 45m (half the string to string distance). The upper lid of the fiducial volume cylinder lays 56m below the upper DOM of each string, which is about 20m above the 16th DOM of each DU. Finally, the lower lid is just 6m above the lowest DOM of each string. This value has been chosen in such a way to reject incoming muons (created by neutrinos interacting outside the detector) from below, but since these are not as frequent as the atmospheric muon background, a larger reduction of the volume in this direction has not been considered necessary. The footprint of ARCA (left) and the projection of a string on the z axis (right) as well as the boundaries of the fiducial volume are shown in Figure 7.6.

The vertex reconstruction accuracy is decisive for the efficiency of the containment requirement. As it will be discussed in Chapter 7.2.5, the event based variables used in the

BDT classifier depend on the reconstructed vertex position. In particular, the more the reconstructed vertex approximates the interaction vertex the better the discriminating power that these variables have. Even though *JStart* is the official vertex reconstruction used in KM3NeT, in order to achieve the best possible results a simple, yet effective method to estimate the neutrino interaction vertex for a given reconstructed track direction was developed. For this method *JGandalf* was used for the track reconstruction. This reconstructed vertex is defined as the emission point of the photon (Cherenkov hypothesis) along the reconstructed track, that gave the first in time triggered hit satisfying the following requirements:

- |Time residual| $\leq$ 30 ns.
- Maximum photon path length $\leq$ 165m (3 times the absorption length). The photon path length was defined as the distance from the hypothetical Cherenkov photon production point along the reconstructed track to the PMT which had been hit.
- Angle between the direction of the hypothetical Cherenkov photon and the PMT direction $< 90°$.

It should be noted that before any information based on hits (either triggered or not) was utilized, a noise filtering method [112] was applied to remove the bulk of hits due to the ^{40}K decays. This method rejects hits which are not causally connected to the hit with the largest ToT (^{40}K hits have small ToTs) applying loose requirements. It provides a powerful rejection on noise hits while retaining a very high efficiency on direct photon hits truly associated with the products of the neutrino interaction.

This method seems to produce excellent results for identifying the interaction vertex of contained events. When tested to ν_μ and $\overline{\nu_\mu}$ CC events fulfilling the quality criteria discussed in Chapter 7.2.2, the following results were obtained:

- 97% of the events having their true (MC) interaction vertex inside the fiducial volume, also had the reconstructed vertex inside the fiducial volume.
- for events having both the reconstructed and the true (MC) neutrino interaction vertex inside the fiducial volume the median of the distance between these vertices was 16.9m. This is slightly less than half the DOM to DOM distance in the DU (18 m). The distribution of this distance is presented in Figure 7.2 in black.
- 16% of the events having their true (MC) interaction vertex out of the fiducial volume, were misreconstructed as having the reconstructed vertex inside the fiducial volume.

The standard production has also been processed with *JStart*, (*JPP* version 6231). A comparison between the vertex found by this method and by *JStart* was carried out. Using *JStart*:

- 88% of the events having their true (MC) interaction vertex inside the fiducial volume, also had the reconstructed vertex inside the fiducial volume.
- for events having both the reconstructed and the true (MC) neutrino interaction vertex inside the fiducial volume the median of the distance between these vertices was 32.2m which is slightly less than the DOM to DOM distance in the DU (36 m). The distribution of this distance is also presented in Figure 7.2 in red.

- 6% of the events having their true (MC) interaction vertex out of the fiducial volume, were misreconstructed as having the reconstructed vertex inside the fiducial volume.

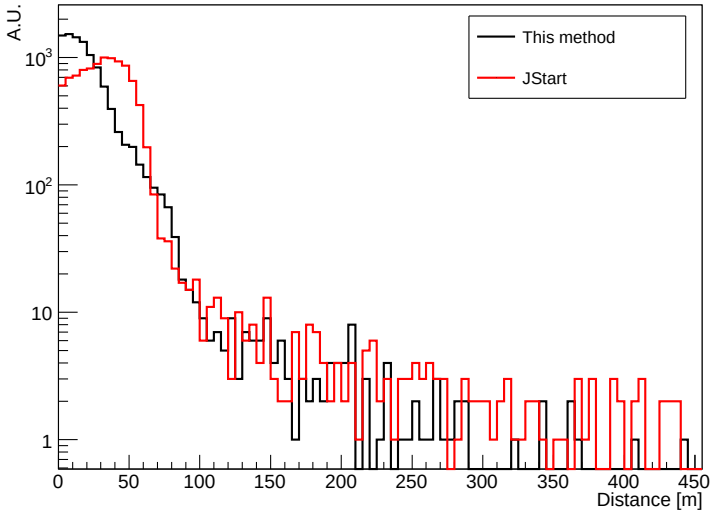

Figure 7.2: Distance of the reconstructed vertex to the neutrino interaction vertex for events truly contained in the fiducial volume also having both reconstructed vertices, by this method and JStart, inside the fiducial volume. Black: This method. Red: JStart.

The comparison of this method for finding the interaction vertex with *JStart* indicates that this method is better in identifying contained events while *JStart* is better in identifying incoming events to the detector (for *JStart* this improves even more if one considers the containment in the instrumented volume). For the MAMBA rejection, as already mentioned, the most important aspect is the proximity of the reconstructed vertex to the neutrino interaction vertex. Since this method better approximates the interaction vertex it is better suited for the MAMBA rejection tool.

The requirement for the reconstructed vertex to be inside the fiducial volume provides a powerful reduction of through-going events, rejecting up to 99.8% of the events belonging tside o the high energy atmospheric muon sample, while the efficiency on HEST neutrino events truly contained in the instrumented volume is approximately 80%, as reported in Table 7.1. By considering the vertex containment inside the fiducial and not inthe instrumented volume the question of how many contained and through-going events are rejected rises. In Table 7.2 the percentage of the events having their reconstructed vertices inside the instrumented but not in the fiducial volume are presented. The loss of trully contained events is of the order of 17% while for truly through-going events this fraction ranges from 63% (for ν_μ CC interacting outside the detector) up to 95% for the high energy atmospheric muon events sample. This effect is visualized in Figures 7.3 and 7.4 where the reconstructed vertices of atmospheric muon events with $E_{bundle} \geq 10$ TeV, $E_{bundle} \geq 50$ TeV and ν_μ CC events interacting inside or outside the detector are shown along with the borders of the instrumented and the fiducial volume. In Figure 7.3 it can be observed that the fraction of atmospheric muon events with $E_{bundle} \geq 10$ TeV that have their vertices wrongly reconstructed as inside the fiducial volume is much higher than that of atmospheric muon events with $E_{bundle} \geq 50$ TeV. This effect was rather expected since muons with lower energies

produce less light, so they can penetrate deeper to the detector before inducing a clear, detectable signal.

ν_μ CC interacting in the detector	ν_μ CC interacting outside the detector	atmospheric muons $E_{bundle} \geq 10$ TeV	atmospheric muons $E_{bundle} \geq 50$ TeV
79.6%	15.8%	2.8%	0.2%

Table 7.1: Percentage of the number of events having their reconstructed vertices inside the fiducial volume compared to all well reconstructed events, for the various types of events.

ν_μ CC interacting in the detector	ν_μ CC interacting outside the detector	atmospheric muons $E_{bundle} \geq 10$ TeV	atmospheric muons $E_{bundle} \geq 50$ TeV
17%	63%	84%	95%

Table 7.2: Percentage of the number of events having their reconstructed vertices inside the instrumented but not in the fiducial volume compared to those having their reconstructed vertices inside the instrumented volume, for the various types of events.

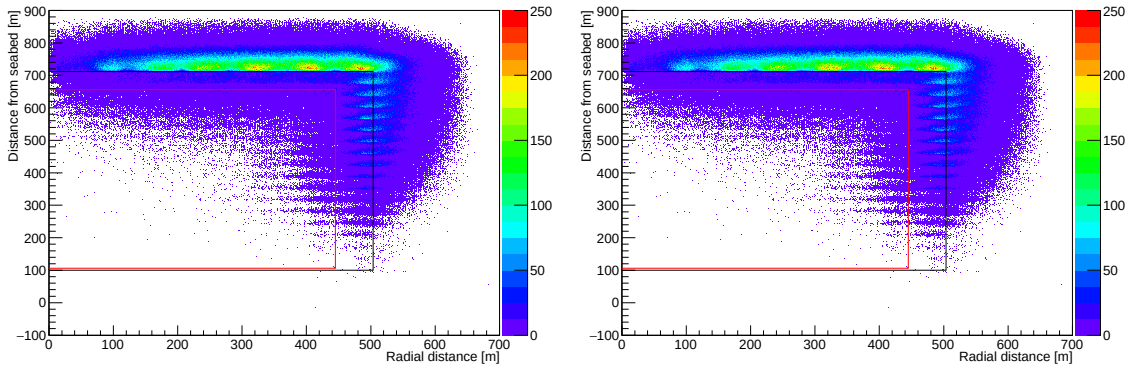

Figure 7.3: Reconstructed vertices of atmospheric muon events with $E_{bundle} \geq 10$ TeV on the left and $E_{bundle} \geq 50$ TeV on the right. Black line: Instrumented volume border. Red line: Fiducial volume border.

The clustering of the reconstructed vertices observed in both Figures 7.3 and Figure 7.4 left, along the vertical axis in "zones" with higher density is due to the method used for the reconstructed vertex (the production point of the hypothetical Cerenkov photon responsible for the first in time hit, satisfying the requirements set). Considering that muons travel faster than light in water, the photons responsible for the first in time hit are those produced closer to a DOM rather than those produced first in time but further away. The effect observed in both Figures 7.3 is a combination of the vertex finding method with the fact that atmospheric muons are down-going, so the reconstructed vertices tend to "accumulate" in high density zones above the vertical position of the DOMs. In the case of Figure 7.4 left, through-going muons from ν_μ CC interactions outside the detector reach the detector from all directions, thus the reconstructed vertices tend to "accumulate" in high density zones around the vertical position of the DOMs.

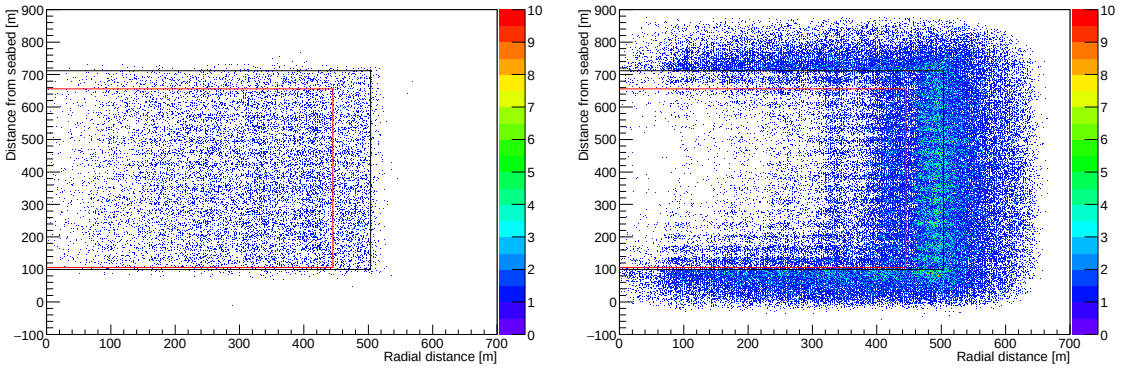

Figure 7.4: Reconstructed vertices of ν_μ CC events interacting in the detector on the left and interacting outside the detector on the right. Black line: Instrumented volume border. Red line: Fiducial volume border.

Even though just by requiring the containment of the reconstructed vertex the reduction of the incoming events to ARCA ranges from 84.2% up to 99.8%, the number of events fulfilling this requirement is extremely large, as illustrated in Figure 7.3. More specifically from the samples of atmospheric muons with $E_{bundle} \geq 50$ and 10 TeV, about 0.15 and 52 events per hour are expected to survive the containment cut. Therefore, in order to further reject incoming events to ARCA a BDT classifier is employed.

7.2.4 Boosted Decision Trees

The term "Decision Tree" is used for a large class of non-linear classifiers [113]. They are used to solve either classification or regression problems. In the case of classification, binary decision trees sequentially split the feature space by posing a test at each decision node and by assigning a class label to each segment, Figure 7.5 right. So when a new feature vector arrives for evaluation, the predicted class is derived by the label of the segment of the feature space this vector lands on. As an example the feature vector (e,f) (blue point) of Figure 7.5 right will be classified as "B". Using a graphical representation, a decision tree consists of one root node and various decision and leaf nodes, as shown in Figure 7.5 left. To evaluate a new example a descending path is followed down to a leaf node, thus a class label is predicted. The feature vector (e, f) will follow the right path of the root node (e $>$ a), then the right path of the first decision node (f $>$ c) and finally the left path of the second decision node (e $<$ b) thus landing on the leaf with label "B". For a decision tree to have a powerful classification performance in cases where the features are many and the classes overlap in each feature, a lot of sequential nodes need to be created (the number of sequential nodes excluding the root is called tree depth). However large decision trees are prone to over-training. Over-training is the term used in the case that a classifier "learns" a sample of events extremely well but fails to generalize this "knowledge" to similar but not exactly the same events. In order to overcome this issue of large decision trees, a classifier based on decision trees called Boosted Decision Trees [114] is widely used.

A Boosted Decision Trees (or BDT) classifier is an ensemble of decision trees usually with a small depth. A single decision tree with a small depth used for a classification problem is expected to perform poorly (poorly performing classifiers are referred to as weak classifiers). On the other hand a decision tree with 3 or 4 layers does not suffer from over-training

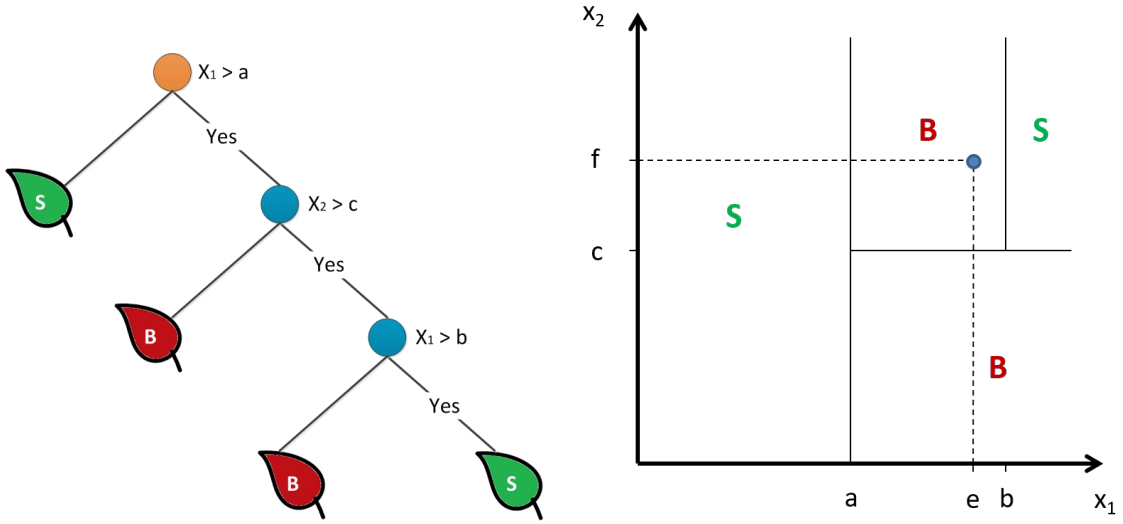

Figure 7.5: Left: A schematic representation of a binary Decision Tree with tree depth = 3. The orange circle represents the root and blue circles the decision nodes. The tests posed by the root node and each decision node are shown at the right of the nodes. The leaves hold the class labels "S" and "B". Right: A representation of the feature phase space of the Decision Tree depicted on the left and the class labels of each segment.

[114], moreover the training phase of such a tree requires very little time. What makes a BDT a strong classifier though, is the power gained by using many decision trees each one trained with a different part of the original training sample. Training many decision trees with small depth is not time consuming since the training time of each individual tree is really small, especially when compared to the time required for the training of classifiers like Artificial Neural Networks (ANNs). The procedure used for training each tree with a different sample extracted from the original one is called boosting and it is critical for building a strong classifier. The most common methods of boosting are AdaBoost (Adaptive Boost) and Gradient Boost. Using AdaBoost the training sample used for growing each individual decision tree is selected form the training sample (TS) of the BDT classifier with a weighted scheme. Before training any tree the weights of all events in sample TS are equalized and normalized, so the training sample used for the first tree ($ts1$) is randomly selected from TS. After training the first tree, to each miss-classified event of $ts1$ a larger weight is assigned and the weights of the whole sample TS are re-normalized. By this procedure the miss-classified events have a larger probability to be selected for the training sample of the next tree. This procedure is followed after the training of each decision tree, so each tree learns a different part of the training sample TS, specifically the part that the previous trees failed to learn. To classify an unknown instance all decision trees predict a class and the final class label is derived by a weighted majority vote.

The BDT classifier used in MAMBA rejection is contained in the *TMVA* package [114] of the *ROOT* Data Analysis Framework [115]. It comprises $1,150$ decision trees with a maximum depth of 4 layers. For a leaf node to be created it should comprise at minimum 9% of the events used for the training. Moreover the splitting of each node is decided based on the gini index. The boosting is preformed with AdaBoost with a beta exponent of 0.6 and the training sample used for each tree is created by bagging a sample with size 90%

the size of training sample of the BDT classifier[1].

7.2.5 Features used for the BDT training

In order to achieve the best possible classification results when using any classifier, other than deep neural networks, the features (attributes or variables) used in the model construction are of critical importance. By selecting features in which the different classes occupy different regions in that phase space even the simplest classifiers can have excellent results. On the other hand if the selected features do not have any discriminating power the results provided even by the more complicated classifiers can be very poor. In order to extract variables with discriminating power a deep understanding of the classification of the problem in hand is needed. In this case the goal is to differentiate HEST from through-going track events created outside the detector (two classes problem). The former is considered as the signal class while the later as background. To this end, ten event based variables have been created aiming to identify the following characteristics:

1. High energy events (signal).
2. Events entering the instrumented volume, even though the reconstructed vertex was wrongly found inside the fiducial volume (background).
3. Event exhibiting shower like activity around the reconstructed vertex, which can be a strong indication of a hadronic shower from a neutrino interaction inside the detector (signal).

When describing these variables, the following terminology will be used:

- Strict time and spatial coincidence with the reconstructed track $\Rightarrow$ |Time residual| $\leq$ 10ns and vertical distance of the PMT hit to the reconstructed track $\leq$ 100m.
- Time coincidence with the reconstructed track $\Rightarrow$ |Time residual| $\leq$ 20ns.
- Loose time coincidence with the reconstructed track $\Rightarrow$ |Time residual| $\leq$ 30ns.
- Spatial coincidence with the reconstructed track $\Rightarrow$ Vertical distance of the PMT hit to the reconstructed track $\leq$ 111m. This value was chosen so that the path length of the photon $\leq$ 165m (3 absorption lengths).
- Border DOMs $\Rightarrow$ The two upper DOMs (17 and 18).
- Border Strings $\Rightarrow$ Strings: 105, 104, 103, 102, 101, 71, 100, 98, 96, 94, 92, 62, 93, 95, 97, 99, 91, 115, 114, 113, 112, 87, 86, 85, 111, 110, 109, 82, 81, 80, 108, 107, 106, 77 and 76. In Figure 7.6 a detector layout is displayed with all border strings (left) and upper DOMs (right) marked in red.

Variables used in the BDT:

1. The activity in border DOMs and border strings in strict time and spatial coincidence with the reconstructed track is investigated. If the first hit of the event, after the noise suppression, or the DOM with the largest cumulative ToT of the event is in a border DOM or string a boolean is set. This variable targets characteristic 2.

[1]The configuration of the BDT used:
TMVA::Types::kBDT, "BDT", "!H:!V:NTrees=1150:MinNodeSize=9.0%:MaxDepth=4:BoostType=AdaBoost:AdaBoostBeta=0.6:UseBaggedBoost:BaggedSampleFraction=0.9:SeparationType=GiniIndex:nCuts=17.

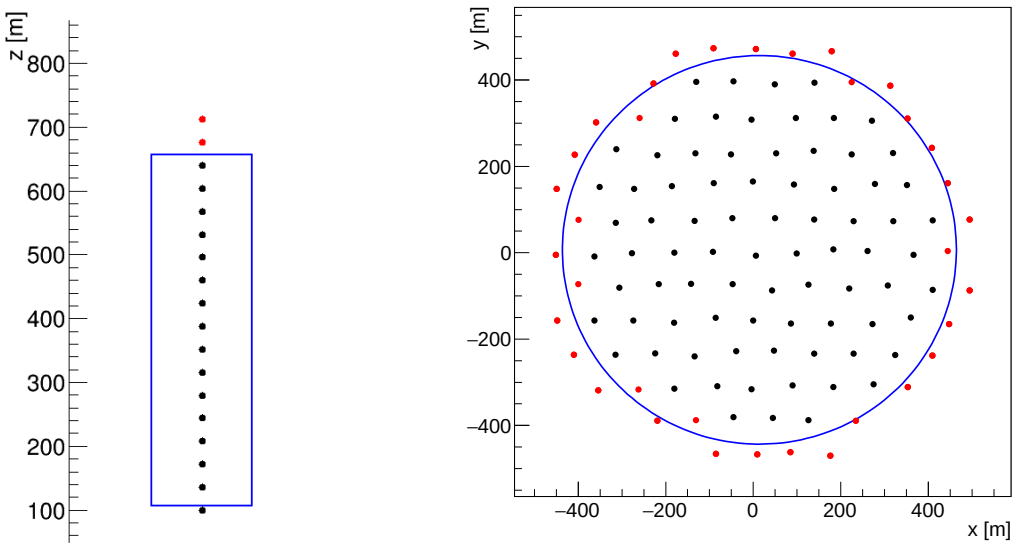

Figure 7.6: Left: Projection of an ARCA string on the Z axis. Right: Footprint of the ARCA detector. Border strings and DOMs are marked in red. The fiducial volume border is marked in blue.

2. Hits in coincidence with the reconstructed track produced by photons emitted behind the reconstructed vertex are considered. These are grouped in two categories: one group with those hits in strict time and with a spatial coincidence with the reconstructed track and a second group with those in loose time coincidence. If the emission point of a hit belonging to first group is close (up to 5m) to the emission point of another hit (belonging to either the first or the second group), that emission point is kept for investigation. In the case that the emission point farthest from the reconstructed vertex is not contained in the fiducial volume, a boolean is set. This variable targets characteristic 2.

3. A clustering of the emission points of the hits in time and spatial coincidence with the reconstructed track is performed in clusters with a minimum number of 3. A requirement of a minimum distance of 100m from one cluster to the next is used. A boolean is set if the emission point farthest to the vertex is contained inside the fiducial volume. This variable targets characteristic 2.

4. Number of DOMs with at least 3 hits. This variable targets characteristic 1.

5. Number of DOMs with at least 3 hits in time and spatial coincidence with the reconstructed track. This variable targets characteristic 1.

6. Number of DOMs with at least 3 hits with $|\mathrm{dt}| \leq 20$ns and $\mathrm{d}\phi \leq 60°$. This variable targets characteristic 1.

7. The cumulative ToT of the hits created by photons with emission points behind the reconstructed vertex in spatial coincidence and with |Time residual with respect to the reconstructed track| ≤ 250 ns. This variable targets characteristic 3.

8. Number of DOMs with at least 3 hits with |dt| $\leq$ 20ns, fulfilling the requirement to have been created by photons with emission points behind the reconstructed vertex in spatial coincidence and with |Time residual with respect to the reconstructed track| $\leq$ 250ns. This variable targets characteristic 3.

9. The length behind the reconstructed vertex along the reconstructed track has been divided in 2 halves up to the point it crosses the detector. The cumulative ToT is found of the hits created by photons with emission points in each half in spatial coincidence and with |Time residual with respect to the reconstructed track| $\leq$ 250 ns. The ratio of the cumulative ToT of the half closer to the edge of the detector over the cumulative ToT of the half closer to the reconstructed vertex is used. This variable targets characteristic 3.

10. Same approach as for variable 9 but instead of the ToT, the number of hits is used. This variable targets characteristic 3.

7.2.6 Training, testing and evaluation of the BDT

The BDT classifier is the last stage of MAMBA rejection and aims to discriminate between incoming track events to the ARCA detector and HEST neutrino events, from those events surviving the previous steps. "Well reconstructed" events having the reconstruction vertex inside the fiducial volume (Chapter 7.2.3) were used, to train/test the BDT.The signal sample comprised:

- ν_μ and $\overline{\nu_\mu}$ CC events $E_\nu \geq 30$ TeV having the true (MC) neutrino vertex in the fiducial volume.

while three different samples:

1. atmospheric muon events with $E_{bundle} \geq 10$ TeV,

2. atmospheric muon events with $E_{bundle} \geq 50$ TeV and

3. ν_μ and $\overline{\nu_\mu}$ CC events having the true (MC) neutrino vertex out of the instrumented volume of ARCA.

have been combined to form the background sample.

The BDT classifier has been trained/tested using part of the available MC simulated events. The rest of the events were left to be used for the evaluation of the trained BDT and in physics analyses. The training/testing signal sample comprised:

- 20% of the available events.

while the training/testing background sample consisted of:

- 2% of the available events from sample 1,

- 2.5% of the available events from sample 2 and

- 2% of the available events from sample 3.

The training/testing of the BDT was conducted using unweighted events. This way, all events are equally important to the training process. It should be noted that the number of events of each class used for the background sample was chosen in such a way to allow for each class to be evenly represented. The use of unweighted events was preferred in order to avoid biases coming from the large difference of the weight values. Using weighted events, the atmospheric muons are weighted to a predefined livetime (so all events of each atmospheric muon sample have the same weight) and the neutrino events are weighted with the weight produced by *GENHEN* convoluted with an astrophysical neutrino flux for that livetime (so a different weight is assigned to each neutrino event). So in this case the weights assigned to the neutrino background events are (orders of magnitude) lower than those assigned to atmospheric muons, indicating to the classifier that these events are less important. Nevertheless, as a test, the classifier has also been trained using such weighted events. The BDT trained with weighted events performed worse than that trained with unweighted events, so this training scheme was abandoned.

Before training the BDT, the values of the variables used have been "normalized", even though BDT classifiers are not sensitive to the relative differences of the values of the variables. Literally the variables were not normalized, since for the normalization the knowledge of the range of the variables is required beforehand. Since it is not possible to know an absolute maximum or minimum derived from all events, as only the training/testing sample was used, an approximating "normalization" procedure has been followed. For each variable from the training/testing sample the distribution of values has been plotted and a value close to the end of the distribution was chosen as maximum. A similar procedure was followed for the minimum value wherever this was required. In Figure 7.7 the distributions of these variables for the events in the training/testing sample after normalization are presented for the signal (blue) and for the background (red). A good separation power of signal and background is observed for most variables.

When building a model for classification an issue that should be addressed is whether the variables are correlated. *TMVA* provides the correlation matrices of the signal and background sample, shown in Figure 7.8. High correlation of variables 4 and 6 as well as 9 and 10 can be observed for both signal and background (which was expected from the construction of the variables). Highly correlated are also variables 4 (6) and 5 in the background sample and variables 7 and 8 in the signal sample. Highly correlated variables should be eliminated when classifiers like ANNs are used. When classifiers like ANNs are utilized the use of variables which are highly correlated should be avoided since for ANNs, models having highly correlated variables, usually perform worse than the same models after removing these variables. Although this is not an issue in the case of BDTs, various tests have been carried out in which the correlated variables have been removed one by one, yielding similar (just in one case) or worse (in the rest of the cases) results. Therefore, all ten variables described in section 7.2.5 have been used.

TMVA also provides a ranking of the variables based on separation power and importance. Separation is an indication of how much the signal and the background distributions are distinguished, while importance is derived by summing the separation gain squared each time the particular variable was used to split a decision node. In other words importance shows how useful each variable is to the classifier used while separation is an intrinsic quantity of each variable. The ranking of the variables is shown in Table 7.3 indicating that the four more important variables (5, 8, 7 and 3) address all 3 characteristics aimed when building these variables. Also the more important variables are not necessarily those with the highest separation ranking.

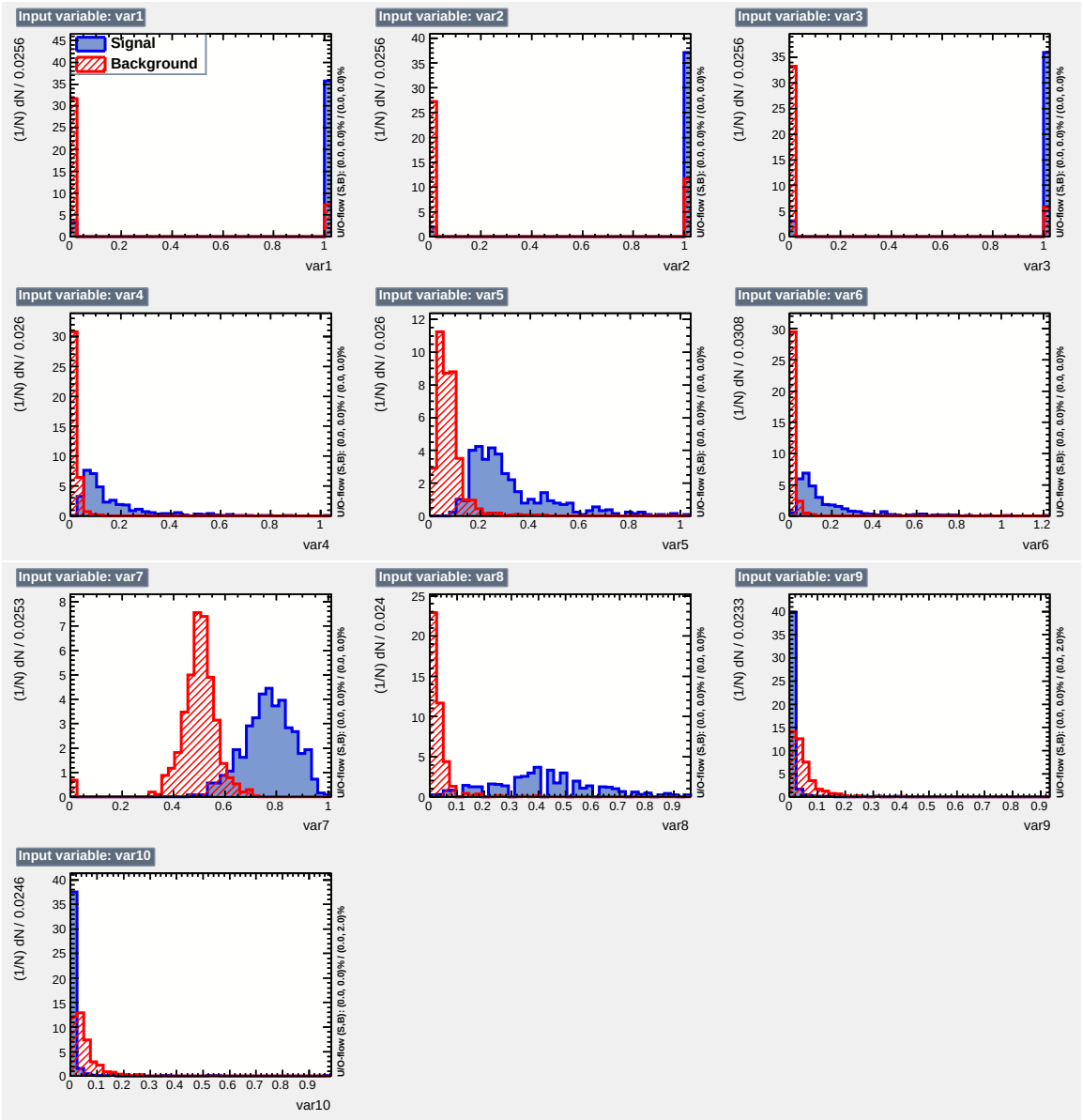

Figure 7.7: BDT input variables for the training/testing sample after normalization. The variables are presented in the same order as in Chapter 7.2.5

During the training/testing phase of the BDT, the events used were split into two subsamples, one used for the training and one for the testing. The splitting of the events has been done randomly with a ratio of 50% - 50% for the training and the testing samples (these fractions are the default values of the *TMVA* package). At the end of the training phase the test sample has been used to provide a check for overtraining. Even though BDTs consisting of trees with limited depth (from 2 to 4) do not generally suffer from overtraining, the overtraining check was performed in order to confirm that this is the case for the specific BDT configuration used in MAMBA rejection. In Figure 7.9 the distributions of the BDT output values of the training (area) and the test (points) samples are overlaid. In the case of overtraining, the performance of the training sample is expected to be superior to that of the test sample. This is not observed here indicating that this trained BDT classifier does

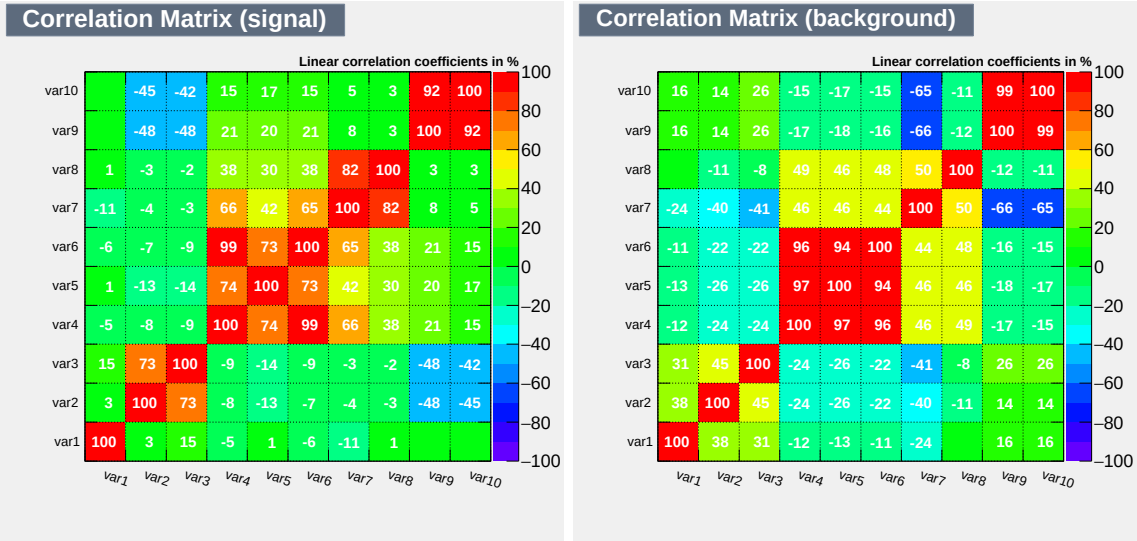

Figure 7.8: The correlation matrices for the signal (left) and the background (right) as provided by TMVA.

Variable	Ranking based on	
	Separation	Importance
var1	7	7
var2	8	5
var3	6	4
var4	4	8
var5	5	1
var6	3	6
var7	2	3
var8	1	2
var9	10	9
var10	9	10

Table 7.3: Ranking of the variables using Separation and Importance.

not suffer from overtraining. As can also be observed in Figure 7.9 the Kolmogorov-Smirnov test for both background and signal events is above the critical value of 0.01 reinforcing the conclusion that no overtraing is observed for the BDT configuration used.

Finally, the files not used for the training/testing procedure were utilized as an evaluation sample in order to establish that the performance of the BDT on this sample is similar to the performance on the training and testing samples. For this test the procedure described below was followed:

1. The efficiency for the training and test sample to identify signal events had been set to a specific value (80 %) and it was achieved by a BDT cut value of 0.51.

2. Events belonging to the rest of the production files that satisfy the quality and the reconstructed vertex containment requirements had been evaluated with the BDT. No MC information have been used.

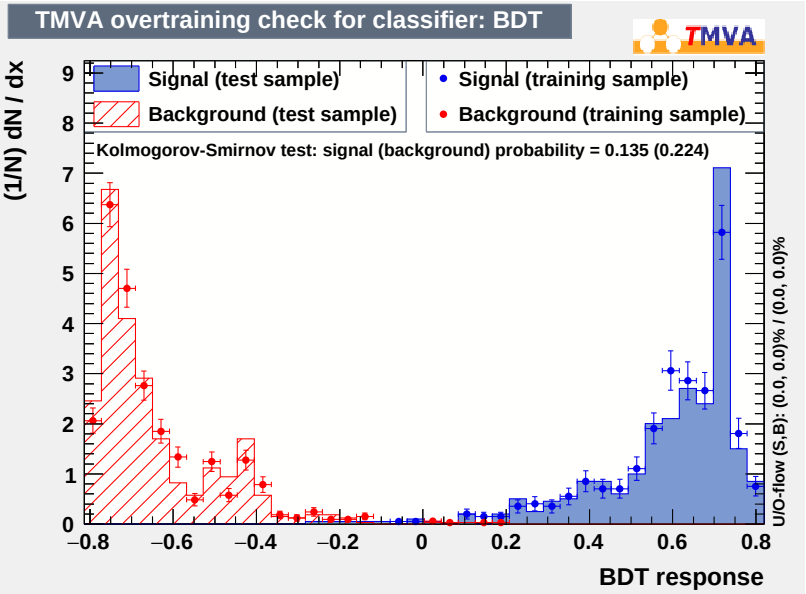

Figure 7.9: The overtraining check as provided by TMVA.

3. A cut on the BDT value $\geq$ was posed. All events fulfilling this condition were accepted for the final sample.

Figure 7.9 shows that for BDT values ≥ 0.51 no background events are found in the sample used to train the BDT. However the events used for the BDT training correspond to only 2.5% of the atmospheric muon events with $E_{bundle} \geq 50$ TeV and 2% of the atmospheric muon events with $E_{bundle} \geq 10$ TeV and of ν_μ and $\overline{\nu_\mu}$ CC events having the true (MC) neutrino vertex out of the fiducial volume. Thus it is expected that few background events will still remain after imposing the BDT cut.

The cut on the BDT value (of 0.51) led to an efficiency of 79.86% for the signal (where as signal the ν_μ and $\overline{\nu_\mu}$ CC events having the true (MC) neutrino vertex in the fiducial volume with $E_\nu \geq 30$ TeV are considered). The background events remaining were:

- 2 ν_μ or $\overline{\nu_\mu}$ CC events having the true (MC) neutrino vertex out of the fiducial volume, but close to the edge of it and well inside the volume of the detector.
- 1 atmospheric muon event with $E_{bundle} \geq 10$ TeV.
- 1 atmospheric muon event with $E_{bundle} \geq 50$ TeV.

The energy distribution of signal events (from the sample of events not used for training/testing) after the quality and the containment cuts (blue line) and of those events consequently surviving the BDT cut (red line) is shown in Figure 7.10. The efficiency of the BDT as a function of E_ν is also shown. At $E_\nu = 30$ TeV (indicated with a magenta vertical line) the efficiency is $\sim 40\%$ and it rises as the energy of the neutrino increases, reaching 80% at $E_\nu \sim 100$ TeV and 90% at $E_\nu \sim 500$ TeV.

The performance of the BDT on signal events belonging to the training and to the evaluation samples is quite similar, so it is clear that the BDT exhibits no overtraining. Finally the BDT is optimized for HE events and it also provides a very powerful rejection for background events.

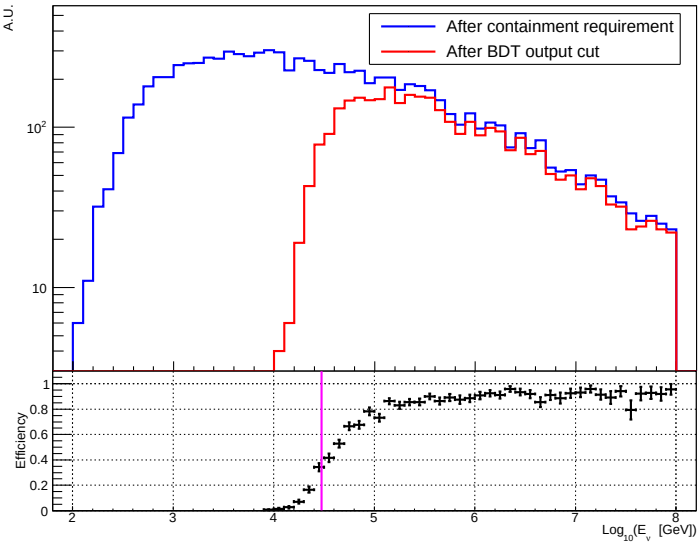

Figure 7.10: Energy distribution of signal events (ν_μ and $\overline{\nu_\mu}$ CC events having the true (MC) neutrino vertex in the fiducial volume) that survive the quality and the containment requirements (blue line) and also satisfy the BDT cut value 0.51 *(red line). The efficiency is also shown as a function of the energy for signal events. The magenta line indicates the* $E_\nu = 30$ *TeV energy threshold, which is the lowest energy required for an event to be considered as signal.*

7.3 Energy reconstruction

JEnergy, contained in the *JPP* package, is sued to estimates the energy of a track in the hit barycenter of the event. This implies that the energy at the reconstructed vertex is found after accounting for the energy losses the muon suffered traveling from the vertex to the hit barycenter. A correction needs to be applied to account for the dependence of the energy resolution on the detector's geometry (Figure 7.11). Such a correction has already been implemented [111] taking into account all track events for the track analysis.

A better approximation of the neutrino energy is obtained for contained events using *JEnergy* than of the muon energy as can be seen in Figure 7.11. This is expected since the light produced by the hadronic shower of the neutrino interaction is also detected, as the interaction vertex is located inside the instrumented volume. Nevertheless an additional correction is needed as can be seen by the slope of the energy resolution in Figure 7.11.

The accuracy of the energy reconstruction depends on the fraction of the muon energy that can be detected and on the length of the muon track inside (or close to) the instrumented volume. For this reason the events are categorized depending on: the estimated track length using the hit information and the potential length of the muon.

- Track length: The distance between the reconstructed vertex and the emission point of the farthest photon (Cherenkov hypothesis) along the reconstructed track (requiring hits with |Time residual| $\leq$ 30 ns and vertical distance of the PMT hit to the reconstructed track $\leq$ 111 m where the angle between the direction of the Cherenkov photon and the PMT direction is $\leq 90°$).

- Potential length: The distance between the reconstructed vertex and the emission

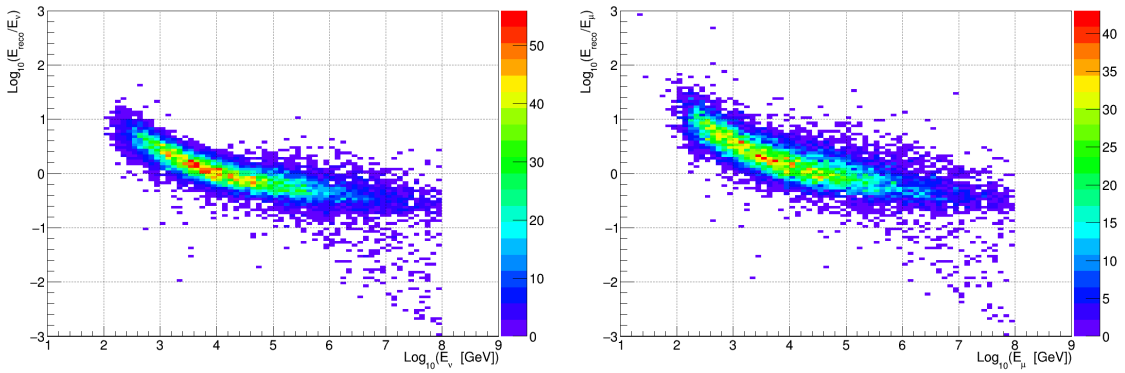

Figure 7.11: Difference between the logarithm of the reconstructed energy (taking into account the energy the muon looses from the reconstructed vertex to the hit barycenter) and the true energy with respect to the true energy. Left: for neutrinos, Right: for muons. Only events having both true (MC) and reconstructed vertex inside the fiducial volume are shown.

point of the most distant hypothetical photon to give a hit in spatial coincidence with the reconstructed track (hit in a DOM having a vertical distance from the reconstructed track $\leq$ 111 m). To find the emission point along the reconstructed track the coordinates of the center of each DOM are used for simplicity (and not those of each PMT).

For a reliable energy estimation events were required to have $\frac{length}{potential\ length} > 60\%$. The selected events were divided into the following four categories depending on the fraction of the energy deposited by the muon in the volume of the detector:

1. length $<$ 500 m and ratio $\frac{length}{potential\ length} < 1$
2. length $<$ 500 m and ratio $\frac{length}{potential\ length} \geq 1$
3. length $\geq$ 500 m and ratio $\frac{length}{potential\ length} < 1$ and
4. length $\geq$ 500 m and ratio $\frac{length}{potential\ length} \geq 1$

The ratio $\frac{length}{potential\ length}$ can get values slightly larger than 1 as the potential length is found using the center of the DOM and not each PMT.

The events used as training and testing sample of the BDT, which comprise 20% of all the ν_μ and $\overline{\nu_\mu}$ CC events, have been used to estimate the correction for each sub-sample and then the correction was applied to the rest 80% of the ν_μ and $\overline{\nu_\mu}$ CC events. The reconstructed energy taking into account the energy losses of the muon from the reconstructed vertex to the hit barycenter has been associated to the true (MC) neutrino energy by a profile using for each energy bin the mean of the reconstructed energy. The profile was fitted with polynomial functions which were utilized as the energy correction. In Figures 7.12, 7.13, 7.14 and 7.15 the estimated correction (using 20% of ν_μ and $\overline{\nu_\mu}$ events) and the resulted distribution after applying the correction to the rest of the production are shown. For events having energies outside the range of the fitted function no correction has been applied, so the value given by *JEnergy* taking into account the energy losses of the muon from the reconstructed vertex to the hit barycenter has been used.

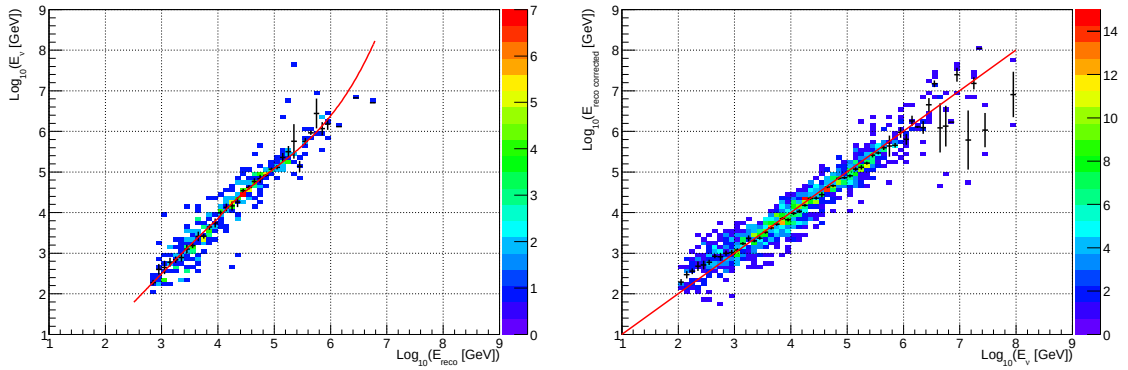

Figure 7.12: Sub-sample 1. Left: True (MC) neutrino energy with respect to the reconstructed energy taking into account the muon energy losses from the reconstructed vertex to the hit barycenter. The crosses represent the mean of each bin with 1σ error bars using 20% of the MC sample. The fitted polynomial function is shown with a red line. Right: The corrected reconstructed energy with respect to the true (MC) energy for the rest 80% of the MC sample. The crosses represent the mean of each bin with 1σ error bars. The diagonal line is shown in red.

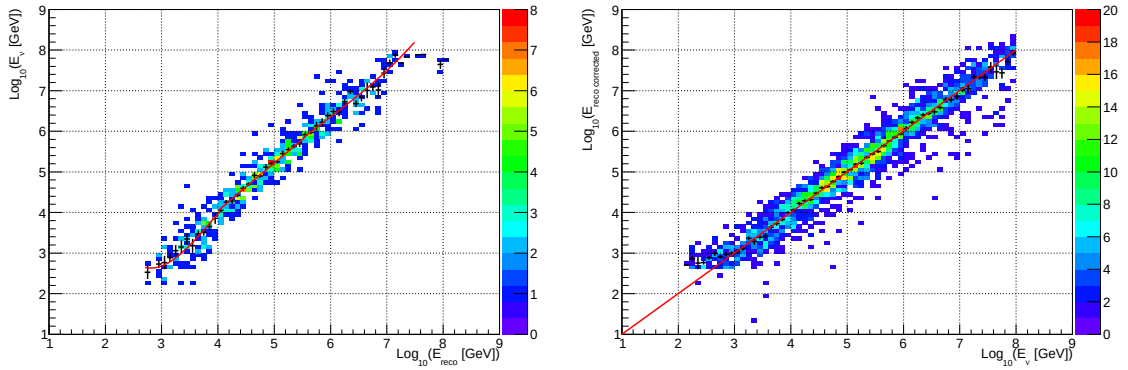

Figure 7.13: Sub-sample 2. As per Figure 7.12.

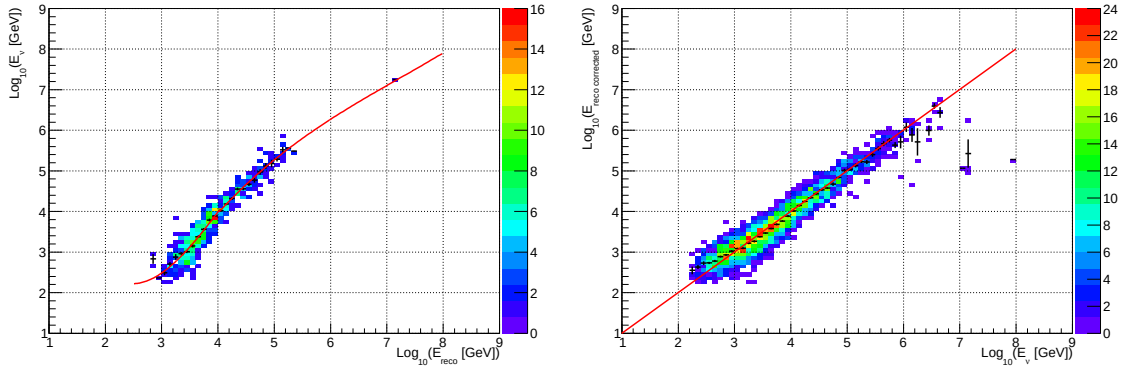

Figure 7.14: Sub-sample 3. As per Figure 7.12.

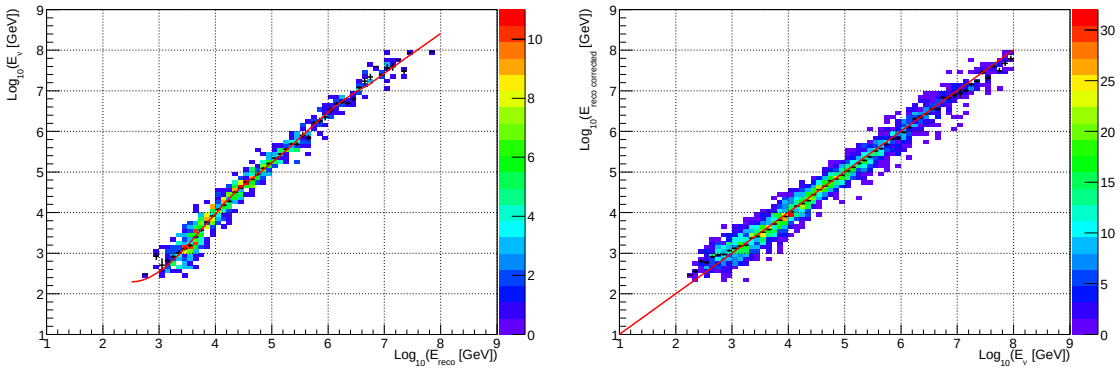

Figure 7.15: Sub-sample 4. As per Figure 7.12.

In Figure 7.16 the difference between the logarithm of corrected reconstructed energy and true neutrino energy with respect to the true neutrino energy is presented for all the events belonging to the sample of ν_μ and $\overline{\nu_\mu}$ events which has not been used to estimate the correction. In Figure 7.17 the difference between the logarithm of the corrected reconstructed energy and true neutrino energy for events with $E_\nu \geq 10$ TeV (left) and $E_\nu \geq 100$ TeV (right) is presented. For events with $E_\nu \geq 10$ TeV the energy resolution obtained using the corrected energy is almost Gaussian peaking at a value very close to 0, as shown in Figure 7.17 left. For events with lower energies no effort has been made to find an appropriate function to correct the reconstructed energy since the analysis focuses on HE events. The distributions shown in Figure 7.17 indicate a slight underestimation of the neutrino energy. The energy resolution for events with $E_\nu \geq 10$ TeV is 21% and for events with $E_\nu \geq 100$ TeV is 22%.

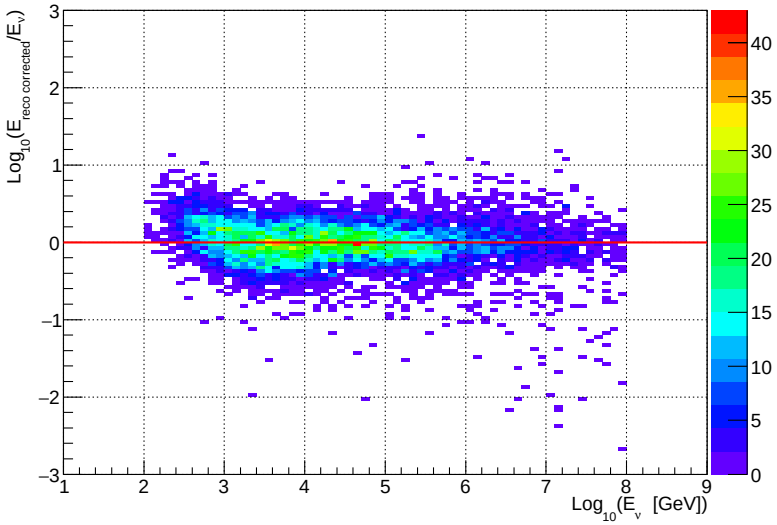

Figure 7.16: Difference between the logarithm of corrected reconstructed energy and true neutrino energy with respect to the true energy for all ν_μ and $\overline{\nu_\mu}$ events which have not been used to estimate the correction.

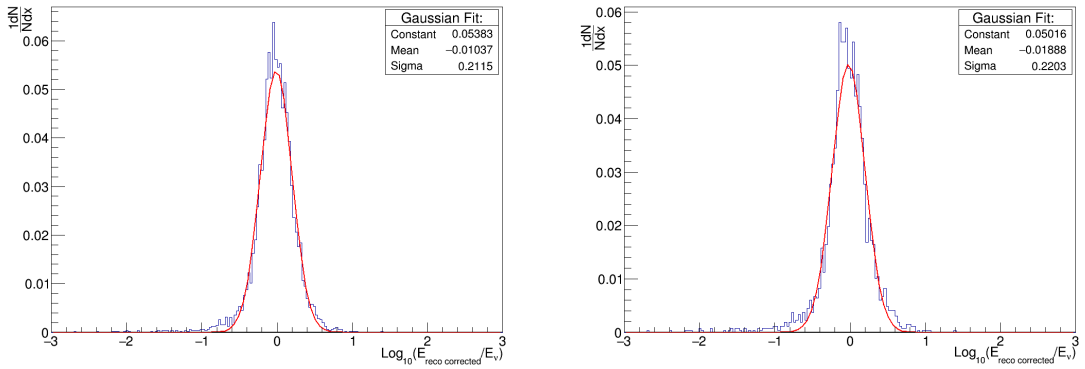

Figure 7.17: Difference between the logarithm of corrected reconstructed energy and true neutrino energy for all events not used to estimate the correction. The Y axis corresponds to $\frac{1}{N}\frac{dN}{dx}$ *where* $x = log_{10}(E_{reco\,corrected}/E_\nu)$*. Left: Events with* $E_\nu \geq 10$ *TeV. Right: Events with* $E_\nu \geq 100$ *TeV. Red Lines: Gaussian fits.*

7.4 ARCA sensitivity and discovery potential using HEST

7.4.1 General

A major objective of the ARCA telescope, as stated in the Letter Of Intent 2.0 for KM3NeT [69], is the detection of a diffuse flux of astrophysical neutrinos corresponding to the signal reported by IceCube. As currently ARCA is under construction the expected sensitivity of the detector to an astrophysical neutrino flux and the time needed to make a discovery of that flux are estimated using Monte Carlo simulations. For this study the Model Rejection Potential (hereafter MRP) [116] method is used for the sensitivity, while for the discovery potential the Model Discovery Potential (hereafter MDP) [117] method is employed.

MRP and MDP are statistical methods commonly employed for searches of a small signal within background events as in the case for an astrophysical neutrino signal. They can be implemented with two approaches:

- the binned approach. Cuts are posed on both the expected (by MC simulations) signal and background distributions in order to select the final sample of events.
- the unbinned approach. The whole signal and background distributions are used to exclude the "no signal" hypothesis.

For this study the binned approach is adopted.

7.4.2 Sensitivity

The sensitivity of the ARCA detector to an astrophysical neutrino flux is derived by the MRP method. With this method upper limits to a theoretical flux can be posed with a certain confidence level. Starting with the expected number of background events (n_b) the upper limit at a predefined confidence level (here 90%) as found in [118], is calculated for all possible number of observed events (n_{obs}), assuming that no signal events are detected. These upper limits (μ_{90}) are averaged weighted with the Poisson probability f(k=n_b; λ=n_{obs}) to obtain the *average upper limit* $\overline{\mu}_{C.L.}$ (here 90% confidence level has been used). The Model Rejection Factor (MRF) is the ratio of the average upper limit over the number

of signal events (n_s) expected by a theoretical flux. The average upper limit on the flux obtained at that confidence level is found by:

$$\Phi_{C.L.} = \Phi_{theoretical} \cdot \frac{\overline{\mu}_{C.L.}}{n_s} \tag{7.1}$$

Any flux $\Phi > \Phi_{C.L.}$ is excluded with a C.L. confidence level. In case the MRF ($\frac{\overline{\mu}_{C.L.}}{n_s}$) < 1 , the detector is considered to be "sensitive" to that theoretical flux. In Figure 7.18 the average upper limit with a 90% confidence level is shown (in green) as a function of the number of background events. It can be observed that $\overline{\mu}_{90}$ increases as n_b increases but sub-proportionally when the number of expected background events is larger than 5. Since the number of expected signal and background events increases proportionally with the observation time, as the observation time increases the MRF decreases and therefore lower upper limits can be achieved. This can be used to find the expected time of observation needed for the detector to become sensitive to a theoretical flux.

When using the MRP method the number of expected signal and background events are represented as a function of some observable variables (i.e. the reconstructed energy), then cuts are posed on these variables (same cuts for signal and background) and the MRF is calculated by the number of signal and background events surviving these cuts. The set of cuts producing the lowest MRF are used to determine whether the experiment is expected to be sensitive to the theoretical flux, or to derive upper limits. Here in order to find the best possible Φ_{90} for ARCA using HEST events, the number of expected signal and background events are found as a function of the corrected reconstructed neutrino energy (Chapter 7.3) and the BDT output.

7.4.3 Discovery potential

In order to find the discovery potential for an astrophysical neutrino flux the MDP method is employed. MC simulations are used to reject the background only hypothesis at a required confidence level with a certain probability. Starting with the number of expected background events (n_b), a critical number of detected events (n_{crit}) is found. For this n_{crit} the probability of being detected only due to background fluctuations (no signal hypothesis) is less or equal to a predefined value. This value is the area below the tail of a Gaussian curve beyond a certain number of standard deviations which represent the confidence level. For example for a 5σ confidence level n_{crit} is calculated to satisfy the Poisson probability:

$$P(n_{crit}|n_b) \leq a \tag{7.2}$$

where $a = 5.73 \cdot 10^{-7}$ (5σ area). The minimum number of signal events or least detectable signal ($n_{l.d.s.}$) is calculated that satisfies the condition that at least n_{crit} events can be detected due to the expected $n_b + n_{l.d.s.}$ with a certain probability:

$$P(n_{crit}|n_b + n_{l.d.s.}) = Pr \tag{7.3}$$

So given the expected number of background events n_b, if the expected number of signal events is at least $n_{l.d.s.}$, an $a\ \sigma$ discovery is expected in a Pr fraction of the experiments conducted. Using the ratio of the least detectable signal over the expected number of signal events (n_s) derived by a theoretical flux $\Phi_{theoretical}$ (model discovery potential), the flux by which an $a\ \sigma$ discovery is expected in a Pr fraction of the experiments conducted (Φ_{disc}) is derived by:

$$\Phi_{disc} = \Phi_{theoretical} \cdot \frac{n_{l.d.s.}}{n_s} \tag{7.4}$$

In Figure 7.18 the $n_{l.d.s.}$ is shown as a function of the number of background events for a 5σ discovery with probability 90% (black) and 50% (red) as well as for a 3σ discovery with probability 50% (blue). It can be observed that in all cases after a certain number of expected background events the distribution of the $n_{l.d.s.}$ becomes sub-proportional (a diagonal magenta dashed line is added to guide the eye). From that value on, any increase in the observation time (proportional increase to the n_b and n_s) will lead to a decrease and the fraction $\frac{n_{l.d.s.}}{n_s}$, so as the observation time increases, discovery of fainter fluxes is expected. As with the MRP method, MDP is used to find optimal cuts on observable variables, by minimizing $\frac{n_{l.d.s.}}{n_s}$ (for a given observation time) in order to determine whether the experiment is expected make a discovery of the theoretical flux, or to derive upper limits. Once more the number of expected signal and background events are found as a function of the reconstructed neutrino energy (Chapter 7.3) and the BDT output.

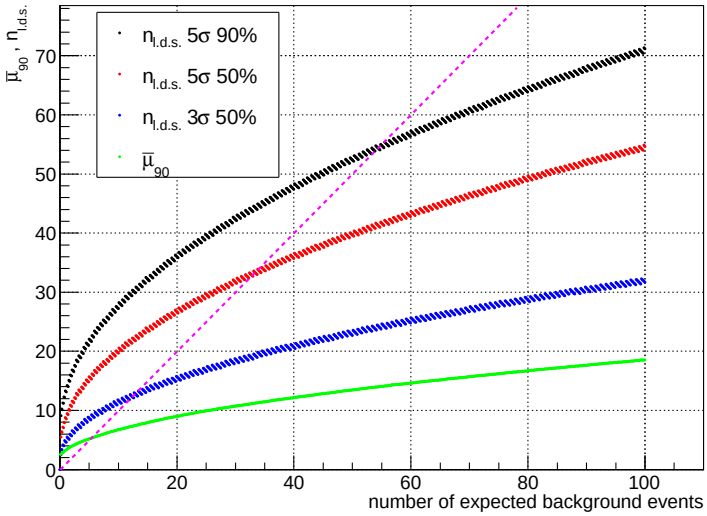

Figure 7.18: Average upper limit for a 90% confidence level $\bar{\mu}_{90}$ (green) and $\mu_{l.d.s.}$ for 3σ in 50% of the experiments (blue), 5σ in 50% of the experiments (red) and for 5σ in 90% of the experiments (black). The diagonal (magenta dashed line) is also shown.

7.4.4 Using HEST events to estimate the sensitivity and the discovery potential of ARCA

The astrophysical flux to which the ARCA detector is sensitive and the discovery potential of ARCA for an astrophysical neutrino flux were calculated using the MAMBA rejection tool to select HEST events. As high energy astrophysical neutrino flux, the benchmark KM3NeT flux without cutoff [119] was adopted. This is an unbroken power law

$$\Phi_{astro} = \Phi_0 \cdot (E/100TeV)^{-\gamma} \tag{7.5}$$

with $\Phi_0 = 2.3 \cdot 10^{-18}\mathrm{GeV}^{-1}\mathrm{cm}^{-2}\mathrm{s}^{-1}\mathrm{sr}^{-1}$ and $\gamma = 2.5$ for each neutrino flavor. This high energy astrophysical neutrino flux is quite similar to the one reported by the IceCube Collaboration [36]. For the atmospheric neutrino fluxes, the Honda 2016 model with the knee correction [23] was used for the conventional component and the Enberg 2008 model [24] was used for the prompt component (this model does not take into account the findings

from IceCube [25, 57], so it probably largely overestimates the prompt component of the atmospheric neutrino fluxes).

Events that satisfy the quality and the reconstructed vertex containment requirements were selected for this analysis. The selected events were evaluated with the BDT and a BDT output value was assigned to each event. In Figure 7.19 left, the distributions of the BDT output values are shown for all ν_μ and $\overline{\nu_\mu}$ CC events interacting inside the fiducial volume with a dashed line and for events with $E_\nu \geq 30$ TeV with a solid line. In Figure 7.19 right the distribution of the BDT output values for atmospheric muons, ν_μ and $\overline{\nu_\mu}$ CC interacting inside and out of the detector volume, NC as well as ν_e and $\overline{\nu_e}$ CC and NC events are shown. All neutrino events have been weighted with the astrophysical flux of equation 7.5 assuming the full ARCA detector (2 building blocks) and an observation time of 1 year. The atmospheric muon events have also been properly weighted to the full ARCA detector and the same observation time. It can be observed that by choosing a high cut value on the BDT output a high purity sample of HEST events can be selected.

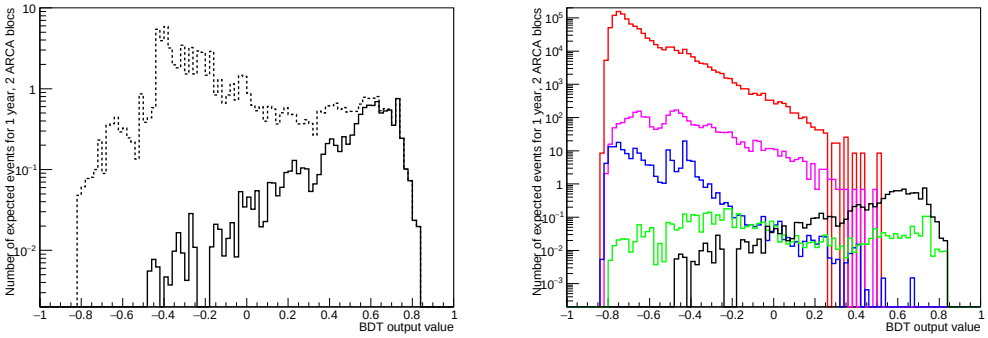

Figure 7.19: Left: Distributions of the BDT output values for all ν_μ and $\overline{\nu_\mu}$ CC events interacting inside the fiducial volume (dashed line) and for events with $E_\nu \geq 30$ TeV (solid line). Right: Distributions of the BDT output value for ν_μ and $\overline{\nu_\mu}$ CC events interacting inside the fiducial volume having $E_\nu \geq 30$ TeV (black), ν_μ and $\overline{\nu_\mu}$ CC events interacting outside the fiducial volume (blue), all NC as well as ν_e and $\overline{\nu_e}$ CC events (green), atmospheric muon events with $E_{bundle} \geq 10$ TeV (red) and atmospheric muon events with $E_{bundle} \geq 50$ TeV (magenta). Since the BDT output value is used to select HEST events and reject the incoming track events to ARCA, atmospheric neutrino events are not included in the plot.

The distributions in Figure 7.19 are illustrated as a visual representation of the effectiveness of the BDT used in the final setp of the MAMBA rejection. The distribution of the events considered as signal for the BDT (ν_μ and $\overline{\nu_\mu}$ CC events interacting inside the fiducial volume having $E_\nu \geq 30$ TeV) peaks at high BDT output values. On the other hand the distributions of those events considered as background (ν_μ and $\overline{\nu_\mu}$ CC events interacting out of the fiducial volume, as well as atmospheric muon events with $E_{bundle} \geq 10$ TeV and $E_{bundle} \geq 50$ TeV) peak at low BDT output values. Finally the NC events (which do not have a similar signature to either signal or background events) have a relatively flat distribution. In Figure 7.20 the distribution of the BDT output values for all neutrino events (ν_μ, $\overline{\nu_\mu}$, ν_e, $\overline{\nu_e}$, ν_τ and $\overline{\nu_\tau}$ CC and NC) weighted with the astrophysical flux (equation 7.5) and for all atmospheric muon events weighted to the same livetime are shown.

To find the sensitivity and the discovery potential of ARCA to the astrophysical flux of eq 7.5, all neutrino events weighted with the astrophysical flux are considered as signal events (expected astrophysical neutrino events). The ν_μ, $\overline{\nu_\mu}$, ν_e and $\overline{\nu_e}$ events, weighted with

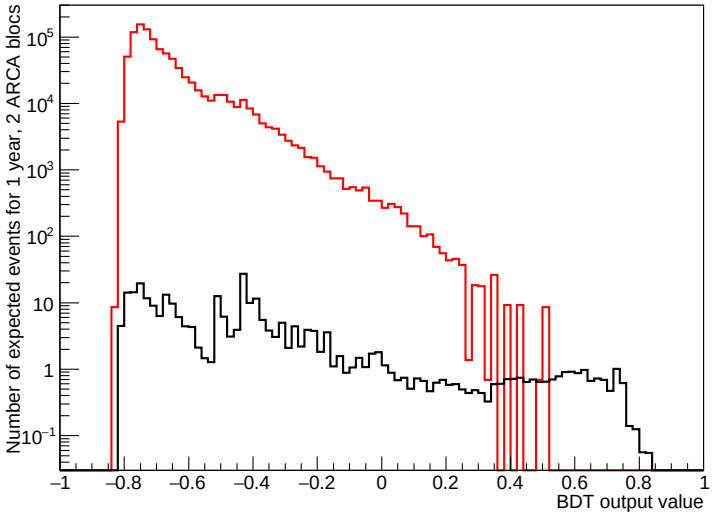

Figure 7.20: Number of events expected in 1 *year for* 2 *ARCA blocks Black: all astrophysical neutrino events, Red: atmospheric muon event from both samples with* $E_{bundle} \geq 10$ *and* $E_{bundle} \geq 50$ *TeV.*

the atmospheric neutrino fluxes and the atmospheric muon events (with $E_{bundle} \geq 10$ TeV and $E_{bundle} \geq 50$ TeV) comprise the sample of background events. At this point it should be stressed that what is considered as signal / background to a search for an astrophysical neutrino flux should not be confused to what was used as signal and background for the BTD tool used to select HEST events. The BDT was trained to select HEST, so any HEST event is considered as signal for the BDT (i.e. an atmospheric neutrino interacting inside the volume of ARCA). For the search for an astrophysical neutrino flux any astrophysical neutrino is considered as signal (i.e. an astrophysical neutrino event interacting outside the ARCA detector).

Using the MRP and the MDP methods, cuts on the reconstructed muon energy (Chapter 7.3) and the output of the BDT (Chapter 7.2.6) were found. The binning used for the search of the optimal cuts was 0.1 in the logarithm of the reconstructed energy and 0.01 in the BDT output value. Both these techniques, sometimes may find as optimal cuts values right after the last event of the background distribution. In this case, as atmospheric muon background events have much larger weights than neutrino events (as can be observed in Figure 7.20), this effect might lead to artifacts. In order to avoid such effects that might bias the results, the BDT output distribution has been fitted and the background from atmospheric muons was calculated also by using this fitted function. First the optimal cuts on the BDT output and the reconstructed energy have been derived using only the simulated background. Even though in all cases the optimal energy cut has been the same $E_{reco} \geq 10^{5.0}$ GeV, the optimal cut in the BDT output value ranged from 0.29 to 0.35 (different BDT cut values have been obtained from the MRP method and from the MDP for different observation times and for different confidence intervals). Then the BDT output value distribution for events satisfying the requirement $E_{reco} \geq 10^{5.0}$ GeV from both atmospheric muon samples have been plotted (Figure 7.21). The last event from the sample with $E_{bundle} \geq 10$ TeV satisfying $E_{reco} \geq 10^{5.0}$ GeV has a BDT output value ~ 0.2, as shown in Figure 7.21 (in black), while the cuts derived by the MRP and the MDP minimization

methods were ≥ 0.29. So for this sample no such effect was observed. Contrary, the last event of the sample with $E_{bundle} \geq 50$ TeV satisfying $E_{reco} \geq 10^{5.0}$ GeV was found in the bin [0.28, 0.29) (Figure 7.21, in red), so for this sample the BDT output distribution has been fitted.

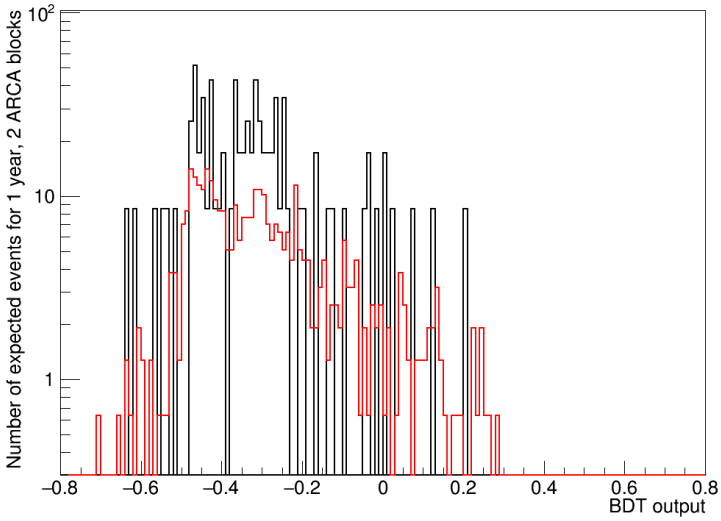

Figure 7.21: Distributions of the BDT output values for atmospheric muons with $E_{bundle} \geq 10$ TeV in black and for atmospheric muons with $E_{bundle} \geq 50$ TeV satisfying $E_{reco} \geq 10^{5.0}$ GeV.

Since both the MRP and the MDP methods depend on the total number of background events, the distribution of the cumulative number of background events was fitted. In order to have a statistical sample adequate for a reliable fit and also allow the possibility of finding a lower value of the cut on the reconstructed energy after adding background events, the distribution of the BDT output values for those events satisfying $E_{reco} \geq 10^{4.7}$ GeV and fitted with an exponential function convoluted with a quadratic polynomial. Since this method has been employed to approximate the tail of the BDT output distribution, the fit was performed in the range of the BDT output values [0.15, 0.6]. The distribution of the cumulative number of background events satisfying $E_{reco} \geq 10^{4.7}$ GeV and the fitted function (equation 7.6) are shown in Figure 7.22 left. The distribution of the cumulative number of background events satisfying $E_{reco} \geq 10^{5.0}$ GeV, which is the energy cut given by the MDP method for both the 3σ and 5σ confidence levels is also displayed. In Figure 7.22 right, the distributions of the number of background events satisfying $E_{reco} \geq 10^{4.7}$ GeV, $E_{reco} \geq 10^{5.0}$ GeV and that derived from 7.6, are presented. In order to estimate the number of atmospheric muon events with $E_{bundle} \geq 50$ TeV used in both the MRP and the MDP methods for each BDT output value, both number of events surviving that BDT output cut using the sample of simulated events and the number derived by the fitted function (equation 7.6) for that BDT output value have been evaluated. For a conservative estimate the maximum value of the two approaches was considered for the background calculation.

$$\begin{aligned} &\text{cumulative}\, N_{\text{events}} = (-8.6 \cdot x^2 + 3.6 \cdot x - 0.008) \cdot \exp(5.34 - 9.94 \cdot x) \\ &\text{where x is the BDT output value} \end{aligned} \tag{7.6}$$

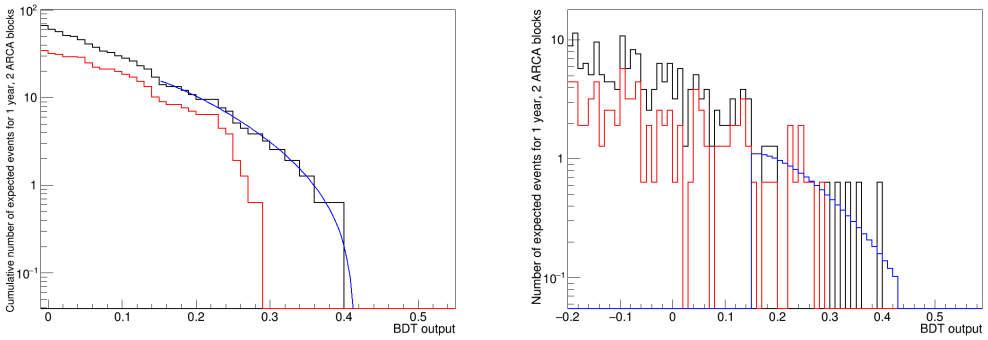

Figure 7.22: Left: Distributions of the BDT output values for atmospheric muons with $E_{bundle} \geq 50$ TeV satisfying $E_{reco} \geq 10^{5.0}$ GeV in red and $E_{reco} \geq 10^{4.7}$ GeV in black. The fitted function of the latter is shown in blue. Right: Distributions of the number of background events satisfying $E_{reco} \geq 10^{5.0}$ GeV in red and $E_{reco} \geq 10^{4.7}$ GeV in black. The number of background events estimated using the function derived from the fitting of the cumulative distribution is overlaid.

As can be observed from Figure 7.22 (right and left) the estimation of the background using equation 7.6 (found by the cumulative distribution of the events satisfying $E_{reco} \geq 10^{4.7}$ GeV) overestimates the number of expected events satisfying $E_{reco} \geq 10^{5.0}$ GeV. As an example, equation 7.6 results to ~ 3.6 events for a BDT value of 0.29 above which no simulated events exist. Nevertheless using this approach to estimate the number of atmospheric muon background events assures that the results obtained do not suffer from bias induced by fluctuations affecting the tail of the background distribution.

The minimization of the MRF for 1 year of observation using 2 ARCA building blocs was achieved for a cut on the BDT output ≥ 0.41 and for $E_{reco} \geq 10^{4.8}$ GeV, leading to an MRF=1.17. This means that for 1 year observations with 2 ARCA building blocks a high energy astrophysical neutrino flux (equation 7.5) with normalization factor $\Phi_0 \geq 2.69$ $GeV^{-1}cm^{-2}s^{-1}sr^{-1}$ can be excluded with a 90% CL. The MRF minimization (MRF = 1.00) was achieved for a cut on the BDT output ≥ 0.41 and on $E_{reco} \geq 10^{4.8}$ GeV, showing that ARCA is expected to be sensitive to the astrophysical flux after an observation time of 1.3 years (2 ARCA building blocks). The number of expected signal and background events for each type of events is shown in Table A.1 in Appendix A.

The fraction of events correctly identified as track events is 92% for the signal and 99% for the background (Table A.1). From the total ~ 0.5 ν_τ CC $\rightarrow \mu$ and $\overline{\nu_\tau}$ CC $\rightarrow \mu$ expected events, more than 99% were double bang events (with both vertices contained inside the fiducial volume) and less than 0.2% had neither the neutrino nor the tau decay vertex inside the fiducial volume. By applying the cuts given by the minimization of the MRF all atmospheric muons have been eliminated, so the number of expected atmospheric muon background events (0.08 events) was found by the fitted function. In Table 7.4 the cuts found by the minimization of the MRF, the number of expected signal and background events and the percentage of correctly identified HEST events are summarized.

The discovery potential for ARCA (2 building blocks) using only HEST was also evaluated. The ratio of the discovery flux normalization factor over Φ_0 for both 3 and 5σ with 50% probability with respect to the observation time are shown in Figure 7.23. Using the HEST sample alone, a 3 and a 5σ discovery can be reached in approximately 3.2 and 8.7 years respectively. In Table 7.5 the cuts on the BDT value and on E_{reco}, the number of

Sensitive to Φ_{astro}	BDT cut	E_{reco} cut	signal events	HEST	background events	HEST
1.3 years	0.41	$10^{4.8}$ GeV	7.80	92%	14.48	99 %

Table 7.4: BDT cuts and number of expected events given by the minimization of MRF for a sensitivity with 90% CL for 2 ARCA blocks. The percentage of events correctly identified as HEST is also given.

signal and background events and the percentage of correctly identified as HEST for 3.2 and 8.7 years, respectively, are presented. In the case of 3σ with 50% probability no atmospheric muon event survived the cuts given by the minimization of MDP, so the number of events (0.64) was found by the fitted function. In the case of 5σ with 50% probability no atmospheric muon event survived the cuts given by the minimization of MDP and the fitted function also yielded no events for the BDT value 0.43. The number of expected signal and background events for each type, for both 3σ and 5σ with 50% probability is shown in Table A.2 in Appendix A. The ratio of the number of events surviving each cut over the number of triggered events are shown in Figure 7.24 for truly contained ν_μ and $\overline{\nu_\mu}$ CC with respect to the true E_ν as well as for atmospheric muon events with $E_{bundle} \geq 50$ TeV with respect to the true E_{bundle}. Also, the expected number of truly contained signal ν_μ and $\overline{\nu_\mu}$ CC events surviving each cut for a livetime of 8.7 years is shown in Figure 7.25 with respect to the true E_ν.

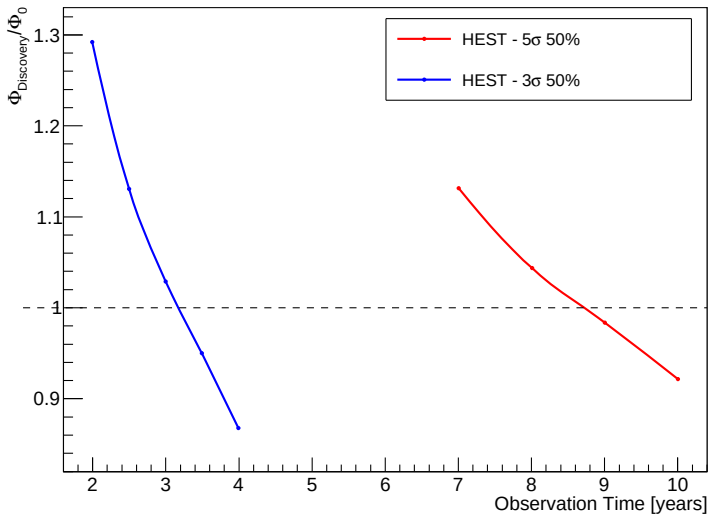

Figure 7.23: Ratio of the discovery flux normalization factor over Φ_0 for 3σ (blue line) and 5σ (red line) with 50% probability, with respect to the observation time in years for 2 ARCA blocks.

Discovery	BDT cut	E_{reco} cut	signal events	HEST	background events	HEST
3σ (3.2 years)	0.40	10^5 GeV	13.62	91%	16.17	95 %
5σ (8.7 years)	0.43	10^5 GeV	36.32	91%	41.33	99 %

Table 7.5: BDT cuts and number of expected events given by the minimization of MDP for a 3 and 5σ discovery. The percentage of events correctly identified as HEST is also given.

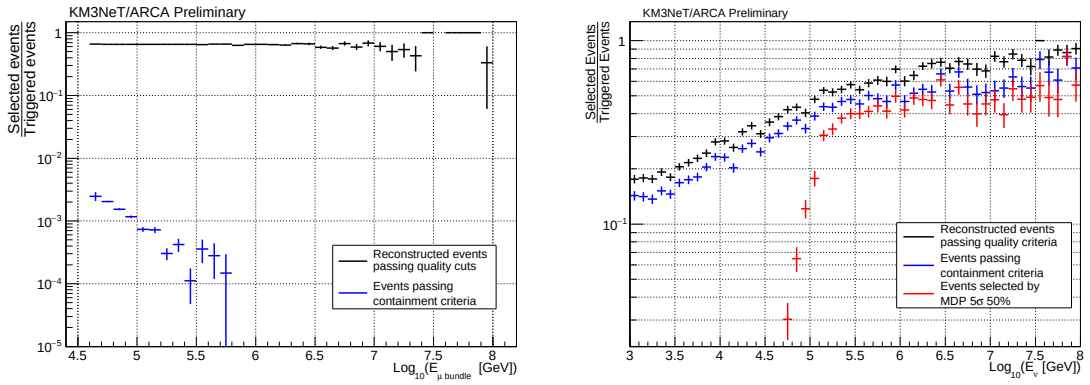

Figure 7.24: Ratios of the number of events surviving each cut over the number of triggered events. Left: Atmospheric muon events with $E_{bundle} \geq 50$ TeV with respect to the E_{bundle}. Right: ν_μ and $\overline{\nu_\mu}$ CC events interacting inside the volume of ARCA with respect to the true E_ν.

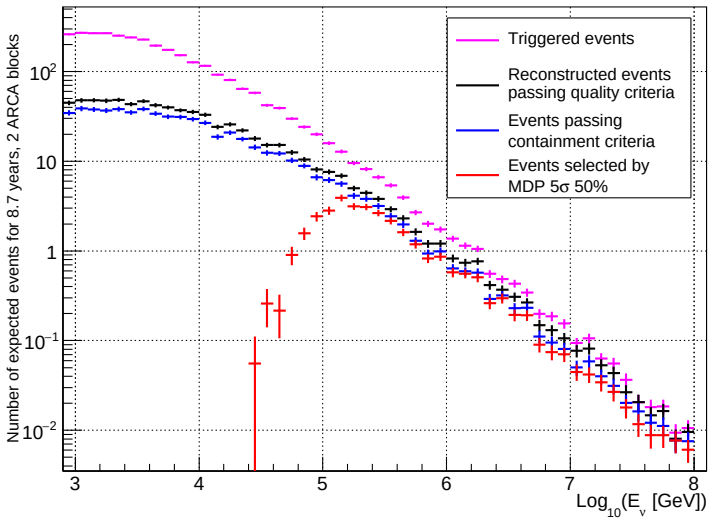

Figure 7.25: Expected number of signal ν_μ and $\overline{\nu_\mu}$ CC events interacting inside the volume of ARCA for a livetime of 8.7 years with respect to the true E_ν.

7.5 Exploring the self-veto effect

7.5.1 General

An improvement to both sensitivity and discovery potential is expected when these atmospheric neutrinos reaching the detector from above which are accompanied by muons created in the same atmospheric shower can be identified as background events. In the case that the atmospheric muons entering the detector have energies above a few TeV they are expected to be detected and rejected by the MAMBA rejection. In order to study this effect, the background sample of events 3 (Chapter 7.1) simulated using the fifth *CORSIKA* production (where *SIBYLL* 2.3 was chosen as high energy interaction model and the option **CHRAMed** was activated, as described in Chapter 6.3) has been used. For this study atmospheric neutrino events with a true (MC) zenith angle $\leq 87°$ from the *CORSIKA* production and events from the standard neutrino production (first production mentioned in Chapter 7.1) for the rest of the sky (zenith angle $> 87°$) have been used. All *CORSIKA* neutrino events have been used irrespective of whether the atmospheric neutrino was accompanied by muons. Also both samples of atmospheric muons have been used and the number of background events was estimated as in the previous section (using both the number of events surviving the BDT output cut and the fitted function for the sample of atmospheric muons with $E_{bundle} \geq 50$ TeV).

7.5.2 Using *CORSIKA* for the atmospheric neutrino background

The energy spectra of *CORSIKA* events after applying the appropriate weights and of the neutrino events weighted accordingly for the atmospheric neutrino fluxes are similar but not the same. In Figure 7.26 the rates of ν_μ events interacting inside the fiducial volume for 1 ARCA block for a livetime of 1 year are shown as an example. The differences observed are due to the different simulation chains and the different assumptions used for the generation of each type of events. Also due to the fact that the *CORSIKA* sample has much lower statistics for high energy neutrinos leading to few events having large weights, compared to the neutrino production where statistics allows lower weights (which is apparent for $E_\nu \geq 10^5$ GeV by the statistical fluctuations). As already detailed in Chapter 6, in *CORSIKA* simulations differences in the final neutrino spectrum are observed when using different inputs in the simulation (like High Energy Interaction Models, Atmospheric models or CR models) consequently the differences observed here were expected.

In order to have compatible results to be used for the sensitivity and the discovery potential calculation, extra weights have been applied to the events of the *CORSIKA* production so that the weighted atmospheric neutrino fluxes match each other. The events have been divided into 8 categories (ν_μ / $\overline{\nu_\mu}$, true (MC) neutrino interaction vertex in / out of the fiducial volume , conventional (Honda flux) / prompt (Enberg flux)) and extra weights have been derived for each energy bin for each one of these 8 categories. For example the number of events in a certain energy bin of prompt ν_μ events with the true (MC) neutrino interaction vertex in the fiducial volume has been compared to the equivalent sample of *CORSIKA* events. After this procedure, the energy spectra were in good agreement as shown in Figure 7.27. Yet some small differences still exist in the high energy region due to the lack of *CORSIKA* events in some of the categories in that region. However, since both sensitivity and discovery potential are based on the cumulative number of events, these differences are negligible for any cut $E_\nu \leq 10^6$ GeV.

The procedure described above was implemented only for ν_μ and $\overline{\nu_\mu}$ CC events since the

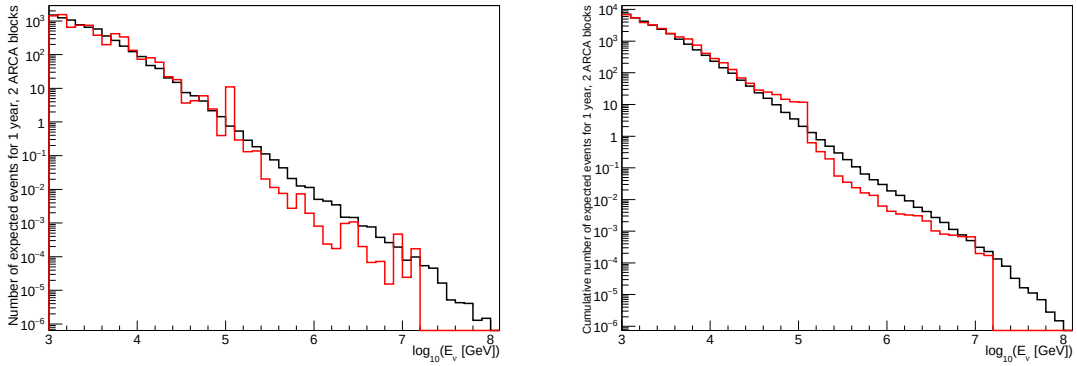

Figure 7.26: Left: Rates of ν_μ events with zenith angle $\leq 87°$ interacting inside the fiducial volume. Black: Standard neutrino production weighted with Honda and Enberg fluxes. Red: CORSIKA events weighted. Right: The equivalent cumulative plots.

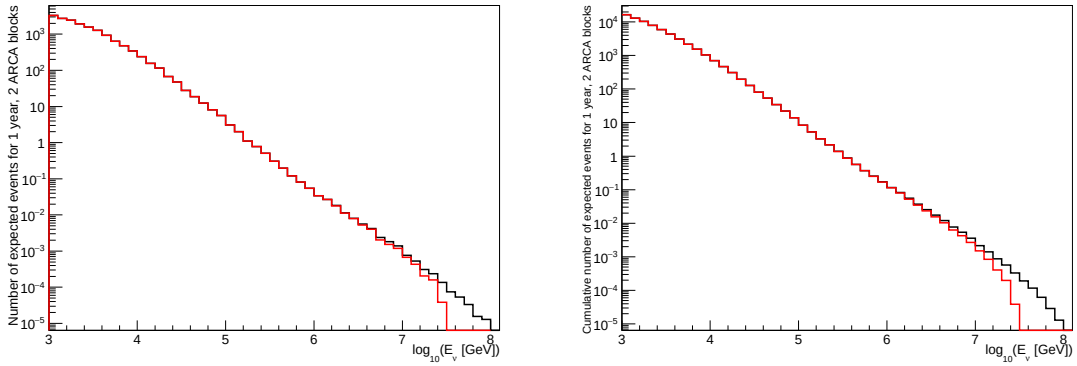

Figure 7.27: Left: Rates of ν_μ and $\overline{\nu_\mu}$ events with zenith angle $\leq 87°$. Black: Standard neutrino production weighted with Honda and Enberg fluxes. Red: CORSIKA events weighted with their weights and the additional weights explained in the text. Right: The equivalent cumulative plots.

current statistics of ν_e and $\overline{\nu_e}$ events in the *CORSIKA* production is poor. Also ν_μ and $\overline{\nu_\mu}$ NC events are excluded from this case study since their contribution to the total neutrino background, after applying the cuts found by the MRF / MDP, was at per mille level (as can be extracted from Tables A.1 and A.2 in Appendix A) so any attempt to reduce it even further is unnecessary.

7.5.3 Sensitivity and discovery potential

The improvement to the sensitivity and the discovery potential expected by identifying atmospheric neutrinos when accompanied by muons generated in the same atmospheric shower due to the application of the self veto is explored in this section. After applying the technique described in the previous section, the energy spectra of atmospheric neutrinos produced by the standard and the *CORSIKA* productions are in good agreement making it possible to use the events created by *CORSIKA* as part of the atmospheric neutrino background sample. It should be noted that the events created by *CORSIKA* do not

necessarily contain neutrinos accompanied by muons; whether a neutrino was accompanied by muons was the outcome of the whole generation/simulation chain (described in Chapter 6). Therefor, the background sample used here comprises:

- atmospheric neutrino events simulated with the *CORSIKA* production, for events with zenith $\leq 87°$,
- atmospheric neutrino events by the standard neutrino production for events coming from the rest of the sky and
- atmospheric muon events (with $E_{bundle} \geq 10$ TeV and $E_{bundle} \geq 50$ TeV).

For the calculation of the sensitivity and the discovery potential the same procedure as in Chapter 7.4.4 has been followed. KM3NeT/ARCA (with 2 building blocks) was found to be sensitive to the astrophysical neutrino flux after an observation time of 1.1 years (MRF = 0.96). The cut values found by the MRF minimization, as well as the number of expected signal and background events are summarized in Table 7.6. Also In Table A.3, located in Appendix A, the number of expected signal and background events for all event categories are detailed. No atmospheric muon event survived the above cuts and the number of ~ 0.2 background events were found by integrating the fitted function. In order to quantify the effect of the self veto, the same cuts on the BDT output and on E_{reco} have been applied on the standard neutrino production for the same observation time resulting to ~ 19.1 (from ~ 13.2 here) expected background events to 19.12 (from 13.22 here), so a 31% background reduction was achieved.

Sensitive to Φ_{astro}	BDT cut	E_{reco} cut	signal events	HEST	background events	HEST
1.1 years	0.40	$10^{4.7}$ GeV	7.82	92%	13.19	98 %

Table 7.6: BDT cuts and number of expected events given by the minimization of MRF for a sensitivity with a 90% CL. The percentage of events correctly identified as HEST is also given.

The ratio of the discovery flux normalization factor over Φ_0 for 3σ and 5σ with 50% probability is shown in Figure 7.28 as a function of the observation time for KM3NeT/ARCA (2 building blocks). A 3σ and a 5σ discovery can be reached in 2.3 and 6.3 years respectively, which translates to a 28% decrease in the observation time needed for both 3 and 5σ discovery. In Table 7.7 the cuts on the BDT value and on E_{reco}, the number of expected signal and background events and the percentage of events correctly identified as HEST for 2.3 and 6.3 years respectively are presented. In both cases no atmospheric muon events survived the cuts given by the minimization of MDP and the fitted function also yielded no events for the BDT output value cut at 0.46. The number of expected signal and background events for all event categories for a 5σ discovery is detailed in Table A.4 located in Appendix A.

To investigate the effect of the self vetoes, the number of expected atmospheric background ν_μ and $\overline{\nu_\mu}$ CC events derived using the *CORSIKA* production was compared to that derived by the standard neutrino production for zenith $\leq 87°$, after applying the same cuts on the BDT output value and on E_{reco}. The cut values used for this comparison are those shown in 7.7 for a 5σ discovery. So for an observation time of 6.3 years

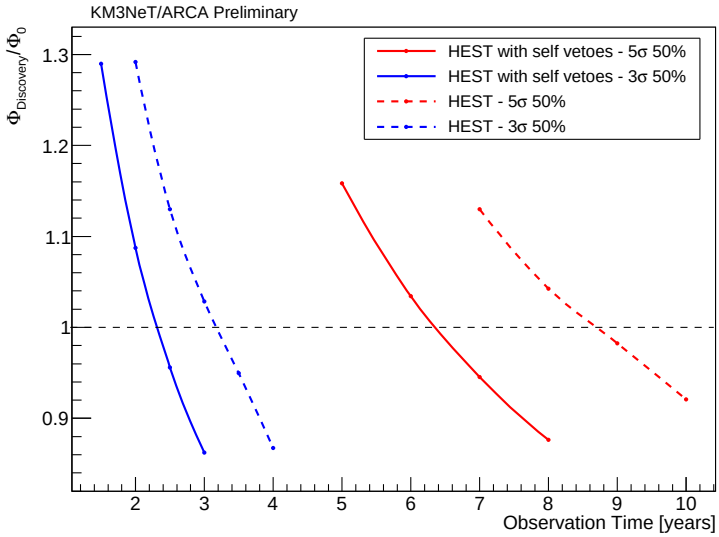

Figure 7.28: Ratio of the discovery flux normalization factor over Φ_0 for a 3σ (blue lines) and 5σ (red lines) with 50% probability for 2 ARCA blocks, as a function of the observation time in years. Solid lines: exploiting the self-veto effect - using both standard neutrino and CORSIKA sample used to extract the atmospheric neutrino background, dashed lines: not taking the self-veto effect into account - using only standard neutrino sample (same as solid lines of Figure 7.23)

Discovery	BDT cut	E_{reco} cut	signal events	HEST	background events	HEST
3σ (2.3 years)	0.46	10^5 GeV	9.50	91%	7.17	99 %
5σ (6.3 years)	0.46	10^5 GeV	26.03	91%	19.65	99 %

Table 7.7: Cuts and number of expected events given by the minimization of MDP for a 3 and 5σ discovery using standard neutrino and CORSIKA samples. The percentage of events correctly identified as HEST are also indicated.

~ 4.8 atmospheric background neutrino events are expected to come from above using the *CORSIKA* sample of events while the corresponding number of events expected by not taking the self-veto effect into account (using the standard neutrino production) is ~ 14.8. This comparison illustrates the improvement that can be achieved. To quantify the quality of the self veto effect, the unweighted *CORSIKA* events were studied further. From the events (unweighted) surviving the cuts only 5 neutrino events were accompanied by muons (stating with ~ 150000 neutrino events accompanied by muons). For these events the E_ν and $E_{\mu\ bundle}$ are presented in Figure 7.29. All these events have neutrinos with energies $E_\nu \gtrsim 100$ TeV. Only 1 event has accompanying muons with $E_{bundle} \sim 2$ TeV, with a corresponding rate of $5.3 \cdot 10^{-5}$ events for 2 ARCA blocks in 6.3 years, while the rest of the atmospheric neutrinos have accompanying muons with $E_{bundle} \lesssim 60$ GeV. So it is clear that practically all atmospheric neutrino events accompanied by muons have been rejected.

Apart from the decrease of the background events coming from above it is also important to identify the reduction on the whole background sample. By applying the cuts: BDT output ≥ 0.46 and $E_{reco} \geq 10^{5.0}$ GeV to the standard neutrino production for an observation time of 6.3 years (5σ discovery), the number of expected background events left in the final

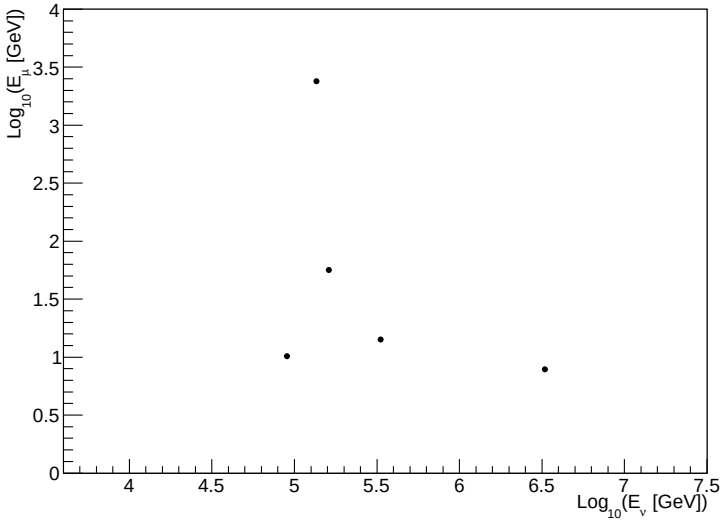

Figure 7.29: True (MC) E_ν and true (MC) E_{bundle} of the CORSIKA events remaining after imposing cuts: BDT output ≥ 0.46 and $E_{reco} \geq 10^{5.0}$ GeV.

sample was 29.71 events. So by using the more realistic *CORSIKA* sample, a reduction of 34% in the total number of the neutrino background events was achieved. Since the cuts found by the minimization of the MDP are the same for a 3σ and a 5σ discovery, the same reduction on the number of background events is expected.

7.6 Conclusion

In this chapter a tool was introduced, the MAMBA rejection, based on a BDT classifier designed to differentiate between incoming events to the ARCA detector and HEST events. By using the MAMBA rejection high purity samples of HEST events were selected analyses were conducted for the sensitivity and the discovery potential of ARCA to an astrophysical neutrino. ARCA is expected to be sensitive to the astrophysical neutrino flux used in approximately 1.3 years and it is also expected to make a 3σ and a 5σ discovery with 50% probability in approximately 3.2 and 8.7 years, respectively, using only HEST events. Then the self-veto effect was also explored using a sample of atmospheric neutrino events accompanied by muons simulated with *CORSIKA*. By selecting HEST practically all atmospheric neutrino events accompanied by muons were practically rejected achieving a reduction of the total atmospheric neutrino background of 34%. By taking into account the self-veto effect, ARCA is expected to be sensitive to the astrophysical neutrino flux considered in approximately 1.1 years and it is also expected to make a 3 and a 5σ discovery with 50% probability in approximately 2.3 and 6.3 years, respectively, using only HEST events.

Chapter 8

Differentiation Of Shower-Like From Track-Like Events

8.1 Introduction

The majority of the neutrino events interacting inside the volume for any neutrino telescope are shower-like events, since this is the signature of all three neutrino flavors interacting via Neutral Current (NC) interaction as well as of electron neutrinos interacting via Charged Current (CC) interaction. Thus the shower channel is very important for all analyses requiring the neutrino interaction to be located inside the detector. Also, in order to focus on the shower channel, the requirement that the reconstructed vertex is contained inside the detector is a very powerful tool. In such analyses, the major background to the shower-like signal are atmospheric muons reconstructed as showers by the shower reconstruction algorithms. As already mentioned in Chapter 2.2 the expected rate of atmospheric muons reaching the ARCA telescope is many orders of magnitude larger than the rate expected from neutrinos, so the suppression of this background is of critical importance.

The approach to the utilization of the shower channel for KM3NeT ARCA, up to now, has been to suppress the atmospheric muon background by exploiting the available information provided by the reconstruction algorithms[69, 120], yielding great results. By this approach a 5σ discovery with 50% probability of an astrophysical neutrino flux, modeled as a power law with a cutoff, is expected to be made by ARCA in less than a year. Another approach to utilize the shower sample is to reliably differentiate all track-like events from the true shower-like events relying on the different event topologies. To explore this approach a BDT-based tool was created to perform this task and an analysis of the discovery potential of ARCA using a high purity shower sample was conducted. This tool can be also used in any analysis requiring a high purity sample of contained shower-like events, like a High Energy Starting Events (HESE) analysis. This tool has already been used in a sensitivity analysis of ARCA to the Glashow resonance [121].

The following samples of MC events have been used for the development and for testing of this tool and the analyses conducted in this chapter:

1. All flavors of neutrino events simulated with *GENEHN*.

2. Atmospheric muon events simulated with *MUPAGE*. Teo different samples have been used: the first one comprising events with $E_{bundle} \geq 10$ TeV having a livetime of approximately 3 months for 1 ARCA block and the second comprising events with $E_{bundle} \geq 50$ TeV having a livetime of approximately 3 years for 1 ARCA block. As in

Chapter 7 both samples have been used in their full energy range in order to achieve better statistics in the high energy region.

8.2 A tool to differentiate showers from tracks

A tool to select shower-like events has been designed for the KM3NeT/ARCA detector. This tool utilizes the different event typologies and characteristics of track-like and shower-like events interacting inside the volume of the ARCA detector. Shower-like events have been considered as signal while track events have been treated as background for the shower selection and were consequently rejected. The tool comprises the following steps:

- Enhancement of the contribution of well reconstructed events to the contained events reconstructed by the shower reconstruction algorithm, by applying quality cuts.
- Rejection of events with a clear track signature.
- Use of a Boosted Decision Tree (BDT) classifier with twelve event based variables to make the final differentiation.

These steps are detailed in the following subsections.

8.2.1 Selection of well reconstructed contained events

AAshowerfit is the official reconstruction of shower events for KM3NeT/ARCA. The shower reconstruction provides an excellent angular resolution with a median of 1.5^o for High Energy shower events ($E_\nu > 60$ TeV) as shown in Figure 5.1. In order to select well reconstructed events having the reconstructed vertex inside the volume of ARCA, the following quality criteria have been posed [122]:

- the reconstructed vertex to be located inside the instrumented volume of ARCA.
- the angular error parameter β, provided by the reconstruction, to be lower than 10^o, for events with reconstructed energy $E_{AAshowerfit} > 10^4$ GeV .
- for events with lower reconstructed energies the beta parameter to fulfill: $\beta > 4 \cdot (4 - log_{10}(E_{AAshowerfit})$ (so β is required to acquire higher values as the reconstructed energy gets lower).

In Figure 8.1 the angular difference of the reconstructed and the neutrino direction (angular resolution) of truly contained ν_μ NC events is presented as an example (similar resolution is obtained for the other types of shower-like events). It can be observed that the vast majority of misreconstructed events are rejected by the use of these quality criteria. In more detail, the selection efficiency is approximately 70% for events with angular resolution up to 1 degree, it drops rapidly to 10% for events with angular resolution up to 8 degrees and it reaches the percent level for events with angular resolution 20 degrees and higher.

8.2.2 Selection of shower-like events based on topological criteria

In order to further remove track events from the shower sample, a series of selection criteria based on event topological characteristics distinct to track-like events have been developed to identify them. Thus, information derived from the track reconstruction has also been

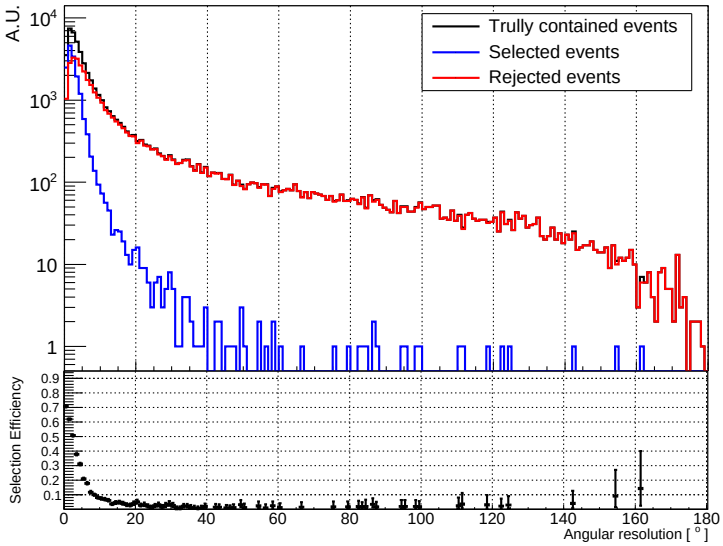

Figure 8.1: Angular difference of the reconstructed and the neutrino direction of truly contained ν_μ NC events. In black: all events; in blue: events fulfilling quality requirements; in red: events failing these cuts. The selection efficiency is also shown.

required and therefore the additional requirement for the events to have been also reconstructed with *JGandalf* has been posed. For the track reconstruction no quality criteria have been applied, the sole requirement has been the existence of at least 1 reconstructed track candidate. This requirement has almost no impact on true contained shower-like events since practically all these events are also reconstructed by the track reconstruction.

Any event fulfilling all of the following criteria has been considered as track event and has been rejected from the shower sample:

- At least 5 triggered hits in spatial and time coincidence with the reconstructed track, in at least 5 DOMs, located in at least 2 strings.
- A minimum track length, estimated using the hits in spatial and time coincidence with the reconstructed track, of 300m.
- On average at least 1 hit consistent with the track hypothesis for every 100m of track length.
- A fraction of the hits in spatial and time coincidence with the reconstructed track found in border areas of less than 95% and those in border areas near or behind the reconstructed vertex being of than 80%.
- Less than 20% of the hits to be found behind the reconstructed vertex and most of the hits to be consistent with the time expected by the reconstructed track hypothesis.

To further reinforce the above requirements two additional criteria have also been posed. If either of the them was fulfilled, the event was considered as track event and it was rejected from the shower sample.

1. At least one PMT hit in a time window defined using two different hypotheses for the arrival time of the emitted photons [Cherenkov photon emitted from a muon using the reconstructed track direction, photon emitted from the reconstructed vertex].

2. Taking the reconstructed track hypothesis having at least one hit consistent (in time and spatial coincidence as described in Chapter 7) with the assumption that it is created by Cherenkov photon emitted at a distance at least 250 away from the reconstructed vertex (along the reconstructed track).

The above criteria were developed to identify well reconstructed true track events. Though the first might seem loose, it is quite strict since the required time window is very narrow, a spatial correlation between the PMT and the reconstructed track is required and also the angle between the PMT orientation and the hypothetical photons is examined.

These selection criteria were developed in such a way so that high efficiency could be retained on true shower events fulfilling the quality requirements and at the same time a high rejection power on true track events could be ensured. The efficiency of the above criteria is presented in Figure 8.2. The efficiency is shown on the right for atmospheric muon events (true tracks) as a function of E_{bundle} and on the left for all types of shower-like events (all ν NC events as well as ν_e and $\overline{\nu_e}$ CC events) as a function of E_ν. On the left plot, a drop of the selection efficiency for $\overline{\nu_e}$ CC events is observed in the energy range of the Glashow resonance. Even though $\overline{\nu_e}$ CC interaction are considered as shower like events, when a W boson is created (Glashow resonance) there is a probability that a muon will be present at the final state due to the leptonic decay modes of the W boson. The drop of the efficiency is due to the fact that these (track-like) events have been identified by the selection criteria and were rejected from the shower sample. The MC particle information of the rejected events was investigated revealing that a muon existed in all of these events.

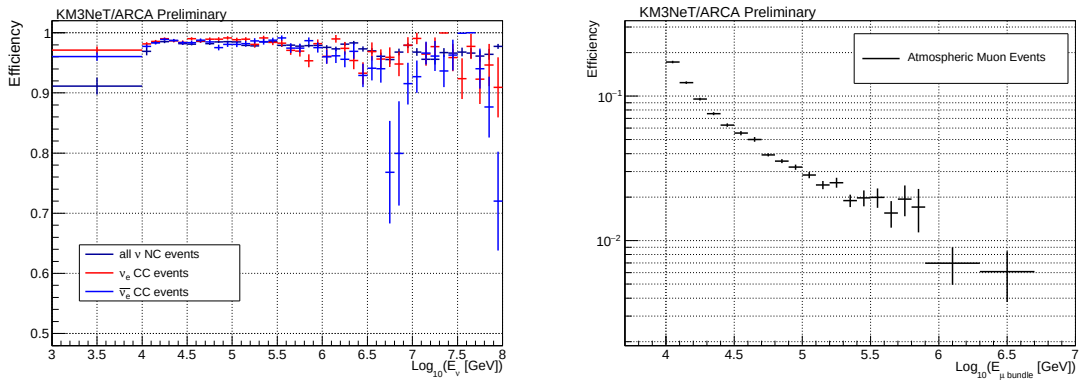

Figure 8.2: Selection efficiency of the criteria developed to reject track-like events applied to all events fulfilling the quality requirements. Left: all types of shower-like events - in black all ν NC events, in red ν_e CC events and in blue $\overline{\nu_e}$ CC events. Right: atmospheric muon events, used as true track events, with respect to E_{bundle}.

8.2.3 BDT and Variables

Even though a large reduction of the contribution of track events to the shower sample has been achieved by applying the requirements described above, by only applying the quality and the selection requirements, track events (predominantly atmospheric muons) still dominate the signal from showers stemming from neutrinos interacting in the volume of the detector. More than 2 and 15 atmospheric muon events per hour are expected to satisfy the above conditions, for atmospheric muons with $E_{bundle} \geq 50$ and $E_{bundle} \geq 10$

TeV, respectively. In order to further suppress the background from tracks a BDT has been employed.

The BDT used is contained in the *TMVA* [114] package of the *ROOT* Data Analysis Framework version 5.34/26 [115]. It comprises 600 decision trees with a maximum depth of 3 layers. For a leaf node to be created it should comprise at minimum 3.5% of the events used for the training. Moreover the splitting of each node is decided based on the gini index. The boosting is preformed with AdaBoost with a beta exponent of 0.1 and the training sample used for each tree is created by bagging a sample with size 90% the size of the training sample of the BDT classifier[1].

To differentiate between shower-like and track-like events, twelve event based variables have been constructed aiming to identify the following characteristics:

1. track-like events
2. incoming track-like events events to the detector
3. shower-like events
4. differences in the track-like and shower-like event topologies

For the description of the BDT variables the following terminology is used:

- Reconstructed track ⇒ Directional reconstruction with *JGandalf* and vertex reconstruction with the method described in Chapter 7.2.3.
- Time coincidence with the reconstructed track ⇒ |Time residual| $\leq$ 20 ns.
- Spatial coincidence with the reconstructed track ⇒ Vertical distance of the PMT hit to the reconstructed track $\leq$ 111 m. This value was chosen so that the path length of the photon is $\leq$ 3 absorption lengths.
- Border DOMs ⇒ The two upper DOMs (17 and 18).
- Border Strings ⇒ Strings: 105, 104, 103, 102, 101, 71, 100, 98, 96, 94, 92, 62, 93, 95, 97, 99, 91, 115, 114, 113, 112, 87, 86, 85, 111, 110, 109, 82, 81, 80, 108, 107, 106, 77 and 76. The border strings are shown in Figure 7.6 left in red.

Variables used in the BDT:

1. An approach based on the selection criteria detailed in Chapter 8.2.2 is followed where slightly stricter requirements are set. If all requirements are met, a boolean is set. This variable targets characteristic 1.
2. A strict containment criterion is formed. Using the Cherenkov hypothesis, the emission points of the hits in time and spatial coincidence with the reconstructed track are clustered in groups. A maximum distance of 100 m between 3 consecutive emission points inside the cluster is required. A boolean is set if both the reconstructed track vertex and the emission point farthest from the vertex are contained inside the volume of the detector. This variable targets characteristic 2.

[1]The configuration of the BDT used:
TMVA::Types::kBDT, "BDT","!H:!V:NTrees=600:MinNodeSize=3.5%:MaxDepth=3:BoostType=AdaBoost:AdaBoostBeta=0.1:UseBaggedBoost:BaggedSampleFraction=0.9:SeparationType=GiniIndex:nCuts=19

3. The fraction of triggered hits in PMTs with distance from the *AAshowerfit* vertex < 165 m which are on border DOMs or border strings is utilized to examine the shower activity in border areas. This variable targets characteristic 1.

4. Using a pseudo-track having as vertex and direction those found by *AAshowerfit* a similar clustering technique of the emission points of hits as in variable 2 is applied. The variable used is the distance from the *AAshowerfit* vertex to the most distant emission point selected. The normalization of this variable depends on the reconstructed *AAshowerfit* energy. This variable targets characteristic 1.

5. The distance of the *AAshowerfit* vertex and the vertex of the reconstructed track. This variable targets characteristic 4.

6. The length of the track found by hits in time and spatial coincidence with the reconstructed track assuming the Cherenkov hypothesis. This variable targets characteristic 1.

7. An approximation of the shower profile using the reconstructed track, the reconstructed vertex and the plane perpendicular to it (using two perpendicular hypothetical tracks on it). This variable targets characteristic 3.

8. Same approach as above using a pseudo-track having as vertex and direction those found by *AAshowerfit*. This variable targets characteristic 3.

9. The number of the hits in time and spatial coincidence with the reconstructed track, in a cylinder round it is found. Also the number of the hits it time and spatial coincidence with the reconstructed shower, in a sphere around the shower reconstructed vertex is found and the ratio of the two densities is used. This variable targets characteristic 4.

10. The fraction of hits consistent with the track hypothesis far from the reconstructed vertex. This variable targets characteristic 1.

11. Number of triggered hits in PMTs in a sphere around the *AAshowerfit* vertex. This variable targets characteristic 3.

12. The angular difference of the reconstructed shower and track directions. This variable targets characteristic 4.

To train/test the BDT, from the events satisfying the quality and selection requirements, the signal sample comprised:

- ν_μ NC events having the true (MC) neutrino vertex inside the volume of ARCA.

while the following atmospheric muon event samples have been combined to form the background sample:

1. with $\mathrm{E}_{bundle} \geq 10$ TeV and

2. with $\mathrm{E}_{bundle} \geq 50$ TeV.

The BDT classifier was trained/tested using part of the available MC simulated events. The rest of the events were used for the evaluation of the trained BDT and in physics analyses. The training/testing signal sample consisted of:

- 10% of the available events.

while the training/testing background sample consisted of:

- 4.6% of the available atmospheric muon events with $E_{bundle} \geq 10$ TeV and
- 5.8% of the available atmospheric muon events with $E_{bundle} \geq 50$ TeV

The training/testing of the BDT was conducted using unweighted events, like the BDT used in the MAMBA rejection (Chapter 7.2.6). This way, all events are equally important to the training process. As in the case of the BDT used in the MAMBA rejection, also in this case tests were conducted to train the BDT using weighted events (atmospheric muon events weighted to a predefined livetime and neutrino events weighted with the weight produced by *GENHEN* convoluted with the astrophysical neutrino flux for that livetime). The BDT trained with weighted events performed worse than that trained with unweighted events, so this training scheme was abandoned. Before training the BDT the values of the variables used were "normalized", like in the case of the variables used in the MAMBA rejection (Chapter 7.2.6). In Figure 8.3 the distributions of the variables of the events contained in the training/testing sample, after normalization, are presented in blue for the signal and in red for the background.

Even though BDTs are not expected to underperform when provided with correlated variables, as already mentioned in Chapter 7.2.6, the correlation matrices of the variables belonging to the signal and background sample, as provided by *TMVA*, are shown in Figure 8.4. As it can be observed the only highly correlated variables are variables 8 and 11 only for the signal sample as well as variables 6 and 10 only for the background sample. This behavior is expected since both variables 6 and 10 have been designed to identify track events while both variables 8 and 11 to exploit the different topologies of shower-like and track-like events. The ranking of the variables based on separation and on importance is shown in Table 8.1. Various tests have been made in which the correlated variables and the variables with low rankings, based both on separation and on importance, have been removed and the BDT was retrained. All these tests resulted to a trained BDT having worse performance, thus the twelve-variable model was adopted.

During the training/testing phase of the BDT, the events used were split into two subsamples, one used for the training and one for the testing. The splitting of the events was done randomly with a ratio of 50% - 50% for the training and the testing samples (these fractions are the default values of the *TMVA* package). At the end of the training phase the test sample was used to provide a check for overtraining. As demonstrated in Figure 8.5, where the distributions of the BDT output values of the training (area) and the test (points) samples are overlaid, no overtraining is observed as expected since the BDT classifier used comprised descision trees with depth 3.

Despite the fact that no overtraining was observed a separate test was performed to validate this claim, as was also done for the case of the MAMBA rejection BDT (Chapter 7.2.6). The files not used for the training/testing procedure were utilized as an evaluation sample in order to establish that the performance of the BDT on this sample is similar to the performance on the training and testing samples. The procedure is described below:

1. The efficiency for the training and test sample to identify signal events was set to a specific value (60 %) which was achieved by a BDT cut value of 0.49.
2. Events belonging to the rest of the production files satisfying the quality and the selection requirements have been evaluated with the BDT. No MC information has been used.

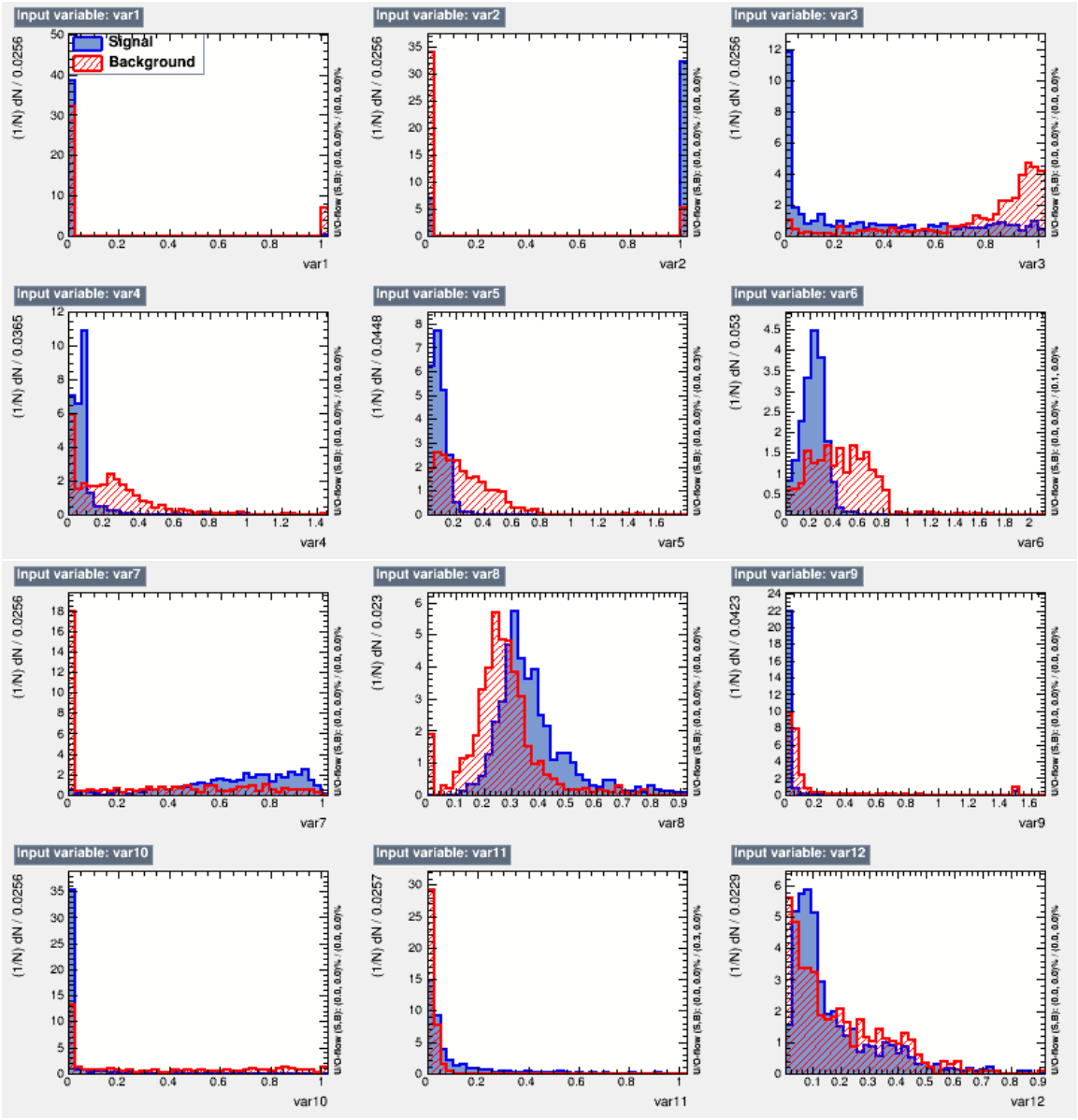

Figure 8.3: BDT input variables for the training/testing sample after normalization.

3. A cut on the BDT value ≥ 0.49 was posed. All events fulfilling this condition were accepted for the final sample.

Figure 8.5 shows that for BDT values ≥ 0.49 very few background events are found in the training and testing sample. However for the training and testing only 4.6% and 5.8% of the atmospheric muon events with $E_{bundle} \geq 10$ TeV and $E_{bundle} \geq 50$ TeV, respectively, have been used. Thus it is expected that after imposing this cut some background events will still survive.

The efficiency found for the rest 90% of the ν_μ NC event sample is 58.58% and the background events remaining are:

- 34 out of $\sim$ 31700 atmospheric muon events with $E_{bundle} \geq 10$ TeV.
- 6 out of $\sim$ 50700 atmospheric muon events with $E_{bundle} \geq 50$ TeV.

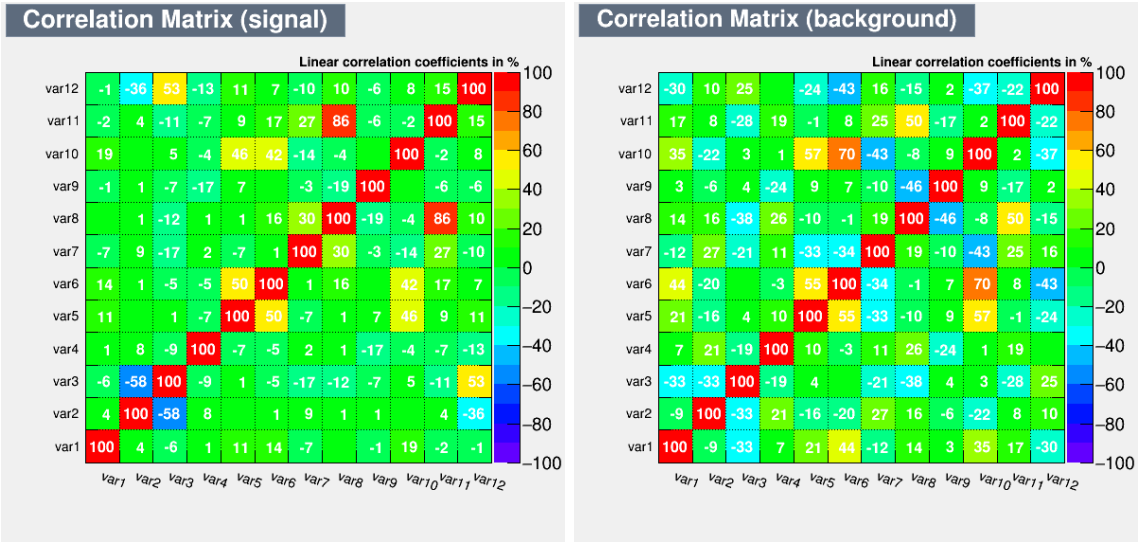

Figure 8.4: The correlation matrices for the signal (left) and the background (right) as provided by TMVA.

Variable	Ranking based on	
	Separation	Importance
var1	11	12
var2	1	2
var3	3	5
var4	2	1
var5	4	9
var6	6	3
var7	5	4
var8	9	8
var9	8	10
var10	7	11
var11	10	6
var12	12	7

Table 8.1: Ranking of the variables using Separation and Importance.

- 571 out of $\sim$ 4000 ν_μ CC events ($\sim$ 14% of the events fulfilling base and initial requirements).

In Figure 8.6 the energy distributions of the ν_μ NC events (which were not used for training/testing) satisfying the quality and the selection requirements and of those events surviving the BDT cut are shown in blue and red respectively. The efficiency of the BDT cut, also shown, rises as the neutrino energy increases, reaching 60% for $E_\nu \sim 100$ TeV and 70% for neutrino energy a few PeV.

Shower-like event samples are dominated by ν_e and $\overline{\nu_e}$ CC events, so in principle these events could have been used for training the BDT. When ν_e ($\overline{\nu_e}$) interact via CC interaction an (anti)electron is produced which creates an electromagnetic cascade in the water. Thus all the energy of the parent neutrino is relished into the hadronic and electromagnetic

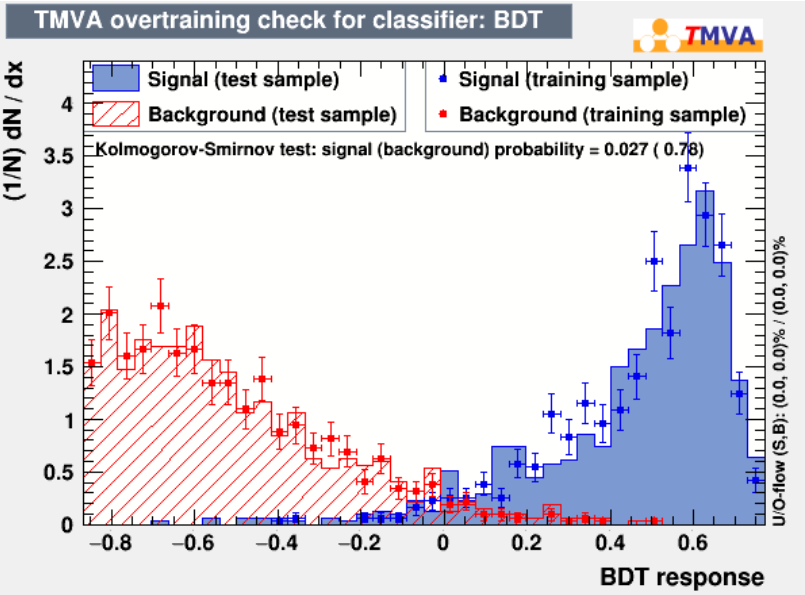

Figure 8.5: The overtraining check as provided by ROOT.

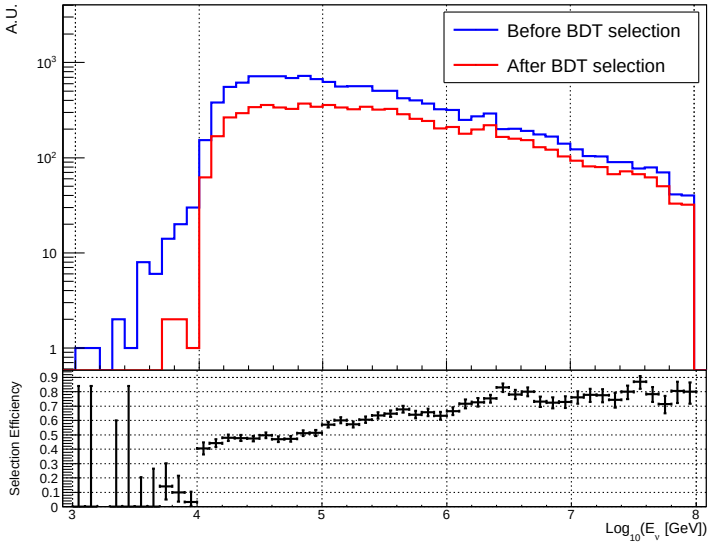

Figure 8.6: Energy distributions of the signal ν_μ NC events satisfying the quality and the selection requirements in blue and of those surviving the BDT cut at 0.49 in red. The selection efficiency, is also shown, as a function of the neutrino energy.

cascades. Contrarily, when any neutrino interacts via NC interaction, only part of the neutrino energy is transferred to the particle it interacted with, so the light output is lower than that yielded by ν_e ($\overline{\nu_e}$) with the same energy interacting via CC interaction. As it can be observed in Figure 8.6 the BDT selection efficiency increases as the energy of the neutrino increases, so ν_e ($\overline{\nu_e}$) interacting via CC interactions are expected to have higher selection efficiencies for the same neutrino energy. In Figure 8.7 the selection efficiency with respect to the neutrino energy for ν_μ NC events, all neutrino NC events as well as ν_e and $\overline{\nu_e}$ CC events is shown in black, blue and red respectively. As expected, the ν_e and $\overline{\nu_e}$ CC

events have higher selection efficiencies for the same neutrino energy.

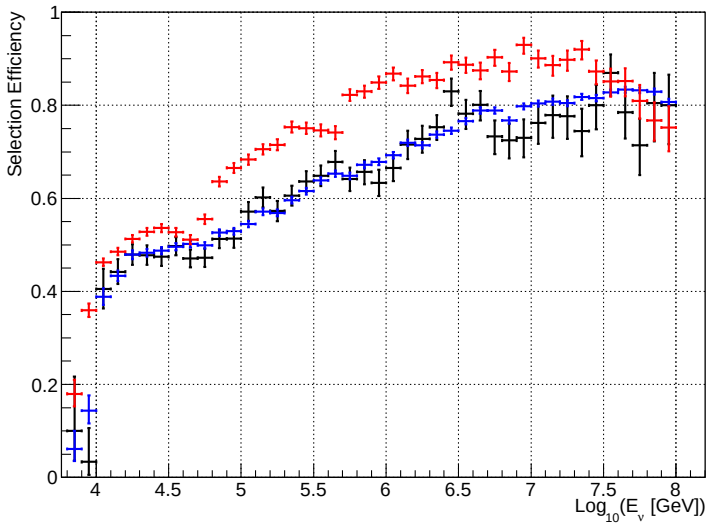

Figure 8.7: Selection efficiency of the BDT for a cut at a value 0.49 *for* ν_μ *NC events in black, all NC events in blue as well as* ν_e *and* $\overline{\nu_e}$ *CC events in red, as a function of the neutrino energy.*

Due to the fact that contained ν_μ CC events can exhibit both track-like and shower-like behavior, depending on the position of the neutrino interaction in the detector and the Bjorken y, these events have not been included in the training/testing sample used. As mentioned above, 571 ν_μ CC events passed the BTD selection cut which was $\sim 14\%$ of the ν_μ CC events fulfilling the quality and selection requirements. Although this percentage is small, the characteristics of these events were further investigated. In Figure 8.8 left, the energy of the hadronic cascade is displayed with respect to the energy of the muon for these events. 63% of these events have larger shower energies than muon energies, resulting to their categorization as shower-like events. Most of the events having muon energies larger than the energy of the hadronic cascade, have the neutrino interaction vertex near the edge of the detector and the muon track is outgoing, as displayed in Figure 8.8 right. Since the muon travels only a short distance in the instrumented volume, the hadronic cascade determines the event classification as a shower.

To conclude, the similar performance of the BDT on the signal events of the training and of the evaluation samples validates the fact that the BDT exhibits no overtraining. Finally, the BDT efficiency is optimized for events with energetic cascades and the background rejection is very powerful.

8.3 Discovery potential with showers

8.3.1 General

The procedure to differentiate showers from tracks described in the previous chapter has been used to estimate the discovery potential of ARCA (2 building blocks) for the astrophysical flux of equation 7.5, using only shower events. As atmospheric neutrino fluxes, the Honda 2016 model with the knee correction [23] and the Enberg 2008 model [24] have been

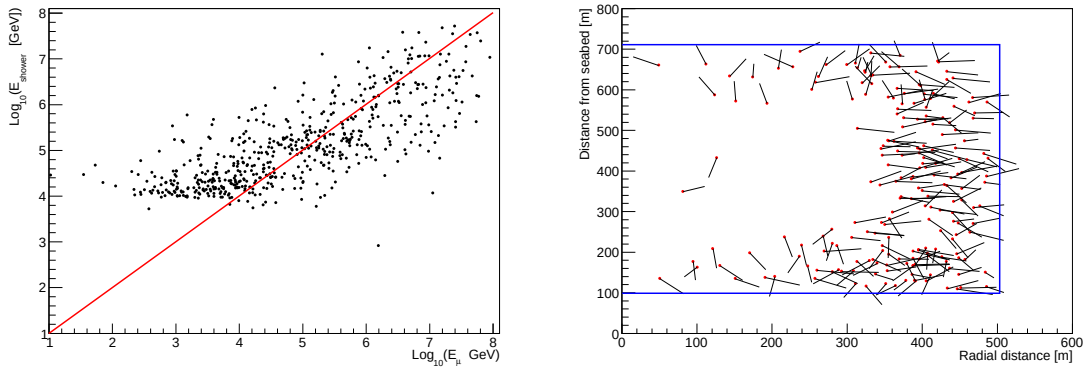

Figure 8.8: Left: The energy of the hadronic cascade with respect to the energy of the muon for the ν_μ CC events categorized as showers by using a cut value of 0.49 *on the BDT output. A red diagonal line is overlaid to guide the eye. Right: The true (MC) interaction vertices and directions of the ν_μ CC events for which the energy of the muon is larger than the energy of the hadronic cascade.*

used for the conventional and the prompt components respectively, as in Chapter 7.4.4. The discovery potential has been estimated using the MDP method.

8.3.2 Discovery potential calculation

From the events not belonging to the sample used to train the BDT, those that satisfy the quality and selection requirements have been selected for this analysis. The selected events were evaluated with the BDT and a BDT output value was assigned to each event. In Figure 8.9 left the BDT values are shown for ν and $\overline{\nu}$ NC (all flavours), ν_e and $\overline{\nu_e}$ CC, ν_μ and $\overline{\nu_\mu}$ CC and for atmospheric muon events. It can be observed that the BDT has a considerable discriminating power between true shower and track events. Then the MDP method was used to find the best cuts to be imposed on the reconstructed energy found by *AAshowerfit* and the output of the BDT. During this procedure no information from MC was used. The binning for the search of the optimal cuts was 0.1 in the logarithm of the reconstructed energy and 0.01 in the BDT output value. All neutrino events weighted with the astrophysical flux (equation 7.5) were considered as signal events. The background sample consisted of atmospheric neutrinos and atmospheric muons. The atmospheric neutrino sample comprised all ν_μ, $\overline{\nu_\mu}$, ν_e and $\overline{\nu_e}$ events weighted with the atmospheric neutrino fluxes. The atmospheric muon sample comprised atmospheric muon events with $E_{bundle} \geq 10$ TeV and $E_{bundle} \geq 50$ TeV. In Figure 8.9 right the BDT output values for all neutrino events weighted with the astrophysical flux and for all atmospheric muon events are presented.

As already detailed in Chapter 7.4.4, the MDP technique might sometimes find as optimal cuts values right after the last event of the background distribution. In order to avoid such effects that might bias the results the same approach to estimate the atmospheric muon background was followed as in Chapter 7.4.4. So, the cumulative BDT output distributions were fitted and the background from atmospheric muons was calculated also by this fitted functions. Since the energy spectra of the two atmospheric muon samples overlap, the sample with $E_{bundle} \geq 10$ TeV was split into a subsample with $E_{bundle} < 50$ TeV and a subsample with $E_{bundle} \geq 50$ TeV which was added to the atmospheric muons with $E_{bundle} \geq 50$ TeV. This was done in order to have two non overlapping samples in

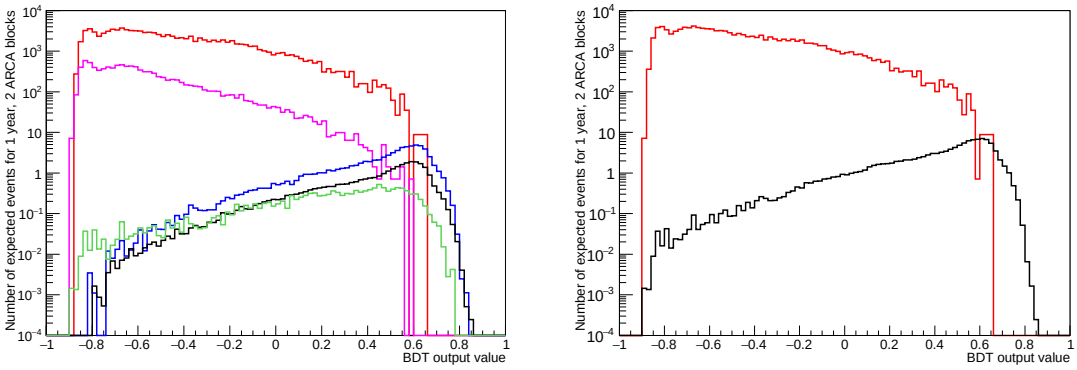

Figure 8.9: Left: BTD output values for ν and $\overline{\nu}$ NC events (black), ν_e and $\overline{\nu_e}$ CC (blue), ν_μ and $\overline{\nu_\mu}$ CC (green), atmospheric muon events with $E_{bundle} \geq 10$ TeV (red) and atmospheric muon events with $E_{bundle} \geq 50$ TeV (magenta). Right: Number of events expected in 1 year for 2 ARCA blocks with respect to the BDT output value for all astrophysical neutrino events (black) and atmospheric muon events from both samples with $E_{bundle} \geq 10$ and 50 TeV (red).

energy. Before fitting the BDT output distribution, the MDP has been employed and the cut on the reconstructed energy has been found to be: $E_{AAshowerfit} \geq 10^{4.3}$ GeV. In order to allow the possibility of finding a lower cut value on the reconstructed energy after adding background events, the distribution of the BDT output values for those events satisfying $E_{AAshowerfit} \geq 10^{4.2}$ GeV was plotted and fitted. Since this method has been employed to approximate the tail of the BDT output distributions, the fits were performed in the range of the BDT output values [0.3, 0.7]. The cumulative BDT output distributions for the atmospheric muon event samples with 10 TeV $\leq E_{bundle} <$ 50 TeV and $E_{bundle} \geq$ 50 TeV and the fitted functions (equations 8.1 and 8.2 respectively) are shown in Figures 8.10 and 8.11 left. In Figures 8.10 and 8.11 right, the distributions of the number of background events satisfying $E_{reco} \geq 10^{4.2}$ GeV and those derived from equations 8.1 and 8.2, are also shown. To estimate the total number of atmospheric muon events for each BDT output value, the number of events surviving that BDT output cut and the value of the fitted cumulative function were found. The number of events derived from both samples (of atmospheric muon events with 10 TeV $\leq E_{bundle} <$ 50 TeV and $E_{bundle} \geq$ 50 TeV) were added (separately for the cut and count and for the fitting procedures) and the maximum number of events from these procedures was considered for the background calculation.

$$\text{cumulative N}_{\text{events 10 TeV} \leq \text{E}_{\text{bundle}} < \text{50 TeV}} = \sqrt{18.3 - 27.9 \cdot \text{x}} \cdot (269.1 - 509.8 \cdot \text{x}) \quad (8.1)$$

$$\text{cumulative N}_{\text{events E}_{\text{bundle}} \geq \text{50 TeV}} = (0.36 \cdot \text{x}^2 + 0.35 \cdot \text{x} - 0.05) \cdot \exp(18.2 - 27.0 \cdot \text{x}) \quad (8.2)$$

where x is the BDT output value

The discovery potential for ARCA (2 building blocks) using contained shower-like events was found using the MDP method. In Figure 8.12 the ratio of the discovery flux normalization factor over Φ_0 for 5σ discovery with 50% probability (blue) and 90% probability (red) with respect to the observation time is displayed. ARCA is expected to make a 5σ discovery with 50% and 90% probability in approximately 0.5 and less than 0.9 years respectively. In Table 8.2 the cuts on the BDT value and on $E_{AAshowerfit}$, the number of signal and

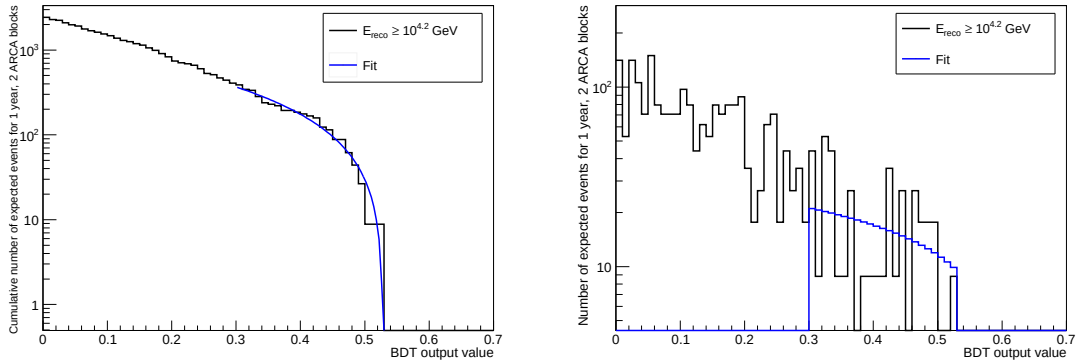

Figure 8.10: Left: Distributions of the BDT output values for atmospheric muons with $10\ TeV \leq E_{bundle} < 50\ TeV$ *satisfying* $E_{reco} \geq 10^{4.2}\ GeV$ *in black and the fitted function in blue. Right: Distributions of the number of events satisfying* $E_{reco} \geq 10^{4.2}\ GeV$ *in black. The function derived from the fitting of the cumulative distribution showing the number of background events is also presented in blue.*

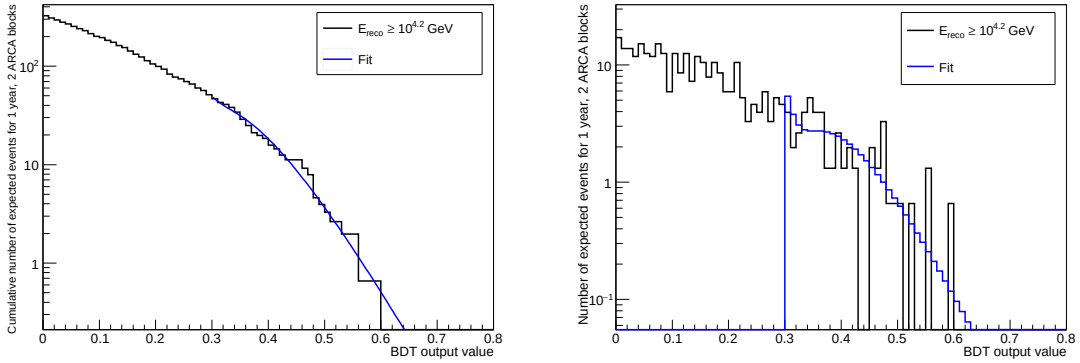

Figure 8.11: Left: Distributions of the BDT output values for atmospheric muons with $E_{bundle} \geq 50\ TeV$ *satisfying* $E_{reco} \geq 10^{4.2}\ GeV$ *in black and the fitted function in blue. Right: Distributions of the number of events satisfying* $E_{reco} \geq 10^{4.2}\ GeV$ *in black. The function derived from the fitting of the cumulative distribution showing the number of background events is also presented in blue.*

background events and the percentage of correctly identified events as shower-like for 0.5 and 0.9 years, respectively, are presented. In both cases (5σ discovery with 50% and 90% probability), the cuts found by the MDP were the same. In Figure 8.13 the values of the MDP for a 5σ discovery with 90% probability (livetime of 0.9 years) for various BDT output values and E_{reco} values are presented. In order to focus on low MDP values, MDP values larger than 10 (left plot) or larger than 5 (right plot) are not taken into account in the plot. As it is illustrated on the right plot, a rectangular like shaped area of low MDP values appears for BDT output values from $\sim$ 0.50 to 0.60 and for E_{reco} from $\sim 10^{4.1}$ to $10^{4.7}$ GeV. The values $E_{AAshowerfit} = 10^{4.2}$ GeV and BDT output = 0.53 for which the MDP is minimized reside inside this area which appears in the right plot as an even darker blue rectangle. The number of expected signal and background events for each type, for both 5σ with 50% and 90% probability is shown in Table B.1 in Appendix B. The expected number

of signal events surviving each cut, for a livetime of 0.9 years, is shown in Figure 8.14 for ν_e CC (top left), $\overline{\nu_e}$ CC (top right), all NC (bottom left) events as well as for all types of events considered as shower-like events, the sum of the previous three plots, (bottom right) with respect to the true E_ν. Also, the ratio of the number of events surviving each cut over the number of triggered events is shown in Figure 8.15 left, for all shower events (ν NC all flavors, ν_e and $\overline{\nu_e}$ CC) with respect to the true E_ν. In Figure 8.15 right the selection efficiencies for well reconstructed shower events with respect to the true E_ν are also presented.

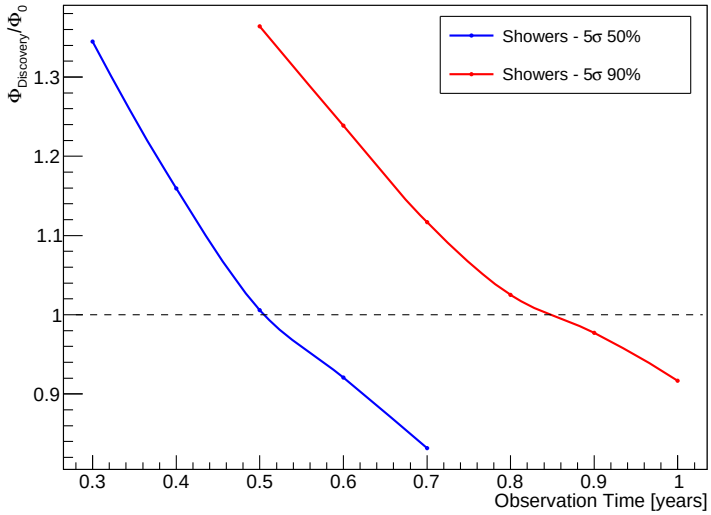

Figure 8.12: Ratio of the discovery flux normalization factor over Φ_0 for 5σ discovery with 50% probability (blue) and 90% probability (red) with respect to the observation time in years for 2 ARCA blocks.

5σ Discovery	BDT cut	$E_{AAshowerfit}$ cut	signal events	true showers	background events	shower like
50% Prob. (0.5 years)	0.53	$10^{4.2}$ GeV	24.90	96%	17.62	94%
90% Prob. (0.9 years)	0.53	$10^{4.2}$ GeV	44.82	96%	31.72	94%

Table 8.2: BDT and AAshowerfit energy cuts and number of expected events given by the minimization of MDP for a 5σ discovery with probability of 50% and 90%. The percentage of events correctly identified as shower-like is also given.

For 5σ discovery with 90% probability, which is expected to be reached in 0.9 years of observation, approximately 96% of the signal events are correctly identified as showers. The number of expected background events is 31.72 out of which 1.92 are atmospheric muons (6%), leading to a correct identification of 94%. The 1.92 expected atmospheric muon events are the result of the cut and count technique since the use of the fitted functions resulted to slightly less events. The remaining ν_μ and $\overline{\nu_\mu}$ CC events in the final sample are 7.47 (23%). For most of these events the energy of the hadronic cascade is larger than the energy of the muon. The rest have the neutrino interaction vertex near the edge of

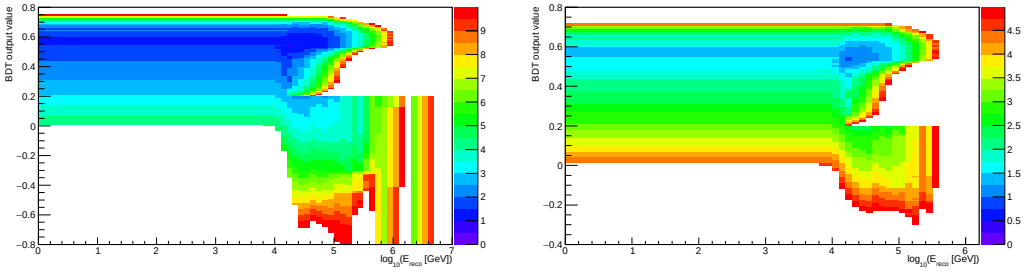

Figure 8.13: MDP values for a 5σ *discovery with* 90% *probability (livetime of* 0.9 *years) color coded, for various BDT output and* E_{reco} *values. The empty bins correspond to MDP values greater than the maximum used for each plot, or to bins where the number of background events is more than* 10000*. Left: MDP values up to* 10 *are shown. Right: MDP values up to* 5 *are shown.*

the detector and the muon track is outgoing. So they exhibit a shower-like behavior in a similar manner to those shown in Figure 8.8.

8.4 Conclusion

A BDT based tool developed to differentiate shower-like from track-like events for the ARCA detector was introduced. By using this tool, high purity shower-like samples of events were selected and an analysis to estimate the discovery potential of ARCA to an astrophysical neutrino flux was conducted. ARCA is expected to make a 5σ discovery with 50% and 90% probability in approximately 0.5 years and less than 0.9 years respectively, using only shower-like events.

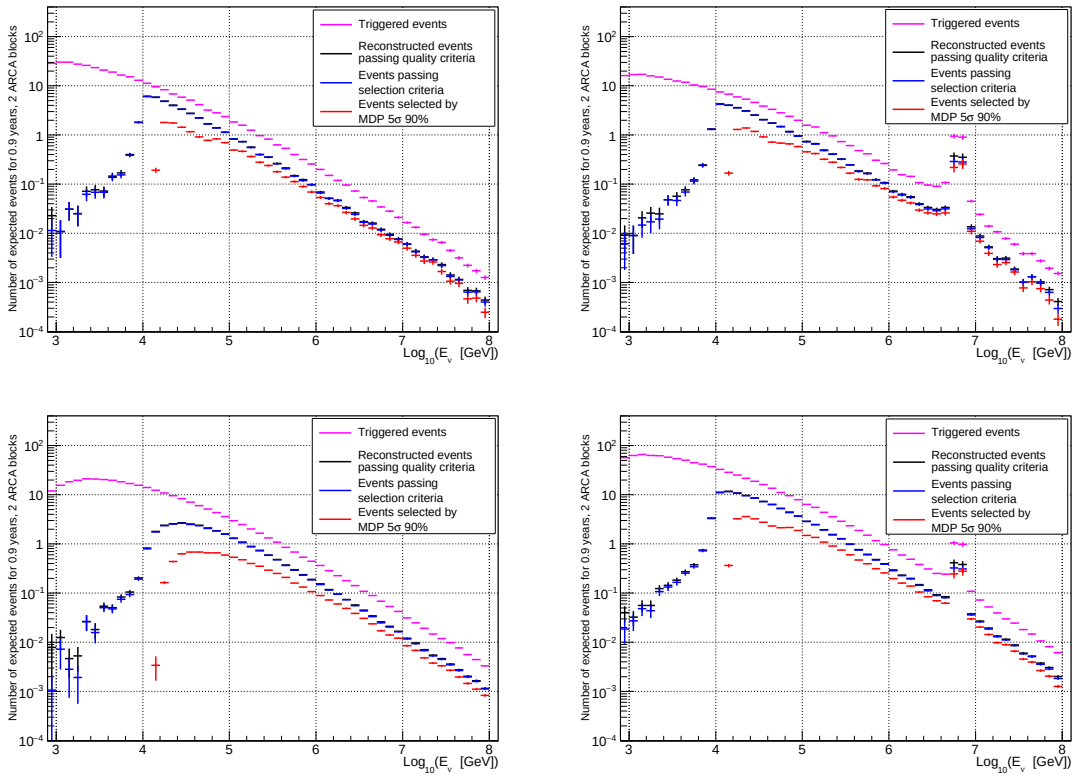

Figure 8.14: Expected number of signal events for a livetime of 0.9 *years with respect to the true* E_ν*. Top left:* ν_e *CC, top right:* $\overline{\nu_e}$ *CC, bottom left: all NC events and bottom right: all shower-like events, the sum of the rest three plots.*

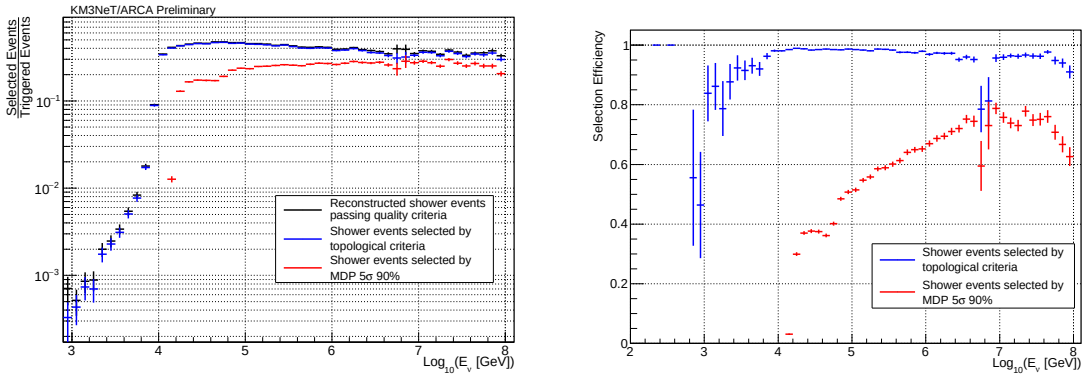

Figure 8.15: Left: Ratio of the number of events surviving each cut over the number of triggered events with respect to the true E_ν*, for all shower events (*ν *NC all flavors,* ν_e *and* $\overline{\nu_e}$ *CC). Right: Selection efficiencies for well reconstructed shower events with respect to the true* E_ν*.*

Chapter 9

A High Energy Starting Events Analysis With KM3NeT/ARCA

9.1 Introduction

In the previous chapters two tools designed to select HEST and contained shower-like events for KM3NeT/ARCA were presented. These tools have been very successful in selecting high purity samples of HEST events and contained shower-like events. The samples provided by these tools were combined to a High Energy Strating Events (HESE) sample. The advantages of a HESE analysis is that the atmospheric muon background is highly suppressed, as already demonstrated for both the HEST and the contained shower-like event samples. Also, by selecting contained events, increased accuracy of the measured neutrino energy is expected, leading to a reliable estimation of the diffuse astrophysical high energy neutrino flux spectrum. Finally, the self veto effect (described in Chapter 7.5) is expected to further reduce the contribution of the atmospheric neutrino background. The IceCube collaboration, based on a sample of High Energy Starting Events, has presented results on the estimation of the diffuse astrophysical neutrino flux [36, 123, 53] as well as on the flavor composition [54] and on dark matter searches [124] among others.

In this chapter an analysis of the discovery potential of ARCA using HESE is described. In this analysis the following samples of MC events have been used:

1. All flavors of neutrino events simulated with *GENEHN*.

2. Atmospheric muon events simulated with *MUPAGE* (two different samples) were used, the first one comprising events with $E_{bundle} \geq 10$ TeV having a livetime of approximately 3 months for 1 ARCA block and the second comprising events with $E_{bundle} \geq 50$ TeV having a livetime of approximately 3 years for 1 ARCA block. As in Chapter 7 both samples have been used in their full energy range in order to achieve better statistics in the high energy region.

Even though the self veto effect is expected to have a considerable impact on the atmospheric neutrinos accompanied by muons created at the same atmospheric shower, currently the statistics of ν_e and $\overline{\nu_e}$ events in the *CORSIKA* production (Chapter 6.3) is poor. Thus the self veto effect has not been explored for the HESE sample so no *CORSIKA* sample has been used.

9.2 An analysis of the discovery potential of ARCA using HESE

In order to estimate the discovery potential of ARCA to the astrophysical neutrino flux of eq 7.5, the tools described in the previous chapters were combined. The outcome of using both tools was two samples of events, a sample of contained shower events and a sample of HEST, the combination of which formed the HESE sample. The MDP method was used in order to find the optimal cuts on the BDT output values as well as on the reconstructed shower and track energies. The procedure followed is described below:

1. All events were processed by the shower-track differentiation tool and a differentiator BDT output was applied to each of the events that survived the selection criteria of this tool. The BDT output value was used to select the shower-like and the track-like samples.

2. All events were processed by the MAMBA rejection and a MAMBA BDT output was applied to each of the events that survived the selection criteria posed by the MAMBA rejection. The BDT output value was used to select the contained tracks from the track sample.

3. Minimization of MDP was applied. The MDP was calculated for the different values of the differentiator BDT output, the MAMBA BDT output, the reconstructed track energy (Chapter 7.3) and the *AAshowerFit* energy and for various observation times. The set of these four values leading to a minimum MDP was used to select the final samples of events for each observation time period.

A flow chart of this procedure is depicted in Figure 9.1.

The procedure described above represents a self-consistent method of treating all detected events as each event is classified in only one of the distinct categories of shower-like or HEST or through-going track events. For a 5σ discovery with 50% and 90% probability it has led to an observation time of less than 0.5 years and of 0.8 years respectively. In Table 9.1 the values of the four parameters, above which an event was selected by the MDP, are presented for both cases. For both HEST and shower-like events samples, the number of expected atmospheric muon background events was calculated using the cut and count method and the value derived by the fitted functions as described in Chapters 7.4.4 and 8.3.2 respectively and the maximum of these two values was taken into account. In Figure 9.2 the ratio of the discovery flux normalization factor over Φ_0 for 5 σ discovery with 50% probability (blue) and 90% probability (red) is shown with respect to the observation time. It is clear that an increase in the significance was achieved by combining the HEST event sample with the shower-like event sample. Moreover, a further increase is expected by exploiting the self veto effect for which, in this analysis, the lack of CORSIKA statistics is the limiting factor. This is a point on which KM3NeT is currently investing effort in order to significantly improve the statistics.

A 5σ discovery with 90% probability can be achieved in an observation time of 0.8 years. For this livetime the expectation is 42.49 signal events (39.84 categorized as showers and 2.65 categorized as HEST) and 30.87 background events (28.20 categorized as showers and 2.67 categorized as HEST). From the signal events found as showers approximately 96% is correctly identified and from the starting track sample approximately 94% is correctly identified. For the expected background to the track sample (2.67 events) all atmospheric muons have been eliminated by the cut and count method, so the number of events (0.05

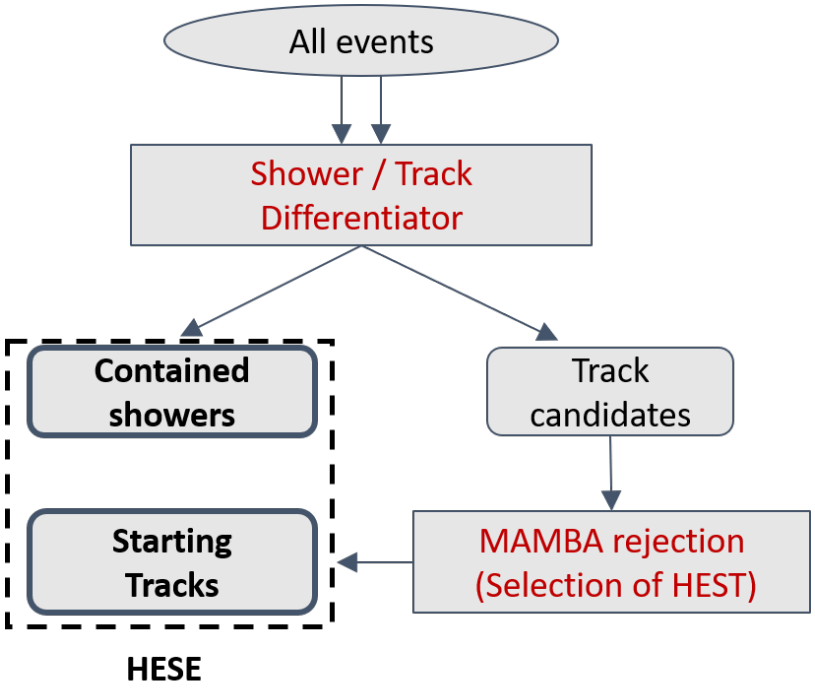

Figure 9.1: A flow chart of the procedure followed to select the HEST and shower-like event samples that form the HESE sample.

5 σ Discovery	"differentiator" BDT output	*AAFit* energy	MAMBA BDT output	Reconstructed track energy
50% Prob. (0.5 years)	0.53	$10^{4.2}$ GeV	0.40	$10^{5.3}$ GeV
90% Prob. (0.8 years)	0.53	$10^{4.2}$ GeV	0.41	$10^{5.1}$ GeV

Table 9.1: Cut values found by the minimization of the MDP for a 5σ discovery with 50% and 90% probability.

events) was found by the fitted function. For the expected background to the shower sample (28.20 events) 1.71 events are atmospheric muons found by the cut and count method (the sum of the fitted functions resulted to slightly less events). A brief summary of the expected signal and background events for both cases is presented in Table 9.2. In the detailed Tables C.1 and C.2, found in Appendix C, the number of signal and background events for each type of events for both shower and starting track samples and for the time of observation needed for both cases are presented.

From the number of expected events shown in Table 9.2, it can be observed that the contribution of HEST events to the HESE signal sample is $\sim$ 6% (when considering the sample derived by the MDP for a 5σ discovery with 90% probability). This is due to the high value cut on the reconstructed track energy, resulting from minimization of the MDP, which is required to minimize the contribution of the atmospheric neutrino events to the track sample. It is worth mentioning that with the same MAMBA BDT output cut (at 0.41), a cut on the reconstructed track energy can be placed as low as $10^{4.7}$ GeV without any atmospheric muon event entering the final event sample, leading to just 0.06 events from the fitted function. As indicated in Figure 9.3, this is expected since the flux of

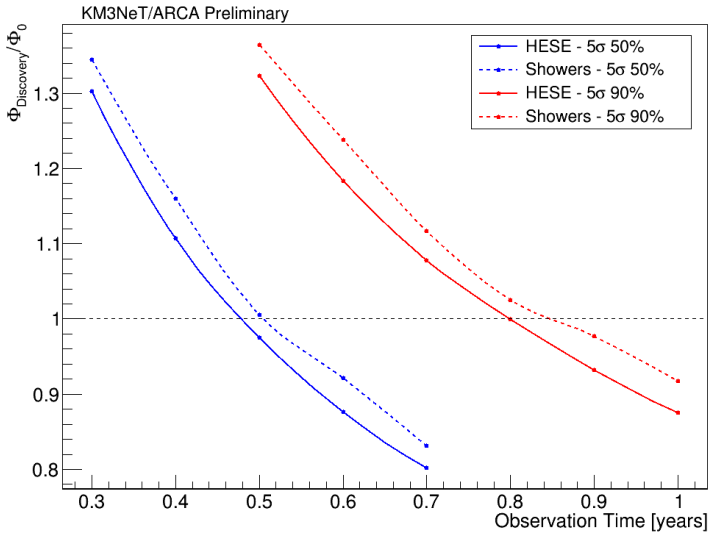

Figure 9.2: Ratio of the discovery flux normalization factor over Φ_0 for a 5 σ discovery with 50% probability (blue) and 90% probability (red) with respect to the observation time in years, for 2 ARCA blocks. Solid lines: Ratio found by HESE analysis, dashed lines: Ratio found using only the shower-like event sample (same as solid lines of Figure 8.12).

	expected signal events		expected background events	
5 σ Discovery	shower sample	track sample	shower sample	track sample
50% Prob. (0.5 years)	24.90	1.07	17.62	0.70
90% Prob. (0.8 years)	39.84	2.65	28.20	2.67

Table 9.2: Number of expected signal and background events for the equivalent livetimes for a 5σ discovery with a probability of 50% and 90% (using the cuts given by the minimization of the MDP) for both shower and HEST event categories.

atmospheric ν_μ events rises much faster than the astrophysical neutrino flux as the neutrino energy decreases. So the minimum MDP is achieved for a lower cut on the *AAshowerfit* energy and a higher cut on the track reconstructed energy in order to minimize the number of atmospheric ν_μ background events. Moreover, the cuts for the shower-like event sample found by the MDP are the same to those found when only the shower-like event sample was used (Table 8.2). This is due to the fact that the shower-like signal sample contains much more events than the HEST signal sample. Thus the minimum MDP for the HESE sample is achieved for those cuts that minimize the MDP for the shower-like sample and then the optimal cuts for the HEST events sample are found in such a way that the number of HEST events added to the much larger shower-like events sample is minimizing the MDP. As a test the optimal cuts for a 5σ discovery with 90% probability were found by requiring the cut values on the reconstructed track and shower energies to be the same. The cut values found by the MDP for the shower-like sample were: $E_{AAshowerfit} \geq 10^{4.2}$ GeV and BDT output ≥ 0.53, the same as above. Also the cut on the MAMBA BDT output was found at the high value of 0.60, minimizing the contribution of atmospheric (and also astrophysical) neutrino track events.

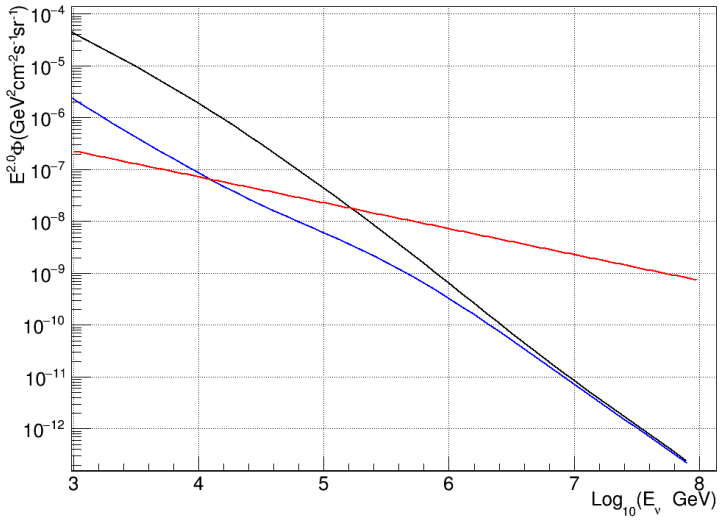

Figure 9.3: Sum of Honda and Enebrg fluxes for atmospheric ν_μ (black), ν_e (blue) events and astrophysical flux used (red).

9.3 Conclusion

A High Energy Starting Events analysis for the full KM3NeT/ARCA (2 building blocks) detector was conducted by combing the tools described in the previous chapters, designed to select high purity samples of HEST and shower-like events. It is expected that KM3NeT/ARCA (2 building blocks) will be able to make a 5σ discovery of the astrophysical neutrino flux with 50% and 90% probability in less than 0.5 and approximately 0.8 years respectively. A decrease of the observation time needed for the discovery is expected if the self veto effect is also taken into account.

Chapter 10

Conclusion

The ARCA/KM3NeT telescope is optimized for the detection of high energy neutrinos from astrophysical sources. An increase of the sensitivity for the detection of ultra high energy neutrinos, like those expected from GRBs, can be achieved by sparsely instrumenting larger volumes. However one of the most cost demanding parts of large underwater telescopes is the sea-bed network thus making the sparse instrumentation of large volumes quite cost ineffective. A cost effective way to instrument large volumes is by using autonomous neutrino detectors like the Gamma Ray Burst Neutrino Telescope (GRBNeT) prototype. GRBNeT was a project aiming to design, build and deploy an autonomous prototype neutrino detector. It was successfully completed with the deployment of a prototype detector on the 28th of October 2015 and the prototype was recovered on the 11th of April 2017, after approximately one and a half years. Since the most crucial part of the whole project was autonomy, very low power electronics were designed and implemented. Simulations were conducted in order to optimize the trigger used at each floor to enhance the potential signal from High Energy (HE) neutrinos from GRBs and at the same time minimize the contribution from all background sources, but not completely eliminate the signal from atmospheric muons. These simulations served to estimate the event rate and provide input to the electronics group for the design of the electronics of the prototype.

The standard approach in KM3NeT to achieve the necessary suppression of the atmospheric muon background for the ARCA telescope to the track channel has been the rejection of all events reconstructed as downgoing. However, a significant suppression of the atmospheric muon background can also be achieved by selecting events for which the neutrino interaction vertex is located inside the detector. A BDT based tool, the MAMBA rejection, was developed to reject through-going muons and select HEST events. Using the MAMBA rejection a study was conducted to estimate the sensitivity and the discovery potential analysis of ARCA to a high energy astrophysical neutrino flux using high purity samples of HEST events. The analysis showed that ARCA is expected to be sensitive to the astrophysical neutrino flux under study in approximately 1.3 years of observation time. It was also shown that ARCA is expected to make a 3σ and a 5σ discovery with 50% probability in less than 3.5 and 9 years respectively, using solely HEST events.

The previous results were obtained by using as background a sample of atmospheric muon events and an "unrelated" sample of atmospheric neutrinos. However, atmospheric muons and neutrinos are produced in the same atmospheric showers, so atmospheric neutrinos reaching the detector from above may be accompanied by muons. In order to explore the self-veto effect the *CORSIKA* program has been used in order to simulate a sample of atmospheric shower events. The impact of several effects was studied including different: i)

High Energy interaction models, ii) models describing the atmosphere above the detector, iii) ways to handle the interaction and decays of charmed particles and iv) Cosmic Ray models have been evaluated. Moreover, comparisons of the neutrino spectra derived by the simulations at the sea level to theoretical models had been conducted in order to identify the optimal simulation parameters. Once the optimal parameters have been identified, the sample of events simulated by using these parameters was further processed (the particles were propagated from the sea level to the detector and the detector response was simulated). The analyses of the sensitivity and the discovery potential using HEST events were repeated using that sample of events as a background sample of atmospheric neutrinos reaching ARCA from above. All neutrino events interacting inside the detector accompanied by muons were rejected from the HEST events sample by the MAMBA rejection. Thus a reduction of the total atmospheric neutrino background of 34% was achieved. Moreover the observation time needed for ARCA to be sensitive to the astrophysical neutrino flux used was decreased to 1.1 years. Finally the observation time expected for ARCA to make a 3σ and a 5σ discovery with 50% probability decreased to less than 2.5 and 6.5 years respectively, which translates to a $\sim 30\%$ decrease in the observation time.

Since for neutrino events interacting inside any neutrino telescope most of the observed and reconstructed events will be shower-like a BDT based tool was also developed to select shower-like and reject track-like events. This tool provides high purity samples of shower-like events having the neutrino interaction vertex inside the instrumented volume of ARCA. Using this sample of events an analysis aiming to extract the discovery potential of ARCA to the high energy astrophysical neutrino flux was conducted. Here the self-veto effect was not taken into account due to the limited statistics of simulated atmospheric showers at the time of the analysis. A 5σ discovery with the ARCA telescope with 50% and 90% probability in approximately 0.5 and less than 0.9 years respectively, was extracted.

Finally, a High Energy Starting Events analysis for ARCA was conducted by using both previously mentioned tools. First, each event was categorized as shower-like or track-like and then the HEST events were selected from the track sample. Thus two high purity samples, one of contained showers and one of HEST events were combined into a HESE sample. Using this sample of events and without considering the self-veto effect, ARCA is expected to make a 5σ discovery with 50% and 90% probability in less than 0.5 and approximately 0.8 years respectively.

The work presented here would profit significantly from an increase of the simulated samples of atmospheric shower events. Due to the limited statistics of the ν_e and $\overline{\nu_e}$ sample of *CORSIKA* simulated events, the self-veto effect has not been taken into account in the HESE analysis. A reduction of the total atmospheric neutrino background of 34% has been achieved for the HEST events sample where the self veto effect was explored. For the shower-like events sample it can only be said that an equivalent reduction of the atmospheric neutrino background is expected. Hence, the self veto effect should be evaluated and the reduction of the atmospheric neutrino background should be quantified using simulated events. The HESE analysis presented in this work offers a self-consistent method of treating all detected events as each event is classified in only one of the distinct categories of shower-like or HEST or through-going events. So, it can be expanded into a global neutrino analysis by incorporating the through-going track events.

Bibliography

[1] Α. Μαστιχιάδης και Ν. Βλαχάκης, *Αστροφυσική Υψηλών Ενεργειών*. Hellenic Academic Libraries Link, 2015.

[2] J. Blumer, R. Engel, and J. R. Horandel, "Cosmic Rays from the Knee to the Highest Energies," *Prog. Part. Nucl. Phys.*, vol. 63, pp. 293–338, 2009.

[3] M. Tanabashi *et al.*, "Review of particle physics," *Phys. Rev. D*, vol. 98, p. 030001, Aug 2018.

[4] T. K. Gaisser, R. Engel, and E. Resconi, *Cosmic Rays and Particle Physics*. Cambridge University Press, 2 ed., 2016.

[5] U. F. Katz and C. Spiering, "High-Energy Neutrino Astrophysics: Status and Perspectives," *Prog. Part. Nucl. Phys.*, vol. 67, pp. 651–704, 2012.

[6] `http://courses.atlas.illinois.edu/fall2009/astr/astr596npa/LECTURES/Lect39.html`. Accessed on: 2019-05-06.

[7] A. M. Hillas, "Can diffusive shock acceleration in supernova remnants account for high-energy galactic cosmic rays?," *J. Phys.*, vol. G31, pp. R95–R131, 2005.

[8] T. K. Gaisser, "Spectrum of cosmic-ray nucleons, kaon production, and the atmospheric muon charge ratio," *Astropart. Phys.*, vol. 35, pp. 801–806, 2012.

[9] T. K. Gaisser *et al.*, "Cosmic Ray Energy Spectrum from Measurements of Air Showers," *Front. Phys.(Beijing)*, vol. 8, pp. 748–758, 2013.

[10] M. S. Longair, *High Energy Astrophysics*. Feb. 2011.

[11] U. Katz, "Future neutrino telescopes in water and ice," June 2018.

[12] Α. Μαστιχιάδης, *Φυσική των Αστέρων*. Πανεπιστήμιο Αθηνών, 2013.

[13] Barrios Martí, Javier, *Search for cosmic sources in neutrino telescopes and time calibration in the ANTARES neutrino telescope*. PhD thesis, Universitat de València, 2018.

[14] E. Waxman and J. N. Bahcall, "High-energy neutrinos from cosmological gamma-ray burst fireballs," *Phys. Rev. Lett.*, vol. 78, pp. 2292–2295, 1997.

[15] Α. Μαστιχιάδης, *Αστοφυσική ΙΙ, σημειώσεις από ατις παραδώσεις του μαθήματος*. 2001.

[16] M. Kachelriess, "Lecture notes on high energy cosmic rays," 2008.

[17] B. P. Abbott *et al.*, "Multi-messenger Observations of a Binary Neutron Star Merger," *Astrophys. J.*, vol. 848, no. 2, p. L12, 2017.

[18] M. G. Aartsen *et al.*, "Multimessenger observations of a flaring blazar coincident with high-energy neutrino IceCube-170922A," *Science*, vol. 361, no. 6398, p. eaat1378, 2018.

[19] "Gamma-ray Coordinates Network." `https://gcn.gsfc.nasa.gov/amon.html`. Accessed: 2019-05-15.

[20] K. Murase *et al.*, "Blazar Flares as an Origin of High-Energy Cosmic Neutrinos?," *Astrophys. J.*, vol. 865, no. 2, p. 124, 2018.

[21] P. Padovani *et al.*, "TXS 0506+056, the first cosmic neutrino source, is not a BL Lac," *Mon. Not. Roy. Astron. Soc.*, vol. 484, no. 1, pp. L104–L108, 2019.

[22] D. Soldin, "Atmospheric Muons Measured with IceCube," in *20th International Symposium on Very High Energy Cosmic Ray Interactions (ISVHECRI 2018) Nagoya, Japan, May 21-25, 2018*, 2018.

[23] M. Honda *et al.*, "Calculation of atmospheric neutrino flux using the interaction model calibrated with atmospheric muon data," *Phys. Rev. D*, vol. 75, p. 043006, Feb 2007.

[24] R. Enberg *et al.*, "Prompt neutrino fluxes from atmospheric charm," *Phys. Rev. D*, vol. 78, p. 043005, Aug 2008.

[25] M. G. Aartsen *et al.*, "An All-Sky Search for Three Flavors of Neutrinos from Gamma-Ray Bursts with the IceCube Neutrino Observatory," *Astrophys. J.*, vol. 824, no. 2, p. 115, 2016.

[26] Y. S. Jeong, A. Bhattacharya, R. Enberg, C. S. Kim, M. H. Reno, I. Sarcevic, and A. Stasto, "Prompt atmospheric neutrino flux," *PoS*, vol. ICHEP2016, p. 083, 2016.

[27] A. Bhattacharya, R. Enberg, Y. S. Jeong, C. S. Kim, M. H. Reno, I. Sarcevic, and A. Stasto, "Prompt atmospheric neutrino fluxes: perturbative QCD models and nuclear effects," *JHEP*, vol. 11, p. 167, 2016.

[28] Y. S. Jeong, A. Bhattacharya, R. Enberg, C. S. Kim, M. H. Reno, I. Sarcevic, and A. Stasto, "Prompt atmospheric neutrino flux from the various QCD models," *EPJ Web Conf.*, vol. 141, p. 07002, 2017.

[29] D. Stavropoulos, "Μελέτη της απόδοσης των οπτικών στοιχείωντου ανιχνευτή ARCA του υποθλάσσιου πειράματος νετρίνο KM3NeT.," Master Thesis, National Technical Univercity of Athens, 2019.

[30] F. Vannucci, "Interactions of neutrinos with matter," *Prog. Part. Nucl. Phys.*, vol. 95, pp. 1–47, 2017.

[31] J. A. Formaggio and G. P. Zeller, "From eV to EeV: Neutrino Cross Sections Across Energy Scales," *Rev. Mod. Phys.*, vol. 84, pp. 1307–1341, 2012.

[32] S. L. Glashow, "Resonant scattering of antineutrinos," *Phys. Rev.*, vol. 118, pp. 316–317, Apr 1960.

[33] I. F. M. Albuquerque, J. Lamoureux, and G. F. Smoot, "Astrophysical neutrino event rates and sensitivity for neutrino telescopes," *Astrophys. J. Suppl.*, vol. 141, pp. 195–209, 2002.

[34] R. Gandhi, C. Quigg, M. H. Reno, and I. Sarcevic, "Ultrahigh-energy neutrino interactions," *Astropart. Phys.*, vol. 5, pp. 81–110, 1996.

[35] E. Drakopoulou, *Muon and Neutrino Energy Reconstruction for KM3NeT.* PhD thesis, NATIONAL TECHNICAL UNIVERSITY OF ATHENS, 2016.

[36] M. G. Aartsen *et al.*, "A combined maximum-likelihood analysis of the high-energy astrophysical neutrino flux measured with IceCube," *Astrophys. J.*, vol. 809, no. 1, p. 98, 2015.

[37] B. Baret and V. Van Elewyck, "High-energy neutrino astronomy: Detection methods and first achievements," *Rept. Prog. Phys.*, vol. 74, p. 046902, 2011.

[38] . Τσιριγώτης, *Λειτουργικά χαρακτηριστικά και ανιχνευτική ικανότητα πρότυπου ανιχνευτή του υποθαλάσσιου τηλεσκοπίου νετρίνων ΝΕΣΤΩΡ: Μέτρηση της ροής των ατμοσφαιρικών μιονίων σε θαλάσσιο βάθος* 3800m. PhD thesis, 2004.

[39] "Report on evaluation of existing water, oceanographic, biological and geological data from candidate sites." `https://indico.cern.ch/event/808299/contributions/3364899/attachments/1815976/2968018/WP5_Deliverable5_1_0904071.pdf`. Accessed on: 2018-5-15.

[40] A. Roberts, "The Birth of high-energy neutrino astronomy: A Personal history of the DUMAND project," *Rev. Mod. Phys.*, vol. 64, pp. 259–312, 1992.

[41] A. D. Avrorin *et al.*, "Baikal-GVD: first results and prospects," *EPJ Web Conf.*, vol. 209, p. 01015, 2019.

[42] E. Andres, "The amanda neutrino telescope: Principle of operation and first results," *Astroparticle Physics*, vol. 13, 06 1999.

[43] L. K. Resvanis *et al.*, "NESTOR: A Neutrino particle astrophysics underwater laboratory for the Mediterranean," *Nucl. Phys. Proc. Suppl.*, vol. 35, pp. 294–300, 1994.

[44] P. Sapienza, "Status of the NEMO Project," in *Proceedings, 20th European Cosmic Ray Symposium (ECRS 2006): Lisbon, Portugal, September 5-8, 2006*, pp. S5–41, 2006.

[45] F. Blondeau, "The ANTARES demonstrator: Towards a high-energy undersea neutrino telescope," *Prog. Part. Nucl. Phys.*, vol. 40, pp. 413–414, 1998.

[46] A. Kouchner, "Recent Results from the Antares Neutrino Telescope," *EPJ Web Conf.*, vol. 207, p. 01001, 2019.

[47] M. Spurio, "Overview of ANTARES neutrino telescope: multimessenger results," *PoS*, vol. NOW2018, p. 055, 2019.

[48] M. Spurio, "Results from the ANTARES neutrino telescope," *EPJ Web Conf.*, vol. 116, p. 11006, 2016.

[49] T. Pradier, "The Antares Neutrino Telescope and Multi-Messenger Astronomy," *Class. Quant. Grav.*, vol. 27, p. 194004, 2010.

[50] A. Achterberg *et al.*, "First Year Performance of The IceCube Neutrino Telescope," *Astropart. Phys.*, vol. 26, pp. 155–173, 2006.

[51] A. Ishihara, "Recent results from searches for high energy neutrinos with IceCube," *PoS*, vol. TEXAS2010, p. 213, 2010.

[52] "IceCube web site." `https://icecube.wisc.edu`. Accessed: 2019-05-30.

[53] N. WANDKOWSKY, "Latest results on astrophysical neutrinos using high-energy events with contained vertices," June 2018.

[54] J. STACHURSKA, "New measurement of the flavor composition of high-energy neutrino events with contained vertices in IceCube," June 2018.

[55] J. Stachurska, "IceCube High Energy Starting Events at 7.5 Years – New Measurements of Flux and Flavor," *EPJ Web Conf.*, vol. 207, p. 02005, 2019.

[56] C. Haack and C. Wiebusch, "A measurement of the diffuse astrophysical muon neutrino flux using eight years of IceCube data.," *PoS*, vol. ICRC2017, p. 1005, 2018.

[57] M. G. Aartsen *et al.*, "Observation and Characterization of a Cosmic Muon Neutrino Flux from the Northern Hemisphere using six years of IceCube data," *Astrophys. J.*, vol. 833, no. 1, p. 3, 2016.

[58] "KM3NeT web site." `https://www.km3net.org`. Accessed: 2019-04-30.

[59] "ANTARES web site." `https://www.km3net.org`. Accessed: 2019-04-30.

[60] "NESTOR web site." `http://www.inp.demokritos.gr/nestor/`. Accessed: 2018-09-30.

[61] P. Bagley *et al.*, "KM3NeT: Technical Design Report for a Deep-Sea Research Infrastructure in the Mediterranean Sea Incorporating a Very Large Volume Neutrino Telescope," 2009.

[62] R. Bruijn and D. van Eijk, "The KM3NeT Multi-PMT Digital Optical Module," *PoS*, vol. ICRC2015, p. 1157, 2016.

[63] D. Vivolo, "The KM3NeT Digital Optical Module," *EPJ Web Conf.*, vol. 116, p. 01002, 2016.

[64] P. Amram *et al.*, "The ANTARES optical module," *Nucl. Instrum. Meth.*, vol. A484, pp. 369–383, 2002.

[65] R. Abbasi *et al.*, "The IceCube Data Acquisition System: Signal Capture, Digitization, and Timestamping," *Nucl. Instrum. Meth.*, vol. A601, pp. 294–316, 2009.

[66] S. Aiello *et al.*, "Characterization of the 80-mm diameter hamamatsu pmts for the km3net project," *AIP Conference Proceedings*, vol. 1630, pp. 118–121, 01 2014.

[67] S. Adrián-Martínez *et al.*, "Deep sea tests of a prototype of the KM3NeT digital optical module," *Eur. Phys. J.*, vol. C74, no. 9, p. 3056, 2014.

[68] M. Jongen, "Measurement of the depth dependence of coincidence rates induced by atmospheric muons with the first two KM3NeT Detection Units," *PoS*, vol. ICRC2017, p. 1018, 2018.

[69] S. Adrian-Martinez *et al.*, "Letter of intent for KM3NeT 2.0," *J. Phys.*, vol. G43, no. 8, p. 084001, 2016.

[70] K. Pikounis *et al.*, "GRBNeT – A prototype for an autonomous underwater neutrino detector," *EPJ Web Conf.*, vol. 116, p. 09004, 2016.

[71] K. Manolopoulos *et al.*, "Digital and Analog Electronics for an autonomous,cdeep-sea, Gamma Ray Burst Neutrino prototype detector," *EPJ Web Conf.*, vol. 116, p. 05010, 2016.

[72] "GRBNet web site." `http://www.inp.demokritos.gr/web2/grbnet/index.html`. Accessed: 2018-09-30.

[73] E. G. Anassontzis *et al.*, "The optical module for the NESTOR neutrino telescope," *Nucl. Instrum. Meth.*, vol. A479, pp. 439–455, 2002.

[74] G. Aggouras *et al.*, "LAERTIS, a multidisciplinary station," *Nucl. Instrum. Meth.*, vol. A567, pp. 468–473, 2006.

[75] `https://www.avnet.com/shop/us/products/avnet-engineering-services/aes-s6ev-lx16-g-3074457345630217084/`. Accessed: 2018-09-30.

[76] G. Carminati *et al.*, "Atmospheric MUons from PArametric formulas: A Fast GEnerator for neutrino telescopes (MUPAGE)," *Comput. Phys. Commun.*, vol. 179, pp. 915–923, 2008.

[77] A. Gazizov and M. P. Kowalski, "ANIS: High energy neutrino generator for neutrino telescopes," *Comput. Phys. Commun.*, vol. 172, pp. 203–213, 2005.

[78] D. Chirkin and W. Rhode, "Muon Monte Carlo: A High-precision tool for muon propagation through matter," 2004.

[79] C. Kopper, "A software framework for KM3NeT," *Nucl. Instrum. Meth.*, vol. A602, pp. 107–110, 2009.

[80] P. Bagley *et al.*, "KM3NeT: Technical Design Report for a Deep-Sea Research Infrastructure in the Mediterranean Sea Incorporating a Very Large Volume Neutrino Telescope," 2009.

[81] E. Waxman and J. N. Bahcall, "High-energy neutrinos from astrophysical sources: An Upper bound," *Phys. Rev.*, vol. D59, p. 023002, 1999.

[82] E. Presani, *Neutrino Induced Showers From Gamma-Ray Bursts*. PhD thesis, Amsterdam U., 2011.

[83] A. Sinopoulou, "Μελέτη της δυνατότητας ανίχνευσηςνετρίνο πολύ υψηλής ενέργειας με την πρωτότυπη ανιχνευτκή συστοιχία GRBNeT," Thesis, National Technical Univercity of Athens, 2016.

[84] ""R/V AEGAEO" web site." `https://www.hcmr.gr/en/equipment/researchvessels_underwatervehicles/rvs/`. Accessed: 2018-09-30.

[85] "GRBNet deployment position on Google maps." https://www.google.com/maps/place/36%C2%B050'00.7%22N+21%C2%B030'00.2%22E/@36.913519,21.7959622,47820m/data=!3m1!1e3!4m5!3m4!1s0x0:0x0!8m2!3d36.8335333!4d21.50005?hl=enl. Accessed: 2018-09-30.

[86] C. M. M. Colnard, *Ultra-High Energy Neutrino Simulations*. PhD thesis, Amsterdam U., 2009.

[87] A. Margiotta, "Common simulation tools for large volume neutrino detectors," *Nucl. Instrum. Meth.*, vol. A725, pp. 98–101, 2013.

[88] H. L. Lai *et al.*, "Global QCD analysis and the CTEQ parton distributions," *Phys. Rev.*, vol. D51, pp. 4763–4782, 1995.

[89] G. D. Barr, *The Separation of Signals and Background in a Nucleon Decay Experiment*. PhD thesis, Oxford U., 1987.

[90] A. M. Dziewonski and D. L. Anderson, "Preliminary reference earth model," *Phys. Earth Planet. Interiors*, vol. 25, pp. 297–356, 1981.

[91] P. Antonioli *et al.*, "A Three-dimensional code for muon propagation through the rock: Music," *Astropart. Phys.*, vol. 7, pp. 357–368, 1997.

[92] C. James, "KM3NeT_SIM_2016_001-genhen_v7r5_v1," *Internal note*, 2016.

[93] Y. Becherini *et al.*, "A Parameterisation of single and multiple muons in the deep water or ice," *Astropart. Phys.*, vol. 25, pp. 1–13, 2006.

[94] D. Heck *et al.*, "CORSIKA: A Monte Carlo code to simulate extensive air showers," 1998.

[95] T. Heid, *PHD thesis under preparation*. PhD thesis, ECAP.

[96] D. Bailey, *Monte Carlo tools and analysis methods for understanding the ANTARES experiment and predicting its sensitivity to dark matter*. PhD thesis, Oxford U., 2002.

[97] M. de Jong, "Jpp." https://www.nikhef.nl/~mjg/Jpp/ws/doc/Jpp.pdf. Accessed on: 2018-11-30.

[98] M. de Jong, "Trigger." https://www.nikhef.nl/~mjg/Jpp/ws/doc/JTrigger.pdf. Accessed on: 2018-11-30.

[99] C. De Sio, *Event triggering and deep learning for particle identification in KM3NeT*. PhD thesis, Salerno U., 2018.

[100] M. de Jong, "Reconstruction of muon trajectories." https://www.nikhef.nl/~mjg/Jpp/ws/doc/JGandalf.pdf. Accessed on: 2018-11-30.

[101] A. Sinopoulou, "Μελέτη βελτιστοποιησης του ανιχνευτή KM3NeT για την ανίχνευση νετρίνων υψηλών ενεργειών.," Master Thesis, National Technical Univercity of Athens, 2018.

[102] M. de Jong, "Muon energy estimator." https://www.nikhef.nl/~mjg/Jpp/ws/doc/JEnergy.pdf. Accessed on: 2018-11-30.

[103] D. Heck and T. Pierog, *Extensive Air Shower Simulation with CORSIKA: A User's Guide (Version 74xxx from March 2, 2015).* KIT - Universität des Landes Baden-Württemberg undnationales Forschungszentrum in der Helmholtz-Gemeinschaft.

[104] D. Heck and T. Pierog, *Extensive Air Shower Simulation with CORSIKA: A User's Guide (Version 7.5xxx from February 26, 2016).* KIT - Universität des Landes Baden-Württemberg undnationales Forschungszentrum in der Helmholtz-Gemeinschaft.

[105] S. I. Klimushin *et al.*, "Precise parametrizations of muon energy losses in water," in *27th International Cosmic Ray Conference (ICRC 2001) Hamburg, Germany, August 7-15, 2001*, p. 1009, 2001. [3,1009(2001)].

[106] S. Maus *et al.*, *The US/UK World Magnetic Model for 2010-2015.* NOAA Technical Report NESDIS/NGDC.

[107] D. R. Marsh *et al.*, "Climate change from 1850 to 2005 simulated in cesm1(waccm)," *Atmospheric Sciences*, vol. 26, no. 19, p. 7372–7391, 2013.

[108] F. Riehn *et al.*, "A new version of the event generator Sibyll," *PoS*, vol. ICRC2015, p. 558, 2016.

[109] T. Pierog *et al.*, "EPOS LHC: Test of collective hadronization with data measured at the CERN Large Hadron Collider," *Phys. Rev.*, vol. C92, no. 3, p. 034906, 2015.

[110] S. Ostapchenko, "Monte Carlo treatment of hadronic interactions in enhanced Pomeron scheme: I. QGSJET-II model," *Phys. Rev.*, vol. D83, p. 014018, 2011.

[111] R. Coniglione, "Efit correction, muon energy at the can." Presentaion at the High Energy KM3NeT group: `https://indico.cern.ch/event/522508/contributions/2150903/attachments/1264267/1870558/26-April-2016_My_Ef_at_can.pdf`. Accessed on: 2018-11-30.

[112] A. Trovato, *Development of reconstruction algorithms for large volume neutrino telescopes and their application to the KM3NeT detector.* PhD thesis, Catania U., SSC, 2014.

[113] S. Theodoridis and K. Koutroumbas, *Pattern Recognition, Fourth Edition.* Orlando, FL, USA: Academic Press, Inc., 4th ed., 2008.

[114] A. Hoecker *et al.*, "TMVA: Toolkit for Multivariate Data Analysis," *PoS*, vol. ACAT, p. 040, 2007.

[115] R. Brun and F. Rademakers, "ROOT: An object oriented data analysis framework," *Nucl. Instrum. Meth.*, vol. A389, pp. 81–86, 1997.

[116] G. C. Hill and K. Rawlins, "Unbiased cut selection for optimal upper limits in neutrino detectors: The Model rejection potential technique," *Astropart. Phys.*, vol. 19, pp. 393–402, 2003.

[117] G. C. Hill *et al.*, "Examining the balance between optimising an analysis for best limit setting and best discovery potential," in *Statistical Problems in Particle Physics, Astrophysics and Cosmology (PHYSTAT 05): Proceedings, Oxford, UK, September 12-15, 2005*, pp. 108–111, 2005.

[118] G. J. Feldman and R. D. Cousins, "A Unified approach to the classical statistical analysi of small signals," *Phys. Rev.*, vol. D57, pp. 3873–3889, 1998.

[119] "Interanl km3net web pages for the bunchmark neutirno astrophysical fluxes." `https://wiki.km3net.de/index.php/HE_Astrophysics/ARCA_High_Energy_Analysis/AfterLoI#Benchmark_fluxes`. Accessed on: 2018-12-30.

[120] L. A. Fusco, *Search for a diffuse neutrino emission in the Southern Sky with the ANTARES telescope*. PhD thesis, OCEM, Bologna, 2016-03-26.

[121] J. Mańczak, "Sensitivity study for the Glashow Resonance detection at KM3NeT," Master Thesis, University of Warsaw, Faculty of Physics, 2018.

[122] Barrios Martí, Javier. private communication.

[123] K. J. Meagher, "Neutrino Astronomy with IceCube," *IAU Symp.*, vol. 324, pp. 322–329, 2016.

[124] T. YUAN, "New measurements with high-energy neutrinos in IceCube," June 2018.

Appendix A

Number of Expected Signal and Background HEST events

In the tables below the number of expected signal and background HEST events after imposing the cuts found by the minimization of the MRP and the MDP methods are presented.

Type of event	Signal	Background
ν_μ CC	3.60	9.45
ν_μ NC	0.01	0.01
$\overline{\nu_\mu}$ CC	3.05	4.89
$\overline{\nu_\mu}$ NC	0.02	0.01
all ν_μ	6.68	14.36
ν_e CC	0.11	0.02
ν_e NC	0.01	0.00
$\overline{\nu_e}$ CC	0.28	0.02
$\overline{\nu_e}$ NC	0.01	0.00
all ν_e	0.41	0.04
ν_τ CC $\rightarrow \mu$	0.26	-
ν_τ CC$\rightarrow$ shower	0.09	-
ν_τ NC	0.01	-
$\overline{\nu_\tau}$ CC $\rightarrow \mu$	0.25	-
$\overline{\nu_\tau}$ CC$\rightarrow$ shower	0.09	-
$\overline{\nu_\tau}$ NC	0.01	-
all ν_τ	0.71	-
μ_{atm} $E_{bundle} \geq 10$ TeV	-	0.00
μ_{atm} $E_{bundle} \geq 50$ TeV	-	0.08
total	7.80	14.48

Table A.1: Number of expected signal and background events, for the cuts found by the minimization of the MRF for 90% *CL, for a livetime of* 1.3 *years.*

	3σ discovery		5σ discovery	
Type of event	Signal	Background	Signal	Background
ν_μ CC	6.07	9.87	16.14	26.08
ν_μ NC	0.02	0.02	0.07	0.06
$\overline{\nu_\mu}$ CC	5.47	5.55	14.62	14.93
$\overline{\nu_\mu}$ NC	0.03	0.01	0.07	0.03
all ν_μ	11.59	15.45	30.90	41.10
ν_e CC	0.19	0.03	0.50	0.08
ν_e NC	0.02	0.00	0.05	0.01
$\overline{\nu_e}$ CC	0.60	0.05	1.62	0.13
$\overline{\nu_e}$ NC	0.02	0.00	0.05	0.01
all ν_e	0.83	0.08	2.22	0.23
ν_τ CC $\rightarrow \mu$	0.43	-	1.14	-
ν_τ CC$\rightarrow$ shower	0.16	-	0.42	-
ν_τ NC	0.02	-	0.06	-
$\overline{\nu_\tau}$ CC $\rightarrow \mu$	0.40	-	1.08	-
$\overline{\nu_\tau}$ CC$\rightarrow$ shower	0.17	-	0.44	-
$\overline{\nu_\tau}$ NC	0.02	-	0.06	-
all ν_τ	1.20	-	3.20	-
μ_{atm} $E_{bundle} \geq 10$ TeV	-	0.00	-	0.00
μ_{atm} $E_{bundle} \geq 50$ TeV	-	0.64	-	0.00
total	13.62	16.17	36.32	41.33

Table A.2: Number of expected signal and background events, for the cuts found by the minimization of the MDP for a discovery with 3σ and 5σ significance with 50% probability, for a livetime of 3.2 and 8.7 years respectively.

Type of event	Signal	Background
ν_μ CC	3.75	9.25 including 1.11 from CORSIKA sample
ν_μ NC	0.01	0.01
$\overline{\nu_\mu}$ CC	2.96	3.66 including 0.44 from CORSIKA sample
$\overline{\nu_\mu}$ NC	0.01	0.01
all ν_μ	6.73	12.93
ν_e CC	0.11	0.02
ν_e NC	0.01	0.00
$\overline{\nu_e}$ CC	0.25	0.02
$\overline{\nu_e}$ NC	0.01	0.00
all ν_e	0.38	0.04
ν_τ CC $\rightarrow \mu$	0.26	-
ν_τ CC$\rightarrow$ shower	0.08	-
ν_τ NC	0.01	-
$\overline{\nu_\tau}$ CC $\rightarrow \mu$	0.27	-
$\overline{\nu_\tau}$ CC$\rightarrow$ shower	0.08	-
$\overline{\nu_\tau}$ NC	0.01	-
all ν_τ	0.71	
μ_{atm} $E_{bundle} \geq 10$ TeV	-	0.00
μ_{atm} $E_{bundle} \geq 50$ TeV	-	0.22
total	7.82	13.19

Table A.3: Number of expected signal and background events, for the cuts found by the minimization of the MRF for 90% *CL with the self-vetoes approach, for a livetime of* 1.1 *years.*

Type of event	Signal	Background
ν_μ CC	11.55	11.39 including 2.58 from CORSIKA sample
ν_μ NC	0.05	0.04
$\overline{\nu_\mu}$ CC	10.49	8.04 including 2.18 from CORSIKA sample
$\overline{\nu_\mu}$ NC	0.05	0.02
all ν_μ	22.14	19.49
ν_e CC	0.36	0.06
ν_e NC	0.04	0.01
$\overline{\nu_e}$ CC	1.16	0.09
$\overline{\nu_e}$ NC	0.04	0.00
all ν_e	1.60	0.16
ν_τ CC $\rightarrow \mu$	0.81	-
ν_τ CC$\rightarrow$ shower	0.30	-
ν_τ NC	0.05	-
$\overline{\nu_\tau}$ CC $\rightarrow \mu$	0.77	-
$\overline{\nu_\tau}$ CC$\rightarrow$ shower	0.32	-
$\overline{\nu_\tau}$ NC	0.04	-
all ν_τ	2.29	-
μ_{atm} $E_{bundle} \geq 10$ TeV	-	0.00
μ_{atm} $E_{bundle} \geq 50$ TeV	-	0.00
total	26.03	19.65

Table A.4: Number of expected signal and background events, for the cuts found by the minimization of the MDP for a discovery with 5σ *significance with* 50% *probability exploiting the self-vetoes, for a livetime of* 6.3 *years. Since the minimization of the MDP for both* 3σ *and* 5σ *resulted to the same cuts, the number of expected signal and background events for a* 3σ *discovery with* 50% *probability (for a livetime of* 2.3 *years) can be easily calculated just by scaling each number with* 2.3/6.3.

Appendix B

Number of Expected Signal and Background shower-like events

In the table below the number of expected signal and background shower-like events after imposing the cuts found by the minimization of the MDP methods are presented.

	90% prob. (0.9 years)	
Type of event	Signal	Background
ν_μ CC	0.75	5.22
ν_μ NC	1.49	8.14
$\overline{\nu_\mu}$ CC	0.59	2.25
$\overline{\nu_\mu}$ NC	1.12	3.12
all ν_μ	3.95	18.73
ν_e CC	12.24	5.94
ν_e NC	1.49	0.54
$\overline{\nu_e}$ CC	10.63	4.26
$\overline{\nu_e}$ NC	1.13	0.33
all ν_e	25.49	11.07
ν_τ CC $\rightarrow \mu$	0.25	-
ν_τ CC$\rightarrow$ shower	6.89	-
ν_τ NC	1.50	-
$\overline{\nu_\tau}$ CC $\rightarrow \mu$	0.15	-
$\overline{\nu_\tau}$ CC$\rightarrow$ shower	5.43	-
$\overline{\nu_\tau}$ NC	1.16	-
all ν_τ	15.38	-
μ_{atm} $E_{bundle} \geq 10$ TeV	-	0
μ_{atm} $E_{bundle} \geq 50$ TeV	-	1.92
total	44.82	31.72

Table B.1: Number of expected signal and background events, for all types of events, after applying the cuts found by the minimization of the MDP for 5σ *with* 90% *probability (livetime of* 0.9 *years). Since the minimization of the MDP for* 5σ *with both* 90% *and* 50% *probability resulted to the same cuts, the expected number of events for the latter (livetime of* 0.5 *years) can be easily calculated just by scaling each number with* 5/9.

Appendix C

Number of Expected Signal and Background HESE events

In the tables below, the number of expected signal and background HESE events after imposing the cuts found by the minimization of the MDP for a 5σ discovery with both 50% and 90% probability are presented.

	shower sample		track sample	
Type of event	Signal	Background	Signal	Background
ν_μ CC	0.42	2.90	0.47	0.37
ν_μ NC	0.83	4.52	0.00	0.00
$\overline{\nu_\mu}$ CC	0.33	1.26	0.45	0.23
$\overline{\nu_\mu}$ NC	0.62	1.73	0.00	0.00
all ν_μ	2.20	10.41	0.92	0.60
ν_e CC	6.80	3.30	0.01	0.00
ν_e NC	0.83	0.30	0.00	0.00
$\overline{\nu_e}$ CC	5.9	2.36	0.05	0.00
$\overline{\nu_e}$ NC	0.63	0.18	0.00	0.00
all ν_e	14.16	6.14	0.06	0.00
ν_τ CC $\rightarrow \mu$	0.14	-	0.04	-
ν_τ CC$\rightarrow$ shower	3.83	-	0.01	-
ν_τ NC	0.83	-	0.00	-
$\overline{\nu_\tau}$ CC $\rightarrow \mu$	0.08	-	0.03	-
$\overline{\nu_\tau}$ CC$\rightarrow$ shower	3.02	-	0.01	-
$\overline{\nu_\tau}$ NC	0.64	-	0.00	-
all ν_τ	8.54	-	0.09	-
μ_{atm} $E_{bundle} \geq 10$ TeV	-	0	-	0
μ_{atm} $E_{bundle} \geq 50$ TeV	-	1.07	-	0.10
total	24.90	17.62	1.07	0.70

Table C.1: Number of expected signal and background events for a livetime of 0.5 *years, for all types of events, categorized as either shower-like or HEST. The cuts used were found by the minimum MDP for a* 5σ *discovery with* 50% *probability.*

	shower sample		track sample	
Type of event	Signal	Background	Signal	Background
ν_μ CC	0.67	4.64	1.22	1.58
ν_μ NC	1.32	7.24	0.00	0.00
$\overline{\nu_\mu}$ CC	0.53	2.00	1.10	1.04
$\overline{\nu_\mu}$ NC	0.99	2.78	0.00	0.00
all ν_μ	3.51	16.66	2.32	2.62
ν_e CC	10.88	5.28	0.02	0.00
ν_e NC	1.32	0.48	0.00	0.00
$\overline{\nu_e}$ CC	9.45	3.78	0.08	0.00
$\overline{\nu_e}$ NC	1,01	0.29	0.00	0.00
all ν_e	22.66	9.83	0.10	0.00
ν_τ CC $\rightarrow \mu$	0.22	-	0.09	-
ν_τ CC$\rightarrow$ shower	6.12	-	0.03	-
ν_τ NC	1.33	-	0.00	-
$\overline{\nu_\tau}$ CC $\rightarrow \mu$	0.14	-	0.08	-
$\overline{\nu_\tau}$ CC$\rightarrow$ shower	4.83	-	0.03	-
$\overline{\nu_\tau}$ NC	1.03	-	0.00	-
all ν_τ	13.67	-	0.23	-
μ_{atm} $E_{bundle} \geq 10$ TeV	-	0	-	0
μ_{atm} $E_{bundle} \geq 50$ TeV	-	1.71	-	0.05
total	39.84	28.20	2.65	2.67

Table C.2: Number of expected signal and background events for a livetime of 0.8 *years, for all types of events, categorized as either shower-like or HEST. The cuts used were found by the minimum MDP for a* 5σ *discovery with a* 90% *probability.*